Microseismic full waveform modeling and location

Peidong Shi

Submitted in accordance with the requirements for the degree of
Doctor of Philosophy

The University of Leeds
School of Earth and Environment

December 2018

The candidate confirms that the work submitted is his own, except where work which has formed part of jointly authored publications has been included. The contribution of the candidate and the other authors to this work has been explicitly indicated below. The candidate confirms that appropriate credit has been given within the thesis where reference has been made to the work of others.

The work in Chapter 2 of the thesis has appeared in publication as follows:
Shi, P., D. Angus, A. Nowacki, S. Yuan and Y. Wang (2018), *Microseismic full waveform modeling in anisotropic media with moment tensor implementation*, Surveys in Geophysics, 39(4), 567-611, doi:10.1007/s10712-018-9466-2.

I developed the ideas and methodology in this paper, in particular the implementation of symmetrical and arbitrary moment tensor sources in the staggered grid of the forward modeling scheme. I wrote the forward modeling codes and conducted numerical modelings. I analysed the modeling results, wrote the manuscript and created all of the figures. The co-authors provided comments and suggestions, which improved the manuscript.

The work in Chapter 3 of the thesis has appeared in publication as follows:
Shi, P., D. Angus, S. Rost, A. Nowacki and S. Yuan (2018), *Automated seismic waveform location using multichannel coherency migration (MCM)-I: theory*, Geophysical Journal International, doi:10.1093/gji/ggy132.

I developed the ideas and methodology of an automated microseismic location method using waveform coherency. I proposed to stack the waveform coherency between different stations for imaging the microseismic sources. I also extend this method to a more general multichannel/multidimensional scenario. I wrote the MCM location codes, and conducted numerical modelings and testings. I wrote the manuscript and created all the figures. The co-authors provided valuable suggestions on how to test, evaluate and compare the performance of this method in different situations. The co-authors also provided useful suggestions to improve the manuscript.

The work in Chapter 4 of the thesis has appeared in publication as follows:
Shi, P., A. Nowacki, S. Rost and D. Angus (2018), *Automated seismic waveform location using multichannel coherency migration (MCM)-II: application to induced and volcano-tectonic seismicity*, Geophysical Journal International, doi:10.1093/gji/ggy507.

I developed the ideas and methodology in this paper. I conducted the whole seismic event location processes on two real cases and analysed the results. I wrote the manuscript and created all the figures. The co-authors helped to choose the suitable real datasets and also provided valuable comments and suggestions to improve the manuscript and analysis.

Acknowledgements

After three years and two months, my PhD journey finally comes to an end. Looking back, I find it is harder to accomplish a PhD study than I first thought. In the past three years, I met with many difficulties either in research or in life. But luckily, I have overcome them and find my way to the destination. Studying abroad is not an easy thing, and I am glad to have managed it. I feel so happy and lucky to have studied here in Leeds, where lots of good memories have been generated and lots of unforgettable experience have been gained.

Firstly of all, I must thank my supervisors Andy Nowacki, Sebastian Rost and Doug Angus for their generous help and support. Without their help and guidance, I couldn't have finished my research. We have lots of fruitful discussions which have inspired me a lot and helped to shape my thesis. When I get stuck in research, I can always get useful suggestions from them. They encourage me to think, to act and to explore more in research. They are always ready to support me and I have learned a lot (on both the research and the English usage aspects) from their feedbacks. In addition, they also help me to get involved in the various activities in the institute and school. The research experience I gained from them will continually benefit my research in the future. Apart from that, they also teach me how to dig a nice hole for seismometers and assemble solar panels, which is a quite useful skill for me.

I would also like to thank the Institute of Geophysics and Tectonics and the Institute of Applied Geoscience for providing a wonderful research environment. I benefit a lot from the various group discussions and meetings. The institute seminars broaden my view, and the coffee breaks bring lots of leisure times. The school's IT team especially Richard Rigby provides lots of IT support which I appreciate a lot. My office mates and colleagues at school provide many help and supports during my PhD studying. Thanks David George Taylor, Itahisa Gonzalez Alvarez, Jamie Ward and Corinna Roy for their suggestions and help in improving my conference presentations. Thanks Shen Lin, Alif Mohd Jelani, Hardianshah Saleh, Pawan Primonthong and Gabriella Alodia for bringing many pleasure times. Thanks Antonio Fuggi, Dave Price, Katy Willis, Rodrigo Contreras Arratia, Huw Goodall, Matthew Gaddes, Maurits Metman, Luke Marsden, Jeanne Giniaux, Patrick Sugden, Emmanouil Parastatidis, Charlie Dunham and Dinko Sindija for pleasure talks and discussions. Thanks Jasone Xu for the laughs,

beers and hotpots. Thanks Dr. Sanyi Yuan for his encouragements and supports.

Finally, I would like to thank my family for their support and understanding. No matter what, they always support me and encourage me to do what I like to do. Without their support, I wouldn't have come abroad to pursue my research in Leeds. Special thanks to my wife Yanyan Wang. She always supports me when I have any difficulties, comforts me when I feel depressed, encourages me when I met any challenges. The first year in Leeds was a big challenge for me because of the culture differences and the research pressures. But with the accompany of my wife, that year was not that horrible, but on the contrary becomes the happiest time that I have ever experienced with her. We have left many enjoyable and valuable memories in Leeds, London and York that I will treasure in my whole life. With her standing by my side, I feel happy to make our future together.

Abstract

Seismic waveforms generated by earthquakes contain valuable information about the Earth's interior. Effectively utilizing seismic waveforms is critical for understanding earthquake source mechanism, imaging subsurface structure and monitoring earthquake hazard. In contrast to large earthquakes, microearthquakes have much lower magnitudes and are difficult to detect. Recorded waveforms of microearthquakes have small amplitudes and can be easily contaminated by noise. In this thesis, I develop an automatic method to fully utilize seismic waveforms to locate earthquakes, especially microearthquakes. A seismic modeling tool which can simulate seismic wave propagation in complex media using various seismic sources is also developed to generate synthetic seismic waveforms for testing and analysis.

As seismic anisotropy is common in shale and fractured rocks, I develop an efficient finite-difference full waveform modeling tool for simulating wave propagation in heterogeneous and anisotropic media. In order to model both double-couple and non-double-couple sources, an arbitrary moment tensor source is implemented in the forward modeling tool. The modeling tool can serve as an efficient Eikonal solver for the waveform migration used in source location or subsurface imaging. The modeling tool also provides an efficient way to obtain the Green's function in anisotropic media, which is the key of anisotropic moment tensor inversion and source mechanism characterization. The modeling tool can be used to generate seismic waveforms in complex, anisotropic models using various source-receiver geometries and source mechanisms. I generate and analyse synthetic datasets for vertical downhole arrays and surface arrays using this modeling tool. Due to the influence of seismic anisotropy, seismic location can have a deviation of a few hundred meters. Through analysing the synthetic seismic waveforms, I find that it is feasible to evaluate the seismic anisotropy of the subsurface and further estimate the orientation and density of potential cracks in the subsurface by examining the traveltimes and amplitudes of recorded seismic waveforms.

I propose a novel waveform coherency-based method to locate earthquakes from continuous seismic data. The method can automatically detect (micro-)earthquakes and find the locations and origin times of seismic events directly from recorded seismic waveforms. By continuously calculating the coherency between waveforms from different receiver pairs or groups, this method greatly expands the available information

which can be used for event location and has high imaging resolution. This method does not require phase identification and picking, which allows for a fully automated seismic location process. I have tested and compared this method to other migration-based methods (i.e. envelope, STA/LTA and kurtosis migration) in noise-free and noisy synthetic data. The tests and analysis show that the new developed method is very noise resistant and can obtain reliable location results even when the signal-to-noise ratio is below 0.1. By utilizing waveform coherency, the new method is able to suppress strong interference from other seismic sources occurring at a similar time and location and shows excellent performance in imaging weak seismic events. It can be used with arbitrary 3D velocity models and is able to obtain reasonable location results with smooth but inaccurate velocity models. Computational efficiency test shows the new method can achieve very high speedup ratio easily. This new method exhibits excellent location performance and can be easily parallelized giving it large potential to be developed as a real-time location method for very large datasets.

I apply the new method to automatically locate the induced and volcano-tectonic seismicity using sparse and irregular monitoring arrays. Compared to other migration-based methods, in spite of the often sparse and irregular distribution of monitoring arrays, the new method shows better location performance and obtains more consistent location results with the catalogue obtained by manual picking. The new method successfully locates many volcano-tectonic earthquakes with local magnitude smaller that 0 beneath Uturuncu, where seismicity is triggered by the passage of surface waves caused by the M 8.8 2010 Maule earthquake. The case at Uturuncu demonstrates that this new method can be used to automatically detect and locate microseismic events in large or streaming seismic datasets, which are time consuming and difficult to manually pick. 98.25% of 114 triggered seismic events in the published catalogue have been successfully detected and located. In addition, the new location method also automatically detect and locate 322 verified additional seismic events whose magnitude is smaller than 0. Using this new location method, a more complete seismic catalogue with much lower magnitude threshold can be obtained, which can benefit further seismic analysis. The new location results at Uturuncu show that seismicity is likely deeper than previously thought, down to 7 km below the surface. The event location example at the Aquistore carbon capture and storage site shows that continuous and coherent drilling noise in industrial settings will pose great challenges for source imaging. However, automatic quality control techniques are used to automatically select high quality data, and can thus effectively reduce the effects of continuous drilling noise and improve source imaging quality. By utilizing this new location method in combination with the automatic quality control techniques, event location down to signal-to-noise ratios of 0.025 (1/40) is possible in tests. The location performance of the new method for synthetic and real datasets demonstrates that this new method can perform as a reliable and automatic seismic waveform analysis tool to locate microseismic events.

Contents

List of Figures

List of Tables

Nomenclature

List of acronyms

CCS	Carbon capture and storage
CPU	Central processing unit
DAS	Distributed acoustic sensor
DSI	Diffraction stack imaging
FD	Finite-difference
FWI	Full waveform inversion
FWM	Full waveform modeling
GPU	Graphics processing unit
HTI	Horizontal transverse isotropic
LPO	Lattice-preferred-orientation
LTA	Long-term-average
MCM	Multichannel Coherency Migration
MPI	Message Passing Interface
NSR	Noise-to-signal ratio
RMS	Root-mean-square
RTM	Reverse time modeling
SNR	Signal-to-noise ratio
SPO	Shape-preferred-orientation
SSA	Source scanning algorithm
STA	Short-term-average

TTI	Tilted transverse isotropic
VTI	Vertical transverse isotropic

List of symbols

$\boldsymbol{C}$	Covariance matrix of seismic record in a determined time window	
$\boldsymbol{D}$	Seismic data matrix (all traces) in a determined time window	
$\boldsymbol{d}$	Seismic data vector (one trace) in a determined time window	
$\boldsymbol{G}$	Green's function	[m]
$\boldsymbol{m}$	Seismic moment tensor	[N m]
$\boldsymbol{R}$	Correlation coefficient matrix of seismic record in a determined time window	
δ	One of the Thomsen parameters, related to wave front ellipticity	
ϵ	One of the Thomsen parameters, measurement of P-wave anisotropy	
γ	One of the Thomsen parameters, measurement of S-wave anisotropy	
ϕ	Azimuth angle in the spherical coordinates	[rad]
ρ	Density	[kg m^{-3}]
σ	Component of the stress tensor	[N m^{-2}]
σ^2_{noise}	Variation of the stacked energy of background noise	
θ	Polar angle in the spherical coordinates	[rad]
τ^P	Predicted P-wave arrival time	[s]
τ^S	Predicted S-wave arrival time	[s]
ε	Component of the strain tensor	
c	Component of the elastic stiffness tensor	[N m^{-2}]
$d(t)$	Seismic record	
f_m	Dominant frequency of source time function	[Hz]
M_L	Local magnitude	
M_w	Moment magnitude	
N	Number of seismic records	

N_c	Number of computing cores	
N_s	Number of imaging points in the migration process	
N_t	Number of time samples in a selected time window	
$p(x, y, z, t_0)$	4D migration volume of waveform coherency	
p_c	Coherency threshold	
r	Multidimensional waveform coherency	
$S(t)$	Source time function	
S_{pro}	Source prominence	
t^P	Calculated P-wave traveltime	[s]
t^S	Calculated S-wave traveltime	[s]
T_0	Source origin time	[s]
T_w	Coherency analysis time window length	[s]
V	Effective volume of the grid cell	[m^3]
V_p	P-wave phase velocity	[m s^{-1}]
V_s	S-wave phase velocity	[m s^{-1}]
v_x	Particle velocity in the X direction	[m s^{-1}]
v_y	Particle velocity in the Y direction	[m s^{-1}]
v_z	Particle velocity in the Z direction	[m s^{-1}]
V_{qS1}	Fast S-wave phase velocity	[m s^{-1}]
V_{qS2}	Slow S-wave phase velocity	[m s^{-1}]
w	Weighting factor	
$W(x, y, z, t_0)$	4D migration volume of characteristic function	

Chapter 1

Introduction

1.1 Preface

Recent years have seen a densification of seismic monitoring stations leading to increased accuracy of our recordings of the seismic wavefield. In addition, portable seismic sensors, such as distributed acoustic sensors (DAS) and seismic nodal sensors, have made the deployment of seismic arrays much more convenient, and also recorded well-sampled wavefields. Large and dense monitoring arrays such as the large-N seismic monitoring arrays can reduce spatial aliasing and increase seismic imaging resolution (Brenguier et al., 2015, Bowden et al., 2015, Inbal et al., 2016, Fan & McGuire, 2018). Recorded seismic wavefields enable researchers to use full waveform imaging methods to produce high resolution images of seismic sources and subsurface structures. Since our records of the seismic wavefield are increasingly complete and accurate, seismic waveform-related techniques need continuous improvements to fully utilize the observed wavefields. On the other hand, the increasingly larger recorded dataset also calls for more efficient and intelligent processing techniques. In particular, automated processing techniques, which do not rely on human experience or only require minimal human involvements, are more suitable to handle large dataset or data streams.

Unlike major earthquakes which often cause severe damage to society, microearthquakes or microseismics are often not felt by humans but carry important information of the structure of the Earth. Microearthquakes can be aftershocks following a major earthquake (Rivera & Cisternas, 1990), small seismic events along creeping faults (Rubin et al., 1999) and remotely triggered events by the passage of seismic waves (Jay et al., 2012). Microearthquakes can also be induced or triggered by human activities, such as fluid injection (House, 1987, Shapiro & Dinske, 2009), reservoir impoundments (Gupta, 1985, Xu et al., 2016) and mining activities (Young et al., 1992, Jiang et al., 2006). Monitoring microearthquakes can help us better understand the subsurface geology and rupture mechanics of earthquakes (Rubin, 2002), and has many geo-industrial applications. It can be used to evaluate the reservoir stimulation effect for hydraulic fracturing

or geothermal enhancement (Majer et al., 2007, Maxwell, 2011), and reduce geo-hazard risk for mining and slope stability (Ge, 2005, Xu et al., 2011). Microseismic monitoring can provide geomechanical deformation information, which can be used to evaluate rock failure processes for carbon capture and storage (CCS) and geological disposal of waste. For microseismic monitoring in geo-industrial applications such as fracking and mining, real time monitoring can be important, because the induced fractures need to be assessed in a timely way to optimize the stimulation effects and avoid any potential geological risk. Therefore, effective and automated waveform processing techniques are needed in those applications.

For microseismic monitoring, locations of microearthquakes provide the fundamental information for other analysis such as source mechanism determination and fracture network interpretation. First proposed by Kao & Shan (2004), the source-scanning algorithm or diffraction stacking is used to automatically reveal the origin time and location of a seismic event using recorded seismic waveforms. This kind of analysis is favourable for the automatic processing of large microseismic datasets and also works well on low signal-to-noise ratio (SNR) data by utilizing waveform stacking. Full waveform forward modeling techniques can generate synthetic datasets which can be used to test and verify imaging results of various waveform-based imaging methods. Full waveform forward modeling techniques also form the theoretical basis of many waveform inversion methods, such as reverse time migration and full waveform inversion. This thesis is focused on developing an automated microseismic location method based on seismic waveforms, and also developing a full waveform seismic forward modeling tool to generate synthetic datasets to help analyse recorded seismic wavefields and test seismic location results.

In this chapter, I will first introduce various seismic forward modeling methods with particular emphasis on microseismic modeling. Then, I will introduce the developments of seismic location methods and detail the automatic seismic location techniques. Finally, I will present a review of the applications of microseismic monitoring especially in the field of geo-industrial applications. I will end this chapter by clarifying the objectives and the layout of this thesis.

1.2 Overview of seismic forward modeling methods

Seismic forward modeling is to simulate wave propagation in a particular model which can represent a practical geological structure. Seismic modeling can help analyse the recorded complex wavefield, provide valuable information for seismic interpretation and also forms the basis of seismic inversion. There are different ways to conduct seismic forward modeling, and there are also different classification schemes for forward modeling methods. According to the way to solve the wave equation, the seismic modeling can be classified into direct methods (or full-wave equation methods), integral-equation

methods (or analytical solutions), ray-tracing methods (or asymptotic methods) and reflectivity methods (or plane-wave summation methods) (Carcione et al., 2002).

The integral-equation methods can obtain the exact analytical solution in homogeneous medium (Aki & Richards, 2002). They are based on integral representations of the wavefield. For simple models, such as bounded objects in a homogeneous embedding or homogeneous model containing small-scale fractures, the integral-equation methods are efficient and can obtain accurate solutions (Carcione et al., 2002). However, the integral-equation methods are not suitable for 3D complex heterogeneous models, where the calculation of the Green's function can be tedious and even impossible. Ray-tracing methods are efficient and widely used in seismic modeling and imaging (Cerveny, 2005). They are derived under the high frequency assumption of seismic waves and are very effective in calculating traveltimes of different seismic phases. However, as asymptotic methods, the modeling results can be inaccurate in highly heterogeneous and anisotropic media or low frequency scenarios. Full-wave equation methods directly solve the wave equation on a discretized domain. The solutions to the wave equation give the full wavefield in a model. With a sufficiently fine mesh/grid, the full-wave equation methods can be applied to models with any kind of complexities. Although the solutions to the wave equation are obtained by approximation, the full-wave equation methods can be very accurate by using very fine discretization. The full-wave equation methods are more computationally expensive than the integral-equation methods and ray-tracing methods especially when using fine grids. However, with the development of computer power, it becomes more and more realistic to perform seismic modeling using the full-wave equation methods in complex models or at global scales.

Microseismic modeling is often conducted in a complex medium, such as an anisotropic medium. Seismic waveforms also contain much information about the source mechanism and geomechanics. Calculating high-quality full wavefield synthetics in complex models requires accurate modeling methods with high flexibility. Therefore, I will focus on the introduction of the full-wave equation methods for microseismic modeling. For full-wave equation methods, there are also different division schemes depending on the types of the wave equation and the ways of solving the wave equation (as shown in Table 1.1). Time-domain modeling is flexible and is easy to parallelize, while frequency-domain modeling is more efficient when dealing with many sources/shots. Therefore, frequency-domain modeling is often used in migration and inversion. However, when modeling in 3D media, the complexity of decomposing a large sparse matrix makes it burdensome and unsuitable for practical use. The finite-difference method is easy to implement, while the finite-element method can handle irregular surfaces but is more complicated in implementation especially in 3D scenarios. Here, I mainly focus on the finite-difference modeling of the elastic, two-way wave equation in the time-domain, and stress the challenges and applications of microseismic modeling.

Alterman & Karal Jr (1968) first used the finite-difference (FD) method to solve the

Table 1.1: Different types of full waveform modeling methods according to various division schemes.

Division scheme	Modeling methods or wave equation types
Modeling domain	time domain, frequency domain
Wave equation type	one way wave equation, two way wave equation
Modeling media type	acoustic, elastic, viscoelastic
Way of solving wave equation	finite-difference, finite-element, pseudo-spectral, spectral-element

wave equation in a single layered half-space with a buried compressional source. Alford et al. (1974) compared the solutions of FD methods and analytical approaches in an infinite 2D acoustic medium, and found as long as the grid interval of the FD method is sufficiently small, the modeling results of FD methods fit the analytical solution well. Because the modeling mesh is finite, non-physical reflections will arise at the boundaries of the numerical mesh. Cerjan et al. (1985), Kosloff & Kosloff (1986) proposed absorbing boundary conditions to attenuate the non-physical artifacts at the boundaries of the FD mesh. Berenger (1994) further proposed an improved perfectly matched-layer method to deal with the boundary reflections for electromagnetic waves and achieved good performance. Chew & Liu (1996) introduced the perfectly matched-layer method into the wave equation modeling. Virieux (1986) applied the staggered-grid FD method in seismic modeling to handle the calculation of derivatives, and increased the modeling accuracy. In the staggered-gird scheme, the wavefield components are distributed on different numerical grids to solve the spatial derivatives using a central difference scheme. Robertsson (1996) introduced a simple free-surface boundary condition to the FD modeling and enabled accurate modeling of highly irregular topography, which can be important for earthquake site studies and shallow environment investigations.

For waveform modeling in global seismology, the main interested frequency band is relatively low (often smaller than a few Hz). Therefore, a coarse grid can provide sufficient modeling accuracy. However, for microseismic events, the effective frequency band is much higher (often tens of Hz or even hundreds of Hz). To obtain an accurate wavefield, measures such as a fine numerical grid and higher-order FD scheme are often required. Modeling accuracy and computational efficiency can be enhanced by adopting high-order differential operators and corresponding differential coefficients (Dablain, 1986, Kindelan et al., 1990, Liu & Sen, 2009). Holberg (1987) proposed optimized FD coefficients in the FD modeling scheme to increase modeling accuracy and reduce numerical dispersion.

Seismic anisotropy is an important feature in the Earth interior and will affect seismic wave propagation (Savage, 1999). In an anisotropic medium, the wave propagation velocity is different in different directions. Seismic anisotropy will increase the complexity of recorded wavefields, and thus influence the subsequent seismic in-

terpretation and inversion. Microseismic monitoring is often conducted in anisotropic media such as shales and fractured rocks. Shale normally has fine horizontal layering and is often reported to have observable seismic anisotropy (Johnston & Christensen, 1995). Rocks which contain aligned cracks show seismic anisotropy as well (Schoenberg & Sayers, 1995). Anisotropy in shales comes from a combination of layering, lattice preferred orientation of constituent mineral phases (LPO, the clay minerals of shales can be very anisotropic) and shape and dimensional preferred orientation (SPO, the orientation of the mineral grains themselves, which are plate-like) (Valcke et al., 2006). Interbedded shale-sandstone formations are common and there relatively more of the anisotropy comes from layering. The layering is only effectively anisotropic if the scale of layering is significantly below the seismic wavelength. In order to obtain accurate seismic full wavefield in anisotropic media, seismic modeling which is able to simulate the anisotropic wave propagation is required. The stress-strain relation, i.e. Hooke's law, is fundamental for wave equation modeling. The stress-strain relation in a general anisotropic, elastic medium (triclinic medium) can be expressed as $\sigma_{ij} = c_{ijkl}\varepsilon_{kl}$, where subscripts i, j, k, l represent axis index (ranges from 1 to 3) and summation is implied over the repeated subscripts k and l, σ_{ij} and ε_{kl} are components of the stress and strain tensors, and c_{ijkl} is a component of the fourth-rank elastic stiffness tensor (Mavko et al., 2009). The elastic tensor has a total 81 components. However, with the symmetry of stresses and strains and the existence of a unique strain energy potential, which require

$$c_{ijkl} = c_{jikl} = c_{ijlk} = c_{jilk} = c_{klij}, \tag{1.1}$$

the elastic tensor only has 21 independent components (Mavko et al., 2009). Using an abbreviated Voigt notation, the pair subscripts $ij(kl)$ will convert to the single subscripts as follows

$$\begin{aligned} ij(kl) &\rightarrow I(J) \\ 11 &\rightarrow 1 \\ 22 &\rightarrow 2 \\ 33 &\rightarrow 3 \\ 23(32) &\rightarrow 4 \\ 13(31) &\rightarrow 5 \\ 12(21) &\rightarrow 6\ . \end{aligned} \tag{1.2}$$

The stress and strain tensors are thus rewritten as six-element vectors

$$\boldsymbol{\sigma} = \begin{bmatrix} \sigma_1 = \sigma_{11} \\ \sigma_2 = \sigma_{22} \\ \sigma_3 = \sigma_{33} \\ \sigma_4 = \sigma_{23} \\ \sigma_5 = \sigma_{13} \\ \sigma_6 = \sigma_{12} \end{bmatrix}, \qquad \boldsymbol{\varepsilon} = \begin{bmatrix} \varepsilon_1 = \varepsilon_{11} \\ \varepsilon_2 = \varepsilon_{22} \\ \varepsilon_3 = \varepsilon_{33} \\ \varepsilon_4 = 2\varepsilon_{23} \\ \varepsilon_5 = 2\varepsilon_{13} \\ \varepsilon_6 = 2\varepsilon_{12} \end{bmatrix} \tag{1.3}$$

Therefore, the stress-strain relation can be expressed as (the subscripts 1 and 2 represent the horizontal directions, i.e. X- and Y-axes; the subscript 3 represents the vertical direction, i.e. Z-axis in this chapter)

$$\begin{bmatrix} \sigma_1 \\ \sigma_2 \\ \sigma_3 \\ \sigma_4 \\ \sigma_5 \\ \sigma_6 \end{bmatrix} = \begin{bmatrix} c_{11} & c_{12} & c_{13} & c_{14} & c_{15} & c_{16} \\ c_{21} & c_{22} & c_{23} & c_{24} & c_{25} & c_{26} \\ c_{31} & c_{32} & c_{33} & c_{34} & c_{35} & c_{36} \\ c_{41} & c_{42} & c_{43} & c_{44} & c_{45} & c_{46} \\ c_{51} & c_{52} & c_{53} & c_{54} & c_{55} & c_{56} \\ c_{61} & c_{62} & c_{63} & c_{64} & c_{65} & c_{66} \end{bmatrix} \begin{bmatrix} \varepsilon_1 \\ \varepsilon_2 \\ \varepsilon_3 \\ \varepsilon_4 \\ \varepsilon_5 \\ \varepsilon_6 \end{bmatrix}, \tag{1.4}$$

where σ_i and ε_j represent the corresponding component of the stress tensor $\boldsymbol{\sigma}$ and the strain tensor $\boldsymbol{\varepsilon}$ in the Voigt notation, and c_{ij} represents the component of elastic tensor $\mathbf{C}$ of the medium in the Voigt notation. The elastic tensor $\mathbf{C}$ is symmetrical, i.e. $c_{ij} = c_{ji}$. Therefore, there are 21 independent constants for a triclinic medium which has the minimum symmetry. Using the elastic tensor in triclinic medium, we are able to simulate seismic full wavefields in a medium with the most complicated seismic anisotropy. Since the triclinic medium has 21 independent constants in the elastic tensor, it will be computationally expensive to model full wavefields in heterogeneous triclinic media. However, the number of independent constants in a elastic tensor can be reduced when a medium has a higher symmetry than the triclinic medium.

For isotropic medium which has the maximum symmetry, there are only two independent constants in the elastic tensor. The elastic tenor of an isotropic medium has the following form

$$\begin{bmatrix} c_{11} & c_{12} & c_{12} & 0 & 0 & 0 \\ c_{12} & c_{11} & c_{12} & 0 & 0 & 0 \\ c_{12} & c_{12} & c_{11} & 0 & 0 & 0 \\ 0 & 0 & 0 & c_{44} & 0 & 0 \\ 0 & 0 & 0 & 0 & c_{44} & 0 \\ 0 & 0 & 0 & 0 & 0 & c_{44} \end{bmatrix}, \quad c_{12} = c_{11} - 2c_{44}. \tag{1.5}$$

The P- and S-wave velocities in the isotropic medium are $v_p = \sqrt{c_{11}/\rho}$ and $v_s =$

$\sqrt{c_{44}/\rho}$, where ρ is the density of the medium. Because of the simplicity of the elastic tensor, most full-wave equation modeling methods are implemented in the isotropic medium.

For a medium which is transversely isotropic (hexagonal medium or TI medium), there are five independent constants in the elastic tensor. If the symmetry axis of the transversely isotropic medium is vertical, this kind of medium is referred to as the vertical transversely isotropic (VTI) medium. The VTI medium is often used as an effective medium for rocks with many horizontal layers, such as shales where hydraulic fracturing and microseismic monitoring are often implemented. The elastic tensor of VTI medium has the form (Chapman, 2004)

$$\begin{bmatrix} c_{11} & c_{12} & c_{13} & 0 & 0 & 0 \\ c_{12} & c_{11} & c_{13} & 0 & 0 & 0 \\ c_{13} & c_{13} & c_{33} & 0 & 0 & 0 \\ 0 & 0 & 0 & c_{44} & 0 & 0 \\ 0 & 0 & 0 & 0 & c_{44} & 0 \\ 0 & 0 & 0 & 0 & 0 & c_{66} \end{bmatrix}, \quad c_{12} = c_{11} - 2c_{66}. \tag{1.6}$$

For VTI media, the P- and S-wave velocities travelling in the direction of the symmetry axis (vertical direction) are $v_{p0} = \sqrt{c_{33}/\rho}$ and $v_{s0} = \sqrt{c_{44}/\rho}$, respectively. Thomsen (1986) introduced the Thomsen parameters to measure the anisotropy in the VTI medium, which are defined as

$$\epsilon = \frac{c_{11} - c_{33}}{2c_{33}}, \quad \gamma = \frac{c_{66} - c_{44}}{2c_{44}}, \quad \delta = \frac{(c_{13} + c_{44})^2 - (c_{33} - c_{44})^2}{2c_{33}(c_{33} - c_{44})}. \tag{1.7}$$

ϵ is a measurement of P-wave anisotropy, which shows the fractional difference between the P-wave velocities in the horizontal and vertical directions for a VTI medium. γ is a measurement of S-wave anisotropy, which shows the fractional difference between the SH-wave velocities in the horizontal and vertical directions. δ is related to wave front ellipticity, and controls the near vertical P-wave speed variations and the angular dependence of the SV-wave speed. The Thomsen parameters allow us to physically interpret the seismic anisotropy in a simple way, and are useful in quantifying the seismic anisotropy even with strong seismic anisotropy.

If the symmetry axis of the transversely isotropic medium is horizontal, this kind of medium is referred to as the horizontal transversely isotropic (HTI) medium. The HTI medium can be obtained by rotating the VTI medium along the horizontal direction by 90 degrees. Rocks with many vertically-oriented cracks can be viewed as a HTI medium, such as rocks with many stimulated vertical fractures by hydraulic fracturing. As with the VTI medium, the elastic tensor of HTI medium has five independent constants,

and has the following form

$$\begin{bmatrix} c_{11} & c_{13} & c_{13} & 0 & 0 & 0 \\ c_{13} & c_{33} & c_{23} & 0 & 0 & 0 \\ c_{13} & c_{23} & c_{33} & 0 & 0 & 0 \\ 0 & 0 & 0 & c_{44} & 0 & 0 \\ 0 & 0 & 0 & 0 & c_{66} & 0 \\ 0 & 0 & 0 & 0 & 0 & c_{66} \end{bmatrix}, \quad c_{23} = c_{33} - 2c_{44}. \tag{1.8}$$

If a medium has three mutually perpendicular symmetry axes, this is referred to as an orthorhombic medium. Rocks with horizontal layerings and vertically-aligned fractures can be approximated as an orthorhombic medium, such as shale with stimulated vertical fractures by fracking or fractured limestones. The elastic tensor of orthorhombic medium has nine independent constants, and has the following form

$$\begin{bmatrix} c_{11} & c_{12} & c_{13} & 0 & 0 & 0 \\ c_{12} & c_{22} & c_{23} & 0 & 0 & 0 \\ c_{13} & c_{23} & c_{33} & 0 & 0 & 0 \\ 0 & 0 & 0 & c_{44} & 0 & 0 \\ 0 & 0 & 0 & 0 & c_{55} & 0 \\ 0 & 0 & 0 & 0 & 0 & c_{66} \end{bmatrix}. \tag{1.9}$$

According to its elastic tensor, the orthorhombic medium is the most general anisotropic model that does not couple the normal and shear stresses. Therefore, it has the most general form that can be used on a staggered FD grid without interpolation of stress or strain values (Etgen, 1987).

Figure 1.1 shows simple representatives of the VTI, HTI and orthorhombic media. The VTI, HTI and orthorhombic media are often viewed as the effective media of rocks with abundant aligned fractures, and are widely used in the seismic forward modeling and inversion (Rüger, 2002, Tsvankin, 2012). It is worth noting that for isotropic, VTI, HTI and orthorhombic media, the elastic tensors all share the same format with zero values all appearing at the same locations. For those models, the normal stresses and the shear stresses are not coupled in the wave equation. Therefore, it is convenient to model full wavefields in those media using similar full-wave equation formats.

For seismic forward modeling, the wavefield must be generated by applying a proper wavefield excitation conditions, i.e. source implementation. Generally, there are two kinds of source implementation schemes in a FD full-wave equation modeling. One is the use of body-force terms which apply to momentum conservation equations (Aboudi, 1971). The other one is to add an incremental stress on stress components (Virieux, 1986). Source mechanisms are crucial for seismic data analysis, as they will affect the polarizations and amplitudes of seismic waves. Active seismic sources are normally

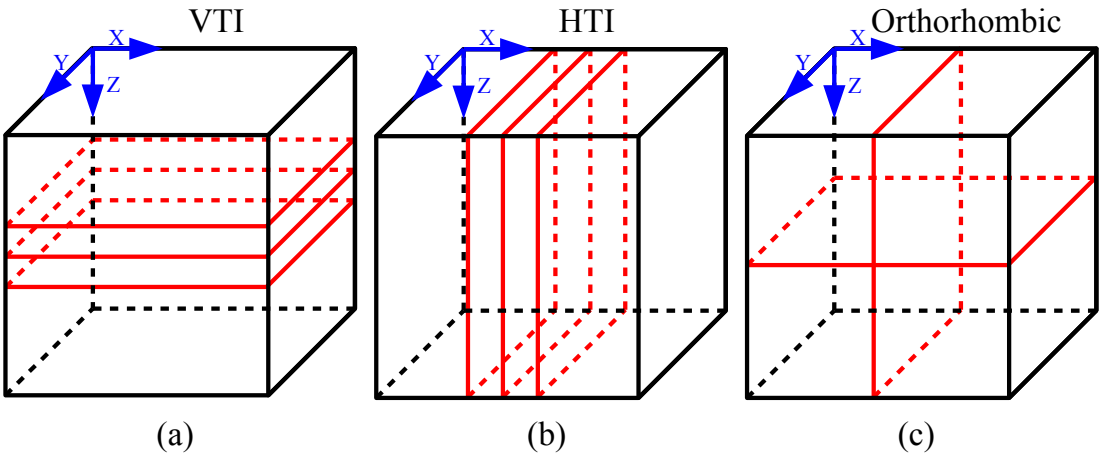

Figure 1.1: Medium with different types of seismic anisotropy. (a) VTI medium which can be viewed as a medium with many horizontal layerings or cracks. (b) HTI medium which can be viewed as a medium with many vertically aligned cracks. (c) Orthorhombic medium which can be viewed as a medium with horizontal layerings and vertical cracks. The red planes denote the plane direction of the aligned cracks or layers.

explosive sources such as explosives or air gun, which will generate seismic waves with isotropic radiation patterns. This kind of source is easy to implement in active source experiments and numerical modelings, thus is often adopted in various seismic modeling methods and inversion processes, especially in exploration geophysics. Generally, natural earthquakes are thought to be generated by fault dislocations in the subsurface. Therefore, double-couple sources are also pervasively used in modeling and inversion of natural earthquakes. However, natural earthquakes can have complex source mechanisms. Non-double-couple source mechanisms have been observed especially for induced and triggered earthquakes (Šílenỳ et al., 2009). For induced seismicity by fracking, non-double-couple mechanisms may come from the opening of cracks by high-pressure fluid injection (Šílenỳ et al., 2009). Since correctly modeling the wavefields of different types of sources is the key to understanding the source mechanisms, a full moment tensor source representative in seismic forward modeling is essential. As microseismic monitoring is often implemented in anisotropic media and is required to deal with different types of sources and frequency bands, seismic forward modeling tool should be able to generate seismic wavefields using accurate representatives of full moment tensor sources in strong anisotropic media with sufficient modeling accuracy. In addition, methods should be developed to further utilize the seismic full wavefields in anisotropic media to reveal the subsurface properties (especially about fractures) and fulfil different microseismic monitoring applications.

1.3 Developments in local seismic location techniques

Earthquake location is the process of finding the place and time of the occurrence of energy release from a seismic event. Most earthquake location methods are based on seismogram recordings. Earthquake location is a fundamental and essential task in practical seismology. In this section, I will introduce and discuss the different seismic location methods with particular emphasis on the automated and waveform-based seismic location methods. Because this thesis focuses on microseismics, I only introduce the location methods which apply to microseismics, and the location methods which apply to the global scale are not stressed. Therefore, factors such as complicated seismic phases and ellipticity of the earth are not considered and discussed in the seismic location process.

1.3.1 Manual location

In the early 20th century, when seismograms were recorded on paper and were not digitized, seismic location was mostly performed manually using triangulation. This kind of location method is also recognised as a graphical method (Milne, 1886, Bolt, 1978, Pujol, 2004). The hypocentral distance between a station and the seismic source can be calculated according to arrival time differences between direct P- and S-phases on the recorded seismogram:

$$D = (t_s - t_p)\frac{v_p v_s}{v_p - v_s}, \tag{1.10}$$

where D is the hypocentral distance from a specific station, t_p and t_s are arrival times of direct P- and S-waves, v_p and v_s are P- and S-wave velocities, respectively. Therefore, when three or more stations are available, the hypocentral location can be determined by finding equidistant lines from the station location (as shown in Figure 1.2). The source location is at the cross point of these circles.

However, there are limitations for this kind of method. First, the calculation of hypocentral distance for each station using equation 1.10 is not applicable for complex subsurface velocity models or variable v_p/v_s. In complex velocity models, seismic ray paths are complicated and thus make it difficult to calculate an exact hypocentral distance. The ray paths of the direct P- and S-waves are different if the v_p/v_s varies within the crust, which also makes equation 1.10 not applicable. Second, equidistant lines will rarely intersect at a single location due to misfits in the onset-time determination or the complexities in the velocity model. In addition, the depth of seismic event is poorly constrained. For seismic event at depth, the hypocentral distance is always larger than the epicentral distance. Therefore, equidistant lines will not be crossing at a single point, but will rather have an overlapping area. This is also referred to as overshoot. Overshoot problems will also occur when the adopted average velocity cannot

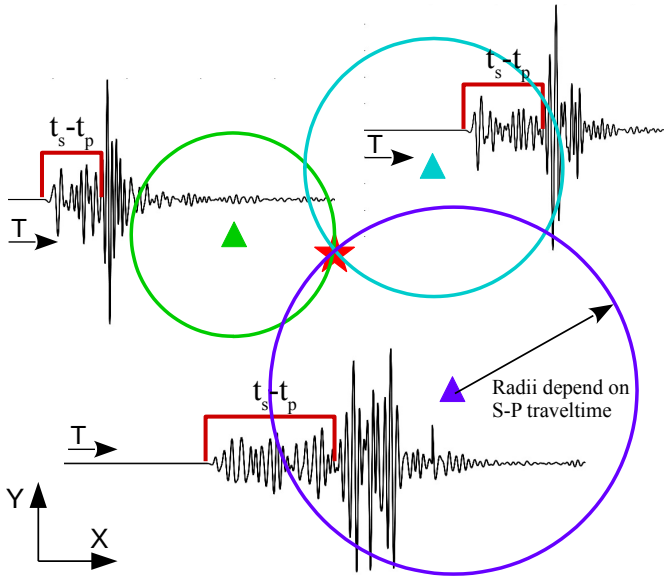

Figure 1.2: Schematic diagram showing the triangulation process of seismic location. The triangles show station location, the red star shows source location, circles shows the hypocentral distance from a station to a source. The radius of the circles are calculated according to arrival time differences of P- and S-waves. In the figure, a mix of time axis and X-Y spatial axes is used.

correctly account for the subsurface heterogeneities. However, different methods have been proposed to deal with overshoot and depth problems (Bath, 2013, Pujol, 2004).

1.3.2 Iterative linearized traveltime inversion

With the development of digital seismometers and computer techniques, seismic source location is now mainly conducted using computer methods rather than manual location approaches. A commonly used location method is the linearized traveltime inversion, also known as the Geiger method (Geiger, 1912). This method first takes an initial guess of a hypocenter and origin time and calculate the arrival time residuals between the true and the trial source location, then gradually approaches the exact source location and origin time by minimizing traveltime residuals iteratively. If the trial hypocenter is not far away from the true hypocenter, the iterative process will converge to the exact solution. The traveltimes at a particular station from any point in the subsurface can be calculated very conveniently using various types of methods even for 3D and highly heterogeneous media (Buland & Chapman, 1983, Vidale, 1988, Podvin & Lecomte, 1991).

The arrival time at station i (at location x_i, y_i, z_i) from a trial source location x_k, y_k, z_k can be expressed as $T_{ik} = T(x_k, y_k, z_k, x_i, y_i, z_i) + t_k$, where t_k is the trial source origin time. The residual between the observed and calculated arrival time is $r_{ik} = t_i - T_{ik}$, where t_i is the observed arrival time at the station i. Assuming the arrival time residual is caused by the error in the trial solution, we can make corrections

to the trial source location and origin time to account for the residual. The arrival time of the corrected solution with corrections $\Delta x, \Delta y, \Delta z, \Delta t$ can be expressed as $T(x_k+\Delta x, y_k+\Delta y, z_k+\Delta z, x_i, y_i, z_i)+t_k+\Delta t$. The traveltime function T is a nonlinear function of the model parameters (velocity model and monitoring geometry), which greatly complicates the source inversion problem. Therefore, linearizing the inversion problem is essential. If the corrections $\Delta x, \Delta y, \Delta z$ are small, we can approximate the arrival times of the new trial point using Taylor series with second order truncation errors:

$$T(x_k+\Delta x, y_k+\Delta y, z_k+\Delta z, x_i, y_i, z_i)+t_k+\Delta t \approx T_{ik}+\frac{\partial T_{ik}}{\partial x}\Delta x+\frac{\partial T_{ik}}{\partial y}\Delta y+\frac{\partial T_{ik}}{\partial z}\Delta z+\Delta t. \tag{1.11}$$

We hope that the arrival time of the trial point can match the observed arrival time. Therefore, we get

$$T_{ik}+\frac{\partial T_{ik}}{\partial x}\Delta x+\frac{\partial T_{ik}}{\partial y}\Delta y+\frac{\partial T_{ik}}{\partial z}\Delta z+\Delta t = t_i, \tag{1.12}$$

which can also be expressed as

$$\frac{\partial T_{ik}}{\partial x}\Delta x+\frac{\partial T_{ik}}{\partial y}\Delta y+\frac{\partial T_{ik}}{\partial z}\Delta z+\Delta t = r_{ik}. \tag{1.13}$$

We can write equation 1.13 for different stations ($i = 1, \cdots, n$) in matrix form as

$$\begin{bmatrix} \partial T_{1k}/\partial x & \partial T_{1k}/\partial y & \partial T_{1k}/\partial z & 1 \\ \partial T_{2k}/\partial x & \partial T_{2k}/\partial y & \partial T_{2k}/\partial z & 1 \\ \vdots & \vdots & \vdots & \vdots \\ \partial T_{nk}/\partial x & \partial T_{nk}/\partial y & \partial T_{nk}/\partial z & 1 \end{bmatrix} \begin{bmatrix} \Delta x \\ \Delta y \\ \Delta z \\ \Delta t \end{bmatrix} = \begin{bmatrix} r_{1k} \\ r_{2k} \\ \vdots \\ r_{nk} \end{bmatrix}, \tag{1.14}$$

where T_{nk} is the traveltime at the n-th station from the k-th trial source location and r_{nk} is the arrival time residual at the n-th station from the k-th trial source location. Equation 1.14 which can be expressed as $\mathbf{GX} = \mathbf{R}$ has four unknowns, and each row stands for the scenario for a particular station and seismic phase. Since the calculation of traveltimes is solvable even in complex media, the traveltimes and its derivatives in equation 1.14 can be calculated easily using pre-calculated traveltime tables (Schweitzer, 2001). Generally the number of stations is much larger than the minimum requirement, i.e. four. Therefore, equation 1.14 is generally overdetermined and can be solved using the least square method. The least square solution to equation 1.14 is $\mathbf{X} = (\mathbf{G^T G})^{-1}\mathbf{G^T R}$. Therefore, we can obtain a new source location solution which is $x_{k+1} = x_k + \Delta x$, $y_{k+1} = y_k + \Delta y$, $z_{k+1} = z_k + \Delta z$ and $t_{k+1} = t_k + \Delta t$. This new solution is then used as the new trial solution for the next iteration. This process is iteratively repeated until a predefined converge criterion is reached. The converge criterion can be a preset minimum total residuals of traveltimes, or a preset minimum

hypocentral distance variance, or a certain total number of iterations.

Instead of locating each seismic event individually, Douglas (1967) proposed a joint hypocenter location method, which jointly determines all seismic event locations in a given area simultaneously. Because errors may exist in the reading of seismograms for different stations, Douglas (1967) added static station corrections to the joint hypocenter location to account for the difference between observed and calculated traveltimes. Thus, the inversion equation 1.13 can be rewritten as

$$\frac{\partial T_{ik}}{\partial x}\Delta x_k + \frac{\partial T_{ik}}{\partial y}\Delta y_k + \frac{\partial T_{ik}}{\partial z}\Delta z_k + \Delta t_k + \Delta S_i = r_{ik} - S_i, \tag{1.15}$$

where Δx_k, Δy_k, Δz_k, and Δt_k are iterative corrections for the location and origin time of the k-th event, S_i is the station correction for the station i, and ΔS_i is the iterative correction for the i-th station correction. In this new equation, there are five unknowns, i.e. the corrections for seismic locations, origin time and station correction, to be solved. In addition, the solutions for all seismic events are solved simultaneously. This can ensure a minimal total residual for the observed arrival times of all seismic events and a good estimates for station corrections (Pujol, 2000). Douglas (1967) showed that the event locations obtained by joint hypocenter location is more accurate than the standard individual traveltime inversion method. The static station correction is a constant time for a particular station to account for the unmodeled velocity variation along the common ray path below the station (Pujol, 1992). Figure 1.3 shows a comparison of seismic location results for the standard single event based traveltime inversion method and the joint hypocenter determination. Compared to the single event based location method, the location results of the joint hypocenter determination are more compact and the located events are distributed along the orientation of the fault. Different to static station correction, Richards-Dinger & Shearer (2000) proposed a source-specific station term technique where the station correction term varies as a function of both station and source location. Because the solution to all the events are solved together, the inversion equations are much larger, which calls for efficient inversion schemes and requires larger computer memory. For the joint epicenter location method, the depth of at least one seismic event is needed to constrain the inversion (Douglas, 1967). This imposes additional requirements for the source location process. Without depth constraints, the convergence of the inversion process is slow and the estimates of event solutions tend to oscillate (Douglas, 1967).

For the traveltime inversion-based location methods, the inversion process itself is efficient. However, manual picking is required to obtain the arrival times of different seismic phases at different stations before the inversion. Although automatic picking methods can be used to obtain the arrival times of direct P- or S-phases, manual picking is still the common practice in real seismic data processing (Rentsch et al., 2006). Manual picking can be a time consuming process when many stations or many

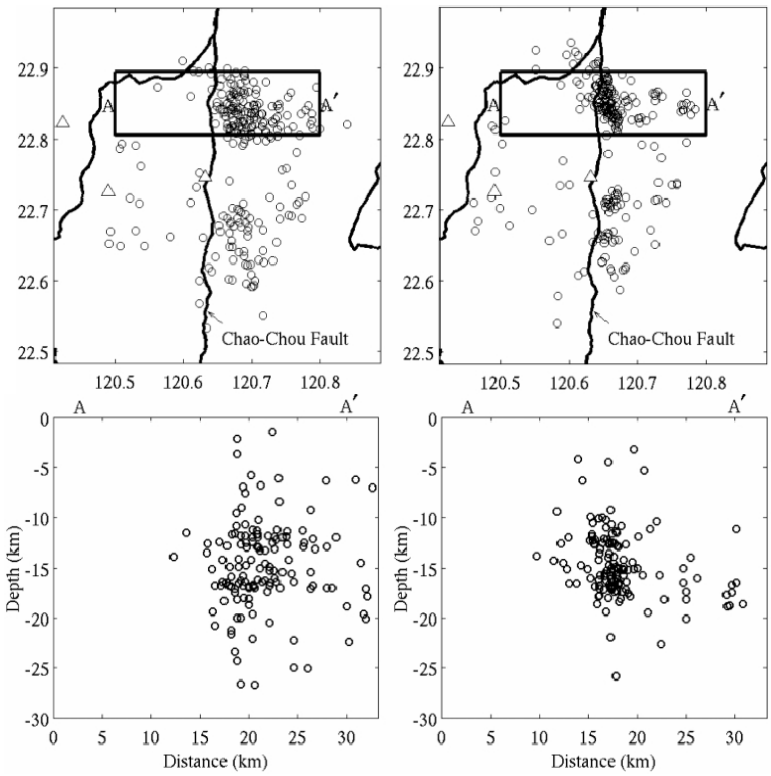

Figure 1.3: Comparison of the seismic location results of different methods around the Chao-Chou Fault. The left panel shows seismic location results of standard single event based method. The right panel shows seismic location results of the joint hypocenter location method. The top row shows map views of the seismic location results. The bottom row shows the cross sections along the black rectangular area (A-A') in the top figures. Each black circle represents an earthquake. Figure modified from Kim et al. (2005).

seismic events are involved, thus is not suitable for real time monitoring. The source location accuracy is largely dependent on the picking accuracy of arrival times. If signal-to-noise ratio of recorded data is low, the phase arrivals can be difficult or even impossible to pick and the location errors can be large. Including other seismic phases such as reflected and converted phases from large velocity contrast can significantly improve the location accuracy and reduce the location uncertainties (Schöffel & Das, 1999). However, this relies on an accurate velocity model for the source location. The location result of the traveltime inversion-based location methods also depends on the initial trial location. If the initial trial location is very far away from the correct source location, the location result may converge to a local minimum or the convergence may be very slow. For solving this problem, a good initial estimate is required or several initial trials can be tested at the same time.

1.3.3 Nonlinear grid search

Linear traveltime inversion is very efficient in locating seismic sources. However, the traveltime function is inherently a nonlinear function especially for heterogeneous media. Thus, the linearized location method may fail to find the correct source location or to estimate the location uncertainties when the inverse problem is ill-posed. Since it is so convenient and efficient to calculate the traveltimes of different seismic phases, a simple strategy to locate seismic source is to perform an exhaustive grid search over all possible source locations and origin times. In this way, one can obtain a probabilistic location result with complete uncertainty estimates (Lomax et al., 2000). The first step is to calculate a traveltime table for every grid point in the velocity model. The hypocenter location and origin time of a source can be determined by finding a point and origin time which has the best agreement with the observed arrival times. The best agreement is often defined as the minimum overall arrival time residual for all stations, i.e. $x_s, y_s, z_s, t_0 = min \sum_{i=1}^{N} [t_i - T_i(x, y, z, t)]^2 / N$ (x_s, y_s, z_s, t_0 are source locations and origin time, t_i is the observed arrival time for station i, $T_i(x, y, z, t)$ is the calculated arrival time for a point in the model and N is the total number of stations). The mean squared residual is often used since it leads to simple forms in the minimization problems and also works well when the residuals are induced by Gaussian noise. However when residuals contain individual large outliers or are not of similar size, other residual formats such as root mean squared residual, absolute residual or weighted residual should be used to reduce the influence of large outliers and the non-Gaussian distribution in the input data.

The traveltime residuals can also be used to estimate the location uncertainties. A complete distribution of the residual space can be determined through a full grid search, which can be further used for uncertainty estimation. Figure 1.4 shows hypocenter location results and the corresponding uncertainties of two seismic events. When seismic location is well-constrained (Figure 1.4 left panel), location uncertainties obtain by grid

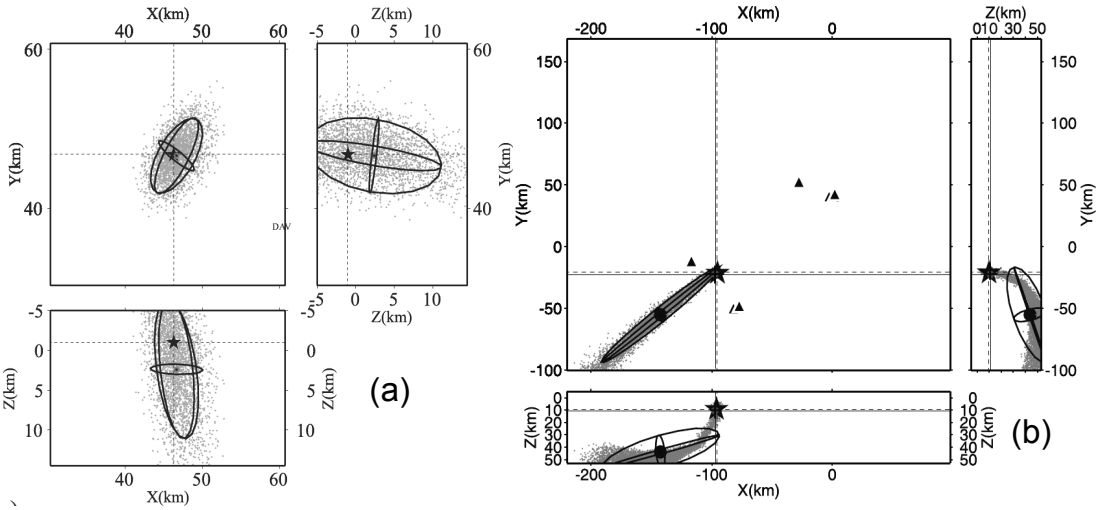

Figure 1.4: Location uncertainties shown by density scatterplots of grid search. Map view in the x-y direction and vertical cross sections in the x-z and y-z directions are shown. Stars and intersection of dashed lines indicate maximum likelihood hypocenter location. The Gaussian estimates of the hypocenter location and uncertainties are shown by the black dots and the ellipsoids, and projection of the 68% confidence ellipsoid is shown in the figures. Left panel (a) shows the results of a relatively well-constrained earthquake location. Right panel (b) shows the results of a a poorly-constrained earthquake location. Intersection of solid lines indicates hypocenter location in the catalogue. Black triangles show station locations. Figure modified from Husen et al. (2003).

search (scatter points) correspond well with the location uncertainties obtained by a Gaussian assumption (ellipsoid). However, when seismic location is poorly-constrained because of the poor coverage of the monitoring geometry (Figure 1.4 right panel), using a Gaussian assumption cannot get a good estimation of location uncertainties and the location results can also be biased in this situation. Grid search methods can obtain an accurate hypocenter location and a complete distribution of location uncertainties.

The exhaustive grid search method is feasible for local seismic location or small models. However, large models or large number of seismic events will make this method inefficient. In order to make the grid search method more efficient, global optimization algorithms such as the genetic algorithm (Kennett & Sambridge, 1992, Sambridge & Gallagher, 1993, Billings et al., 1994), the simulated annealing (Billings, 1994), the differential evolution (Ružek & Kvasnička, 2001) and the neighbourhood algorithm (Sambridge & Kennett, 2001) have been used for a stochastic search in the direct grid search method. The direct utilization of the global optimization algorithms in the grid search method can generate stochastic sampling of the parameter space, but cannot obtain a global or well distributed sampling of the parameter space, which cannot produce complete, probabilistic location results and uncertainty estimations (Lomax et al., 2000).

For conventional grid search methods, the misfits between observed and theoretically calculated data are used to evaluate location results at each grid node, and the

grid node which has the lowest misfit is selected as the best hypocenter location. In contrast to conventional grid search methods, Tarantola & Valette (1982) proposed a probabilistic inversion approach based on Bayes theorem (Stone, 2013) to locate seismic events within the framework of the grid search method. In the probabilistic inversion approach, the observed arrival time measurements together with a-priori model parameter information are utilized to compute a complete probability density function of the model parameters (hypocenter coordinates) (Moser et al., 1992, Wittlinger et al., 1993). Both an exhaustive grid search or Monte-Carlo search can obtain a global or well-distributed sampling of the model space, and can thus obtain complete, probabilistic locations. However, the computational effort is huge when the model space is too large. In order to increase the computational efficiency and also to obtain a well-distributed sampling of the model space at the same time, Lomax et al. (2000) apply the Metropolis-Gibbs sampling technique and simulated annealing in the grid search method. As an importance sampling technique, the Metropolis-Gibbs algorithm adapts the sampling by incorporating information obtained from all previous data samples so that the sampling density will follow the distribution of the target function (Lomax et al., 2000). The obtained probabilistic hypocenter solution is able to depict the location uncertainty due to Gaussian-distributed picking, the traveltime calculation errors, the network-event geometry and the incompatibility of the phase identifications.

1.3.4 Relative location methods

In practice, the exact subsurface velocity structure is usually unknown. Therefore, the uncertainties in the velocity model will cause errors in the calculated traveltimes, and thus accumulate to location errors. If the hypocenter locations of a set of seismic events are compact and within a restricted area, relative location methods, such as master-event location (Deichmann & Garcia-Fernandez, 1992, Deichmann & Giardini, 2009) and the double-difference location (Waldhauser & Ellsworth, 2000), can be used to obtain the locations of the seismic events relative to each other. For relative location methods, the errors and uncertainties in the velocity model mainly come from outside the source region, and thus are identical for observations from two events at the same station and therefore will not affect the relative locations (Deichmann & Giardini, 2009). Figure 1.5 shows microseismic location results for the standard traveltime inversion and relative location method at a hydraulic fracturing site. The microseismic locations of the relative location method (Figure 1.5 right panel) show a narrower fracturing zone with a compact distribution of microseismic events. Distinct horizontal bands also appear in the vertical cross section for the relative location results. However, the distribution of microseismic events is quite disperse for the standard picking and inversion method.

For the master-event location method, a well located seismic event or a seismic event with known location is selected as a master event. All other events which are referred to

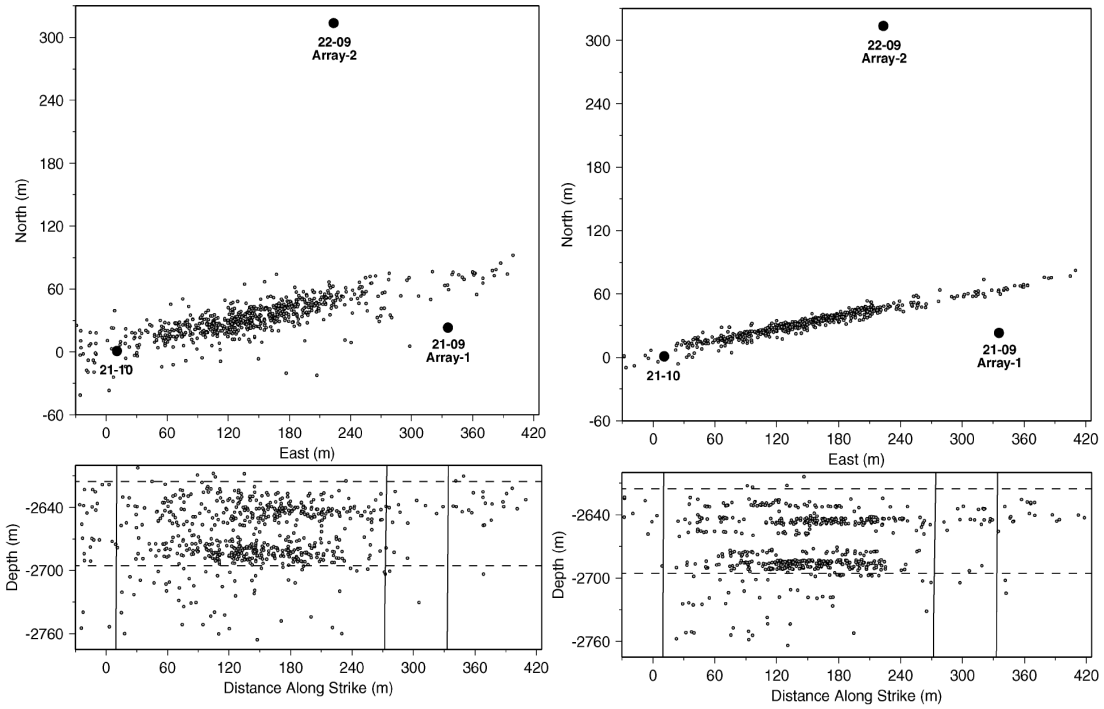

Figure 1.5: Map view and cross section view of microseismic locations for the Cotton Valley hydraulic fracturing. The treatment well is indicated by the black circle and labelled with 21-10. The two monitor wells are indicated by black circles and labelled with 21-09 and 22-09, respectively. Microseismic event locations are indicated by the small dots. The dashed lines in the cross sections (bottom row) mark the injection intervals. The vertical lines mark the depth projections of the treatment and monitor wells. Left panel shows location results from standard absolute location method. Right panel shows location results from relative location method. Figure modified from Rutledge & Phillips (2003).

as slave events are located relative to this master event. The location process essentially follows the same strategy as the linearized traveltime inversion method, in addition to that the arrival time residuals of the master event are used as station corrections for all slave events. As the resulting event locations are relative to the master event, the absolute location accuracy of the slave events relies on the location accuracy of the master event.

For the double-difference method, the hypocenter locations of seismic events in a certain region are all located relative to each other. Instead of directly using absolute arrival times of seismic events, the double-difference method utilize the arrival time difference between two events to relatively locate the seismic event. The double-difference method relates the residual between observed and calculated differential traveltimes between the two events to the distance between the two events (Waldhauser & Ellsworth, 2000). Therefore, the inversion equations are built on all possible different event pairs. It is now a routine process to relocate seismic events located by other absolute location methods using double-difference method in relatively small volumes to obtain a more compact and accurate hypocenter location results. Menke & Schaff (2004) point out that the double-difference method can still obtain absolute location results but the accuracy depends on the adopted velocity model. It is worth noting that the relative location methods are normally only valid for the situation where station-event distances are much larger than the inter-event distances.

1.3.5 Diffraction stack imaging

The aforementioned location methods all rely on picked arrival times of seismic phases. This means specific seismic phases should be identified and associated to a certain seismic event. This can be a very time consuming process when many seismic events exist in the recorded data. In addition, when the recorded data is contaminated by strong noise, phase picking will be very difficult or impossible. All these factors make the picking and arrival time based location methods not favourable for real time and automated seismic location determination. For automated seismic location methods, automatically utilizing the recorded seismic waveforms is important. Kao & Shan (2004) first proposed a source-scanning algorithm (SSA) to locate seismic events without picking. This method automatically stacks the recorded waveforms according to calculated traveltimes and uses the stacked waveforms as an indicator to identify seismic event location and origin time. This source location strategy is also referred to as diffraction stack imaging (Gajewski et al., 2007), backprojection imaging (Beskardes et al., 2017), waveform migration or stacking (Gharti et al., 2010, Grigoli et al., 2013a, Langet et al., 2014) and Kirchhoff reconstruction (Baker et al., 2005). As an automated seismic location method, the waveform migration can save human efforts involved in seismic location, such as arrival time picking. Utilizing seismic waveforms has the ability to identify more seismic events and complete the seismic catalogue. As shown in

Figure 1.6, the waveform migration method has identified 7 times more events than traditional location method and also moves the detection threshold 0.8 lower in magnitude (Beskardes et al., 2017). The located events can better delineate the complexity of the fault zone.

The diffraction stack imaging (DSI) is based on recorded seismograms. As Figure 1.7 a1-a2 shows, the generated seismic waves propagate through the Earth and are recorded by monitoring stations. The recorded seismograms contain information of the source, such as source location and origin time. After applying a simple transformation to remove the polarity of seismic waves (as shown in Figure 1.7 a3), such as calculating the envelope or absolute values, the transformed seismograms can be used to perform automated source location using DSI. The detailed processes of the DSI method are summarized as follows. The traveltimes from each imaging point in the subsurface to the station can be calculated efficiently using e.g. an Eikonal solver (Podvin & Lecomte, 1991). Assuming a trial origin time of the seismic event, the arrival time of a seismic event at a trial imaging point and a trial origin time can be calculated using $T_{ik} = t_{ik} + t_0$, where t_{ik} is the traveltime from imaging point i to station k and t_0 is the trial origin time. Then, waveforms are stacked along different stations at the calculated arrival times. The stacked/imaging value at the trial imaging point can be expressed as $W(x_i, y_i, z_i, t_0) = \sum_{k=1}^{N} S(T_{ik})$, where N is the total number of stations, $S(t)$ are the transformed seismograms and x_i, y_i, z_i are spatial coordinates of the imaging point i. At the same imaging point, the stacking process is performed along different trial origin times to search for a potential correct source origin time. Figure 1.7 b1-b4 shows the stacking process of DSI as a trial imaging point and three different trial origin times. The stacking process is then conducted on each imaging point in the subsurface (as shown in Figure 1.7 b-d). Therefore, the final obtained migration volume is a 4D data volume with 3D in the space domain (source location) and 1D in the time domain (origin time). Because the recorded waveforms are most coherent/consistent across all the stations at the correct source location and origin time, the stacked values will reach the maximum at the correct source location and origin time (as shown in Figure 1.7 c3). Thus, the source location and origin time can be identified from the final migration volume by finding the maximum imaging values: $x_s, y_s, z_s, t_{0s} = max_{t_0 \in [t_1, t_2]}\{W(x, y, z, t_0)\}$ (as shown in Figure 1.7 e1-e4).

Chambers et al. (2010b) investigate the imaging ability of DSI and surface arrays for microseismic activity using perforation dataset. In their studies, perforation shots with known locations and origin times are located using DSI to test the ability and accuracy of surface arrays to detect and locate microseismic events. Since the surface arrays are deployed at surface and away from the perforation shots at depth, the SNR of the seismic records is low and signals from the perforation shots are not visible in the data. However, after stacking and migration clear source energy focuses appear, which reveal the locations and origin times of the perforation shots. Their studies show that surface

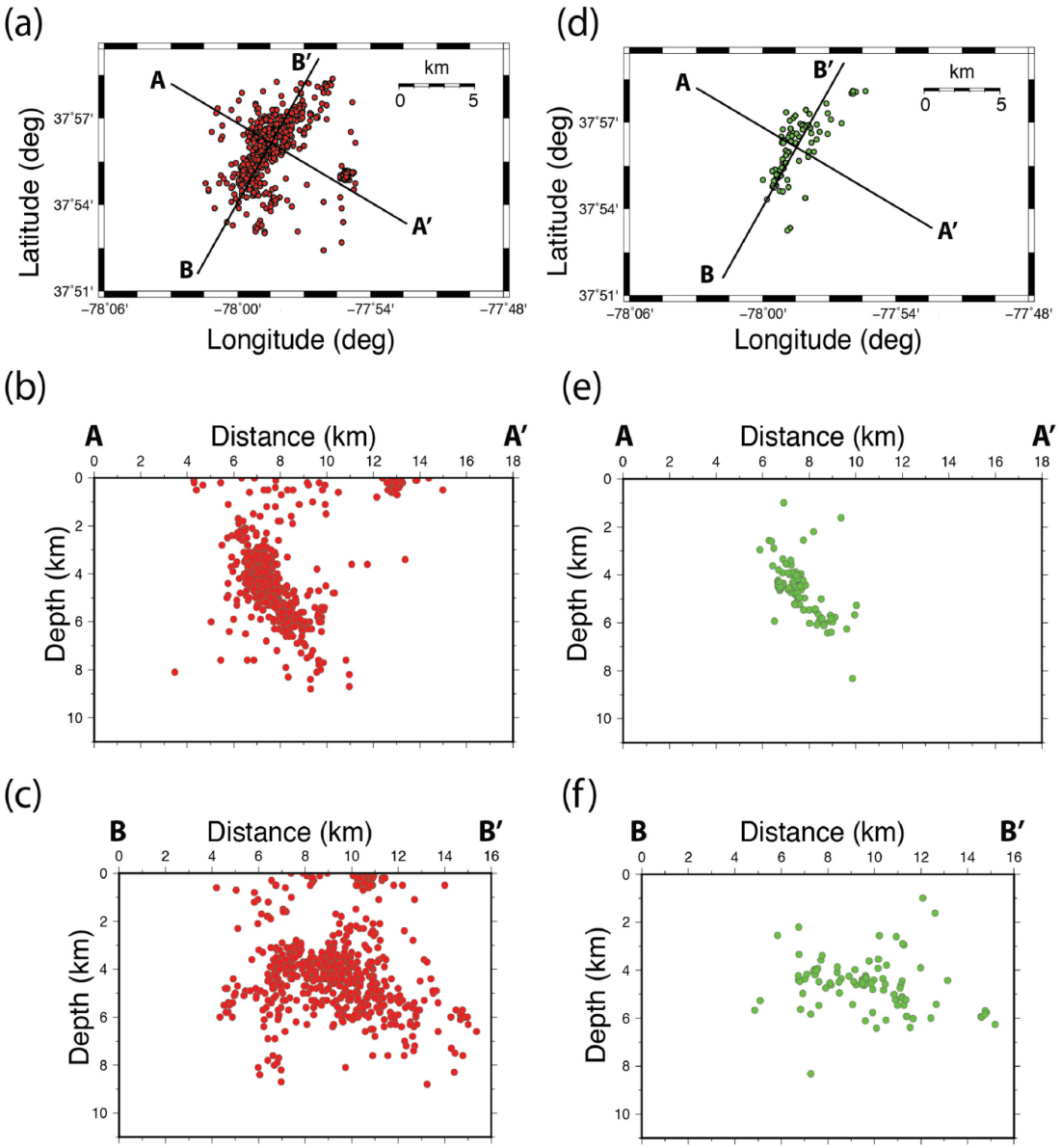

Figure 1.6: Hypocenter locations of earthquakes following the 2011 Virginia earthquake. The top panel shows map view of location results. Middle and bottom panel show cross sections along AA' and BB'. (a-c) Hypocenters located by automated waveform migration. (d-f) Hypocenters located by picking and arrival time based method using traditional aftershock network. Figure from Beskardes et al. (2017).

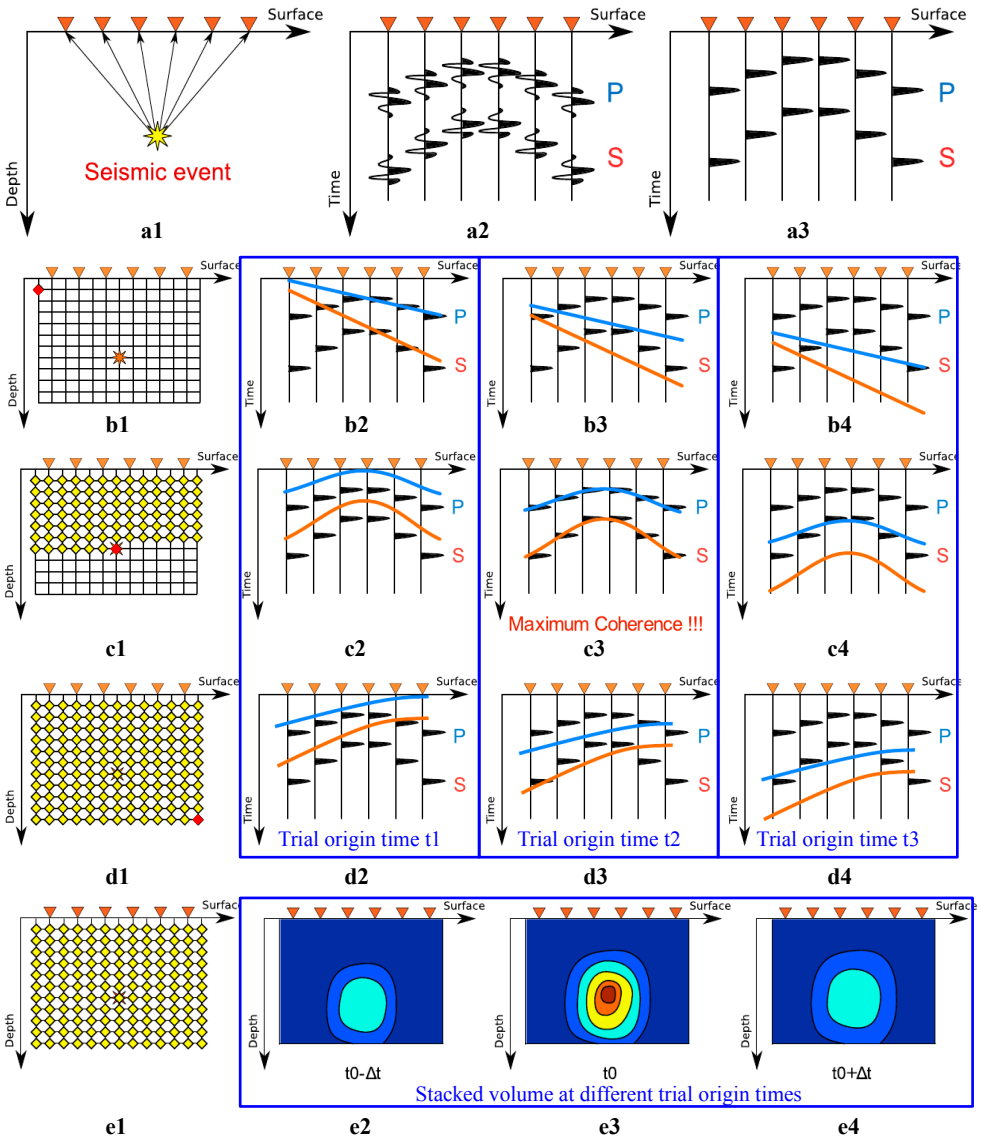

Figure 1.7: Schematic diagram showing the waveform stacking process. The star shows the location of an assumed seismic event. The triangles show the locations of surface stations. Figure a2 represents the recorded seismograms containing the direct P- and S-waves. Figure a3 represents the characteristic functions of the recorded seismograms after transformation. Figures b1-b4 and d1-d4 show the stacking processes at different trial origin times for a imaging point which is away from the exact source location. Figures c1-c4 show the stacking processes at different trial origin times for a imaging point which locates just at the exact source location. Figures e1-e4 show the stacking profiles at different trial origin times. The maximum stacking value appears at the correct source location and origin time. Blue solid lines show the calculated arrival times of P-waves and orange solid lines show the calculated arrival times of S-waves. The yellow diamonds represent the imaging points which have already gone through the stacking process. The red diamond represents the current imaging point. Figure modified from Cesca & Grigoli (2015).

arrays are capable of imaging microseismic events by utilizing DSI method, even when SNR is down to 0.1 and the signals are not visible in individual traces. Chambers et al. (2010a) apply DSI to image microseismic events induced by hydraulic fracturing. They also explore the influence of event magnitude, SNR, source mechanisms and velocity uncertainties to the seismic event location using synthetic tests.

In contrast to controlled explosive sources, natural earthquakes have complex source mechanisms, and thus show different source radiation patterns. For natural earthquakes, many seismic events are caused by fault dislocation and therefore have double-couple source mechanism. For many seismic events induced by hydraulic fracturing, complex source mechanisms such as non-double-couple source time functions are often observed as well (Šílenỳ et al., 2009). This means that the signals recorded at different stations will have different phase polarizations. Therefore, due to complex source radiation patterns, the waveforms may be stacked destructively and the maximum stacked value may not appear at the exact source location. Zhebel & Eisner (2014) show that several maxima will appear around the true source location when stacking the waveforms of pure double-couple sources. Therefore, directly stacking recorded seismograms is not effective and will cause location errors when imaging sources with complex radiation patterns. Instead of directly utilizing recorded waveforms, DSI is often performed on various characteristic functions of recorded waveforms. Characteristic functions are simply some kind of transformation of the original waveforms in order to remove source radiation patterns and obtain non-negative traces. Stacking of characteristic functions can remove the effect of source radiation patterns and obtain an accurate source location. Different characteristic functions have been proposed and used in the DSI, such as the absolute amplitude (Kao & Shan, 2004, 2007), the envelope (Baker et al., 2005, Gharti et al., 2010), the short-term-average/long-term-average (STA/LTA) (Grigoli et al., 2013a,b, Drew et al., 2013) and the kurtosis (Langet et al., 2014) of the waveforms. As shown in Figure 1.8, different characteristic functions can exhibit different imaging resolutions and noise resistance.

Different phases, such as the direct P- and S-phases, can be utilized alone or in combination to image the source. Normally, if the SNR of recorded data is high, jointly using different phases can improve location accuracy. In theory, any phase such as multiples, reflected waves and converted waves can all be used in DSI to locate the source. However, the traveltimes of these additional phases depend more strongly on the adopted velocity model than the primary phases. When the subsurface velocity model is poorly known, utilizing those non-primary phases can cause location deviations.

The techniques developed in other location methods can also be incorporated into the DSI framework. Grigoli et al. (2016) propose a master-event waveform stacking method to locate the source, which combines the master-event location method and the DSI method. By utilizing the techniques developed from relative location methods, this combined method can mitigate the negative effect of uncertainties of the velocity

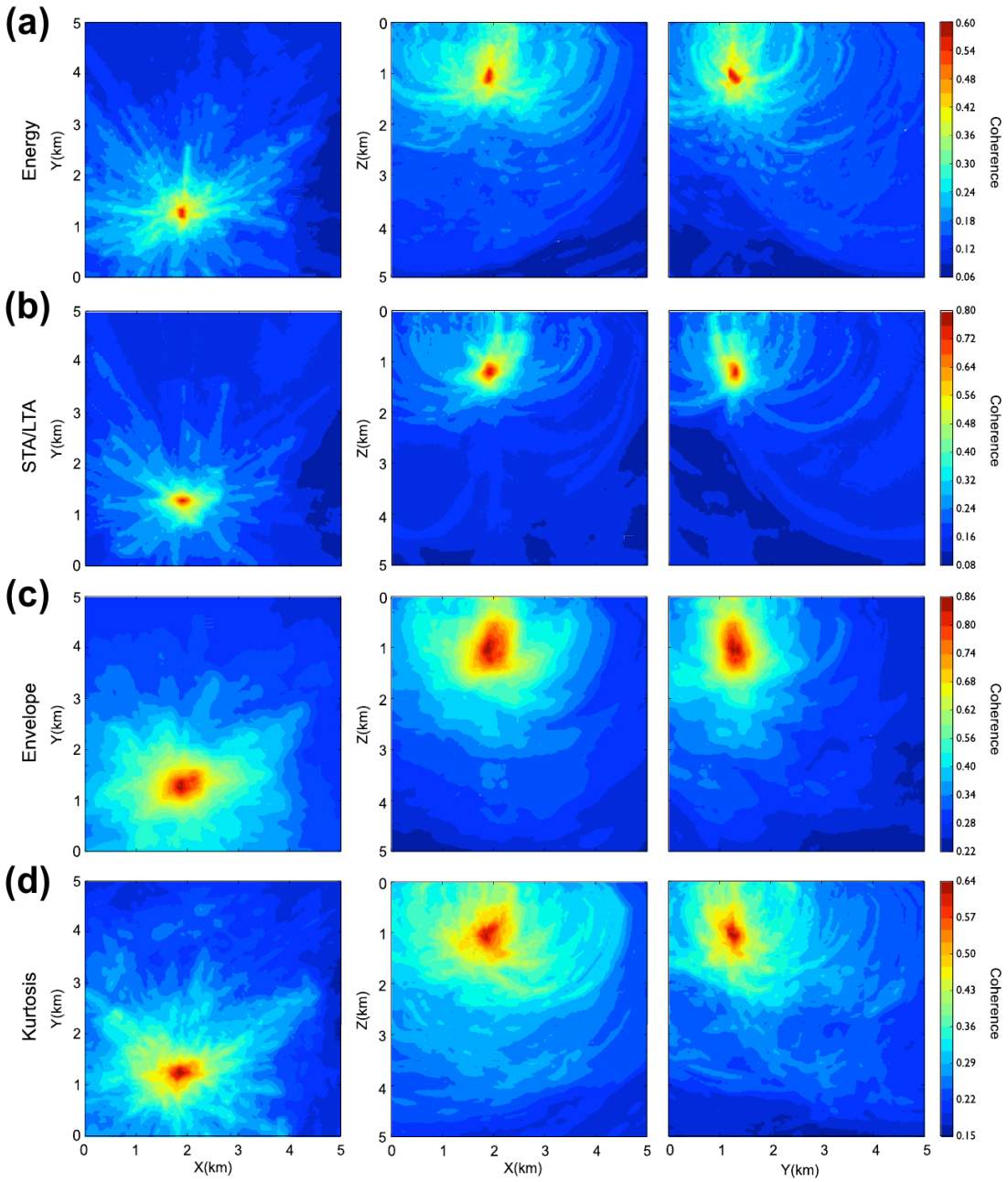

Figure 1.8: Migration profiles of a magnitude 1.4 seismic event for different characteristic functions. Different columns show migration profiles in different directions. The color represents stacked/migration values. Large migration value (red color) represents high possibility of the existence of a seismic event. Different rows show results for different characteristic functions used in migration: (a) the energy, (b) the STA/LTA, (c) the envelope, (d) the kurtosis. Figure from Cesca & Grigoli (2015).

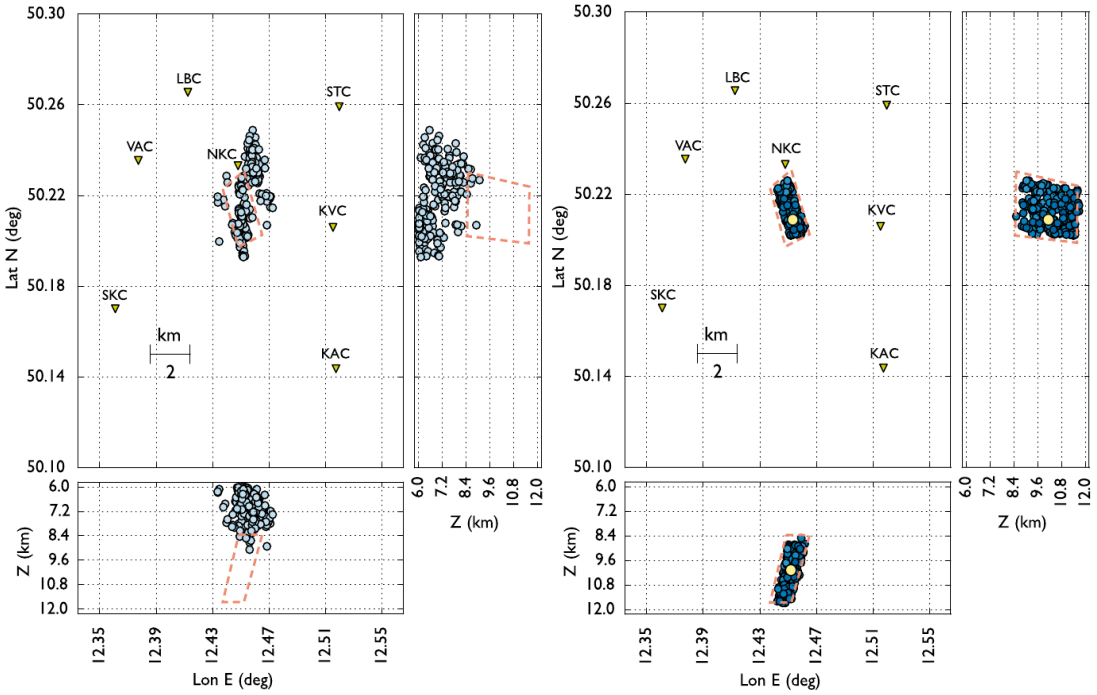

Figure 1.9: Hypocenter locations of synthetic events using a wrong velocity model. The synthetic seismic events are denoted by circles and are all located in the dashed lines. The triangles show locations of stations. Left panel: hypocenter location results of standard migration method using a wrong velocity model. Right panel: hypocenter location results of master-event migration method using the same wrong velocity model. The used master event is highlighted by the yellow circle. Figure modified from Grigoli et al. (2016).

model to seismic location results and reduce the dependence of DSI on velocity models. As shown in Figure 1.9, the master-event waveform stacking/migration method can remove the effect of velocity model outside the source area, and obtain relatively accurate seismic locations even with a wrong velocity model. For finding the global maximum in a migration volume, global optimization algorithm can be more efficient than the full grid search method. As a global optimization technique, the differential evolution algorithm can be used in the nonlinear grid search methods to obtain the global maximum efficiently. Differential evolution is essentially an evolutionary algorithm for global optimization, and it uses a differential scheme to generate new trial source locations and approaches the correct source location iteratively (Gharti et al., 2010). Gharti et al. (2010) applied the differential evolution technique to the DSI framework and improved the efficiency of the DSI algorithm.

Although DSI has many successful applications in automated seismic location, this method still needs further developments, such as handling ultra-low SNR data, estimating location uncertainties and effectively identifying seismic events in a migration volume. For surface monitoring which is common for passive seismic monitoring, the stations are normally deployed away from the seismic events. Therefore, the recorded signals can be very weak due to attenuation and geometric spreading. In addition, sur-

face recordings can easily be contaminated by various kinds of noise, reducing the SNR of the recorded data. Although migration-based methods can utilize the coherence of all stations and have the ability to image source events with low SNR, locating microseismic events in ultra-low SNR scenario is still very challenging. For microseismic events, the recorded waveforms can be highly contaminated by noise and the signals are invisible against background noise, thus pose a great challenge to all location methods. For arrival time based location methods, the location error can be assessed using statistical approaches (Tarantola & Valette, 1982, Lahr, 1999, Lomax et al., 2000). However, the uncertainty estimation for the waveform migration based location methods is not straightforward and is difficult to conduct. The uncertainty is not only related to the raw data quality but also the characteristic functions. In addition, because of data aliasing, it is also difficult to identify different seismic events which occur at the same time or at adjacent time from the migration data volume.

1.3.6 Reverse time modeling

Primary phases (direct P- and S-phases), reflected phases and converted phases can be used in DSI to automatically locate seismic events. However, there is other information, such as scattered waves and coda waves, recorded in the whole wavefield, which cannot be used effectively in the waveform migration. In addition, the DSI methods have difficulty in handling reflected waves and multiple waves in complex velocity models, which might cause source imaging artefacts. In order to fully utilize the whole recorded wavefields, researchers proposed the reverse time modeling (RTM) approach to automatically locate seismic events (McMechan, 1982). The utilization of reverse time modeling approaches to locate seismic sources was first implemented by McMechan (1982). This location approach is often also referred to as time reversal/reverse imaging (Larmat et al., 2006, Kawakatsu & Montagner, 2008, Horstmann et al., 2015), time reverse modeling (Steiner et al., 2008, Zhu, 2014, Kocur et al., 2016), time reversal extrapolation (Li & van der Baan, 2016), reverse time migration (Nakata & Beroza, 2016, Wang et al., 2016) and reverse time imaging (Zou et al., 2014, 2015).

The RTM is essentially a forward modeling method to extrapolate the recorded full seismic wavefield backward in time for imaging seismic sources (McMechan, 1982, Fink et al., 2000, Gajewski & Tessmer, 2005, Larmat et al., 2006). This approach utilizes the time reversibility of the wave equation and solves the inverse problem of seismic forward modeling in the form of a boundary value problem. For each station the recorded seismogram is first reversed in time, and then the time reversed seismograms of all stations are injected back into the modeling process, and afterwards the modeling process is performed as normal. In the reverse modeling process, all the stations are acting as excitation sources, and the time reversed seismograms are acting as the source time functions (source wavelets) for the corresponding sources. When reversely propagating the recorded wavefield back in time, the generated wavefield will

gradually focus at the hypocenter location at the correct source origin time (as shown in Figure 1.10). Therefore, the hypocenter location and origin time can be determined by identifying the location and time of the wavefield focus. The RTM has the ability to handle complex velocity structures and can automatically migrate the reflected waves, scattered waves and coda waves back to the correct source location. McMechan et al. (1985) demonstrated the feasibility of this method to image real earthquake sources. Some necessary preprocessing steps including construction of a true amplitude section (to reveal the source radiation pattern), filtering (to denoise and remove aliasing) and interpolation (to produce a wavefield at discrete grid points that correspond to the grid points of numerical modeling) are required in order to obtain a desirable source image. The relative magnitude of events can be qualitatively represented by the relative size of the source images.

There are still many problems that restrict the application of the RTM approach. As a migration-based method all the problems that make the DSI location method difficult also apply to the RTM location method, such as imaging in ultra-low SNR scenarios and estimating location uncertainties. In addition, RTM also faces many other problems in practical applications. The first is the computational cost. As RTM involves full waveform modeling and requires reversely propagating recorded wavefields back in time, it is computationally expensive. For big models, the waveform modeling is costly and requires large memory to store all the wavefields at different modeling times. The computational expense and memory cost prohibit the practical applications of the RTM methods. Furthermore, the RTM methods require a large recording aperture and dense monitoring arrays, which poses harsh requirement for the deployment of stations. Sparse monitoring arrays or limited recording aperture will lead to insufficient spatial sampling and will further result in incomplete source energy focus and imaging artefacts. The commonly used imaging conditions/criterions of the RTM location methods include maximum energy imaging condition (Artman et al., 2010) and cross-correlation based imaging condition (Nakata & Beroza, 2016). However, the imaging conditions are not always effective in different situations (e.g. complex velocity models, irregular array geometry, complex source mechanisms and earthquake clusters) and for different source events. Efficient imaging conditions for different situations still need further development. Waveform modeling needs a suitable velocity model, and the modeling results highly depend on the adopted velocity model. Since the subsurface velocity model is always unknown, uncertainties in the velocity model will be accumulated into the modeling results and thus can cause location errors.

1.3.7 Full waveform inversion

With the development of monitoring techniques and the proliferation of high-quality seismic data, we are recording the seismic full wavefield in more detail and with more accuracy. Full wavefield-based methods are thus getting increasing attention and have led

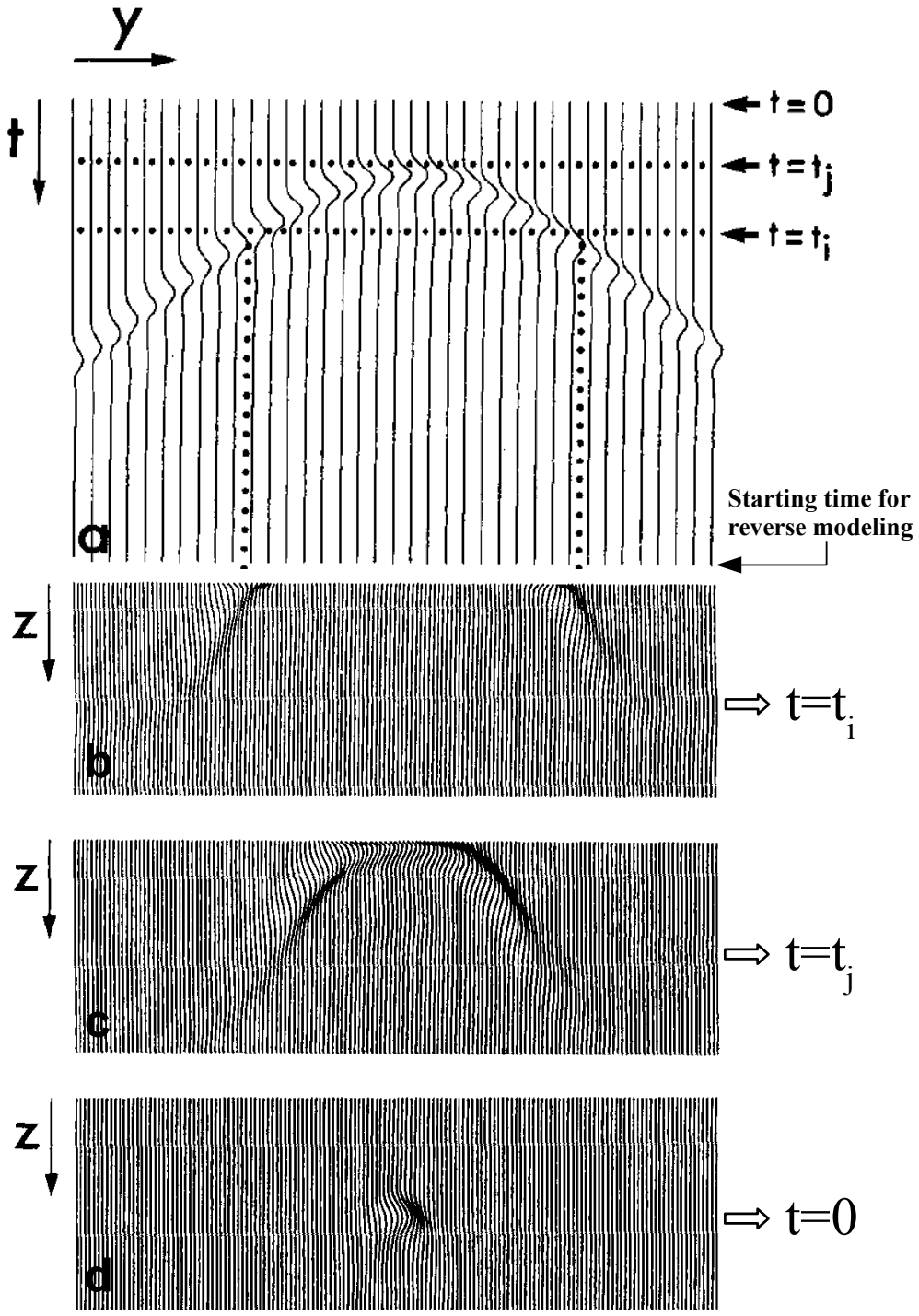

Figure 1.10: Schematic diagram showing the reverse time modeling process. The recorded seismograms (a) are reversely injected into the modeling, and the reversely propagated wavefields gradually focus at the source location at the correct origin time (b-d). Figure modified from McMechan (1983).

to more practical applications. Full waveform inversion (FWI) as a waveform matching technique is increasingly used in geophysical imaging. FWI is extensively used for subsurface velocity imaging in exploration geophysics (Tarantola, 1984, Virieux & Operto, 2009). However, assuming the velocity model is known, FWI can also be used to invert for the source parameters, e.g. source location, source time function and source mechanism. The basic idea of FWI is to find a model which can produce the best matched synthetic waveforms with the current observed data. The best fit model is often found by first assuming an initial guess of the model, and then iteratively updating the model until a certain criterion is fulfilled. The key of FWI is to find a solution which can update the model correctly and efficiently. The solution can be found by minimizing the residuals between the currently generated synthetic data and the observed data. For utilizing FWI to invert for source parameters, the update direction can be determined using an adjoint-state method (Kaderli et al., 2015) or grid-search approach (Zhang et al., 2015). Figure 1.11 shows a 2D synthetic case for seismic location using FWI. The update process in FWI is achieved by adjoint-state method. FWI can achieve good seismic location results even if the data is highly contaminated by random noise. In the synthetic experiment, the noise is assumed to be Gaussian noise and the source time functions and origin times of seismic sources is assumed to be known. However, when both source locations and source time functions need to be determined, the inversion results of FWI (as shown in Figure 1.12) are unsatisfactory.

Early FWI studies were mainly focused on the theory of FWI and the application of FWI on synthetic data. Only recently enhanced computer resources have made practical applications of FWI possible. Wu & McMechan (1996) first utilized FWI to determine the source location, origin time and the amplitude and orientation associated with synthetic double-couple sources in 2D scenario. The velocity and density distribution of the model as well as the source time function are assumed to be known a-priori. Ramos-Martínez & McMechan (2001) estimated the source mechanisms using FWI in 3D heterogeneous viscoelastic anisotropic media with the assumption that both the source location and source time function are known. Michel & Tsvankin (2014a,b) illustrated the calculation of the gradient of the objective function in FWI using the adjoint-state method, and estimated the location, origin time and source mechanism of microseismic source in vertical transversely isotropic media using synthetic data. Zhang et al. (2014) applied elastic FWI for determining microseismic event location and source mechanism simultaneously in layered media based on synthetic data. Kaderli et al. (2015) determined both the source location and the source time function via FWI using the 2D acoustic wave equation and synthetic dataset. Zhang et al. (2015) used a grid-search method and global optimization technique to update the source model in the FWI framework and resolved the source location and mechanism under a given velocity model. The method requires a generated Green's function library and event detection. Wang & Alkhalifah (2018) developed a source time function independent FWI

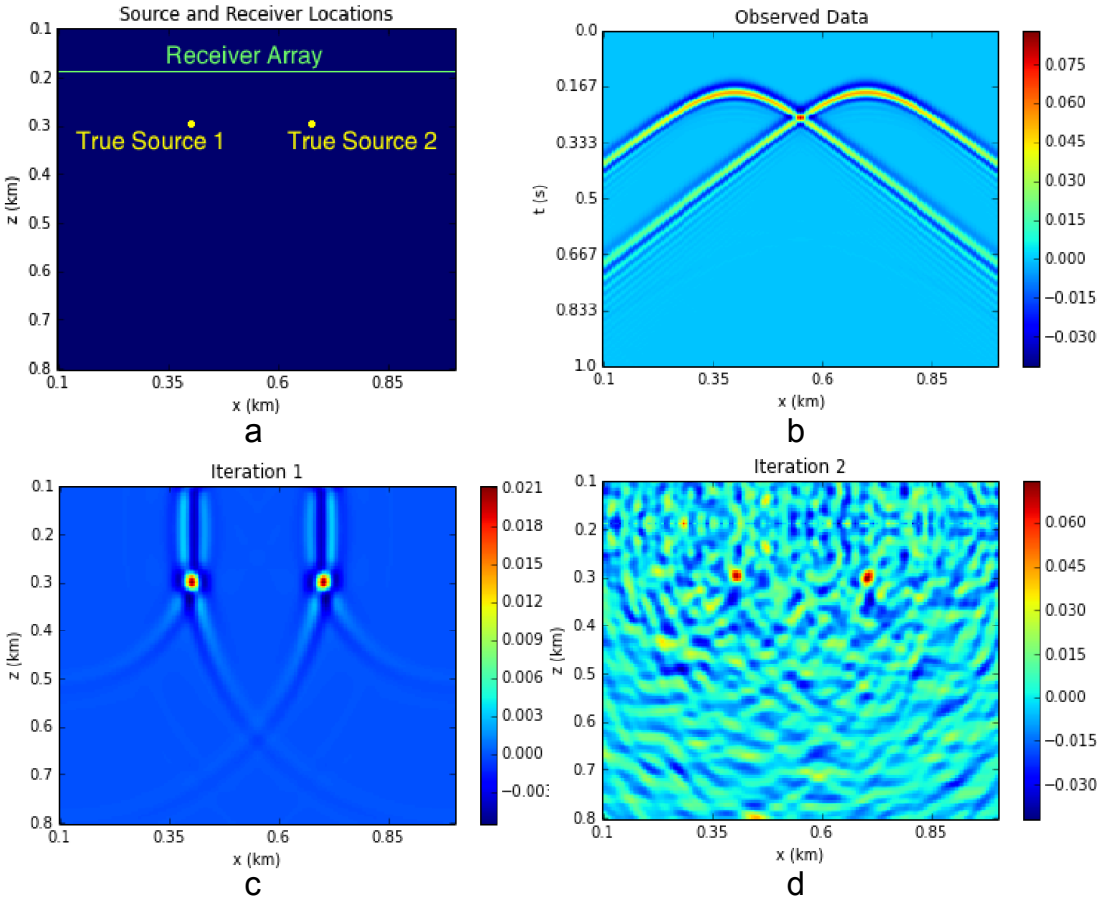

Figure 1.11: A 2D seismic location experiment via full waveform inversion. The source time functions and origin times of the seismic sources is assumed to be known. (a) Source and receiver configuration of a synthetic experiment. Yellow dots represent source locations. Green line shows the receiver array. (b) Synthetic noise free data for the model shown in figure (a). (c) Source estimations after 1 iteration of FWI using the synthetic noise free data. (d) Source estimations after 2 iterations of FWI using a synthetic noisy data with a SNR of 0.008. Figure modified from Kaderli et al. (2015).

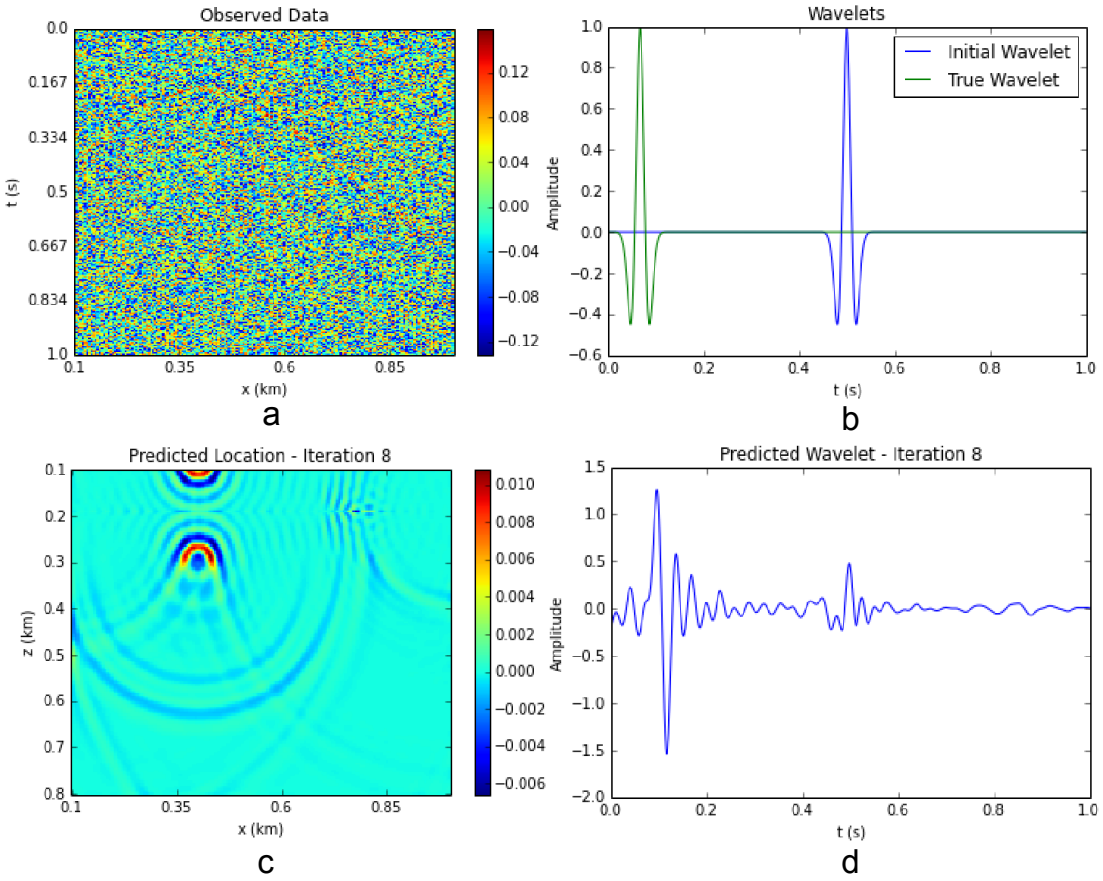

Figure 1.12: A 2D seismic location experiment via full waveform inversion. The source time functions is unknown. (a) Noisy data with a SNR of 0.083. The noisy data is obtained by adding Gaussian noise into the synthetic noise free data (shown in Figure 1.11 (b)). (b) The true and initial source time function. The green line shows the true source time function used in modeling. The blue line shows the initial source time function used in FWI. (c) Source estimations after 8 iteration of FWI using the noisy data. (d) Source time function estimation after 8 iteration of FWI using the noisy data. Figure modified from Kaderli et al. (2015).

to invert for source location, origin time and velocity model simultaneously. By convolving reference traces with observed and modelled traces, the FWI does not require an a-priori source time function, which makes the inversion process more stable.

Most applications of FWI are limited to synthetic data, while the practical usage of FWI is still in its infancy. There are several reasons which limit the practical application of FWI. First, similar to RTM, as FWI needs to conduct forward and backward modeling at each iteration, the computational expense and memory cost of FWI is huge compared to other location methods. In the case of large dataset and model, the costly computational burden inhibits the application of FWI. It also requires a large array aperture and dense monitoring arrays to ensure a good imaging illumination and resolution. In addition, the inversion process requires a good initial model to secure a correct and convergent inversion result. The initial model can be obtained by other location methods such as traveltime inversion. However, this will undermine the role of FWI as an independent and automatic source location method. Because of the huge nonlinearity of FWI, the inversion result may suffer from the local minimum problem, thus may have large location errors. For most FWI approaches, the source time function is assumed to be known a-priori. For practical applications, the unknown source time function or inaccurate estimation of the source time function will make the FWI unsuitable. Although there are ways to implement source time function independent FWI (Wang & Alkhalifah, 2018), simultaneously inverting for source location, source time function and other parameters, e.g. source mechanism and velocity model, would greatly increase the nonlinearity of FWI and make the inversion process unstable, which is already highly ill-posed.

1.4 Applications of microseismic monitoring

The purpose of microseismic monitoring is to monitor the occurrence of microseismic events using recorded seismograms of monitoring arrays. There are different types of monitoring arrays according to the deployment methods, such as downhole arrays, surface arrays and buried arrays. Downhole arrays are normally deployed close to the target monitoring areas, therefore the recorded data often have high SNR. However, the deployment of downhole arrays requires the existence of a well. In practice, due to the availability of monitoring wells, the number of seismometers used in a downhole array is often limited. The surface and buried arrays are deployed at near surface, therefore it is more convenient to deploy dense seismometers. In addition to the dense spatial sampling, the monitoring aperture of surface and buried arrays is often much larger, which is beneficial for seismic imaging. However, for deep monitoring layers, because the surface monitoring arrays are far from the target layer, the SNR of recorded data can be much smaller than that of the downhole arrays. Microseismic monitoring is designed for different kinds of purposes, for example reservoir evaluation and hazard

monitoring (Maxwell et al., 2010, Xu et al., 2011).

1.4.1 Reservoir evaluation

Hydraulic fracking is often used to enhance the properties of reservoirs, such as in the hydrocarbon extraction and geothermal exploration. In those applications, microseismic monitoring is needed to evaluate the effects of reservoir enhancement (Van Der Baan et al., 2013). The role of fracking is to create a fracture network which can facilitate fluid circulation. The injected high-pressure fluid will cause inelastic deformation of the rocks and will further result in the fracture opening in the subsurface. Each fracture opening or inelastic deformation is treated as a microseismic event. The radiated seismic waves of the microseismic events are recorded by monitoring arrays, and are further analysed to help us understand the fracture growth, the subsurface deformation and the geomechanical strain variation in the subsurface (Maxwell et al., 2010).

Microseismic monitoring can provide information about microseismic events, such as their locations and source mechanisms. Microseismic locations represent the locations of the created fractures. The origin times together with the locations of microseismic events can reveal the growth and distribution mode of the stimulated fracture networks. Source mechanisms of microseismic events can exhibit the geometry of the created fractures, i.e. the direction of fracture plane, dimensions of the fracturing and the rupture mode. This information can help decide whether a simple, planar fracture is stimulated or a complex fracture network with multiple, interconnected fracture segments is created during fracking. The interpreted fracture geometries from microseismic monitoring are then utilized to understand, control and optimize the fracking operation (Maxwell, 2014). Figure 1.13 (a) shows microseismic monitoring results at a hydraulic fracturing site. In the figure, different colors represent the microseismic events at different fracking stages. It is obvious that different distribution modes of the fractures have been created at different fracking stages. At the stage one (blue) and two (green), compactly distributed fractures with narrow distribution areas are generated; while at the stage three (red) and four (cyan), widely distributed fractures with a diffuse pattern are created, which suggests that a complex fracture network has been created due to the interaction with pre-existing fractures (Rich & Ammerman, 2010). The microseismic monitoring results can be further used to estimate geomechanical parameters of reservoirs (Figure 1.13 (b)) and provide guidance for engineering applications such as production well design and reservoir productivity optimization. Microseismic monitoring is also used to observe the fracturing and faulting associated with reservoir compaction, production and well completion. Time-lapse microseismic imaging can be used for investigating rock deformation associated with fracturing or fracture reactivation from pressure or stress changes in the overburden (Maxwell & Urbancic, 2005).

For microseismic monitoring of hydraulic fracturing, real time monitoring is becom-

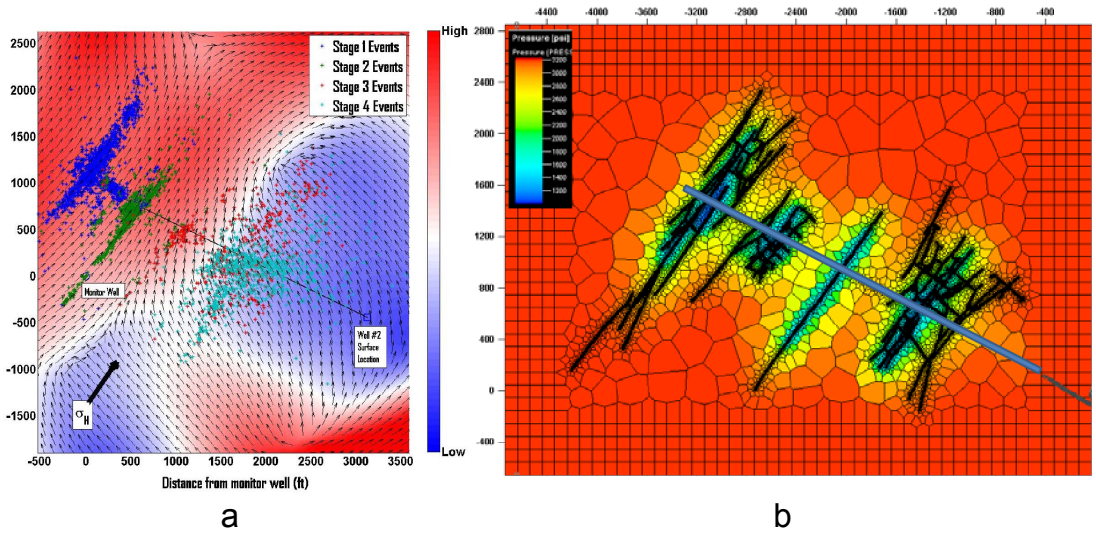

Figure 1.13: (a) Map view of microseismic monitoring results for a four-stage hydraulic fracturing of a horizontal well. Different colors show the microseismic events of different fracking stages. Figure from Rich & Ammerman (2010). (b) Estimation of pressure distribution in reservoir after 20 years of production. The pressures is indicated by color. Black lines show the stimulated fracture system derived from microseismic monitoring results shown in (a). Figure from Cipolla et al. (2012b).

ing more and more important. Real time monitoring and location can provide real time information and is thus critical for dynamically optimizing the hydraulic fracturing process (Cipolla et al., 2012a). Real time monitoring is also needed to avoid the hydraulic fractures growing out of the target layer when fracking, which may cause aquifer contamination or intersection with an existing fault (Vidic et al., 2013). In the traffic light system of microseismic monitoring during hydraulic fracturing, real time monitoring is required to reduce the potential risk for induced earthquakes (Majer et al., 2007). Since the recorded seismic signals need to be processed on the fly, real time monitoring calls for automated microseismic imaging and inversion methods.

In addition, the location accuracy of microseismic events is very important in terms of imaging the fracture process and geometry. Large location errors during the monitoring might contribute to huge economic loss as the fracturing process may be terminated prematurely if the stimulated fracture length has been exaggerated. Large location errors can also bring unexpected damages for shallow aquifers when the stimulated fracture length has been underestimated. Therefore, an automated and accurate seismic location method for microseismic monitoring is always in great demand.

1.4.2 Hazard monitoring

Although only releasing small energy, microearthquakes can still cause damage and need careful monitoring. Microseismic events can be evoked by various activities, such as mining, fluid injection and extraction, volcanic activities, reservoir impoundment

and discharge. Those activities will alter the state of stress or pore pressure in rocks, which may result in the occurrence of microseismic events. The pressure and stress change in the subsurface may induce destructive earthquakes by creating new fractures or faults, and trigger devastating earthquakes by reactivating the pre-existing faults. Microseismic monitoring is widely used to monitor the potential geo-hazard risk due to the induced microseismic events. Microseismic monitoring can dynamically monitor the occurrence of induced microseismic events, prevent the induced earthquakes from causing larger impacts. Now the traffic light system is widely used to stop the fracking process or geothermal pumping if a seismic event larger than a certain magnitude (e.g. local magnitude 0.5 in the UK or local magnitude 2.9 in Switzerland) has been induced (Council, 2013, DECC, 2015, Häring et al., 2008). For the fluid injection or extraction activities and the geological storage of various wastes, such as waste water disposal, nuclear waste storage, carbon capture and storage and hydrocarbon extraction, microseismic monitoring is used to investigate the fracturing process in the subsurface, inspect the integrity of the reservoir, check the wellbore and caprock stability or reduce the risk of potential leakage.

Microseismic monitoring is applied to mining engineering for the purpose of safety (Jiang et al., 2006). Mining operations, such as excavations, will cause stress changes in rocks, thus can result in slip on pre-existing faults or explosive rock failure, i.e. microseismic events. Even though the magnitudes of these microseismic events may be small, the mining-induced seismic events still put the lives of miners at great risk since they are often very close to the actual seismic locations. Safety concerns greatly promoted the development of mining-induced seismic monitoring systems. These induced earthquakes can be detected by microseismic monitoring systems, thus providing valuable safety information as well as additional industrial applications.

Microseismic monitoring is used to monitor the induced seismicity near a dam or large reservoir for safety and slope stability (Xu et al., 2011). Activities like large, surface-water impoundments from dams or reservoirs can cause excessive surface mass and pore pressure variation, which have a high possibility to trigger seismicity. Conducting microseismic monitoring while the reservoir fills can effectively control the process of impoundments and reduce the risk of man made geological hazards. Figure 1.14 shows the induced microseismic events during a slope excavation. Monitoring those microseismic events is essential to evaluate the variation of rock mechanical parameters during rock mass degradation, thus can help monitor the slope stability and reduce geohazard risk.

Earthquakes can be triggered by many volcanic activities such as the moving of magma and volcanic fluids (McNutt, 2005, Zobin, 2012). The volcanic seismicity involves volcano-tectonic earthquakes, long-period earthquakes and volcanic tremor. The moving of magma and volcanic gases toward the surface from depth can cause significant stress changes in the crust and can thus trigger volcanic earthquakes. Distinguishing

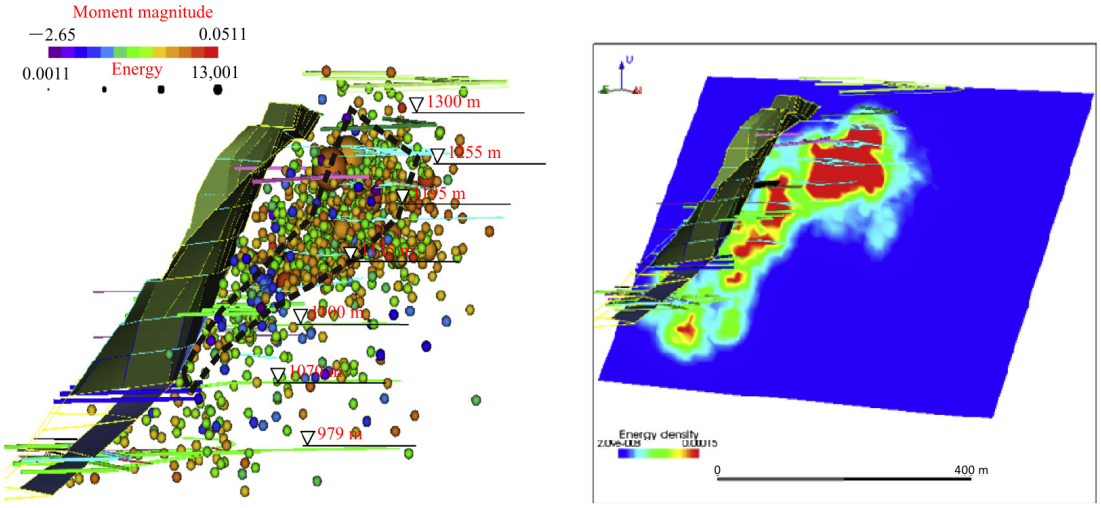

Figure 1.14: Locations of microseismic events (left panel) and energy dissipation density (right panel) during a slope excavation. The microseismic events are indicated by colored balls with the color and size of the ball represent the moment magnitude of microseismic events. The slope surface is marked by the green block. The colored lines indicate the tunnels. Figure from Tang et al. (2015).

and analysing different types of volcanic seismicity can help us understand the volcanic activities and structures beneath the volcano. Most volcano-related earthquakes are small and occur in the shallow part of the crust (McNutt, 2005). They can occur in swarms which contain hundreds of volcano seismic events. Seismic swarms are often observed preceding to volcano eruption. Therefore, monitoring volcanic seismicity can help us determine whether an eruption may occur or not and mitigate the potential volcano-related hazard.

1.5 Objectives and thesis road map

As described in the aforementioned introduction part, the current seismic monitoring systems are getting denser and recorded seismic wavefields are getting larger and more complete. Therefore, automated and full waveform based seismic location methods are in high demand. In addition, microseismic monitoring is often implemented in anisotropic media and needs to deal with different types of source mechanisms. Therefore, full waveform modeling methods which apply to anisotropic media with arbitrary moment tensor sources are required to test and benchmark various full waveform based methods.

The overall objective of this thesis is to develop an efficient full waveform modeling tool and an automated, waveform-based seismic location method. The full waveform modeling tool can be used to generate seismic full wavefields in complex and anisotropic model, which can then be further used to test the developed seismic location method. The developed full waveform modeling tool can also be utilized in a series of full wave-

form based geophysical techniques, such as reverse time imaging and full waveform inversion. The developed seismic location method can be used to automatically locate seismic sources and greatly reduce the human efforts in processing seismic data, such as avoiding manual seismic event identification and arrival time picking. The objectives are achieved in the following Chapters 2, 3 and 4.

In Chapter 2 I develop a staggered-grid FD full waveform modeling tool. This full waveform modeling tool adopts the velocity-stress formation and is able to simulate seismic full wavefields in heterogeneous and anisotropic media. Arbitrary moment tensor source can be used in the developed full waveform modeling tool. I generate surface and downhole seismic records in anisotropic layered models and anisotropic overthrust models using the modeling tool. The effects of seismic anisotropy on recorded seismic amplitudes, traveltimes and radiation patterns are further analysed using the generated seismic records. Seismic location errors in different anisotropic model are discussed. This work was published in Shi et al. (2018) and is linked to the key achievements 1 and 2 in the discussion and conclusions chapter (Chapter 5).

In Chapter 3 I develop an automated seismic location method based on continuous seismic waveforms. The seismic location method calculates waveform coherency among the time windowed records of different stations, and then stacks waveform coherency to image seismic sources. It can automatically locate seismic/microseismic events with only a few parameters to adjust. I analyse the performance of this new automated location method in noisy seismic data with different SNRs. The developed method is much more noise resistant than other commonly used migration-based location methods. Synthetic data examples show the developed location method is robust and has the ability to image weak seismic events since waveform coherency rather than waveform amplitude is used in migration. The effects of velocity uncertainties on seismic location methods are also tested and discussed. A seismic location case on a complex model demonstrates reliability and effectiveness of the new developed location method. This work was published in Shi et al. (2019a) and is linked to the key achievements 3, 4 and 5 in the discussion and conclusions chapter (Chapter 5).

In Chapter 4 I apply the newly developed seismic location method to several practical scenarios. The developed location method is implemented with a parallel computing framework. I analyse the computational efficiency of the new method, and find the speedup ratio can reach the theoretical value since there is little communication to do between different computing nodes. The location method is used to automatically locate triggered seismic events at a volcano setting and a reservoir setting. The location results show the developed method is efficient and can obtain accurate location results even using sparse and irregular monitoring arrays. The developed method can automatically locate microseismic events which are difficult and time consuming to be manually picked up. The new seismic location method can be used to obtain a more complete earthquake catalogue and greatly reduce the human efforts in seismic data

processing. This work was published in Shi et al. (2019b) and is linked to the key achievements 3, 4, 5 and 6 in the discussion and conclusions chapter (Chapter 5).

In Chapter 5 I further discuss the research content in this thesis and summarize all the conclusions and findings that I currently have. Some future works and further studies are also mentioned and discussed.

References

Aboudi, J., 1971. Numerical simulation of seismic sources, *Geophysics*, **36**(5), 810–821. 1.2

Aki, K. & Richards, P. G., 2002. *Quantitative seismology*. 1.2

Alford, R., Kelly, K., & Boore, D. M., 1974. Accuracy of finite-difference modeling of the acoustic wave equation, *Geophysics*, **39**(6), 834–842. 1.2

Alterman, Z. & Karal Jr, F., 1968. Propagation of elastic waves in layered media by finite difference methods, *Bull. Seismol. Soc. Am.*, **58**(1), 367–398. 1.2

Artman, B., Podladtchikov, I., & Witten, B., 2010. Source location using time-reverse imaging, *Geophys. Prospect.*, **58**(5), 861–873. 1.3.6

Baker, T., Granat, R., & Clayton, R. W., 2005. Real-time earthquake location using Kirchhoff reconstruction, *Bull. Seismol. Soc. Am.*, **95**(2), 699–707. 1.3.5, 1.3.5

Bath, M., 2013. *Introduction to seismology*, vol. 27, Birkhäuser. 1.3.1

Berenger, J.-P., 1994. A perfectly matched layer for the absorption of electromagnetic waves, *J. Comput. Phys.*, **114**(2), 185–200. 1.2

Beskardes, G., Hole, J., Wang, K., Michaelides, M., Wu, Q., Chapman, M., Davenport, K., Brown, L., & Quiros, D., 2017. A comparison of earthquake backprojection imaging methods for dense local arrays, *Geophys. J. Int.*, **212**(3), 1986–2002. 1.3.5, 1.6

Billings, S., Kennett, B. L., & Sambridge, M. S., 1994. Hypocentre location: Genetic algorithms incorporating problem-specific information, *Geophys. J. Int.*, **118**(3), 693–706. 1.3.3

Billings, S. D., 1994. Simulated annealing for earthquake location, *Geophys. J. Int.*, **118**(3), 680–692. 1.3.3

Bolt, B. A., 1978. Earthquakes, A Primer, *University of California, Berkeley*. 1.3.1

Bowden, D., Tsai, V., & Lin, F., 2015. Site amplification, attenuation, and scattering from noise correlation amplitudes across a dense array in Long Beach, CA, *Geophys. Res. Lett.*, **42**(5), 1360–1367. 1.1

Brenguier, F., Kowalski, P., Ackerley, N., Nakata, N., Boué, P., Campillo, M., Larose, E., Rambaud, S., Pequegnat, C., Lecocq, T., et al., 2015. Toward 4D noise-based seismic probing of volcanoes: perspectives from a large-N experiment on Piton de la Fournaise volcano, *Seismol. Res. Lett.*, **87**(1), 15–25. 1.1

Buland, R. & Chapman, C., 1983. The computation of seismic travel times, *Bull. Seismol. Soc. Am.*, **73**(5), 1271–1302. 1.3.2

Carcione, J. M., Herman, G. C., & Ten Kroode, A., 2002. Seismic modeling, *Geophysics*, **67**(4), 1304–1325. 1.2

Cerjan, C., Kosloff, D., Kosloff, R., & Reshef, M., 1985. A nonreflecting boundary condition for discrete acoustic and elastic wave equations, *Geophysics*, **50**(4), 705–708. 1.2

Cerveny, V., 2005. *Seismic ray theory*, Cambridge university press. 1.2

Cesca, S. & Grigoli, F., 2015. Full waveform seismological advances for microseismic monitoring, in *Adv. Geophys.*, vol. 56, pp. 169–228, Elsevier. 1.7, 1.8

Chambers, K., Kendall, J., & Barkved, O., 2010a. Investigation of induced microseismicity at Valhall using the Life of Field Seismic array, *The Leading Edge*, **29**(3), 290–295. 1.3.5

Chambers, K., Kendall, J.-M., Brandsberg-Dahl, S., & Rueda, J., 2010b. Testing the ability of surface arrays to monitor microseismic activity, *Geophys. Prospect.*, **58**(5), 821–830. 1.3.5

Chapman, C., 2004. *Fundamentals of seismic wave propagation*, Cambridge university press. 1.2

Chew, W. & Liu, Q., 1996. Perfectly matched layers for elastodynamics: a new absorbing boundary condition, *J. Comput. Acoust.*, **4**(04), 341–359. 1.2

Cipolla, C., Maxwell, S., Mack, M., & Downie, R., 2012a. A practical guide to interpreting microseismic measurements, in *SPE/EAGE European Unconventional Resources Conference & Exhibition-From Potential to Production*. 1.4.1

Cipolla, C. L., Maxwell, S. C., & Mack, M. G., 2012b. Engineering guide to the application of microseismic interpretations, in *SPE Hydraulic Fracturing Technology Conference*, Society of Petroleum Engineers. 1.13

Council, N. R., 2013. *Induced seismicity potential in energy technologies*, National Academies Press, Washington, D.C. 1.4.2

Dablain, M., 1986. The application of high-order differencing to the scalar wave equation, *Geophysics*, **51**(1), 54–66. 1.2

DECC, 2015. Onshore Oil and Gas Exploration in the UK: Regulation and Best Practice. 1.4.2

Deichmann, N. & Garcia-Fernandez, M., 1992. Rupture geometry from high-precision relative hypocentre locations of microearthquake clusters, *Geophys. J. Int.*, **110**(3), 501–517. 1.3.4

Deichmann, N. & Giardini, D., 2009. Earthquakes induced by the stimulation of an enhanced geothermal system below Basel (Switzerland), *Seismol. Res. Lett.*, **80**(5), 784–798. 1.3.4

Douglas, A., 1967. Joint epicentre determination, *Nature*, **215**(5096), 47. 1.3.2, 1.3.2

Drew, J., White, R. S., Tilmann, F., & Tarasewicz, J., 2013. Coalescence microseismic mapping, *Geophys. J. Int.*, **195**(3), 1773–1785. 1.3.5

Etgen, J. T., 1987. Finite-difference elastic anisotropic wave propagation, *Stanford Exploration Project Report*, **56**, 23–58. 1.2

Fan, W. & McGuire, J. J., 2018. Investigating microearthquake finite source attributes with IRIS Community Wavefield Demonstration Experiment in Oklahoma, *Geophys. J. Int.*, **214**(2), 1072–1087. 1.1

Fink, M., Cassereau, D., Derode, A., Prada, C., Roux, P., Tanter, M., Thomas, J.-L., & Wu, F., 2000. Time-reversed acoustics, *Rep. Prog. Phys.*, **63**(12), 1933. 1.3.6

Gajewski, D. & Tessmer, E., 2005. Reverse modelling for seismic event characterization, *Geophys. J. Int.*, **163**(1), 276–284. 1.3.6

Gajewski, D., Anikiev, D., Kashtan, B., Tessmer, E., & Vanelle, C., 2007. Localization of seismic events by diffraction stacking, in *SEG Technical Program Expanded Abstracts 2007*, pp. 1287–1291, Society of Exploration Geophysicists. 1.3.5

Ge, M., 2005. Efficient mine microseismic monitoring, *Int. J. Coal Geol.*, **64**(1-2), 44–56. 1.1

Geiger, L., 1912. Probability method for the determination of earthquake epicenters from the arrival time only, *Bull.St.Louis.Univ*, **8**, 60–71. 1.3.2

Gharti, H. N., Oye, V., Roth, M., & Kühn, D., 2010. Automated microearthquake location using envelope stacking and robust global optimization, *Geophysics*, **75**(4), MA27–MA46. 1.3.5, 1.3.5, 1.3.5

Grigoli, F., Cesca, S., Amoroso, O., Emolo, A., Zollo, A., & Dahm, T., 2013a. Automated seismic event location by waveform coherence analysis, *Geophys. J. Int.*, **196**(3), 1742–1753. 1.3.5, 1.3.5

Grigoli, F., Cesca, S., Vassallo, M., & Dahm, T., 2013b. Automated seismic event location by travel-time stacking: An application to mining induced seismicity, *Seismol. Res. Lett.*, **84**(4), 666–677. 1.3.5

Grigoli, F., Cesca, S., Krieger, L., Kriegerowski, M., Gammaldi, S., Horalek, J., Priolo, E., & Dahm, T., 2016. Automated microseismic event location using master-event waveform stacking, *Sci. Rep.*, **6**, 25744. 1.3.5, 1.9

Gupta, H. K., 1985. The present status of reservoir induced seismicity investigations with special emphasis on Koyna earthquakes, *Tectonophysics*, **118**(3-4), 257–279. 1.1

Häring, M. O., Schanz, U., Ladner, F., & Dyer, B. C., 2008. Characterisation of the Basel 1 enhanced geothermal system, *Geothermics*, **37**(5), 469–495. 1.4.2

Holberg, O., 1987. Computational aspects of the choice of operator and sampling interval for numerical differentiation in large-scale simulation of wave phenomena, *Geophys. Prospect.*, **35**(6), 629–655. 1.2

Horstmann, T., Harrington, R. M., & Cochran, E. S., 2015. Using a modified time-reverse imaging technique to locate low-frequency earthquakes on the San Andreas Fault near Cholame, California, *Geophys. J. Int.*, **203**(2), 1207–1226. 1.3.6

House, L., 1987. Locating microearthquakes induced by hydraulic fracturing in crystalline rock, *Geophys. Res. Lett.*, **14**(9), 919–921. 1.1

Husen, S., Kissling, E., Deichmann, N., Wiemer, S., Giardini, D., & Baer, M., 2003. Probabilistic earthquake location in complex three-dimensional velocity models: Application to Switzerland, *J. Geophys. Res. Solid Earth*, **108**(B2). 1.4

Inbal, A., Ampuero, J. P., & Clayton, R. W., 2016. Localized seismic deformation in the upper mantle revealed by dense seismic arrays, *Science*, **354**(6308), 88–92. 1.1

Jay, J. A., Pritchard, M. E., West, M. E., Christensen, D., Haney, M., Minaya, E., Sunagua, M., McNutt, S. R., & Zabala, M., 2012. Shallow seismicity, triggered seismicity, and ambient noise tomography at the long-dormant Uturuncu Volcano, Bolivia, *Bull. Volcanol.*, **74**(4), 817–837. 1.1

Jiang, F.-X., Yang, S.-H., Cheng, Y.-H., Zhang, X.-M., Mao, Z., & Xu, F., 2006. A study on microseismic monitoring of rock burst in coal mine, *Chinese J. Geophys.*, **49**(5), 1511–1516. 1.1, 1.4.2

Johnston, J. E. & Christensen, N. I., 1995. Seismic anisotropy of shales, *J. Geophys. Res. Solid Earth*, **100**(B4), 5991–6003. 1.2

Kaderli, J., McChesney, M. D., & Minkoff, S. E., 2015. Microseismic event estimation in noisy data via full waveform inversion, in *SEG Technical Program Expanded Abstracts 2015*, pp. 1159–1164, Society of Exploration Geophysicists. 1.3.7, 1.3.7, 1.11, 1.12

Kao, H. & Shan, S.-J., 2004. The source-scanning algorithm: Mapping the distribution of seismic sources in time and space, *Geophys. J. Int.*, **157**(2), 589–594. 1.1, 1.3.5, 1.3.5

Kao, H. & Shan, S.-J., 2007. Rapid identification of earthquake rupture plane using source-scanning algorithm, *Geophys. J. Int.*, **168**(3), 1011–1020. 1.3.5

Kawakatsu, H. & Montagner, J.-P., 2008. Time-reversal seismic-source imaging and moment-tensor inversion, *Geophys. J. Int.*, **175**(2), 686–688. 1.3.6

Kennett, B. L. & Sambridge, M. S., 1992. Earthquake location genetic algorithms for teleseisms, *Phys. Earth Planet. In.*, **75**(1-3), 103–110. 1.3.3

Kim, K.-H., Chiu, J.-M., Pujol, J., & Chen, K.-C., 2005. Earthquake relocations, fault zone geometry and constraints on lateral velocity variations using the joint hypocenter determination method in the Taiwan area, *Earth Planets Space*, **57**(9), 809–823. 1.3

Kindelan, M., Kamel, A., & Sguazzero, P., 1990. On the construction and efficiency of staggered numerical differentiators for the wave equation, *Geophysics*, **55**(1), 107–110. 1.2

Kocur, G. K., Saenger, E. H., Grosse, C. U., & Vogel, T., 2016. Time reverse modeling of acoustic emissions in a reinforced concrete beam, *Ultrasonics*, **65**, 96–104. 1.3.6

Kosloff, R. & Kosloff, D., 1986. Absorbing boundaries for wave propagation problems, *J. Comput. Phys.*, **63**(2), 363–376. 1.2

Lahr, J. C., 1999. *HYPOELLIPSE: A computer program for determining local earthquake hypocentral parameters, magnitude, and first motion pattern*, Citeseer. 1.3.5

Langet, N., Maggi, A., Michelini, A., & Brenguier, F., 2014. Continuous Kurtosis-Based Migration for Seismic Event Detection and Location, with Application to Piton de la Fournaise Volcano, La Réunion, *Bull. Seismol. Soc. Am.*, **104**(1), 229–246. 1.3.5, 1.3.5

Larmat, C., Montagner, J.-P., Fink, M., Capdeville, Y., Tourin, A., & Clévédé, E., 2006. Time-reversal imaging of seismic sources and application to the great Sumatra earthquake, *Geophys. Res. Lett.*, **33**(19). 1.3.6

Li, Z. & van der Baan, M., 2016. Microseismic event localization by acoustic time reversal extrapolation, *Geophysics*, **81**(3), KS123–KS134. 1.3.6

Liu, Y. & Sen, M. K., 2009. An implicit staggered-grid finite-difference method for seismic modelling, *Geophys. J. Int.*, **179**(1), 459–474. 1.2

Lomax, A., Virieux, J., Volant, P., & Berge-Thierry, C., 2000. Probabilistic earthquake location in 3D and layered models, in *Advances in seismic event location*, pp. 101–134, Springer. 1.3.3, 1.3.3, 1.3.5

Majer, E. L., Baria, R., Stark, M., Oates, S., Bommer, J., Smith, B., & Asanuma, H., 2007. Induced seismicity associated with enhanced geothermal systems, *Geothermics*, **36**(3), 185–222. 1.1, 1.4.1

Mavko, G., Mukerji, T., & Dvorkin, J., 2009. *The rock physics handbook: Tools for seismic analysis of porous media*, Cambridge university press. 1.2, 1.2

Maxwell, S., 2011. Microseismic hydraulic fracture imaging: The path toward optimizing shale gas production, *The Leading Edge*, **30**(3), 340–346. 1.1

Maxwell, S., 2014. *Microseismic imaging of hydraulic fracturing: Improved engineering of unconventional shale reservoirs*, Society of Exploration Geophysicists. 1.4.1

Maxwell, S. & Urbancic, T., 2005. The potential role of passive seismic monitoring for real-time 4D reservoir characterization, *SPE Reservoir Evaluation & Engineering*, **8**(01), 70–76. 1.4.1

Maxwell, S. C., Rutledge, J., Jones, R., & Fehler, M., 2010. Petroleum reservoir characterization using downhole microseismic monitoring, *Geophysics*, **75**(5), 75A129–75A137. 1.4, 1.4.1

McMechan, G. A., 1982. Determination of source parameters by wavefield extrapolation, *Geophys. J. Roy. Astron. Soc.*, **71**(3), 613–628. 1.3.6

McMechan, G. A., 1983. Migration by extrapolation of time-dependent boundary values, *Geophys. Prospect.*, **31**(3), 413–420. 1.10

McMechan, G. A., Luetgert, J., & Mooney, W., 1985. Imaging of earthquake sources in Long Valley Caldera, California, 1983, *Bull. Seismol. Soc. Am.*, **75**(4), 1005–1020. 1.3.6

McNutt, S. R., 2005. Volcanic seismology, *Annu. Rev. Earth Planet. Sci.*, **32**, 461–491. 1.4.2

Menke, W. & Schaff, D., 2004. Absolute earthquake locations with differential data, *Bull. Seismol. Soc. Am.*, **94**(6), 2254–2264. 1.3.4

Michel, O. J. & Tsvankin, I., 2014a. Gradient calculation for waveform inversion of microseismic data in VTI media, *J. Seism. Explor.*, **23**(3), 201–217. 1.3.7

Michel, O. J. & Tsvankin, I., 2014b. Waveform inversion for parameters of microseismic sources in VTI media, in *SEG Technical Program Expanded Abstracts 2014* , pp. 1045–1049, Society of Exploration Geophysicists. 1.3.7

Milne, J., 1886. *Earthquakes and other earth movements*, vol. 56, K. Paul, Trench. 1.3.1

Moser, T., Eck, T., & Nolet, G., 1992. Hypocenter determination in strongly heterogeneous Earth models using the shortest path method, *J. Geophys. Res. Solid Earth*, **97**(B5), 6563–6572. 1.3.3

Nakata, N. & Beroza, G. C., 2016. Reverse time migration for microseismic sources using the geometric mean as an imaging condition, *Geophysics*, **81**(2), KS51–KS60. 1.3.6, 1.3.6

Podvin, P. & Lecomte, I., 1991. Finite difference computation of traveltimes in very contrasted velocity models: a massively parallel approach and its associated tools, *Geophys. J. Int.*, **105**(1), 271–284. 1.3.2, 1.3.5

Pujol, J., 1992. Joint hypocentral location in media with lateral velocity variations and interpretation of the station corrections, *Phys. Earth Planet. In.*, **75**(1-3), 7–24. 1.3.2

Pujol, J., 2000. Joint event location the JHD technique and applications to data from local seismic networks, in *Advances in seismic event location*, pp. 163–204, Springer. 1.3.2

Pujol, J., 2004. Earthquake location tutorial: graphical approach and approximate epicentral location techniques, *Seismol. Res. Lett.*, **75**(1), 63–74. 1.3.1, 1.3.1

Ramos-Martínez, J. & McMechan, G. A., 2001. Source-parameter estimation by full waveform inversion in 3D heterogeneous, viscoelastic, anisotropic media, *Bull. Seismol. Soc. Am.*, **91**(2), 276–291. 1.3.7

Rentsch, S., Buske, S., Lüth, S., & Shapiro, A., 2006. Fast location of seismicity: A migration-type approach with application to hydraulic-fracturing data, *Geophysics*, **72**(1), S33–S40. 1.3.2

Rich, J. & Ammerman, M., 2010. Unconventional geophysics for unconventional plays, in *SPE Unconventional Gas Conference*, Society of Petroleum Engineers. 1.4.1, 1.13

Richards-Dinger, K. & Shearer, P., 2000. Earthquake locations in southern California obtained using source-specific station terms, *J. Geophys. Res. Solid Earth*, **105**(B5), 10939–10960. 1.3.2

Rivera, L. & Cisternas, A., 1990. Stress tensor and fault plane solutions for a population of earthquakes, *Bull. Seismol. Soc. Am.*, **80**(3), 600–614. 1.1

Robertsson, J. O., 1996. A numerical free-surface condition for elastic/viscoelastic finite-difference modeling in the presence of topography, *Geophysics*, **61**(6), 1921–1934. 1.2

Rubin, A. M., 2002. Aftershocks of microearthquakes as probes of the mechanics of rupture, *J. Geophys. Res. Solid Earth*, **107**(B7). 1.1

Rubin, A. M., Gillard, D., & Got, J.-L., 1999. Streaks of microearthquakes along creeping faults, *Nature*, **400**(6745), 635. 1.1

Rüger, A., 2002. *Reflection coefficients and azimuthal AVO analysis in anisotropic media*, Society of Exploration Geophysicists. 1.2

Rutledge, J. T. & Phillips, W. S., 2003. Hydraulic stimulation of natural fractures as revealed by induced microearthquakes, Carthage Cotton Valley gas field, east Texas, *Geophysics*, **68**(2), 441–452. 1.5

Ružek, B. & Kvasnička, M., 2001. Differential evolution algorithm in the earthquake hypocenter location, *Pure Appl. Geophys.*, **158**(4), 667–693. 1.3.3

Sambridge, M. & Gallagher, K., 1993. Earthquake hypocenter location using genetic algorithms, *Bull. Seismol. Soc. Am.*, **83**(5), 1467–1491. 1.3.3

Sambridge, M. S. & Kennett, B. L., 2001. Seismic event location: nonlinear inversion using a neighbourhood algorithm, *Pure Appl. Geophys.*, **158**(1-2), 241–257. 1.3.3

Savage, M., 1999. Seismic anisotropy and mantle deformation: what have we learned from shear wave splitting?, *Rev. Geophys.*, **37**(1), 65–106. 1.2

Schoenberg, M. & Sayers, C. M., 1995. Seismic anisotropy of fractured rock, *Geophysics*, **60**(1), 204–211. 1.2

Schöffel, H.-J. & Das, S., 1999. Fine details of the Wadati-Benioff zone under Indonesia and its geodynamic implications, *J. Geophys. Res. Solid Earth*, **104**(B6), 13101–13114. 1.3.2

Schweitzer, J., 2001. HYPOSAT–An enhanced routine to locate seismic events, *Pure Appl. Geophys.*, **158**(1-2), 277–289. 1.3.2

Shapiro, S. & Dinske, C., 2009. Fluid-induced seismicity: Pressure diffusion and hydraulic fracturing, *Geophys. Prospect.*, **57**(2), 301–310. 1.1

Shi, P., Angus, D., Nowacki, A., Yuan, S., & Wang, Y., 2018. Microseismic Full Waveform Modeling in Anisotropic Media with Moment Tensor Implementation, *Surv. Geophys.*, **39**(4), 567–611. 1.5

Shi, P., Angus, D., Rost, S., Nowacki, A., & Yuan, S., 2019a. Automated seismic waveform location using Multichannel Coherency Migration (MCM)–I. Theory, *Geophys. J. Int.*, **216**(3), 1842–1866. 1.5

Shi, P., Nowacki, A., Rost, S., & Angus, D., 2019b. Automated seismic waveform location using Multichannel Coherency Migration (MCM)–II. Application to induced and volcano-tectonic seismicity, *Geophys. J. Int.*, **216**(3), 1608–1632. 1.5

Šílenỳ, J., Hill, D. P., Eisner, L., & Cornet, F. H., 2009. Non-double-couple mechanisms of microearthquakes induced by hydraulic fracturing, *J. Geophys. Res. Solid Earth*, **114**(B8). 1.2, 1.3.5

Steiner, B., Saenger, E. H., & Schmalholz, S. M., 2008. Time reverse modeling of low-frequency microtremors: Application to hydrocarbon reservoir localization, *Geophys. Res. Lett.*, **35**(3). 1.3.6

Stone, J. V., 2013. *Bayes' rule: A tutorial introduction to Bayesian analysis*, Sebtel Press. 1.3.3

Tang, C., Li, L., Xu, N., & Ma, K., 2015. Microseismic monitoring and numerical simulation on the stability of high-steep rock slopes in hydropower engineering, *J. Rock Mech. Geotech. Eng.*, **7**(5), 493–508. 1.14

Tarantola, A., 1984. Inversion of seismic reflection data in the acoustic approximation, *Geophysics*, **49**(8), 1259–1266. 1.3.7

Tarantola, A. & Valette, B., 1982. Inverse problems= quest for information, *J. Geophys.*, **50**(3), 150–170. 1.3.3, 1.3.5

Thomsen, L., 1986. Weak elastic anisotropy, *Geophysics*, **51**(10), 1954–1966. 1.2

Tsvankin, I., 2012. *Seismic signatures and analysis of reflection data in anisotropic media*, Society of Exploration Geophysicists. 1.2

Valcke, S., Casey, M., Lloyd, G., Kendall, J.-M., & Fisher, Q., 2006. Lattice preferred orientation and seismic anisotropy in sedimentary rocks, *Geophys. J. Int.*, **166**(2), 652–666. 1.2

Van Der Baan, M., Eaton, D., & Dusseault, M., 2013. Microseismic monitoring developments in hydraulic fracture stimulation, in *ISRM International Conference for Effective and Sustainable Hydraulic Fracturing*, International Society for Rock Mechanics and Rock Engineering. 1.4.1

Vidale, J., 1988. Finite-difference calculation of travel times, *Bull. Seismol. Soc. Am.*, **78**(6), 2062–2076. 1.3.2

Vidic, R. D., Brantley, S. L., Vandenbossche, J. M., Yoxtheimer, D., & Abad, J. D., 2013. Impact of shale gas development on regional water quality, *Science*, **340**(6134), 1235009. 1.4.1

Virieux, J., 1986. P-SV wave propagation in heterogeneous media: Velocity-stress finite-difference method, *Geophysics*, **51**(4), 889–901. 1.2, 1.2

Virieux, J. & Operto, S., 2009. An overview of full-waveform inversion in exploration geophysics, *Geophysics*, **74**(6), WCC1–WCC26. 1.3.7

Waldhauser, F. & Ellsworth, W. L., 2000. A double-difference earthquake location algorithm: Method and application to the northern Hayward fault, California, *Bull. Seismol. Soc. Am.*, **90**(6), 1353–1368. 1.3.4, 1.3.4

Wang, H. & Alkhalifah, T., 2018. Microseismic imaging using a source function independent full waveform inversion method, *Geophys. J. Int.*, **214**(1), 46–57. 1.3.7

Wang, Z., Ding, H., Lu, G., & Bi, X., 2016. Reverse-time migration based optical imaging, *IEEE Trans. Med. Imag.*, **35**(1), 273–281. 1.3.6

Wittlinger, G., Herquel, G., & Nakache, T., 1993. Earthquake location in strongly heterogeneous media, *Geophys. J. Int.*, **115**(3), 759–777. 1.3.3

Wu, Y. & McMechan, G. A., 1996. Elastic full-waveform inversion for earthquake source parameters, *Geophys. J. Int.*, **127**(1), 61–74. 1.3.7

Xu, N., Tang, C., Li, L., Zhou, Z., Sha, C., Liang, Z., & Yang, J., 2011. Microseismic monitoring and stability analysis of the left bank slope in Jinping first stage hydropower station in southwestern China, *Int. J. Rock Mech. Min. Sci.*, **48**(6), 950–963. 1.1, 1.4, 1.4.2

Xu, N., Dai, F., Zhou, Z., Jiang, P., & Zhao, T., 2016. Microseismicity and its time–frequency characteristics of the left bank slope at the Jinping first-stage hydropower station during reservoir impoundment, *Environ. Earth Sci.*, **75**(7), 608. 1.1

Young, R., Maxwell, S. C., Urbancic, T., & Feignier, B., 1992. Mining-induced microseismicity: monitoring and applications of imaging and source mechanism techniques, *Pure Appl. Geophys.*, **139**(3-4), 697–719. 1.1

Zhang, X., Zhang, W., & Zhang, J., 2014. Elastic full waveform inversion of microseismic data for location and source mechanism, in *SEG Technical Program Expanded Abstracts 2014*, pp. 2256–2260, Society of Exploration Geophysicists. 1.3.7

Zhang, X., Zhang, J., & Zoback, M. D., 2015. Fast elastic full waveform inversion for microseismic location and focal mechanism, in *SEG Technical Program Expanded Abstracts 2015*, pp. 2517–2521, Society of Exploration Geophysicists. 1.3.7, 1.3.7

Zhebel, O. & Eisner, L., 2014. Simultaneous microseismic event localization and source mechanism determination, *Geophysics*, **80**(1), KS1–KS9. 1.3.5

Zhu, T., 2014. Time-reverse modelling of acoustic wave propagation in attenuating media, *Geophys. J. Int.*, **197**(1), 483–494. 1.3.6

Zobin, V. M., 2012. *Introduction to volcanic seismology*, vol. 6, Elsevier. 1.4.2

Zou, Z., Zhou, H.-w., & Gurrola, H., 2014. Reverse-time imaging of a doublet of microearthquakes in the Three Gorges Reservoir region, *Geophys. J. Int.*, **196**(3), 1858–1868. 1.3.6

Zou, Z., Zhou, H.-W., Bian, A., Zhang, J., & Xing, L., 2015. An evaluation of reverse-time imaging of clustering earthquakes, *J. Earth Sci.*, **26**(4), 548–555. 1.3.6

Chapter 2

Microseismic Full Waveform Modeling in Anisotropic Media with Moment Tensor Implementation

P. Shi[1], D. Angus[2], A. Nowacki[1], S. Yuan[3], and Y. Wang[4]

[1] *School of Earth and Environment, University of Leeds, Leeds, United Kingdom*
[2] *ESG Solutions, Kingston, Canada*
[3] *College of Geophysics, China University of Petroleum, Beijing, China*
[4] *Department of Earth Sciences, ETH Zurich, Zurich, Switzerland*

Abstract

Seismic anisotropy which is common in shale and fractured rocks will cause travel-time and amplitude discrepancy in different propagation directions. For microseismic monitoring which is often implemented in shale or fractured rocks, seismic anisotropy needs to be carefully accounted for in source location and mechanism determination. We have developed an efficient finite-difference full waveform modeling tool with an arbitrary moment tensor source. The modeling tool is suitable for simulating wave propagation in anisotropic media for microseismic monitoring. As both dislocation and non-double-couple source are often observed in microseismic monitoring, an arbitrary moment tensor source is implemented in our forward modeling tool. The increments of shear stress are equally distributed on the staggered grid to implement an accurate and symmetric moment tensor source. Our modeling tool provides an efficient way to obtain the Green's function in anisotropic media, which is the key of anisotropic moment tensor inversion and source mechanism characterization in microseismic monitoring. In our

research, wavefields in anisotropic media have been carefully simulated and analyzed in both surface array and downhole array. The variation characteristics of travel-time and amplitude of direct P- and S-wave in vertical transverse isotropic media and horizontal transverse isotropic media are distinct, thus providing a feasible way to distinguish and identify the anisotropic type of the subsurface. Analyzing the travel-times and amplitudes of the microseismic data is a feasible way to estimate the orientation and density of the induced cracks in hydraulic fracturing. Our anisotropic modeling tool can be used to generate and analyze microseismic full wavefield with full moment tensor source in anisotropic media, which can help promote the anisotropic interpretation and inversion of field data.

2.1 Introduction

Full waveform modeling (FWM) can help us understand elastic wave propagation in complex media and is widely used in reverse time migration, full waveform inversion and seismic source imaging (Baysal et al., 1983, Boyd, 2006, Virieux & Operto, 2009, Xuan & Sava, 2010, Yuan et al., 2014). There are two ways to calculate the full waveform solution in an elastic medium: analytical solutions and numerical simulation. Analytical solutions, such as Green's function in an infinite half-space medium (Aki & Richards, 2002), are mostly used in simple models such as homogeneous or layered media. Numerical solutions, such as finite-difference method (Kelly et al., 1976), finite-element method (Zienkiewicz et al., 1977) and spectral element method (Tromp et al., 2008), are more suitable for modeling wave phenomena in complex media, but are computationally more expensive. Among the FWM methods, the finite-difference (FD) approach is widely used because of its flexibility in modeling wave propagation in complex media and excellent computational efficiency (Alterman & Karal, 1968, Zienkiewicz et al., 1977, Saenger et al., 2000, Moczo et al., 2002, 2014, Robertsson et al., 2015). With the increase in modeling scale and complexity, a variety of ways have been proposed to improve the computational efficiency and modeling accuracy of the FD approach (Bohlen, 2002, Michéa & Komatitsch, 2010, Zhang & Yao, 2013, Yao et al., 2016).

In microseismic monitoring, FWM has been used as a reverse time modeling tool to locate the microseismic source using full waveform data (Gajewski & Tessmer, 2005, Steiner et al., 2008, Artman et al., 2010, O'Brien et al., 2011, Saenger et al., 2011, Nakata & Beroza, 2016). This method does not depend on arrival time picking and therefore can be used on data with low signal-to-noise ratio. FWM is also used as a tool to generate and analyze the often complex full wavefield of microseismic data (Brzak et al., 2009, Jin et al., 2013, Li et al., 2015), and to help improve the quality of microseismic imaging. The Green's function of the subsurface can be obtained through FWM, which is critical for the characterization of source mechanisms (Vavryčuk, 2007, Kawakatsu & Montagner, 2008, Song & Toksöz, 2011, Li et al., 2011, Chambers et al.,

2014, Linzer et al., 2015). However, high-frequency contents and accuracy requirement in microseismic monitoring have placed stringent demands on FWM (Hobro et al., 2016). Compared with seismic data in conventional reflection seismology and global seismology, microseismic data have relatively high dominant frequency, which can have a significant influence on the characteristics of the wavefield and waveforms (Usher et al., 2013, Angus et al., 2014). For downhole arrays which are deployed near microseismic events, the dominant frequency of microseismic signals can be a few hundred Hertz. In order to obtain a reliable source mechanism characterization and comprehensive description of full wavefield, FWM with high-precision both in the space and time domain is required for microseismic monitoring.

The moment tensor has been widely used to describe the source mechanisms of earthquakes (Aki & Richards, 2002, Jost & Herrmann, 1989). In natural and induced earthquakes (e.g., microseismicity), both double-couple and non-double-couple sources are observed. Earthquakes in volcanic, landslide and geothermal areas often have strong non-double-couple mechanisms (Miller et al., 1998, Julian et al., 1998). For induced earthquakes such as microseismicity due to hydraulic fracturing and mining, predominant non-double-couple source mechanisms are often observed (Foulger et al., 2004, Šílenỳ & Milev, 2008, Šílenỳ et al., 2009). The induced non-double-couple events may result from opening cracks by high-pressure fluid injection (Šílenỳ et al., 2009). Full moment tensor inversion is an efficient way to characterize the source mechanisms of microseismic events. Cesca et al. (2013) used the full moment tensor inversion and decomposition to discriminate natural and induced seismicity. Modeling different types of sources and obtaining highly accurate Green's function is the key to perform full moment tensor inversion. Thus, arbitrary moment tensor source representation in FWM is needed to fully describe the source mechanism of microseismic events.

Strong seismic anisotropy is often observed in shale and reservoirs which contain lots of natural and/or induced fractures (Johnston & Christensen, 1995, Schoenberg & Sayers, 1995, Vernik & Liu, 1997, Wang, 2002, Wang et al., 2007, Yan et al., 2016). Seismic anisotropy can have a significant influence on the recorded wavefields (both in travel-time and amplitude) and therefore increases the difficulty of microseismic data interpretation and inversion (Warpinski et al., 2009). Both source location and mechanism inversion will be biased if seismic anisotropy is not incorporated or properly processed. The location error induced by seismic anisotropy is also related to the recording geometries of microseismic monitoring (Warpinski et al., 2009). Rössler et al. (2004) and Vavryčuk (2005) demonstrated that moment tensors for pure-shear sources will generally exhibit significant non-double-couple components in anisotropic media. Their studies show anisotropy can have a significant influence on the interpretation of the source mechanisms. Stierle et al. (2016) demonstrated that the retrieval of moment tensor and source mechanism critically depend on anisotropy using laboratory acoustic emission experiments. Their study also shows that the tensile events are more

sensitive to P-wave anisotropy than shear events. For source mechanism characterization, the P- and T-axes of the moment tensors are affected by velocity anisotropy and deviated form the true orientation of faulting (Stierle et al., 2016). Understanding and correcting for wave propagation phenomena in anisotropic media will help to reduce uncertainties in source location and mechanism inversion. Grechka & Yaskevich (2013a) demonstrated that the travel-times of microseismic events can provide sufficient information to constrain both locations of microseismic events and the underlying anisotropic velocity model. They use the shear-wave splitting to improve the precision of event locations and locate events whose P-wave time picks are unavailable. A correct analysis of the source mechanism is also achievable through anisotropic moment tensor inversion (Rössler et al., 2004). Seismic anisotropy can be retrieved from the recorded microseismic data (Al-Harrasi et al., 2011, Zhang et al., 2013). For a reliable estimation of seismic anisotropy, a wide aperture of recording array is normally required (Grechka & Yaskevich, 2013b). Furthermore, seismic anisotropy attributes can also provide more information about the fractured media and for seismic source inversion. Hydraulic fracturing can cause time-lapse changes in the anisotropy parameters. Grechka et al. (2011) found the time-lapse changes in the anisotropy parameters rather than velocity heterogeneity need to be introduced to explain the microseismic data recorded at different fracturing stage. The time-lapse changes in the anisotropy parameters can be used to characterize the stimulated reservoir volume or crustal stress variation in cracked rock (Teanby et al., 2004). The crack properties such as orientation and density can be studied using seismic anisotropy (Verdon et al., 2009, Wuestefeld et al., 2010). Therefore, anisotropic FWM is required in order to investigate the induced fracture properties and conduct accurate microseismic source inversion in anisotropic media.

In exploration seismology, FWM with an explosive source is widely used because seismic waves are often excited by explosives (Sheriff & Geldart, 1995). In addition, anisotropic effect is often ignored in order to accelerate the computation of FWM. As seismic anisotropy and moment tensor source are important for microseismic monitoring, we developed an efficient FWM tool based on FD method, which is suitable for anisotropic media and arbitrary moment tensors. First, we describe the elastodynamic equations in anisotropic media and the special way to implement an accurate and symmetrical moment tensor source in the staggered grid. Then, we compared the modeling results of a general non-double-couple moment tensor source with analytical solutions in homogeneous medium to confirm the correctness of this method. Because the far-field approximations are often used in microseismic monitoring, the magnitude of near-field components and far-field components is also compared and discussed in detail in the paper. In the modeling examples part, the wave propagation phenomena are simulated and discussed in both anisotropic layered model and 3-dimensional (3D) anisotropic overthrust model. And the influence of seismic anisotropy on microseismic data are simulated and analyzed in detail both for surface and downhole arrays. We examine

the feasibility of utilizing recorded microseismic data to estimate seismic anisotropy of the subsurface.

2.2 Theory

In this section, we present the elastodynamic equations in velocity-stress formation, moment-tensor source representation for the wavefield excitation and the numerical implementation of the elastodynamic equations.

2.2.1 Elastic Wave Equation in Inhomogeneous and Anisotropic Media

In 3D Cartesian coordinate system, the equations of momentum conservation are given by

$$\begin{aligned}
\rho\frac{\partial v_x}{\partial t} &= \frac{\partial \tau_{xx}}{\partial x} + \frac{\partial \tau_{xy}}{\partial y} + \frac{\partial \tau_{xz}}{\partial z},\\
\rho\frac{\partial v_y}{\partial t} &= \frac{\partial \tau_{xy}}{\partial x} + \frac{\partial \tau_{yy}}{\partial y} + \frac{\partial \tau_{yz}}{\partial z},\\
\rho\frac{\partial v_z}{\partial t} &= \frac{\partial \tau_{xz}}{\partial x} + \frac{\partial \tau_{yz}}{\partial y} + \frac{\partial \tau_{zz}}{\partial z}.
\end{aligned} \tag{2.1}$$

After some transformation, the stress-strain relations can be expressed as

$$\begin{aligned}
\frac{\partial \tau_{xx}}{\partial t} &= c_{11}\frac{\partial v_x}{\partial x} + c_{12}\frac{\partial v_y}{\partial y} + c_{13}\frac{\partial v_z}{\partial z} + c_{14}\left(\frac{\partial v_y}{\partial z} + \frac{\partial v_z}{\partial y}\right)\\
&\quad + c_{15}\left(\frac{\partial v_x}{\partial z} + \frac{\partial v_z}{\partial x}\right) + c_{16}\left(\frac{\partial v_x}{\partial y} + \frac{\partial v_y}{\partial x}\right),\\
\frac{\partial \tau_{yy}}{\partial t} &= c_{21}\frac{\partial v_x}{\partial x} + c_{22}\frac{\partial v_y}{\partial y} + c_{23}\frac{\partial v_z}{\partial z} + c_{24}\left(\frac{\partial v_y}{\partial z} + \frac{\partial v_z}{\partial y}\right)\\
&\quad + c_{25}\left(\frac{\partial v_x}{\partial z} + \frac{\partial v_z}{\partial x}\right) + c_{26}\left(\frac{\partial v_x}{\partial y} + \frac{\partial v_y}{\partial x}\right),\\
\frac{\partial \tau_{zz}}{\partial t} &= c_{31}\frac{\partial v_x}{\partial x} + c_{32}\frac{\partial v_y}{\partial y} + c_{33}\frac{\partial v_z}{\partial z} + c_{34}\left(\frac{\partial v_y}{\partial z} + \frac{\partial v_z}{\partial y}\right)\\
&\quad + c_{35}\left(\frac{\partial v_x}{\partial z} + \frac{\partial v_z}{\partial x}\right) + c_{36}\left(\frac{\partial v_x}{\partial y} + \frac{\partial v_y}{\partial x}\right),\\
\frac{\partial \tau_{yz}}{\partial t} &= c_{41}\frac{\partial v_x}{\partial x} + c_{42}\frac{\partial v_y}{\partial y} + c_{43}\frac{\partial v_z}{\partial z} + c_{44}\left(\frac{\partial v_y}{\partial z} + \frac{\partial v_z}{\partial y}\right)\\
&\quad + c_{45}\left(\frac{\partial v_x}{\partial z} + \frac{\partial v_z}{\partial x}\right) + c_{46}\left(\frac{\partial v_x}{\partial y} + \frac{\partial v_y}{\partial x}\right),\\
\frac{\partial \tau_{xz}}{\partial t} &= c_{51}\frac{\partial v_x}{\partial x} + c_{52}\frac{\partial v_y}{\partial y} + c_{53}\frac{\partial v_z}{\partial z} + c_{54}\left(\frac{\partial v_y}{\partial z} + \frac{\partial v_z}{\partial y}\right)\\
&\quad + c_{55}\left(\frac{\partial v_x}{\partial z} + \frac{\partial v_z}{\partial x}\right) + c_{56}\left(\frac{\partial v_x}{\partial y} + \frac{\partial v_y}{\partial x}\right),
\end{aligned} \tag{2.2}$$

$$\frac{\partial \tau_{xy}}{\partial t} = c_{61}\frac{\partial v_x}{\partial x} + c_{62}\frac{\partial v_y}{\partial y} + c_{63}\frac{\partial v_z}{\partial z} + c_{64}\left(\frac{\partial v_y}{\partial z} + \frac{\partial v_z}{\partial y}\right) + c_{65}\left(\frac{\partial v_x}{\partial z} + \frac{\partial v_z}{\partial x}\right) + c_{66}\left(\frac{\partial v_x}{\partial y} + \frac{\partial v_y}{\partial x}\right).$$

In these equations, (v_x, v_y, v_z) represent the particle velocity components along x, y and z directions, respectively, and $(\tau_{xx}, \tau_{yy}, \tau_{zz}, \tau_{yz}, \tau_{xz}, \tau_{xy})$ are the components of the stress tensor. The medium is characterized by the elastic tensor c_{IJ} and density ρ. Here the fourth-order elastic tensor c_{ijkl} is expressed in Voigt notation (c_{IJ}). Because of symmetry, the elastic tensor has only 21 independent parameters in a generally anisotropic medium, which describe a minimally symmetrical, triclinic system (Sheriff & Geldart, 1995, Nowacki et al., 2011). However, the number of independent parameters can be further reduced if the symmetry system of the medium is higher than that of a generally anisotropic medium. For an isotropic medium which is commonly used in seismic modeling and has the highest symmetry system, there are only 2 independent elastic parameters. For vertical transverse isotropic (VTI) and horizontal transverse isotropic (HTI) medium, there are 5 independent elastic parameters (Thomsen, 1986, Rüger, 1997). For tilted transverse isotropic (TTI) medium, there are 7 independent elastic parameters (Montagner, 1998). For orthorhombic medium, there are 9 independent elastic parameters (Tsvankin, 1997). For monoclinic medium, there are 13 independent elastic parameters (Sayers, 1998). When modeling in a medium with a lower symmetry system, the memory cost will increase greatly. Table 2.1 shows the comparison of memory costs in different symmetry systems. In a specific medium whose symmetry system is higher than or equal to that of orthorhombic media (e.g., orthorhombic, HTI, VTI and isotropic media), the elastic tensor has the same null components. Thus, the stress-strain relations can be further simplified as

$$\begin{aligned}
\frac{\partial \tau_{xx}}{\partial t} &= c_{11}\frac{\partial v_x}{\partial x} + c_{12}\frac{\partial v_y}{\partial y} + c_{13}\frac{\partial v_z}{\partial z},\\
\frac{\partial \tau_{yy}}{\partial t} &= c_{21}\frac{\partial v_x}{\partial x} + c_{22}\frac{\partial v_y}{\partial y} + c_{23}\frac{\partial v_z}{\partial z},\\
\frac{\partial \tau_{zz}}{\partial t} &= c_{31}\frac{\partial v_x}{\partial x} + c_{32}\frac{\partial v_y}{\partial y} + c_{33}\frac{\partial v_z}{\partial z},\\
\frac{\partial \tau_{yz}}{\partial t} &= c_{44}\left(\frac{\partial v_y}{\partial z} + \frac{\partial v_z}{\partial y}\right),\\
\frac{\partial \tau_{xz}}{\partial t} &= c_{55}\left(\frac{\partial v_x}{\partial z} + \frac{\partial v_z}{\partial x}\right),\\
\frac{\partial \tau_{xy}}{\partial t} &= c_{66}\left(\frac{\partial v_x}{\partial y} + \frac{\partial v_y}{\partial x}\right).
\end{aligned} \tag{2.3}$$

Finally equations (2.1) together with equations (2.3) forms the basic elastodynamic equations which can be used to simulate elastic wave propagation in orthorhombic, HTI, VTI and isotropic media. For HTI and VTI media, the elastic parameters can be

Table 2.1: Memory cost for storing elastic parameters (including density of the medium) of different types of medium. M represents the model size

Medium type	Memory cost
Isotropic	3M
VTI/HTI	6M
TTI	8M
Orthorhombic	10M
Monoclinic	14M
Triclinic	22M

characterized by elastic parameters of the corresponding isotropic medium in combination with Thomsen anisotropic parameters (Thomsen, 1986). If the anisotropic zone of the model is simple such as layered or blocky zone, our FD modeling algorithm will first set up indexes which can represent the anisotropy of the model before modeling and then obtain the elastic parameters from isotropic elastic parameters and Thomsen anisotropic parameters in the process of simulation. In this way, we can reduce the memory cost of HTI and VTI media to the same level as for isotropic media.

2.2.2 Numerical Implementation

The standard staggered-grid FD method (Virieux, 1984, 1986, Dong & McMechan, 1995) is employed to solve the elastodynamic equations of velocity-stress formation. In the standard staggered-grid method, wavefield components are discretized and distributed on different numerical grids both in the time and space directions in order to solve the wavefield derivatives using central difference at the corresponding grid locations. The standard staggered-grid method is especially suitable and efficient for handling orthorhombic, HTI, VTI and isotropic medium. When modeling in these media using the standard staggered-grid method, no interpolation is necessary. Thus, it is computationally fast and of low memory cost compared to the rotated-staggered grid method (Saenger et al., 2000) or Lebedev scheme (Lisitsa & Vishnevskiy, 2010, Xu, 2012). Figure 2.1 shows the discrete standard staggered-grid used in the FD modeling. The wavefield components and medium elastic parameters are distributed on seven different staggered grids.

The spatial and temporal derivatives of the wavefield components in elastodynamic equations (2.1) and (2.3) are calculated through

$$\frac{\partial f}{\partial x} = \frac{1}{\Delta x} \sum_{n=1}^{L} c_n \left[f(x + n\Delta x - 0.5\Delta x) - f(x - n\Delta x + 0.5\Delta x) \right], \tag{2.4}$$

where c_n represents FD coefficients and $2L$ is the order of the FD scheme. For FD modeling, serious numerical artifacts will arise in the presence of high-frequency wave-

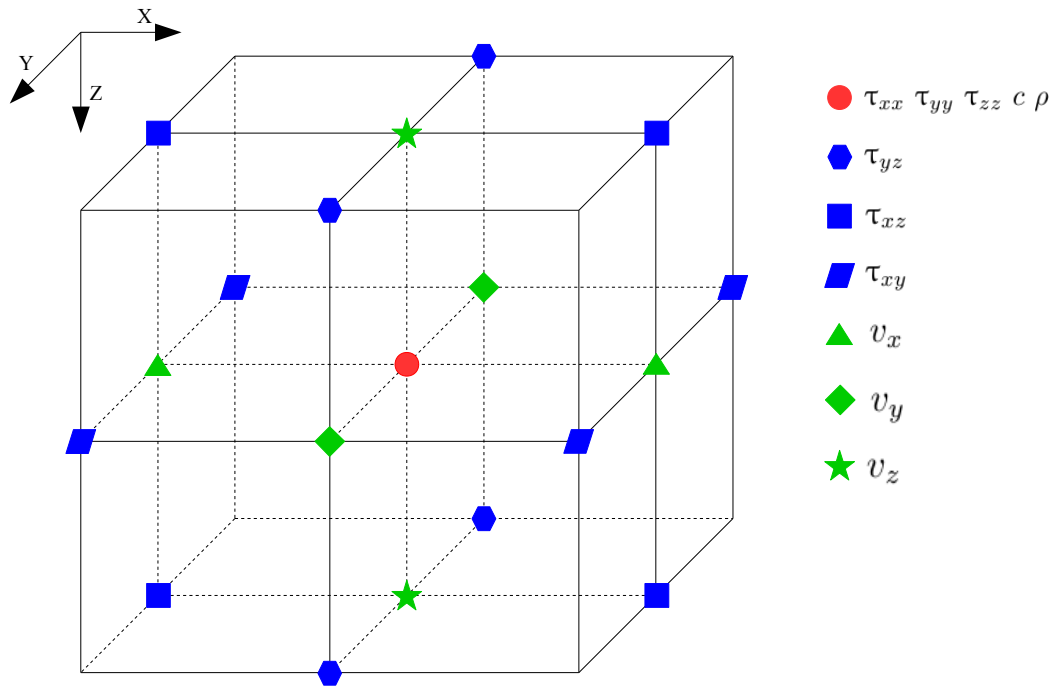

Figure 2.1: Schematic representation of standard staggered-grid. v_x, v_y, v_z represent the particle velocity components along x, y and z directions, respectively; $\tau_{xx}, \tau_{yy}, \tau_{zz}, \tau_{yz}, \tau_{xz}, \tau_{xy}$ represent six components of the stress tensor; c and ρ represent the elastic tensor and density of the media

field components or coarse grids (Zhang & Yao, 2013). Different from global or regional earthquake data, high-frequency components of the recorded signals are often observed in microseismic monitoring. For microseismic applications, amplitude fidelity and azimuthal variations of signals are critical to microseismic processing and interpretation. Thus, an accurate FD scheme is required for microseismic full waveform modeling. Through equation 2.4, an FD scheme of arbitrary order can be easily achieved. High-order FD schemes can ensure high modeling accuracy, but bring extra computational and memory cost. In practice, a balance between modeling accuracy and computational cost is needed. For FWM in anisotropic media, the wavefield complexity caused by seismic anisotropy is sometimes subtle. The relative wavefield difference compared to the isotropic scenario may be just a few percent. In addition, due to the influence of source radiation pattern, near-field effects also need to be considered. (Detailed discussion can be found in Appendix 2.4.) Therefore, a high-order FD scheme is necessary. A FD scheme of tenth-order in space domain and second-order in time domain is employed in our FWM, which provides sufficient accuracy requirement for anisotropic modeling with arbitrary moment tensor. There are many optimized schemes of FD methods which try to increase modeling accuracy and reduce numerical dispersion (Holberg, 1987, Lele, 1992, Liu & Sen, 2009). Optimized FD coefficients are adopted in this standard staggered-grid FD modeling scheme according to Holberg (1987).

Table 2.2: Simulation time (in second) of 10 time steps for different grid sizes and number of cores in anisotropic media.

Model size	1 core	2 cores	4 cores	8 cores	16 cores
100*100*100	1.7	0.9	0.5	0.3	0.2
200*200*200	15.9	7.9	4.0	2.1	1.2
400*400*400	140.1	70.5	35.5	18.3	10.1
600*600*600	617.5	310.0	150.5	75.3	39.6
800*800*800	1356.6	669.5	321.3	176.3	93.6

Before starting forward modeling, the spatial interval Δh (constant in three directions here) of the grid needs to be determined by fulfilling the grid dispersion criterion $\Delta h \leq v_{min}/(2nf_m)$, where v_{min} is the minimal S-wave velocity of the model, f_m is the peak frequency of the source time function and n is the number of grid-points per wavelength. If tenth-order and Holberg type of FD operators are used in the modeling, n is 3.19. For a stable numerical modeling, the temporal interval Δt must satisfy the Courant-Friedrichs-Lewy criterion $\Delta t \leq \Delta h/(\sqrt{3}mv_{max})$, where v_{max} is the maximum P-wave velocity of the model and m is a factor which depends on the order and type of the FD operator. If tenth-order and Holberg type of FD operators are used in the modeling, m is 1.38766.

2.2.3 Modeling efficiency and memory cost

The spatial interval of the grid (Δh) and temporal interval (Δt) are constrained by the dominant frequency (f_m) of the source time function. If high frequency is used in the modeling (which is often the case in microseismic modeling), the spatial and temporal intervals need to be reduced to make the modeling stable. Thus, the simulation time will increase greatly. Our FWM tool is parallelized based on a shared memory architecture using OpenMP. In order to examine the parallel performance, we conducted anisotropic full waveform simulations of 10 time steps on different grid sizes and number of computer cores. The simulation time is illustrated in Table 2.2. Based on Table 2.2, we can analyze the speedup ratio and parallel performance of our anisotropic FWM tool.

Figure 2.2(a) shows the speedup ratios of different model sizes. The dark dashed line exhibits the theoretical speedup ratio. We can see the model size of $600 \times 600 \times 600$ shows the best speedup ratio. Under the model size of $600 \times 600 \times 600$, the speedup ratio increases with the model size. In our parallel FD modeling algorithm, the computational workload is not equally allocated on all the available computational cores or threads at the beginning of parallel computing (static scheduling scheme). In order to distribute the workload more wisely and dispatch the calculation more efficiently, we adopt dynamic scheduling scheme of the workload. During parallel computing, each computational core/thread will be immediately assigned a new job after finishing the

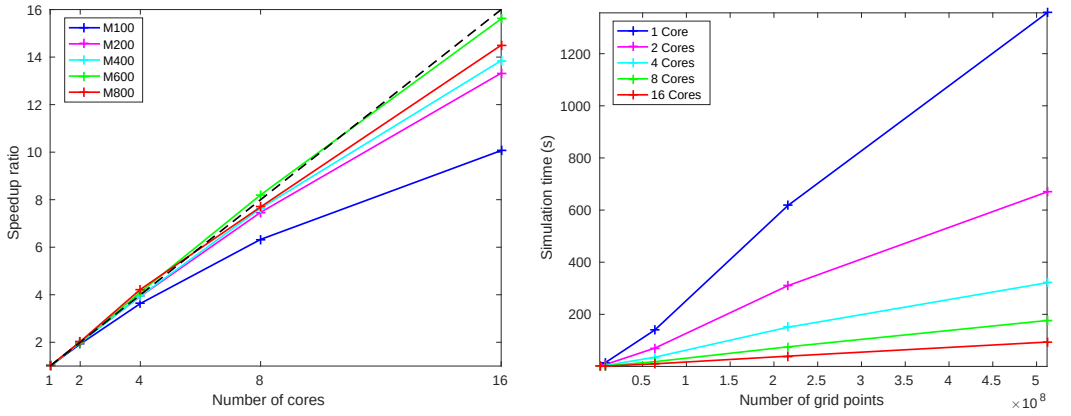

(a) (b)

Figure 2.2: (a) Variation of speedup ratios with the number of computer cores for different model sizes. Blue, magenta, cyan, green and red lines show the simulation times with model size of $100 \times 100 \times 100$, $200 \times 200 \times 200$, $400 \times 400 \times 400$, $600 \times 600 \times 600$ and $800 \times 800 \times 800$, respectively. (b) Variation of simulation times with the number of grid points for different number of compute cores. Blue, magenta, cyan, green and red lines show the simulation times with computer cores of 1, 2, 4, 8 and 16, respectively

former assigned job. After testing, we find the dynamic scheduling scheme can achieve much better computational efficiency than the static scheduling scheme. However, when the modeling size is very large, the overhead computational cost due to the handling and distributing of the workload dynamically may hinder the parallel computing efficiency. As presented in Figure 2.2(a), the speedup ratios vary with different model sizes, and are all satisfactory for large model sizes (except $100 \times 100 \times 100$). The subtle difference of speedup performance on large model size may be due to the dynamic allocation of the workload on computational cores. Figure 2.2(b) shows the variation of simulation times with different grid sizes. The simulation time increases linearly with the grid size, which demonstrates our FWM tool scales well.

For microseismic modeling, high dominant frequency components often need to be simulated. This will involve long simulation time and huge memory cost. If the dominant frequency of source time function is increased by n times ($f_m \rightarrow nf_m$), the spatial and temporal intervals will need to be reduced by n times. Thus, in 3 dimensions, the calculation will increase by n^4 times under ideal conditions. Table 2.3 compares the modeling parameters and requirements under different frequencies. Here we assume that the maximum P-wave velocity is 6000 m/s, the minimal S-wave velocity is 2000 m/s, the length of the simulation area is 3 km in each direction, and the simulation time is 4 second (which is a common parameter settings for microseismic modeling). The CPU times (hour/CPU) are estimated using the simulation time of 10 time steps for model size $100 \times 100 \times 100$ and 1 core (1.730469 s in Table 2.2). Here we assume that the computational complexity increases linearly with the grid size. Memory costs are estimated based on single precision. When parallel computing

Table 2.3: Modeling parameters and CPU times (hour/CPU) for different main frequencies of the source time function.

f (Hz)	Δh (m)	Δt (s)	Grid size	Time steps	Memory cost (Gb)	CPU time
10	31.35	0.00220	$96 \times 96 \times 96$	1841	0.046	0.08
20	15.67	0.00110	$192 \times 192 \times 192$	3681	0.369	1.25
40	7.84	0.00054	$383 \times 383 \times 383$	7361	2.930	19.88
80	3.92	0.00027	$766 \times 766 \times 766$	14721	23.441	318.04
100	3.13	0.00021	$957 \times 957 \times 957$	18402	45.711	775.29
120	2.61	0.00018	$1149 \times 1149 \times 1149$	22082	79.113	1610.10
150	2.09	0.00014	$1436 \times 1436 \times 1436$	27602	154.437	3928.80

is applied, the calculation burden and memory cost are still acceptable for dominant frequency up to 150 Hz.

2.2.4 Moment Tensor Source Implementation in Staggered-Grid

Two kinds of wavefield excitation conditions are commonly used in full waveform FD modeling. One is the use of body-force term which acts on momentum conservation equations (Aboudi, 1971, Kosloff et al., 1989, Yomogida & Etgen, 1993, Graves, 1996). The other one is to add an incremental stress on stress components (Virieux, 1986, Coutant et al., 1995, Pitarka, 1999, Narayan, 2001, Li et al., 2014). Compared with the direct use of body-force term, the implementation of incremental stress in FD scheme is more straightforward. In this paper, the incremental stress method is adopted in order to implement an arbitrary moment tensor source into the FWM scheme.

Seismic moment tensor can be expressed as

$$\mathbf{M} = M_0 \cdot \mathbf{m} \cdot S(t), \tag{2.5}$$

where M_0 is the seismic moment, $\mathbf{m}$ contains nine moment tensor components m_{ij} and $S(t)$ is the source time function. The scalar seismic moment could be expressed as $M_0 = \mu AD$, where μ is shear modulus of the rocks involved in the source area[1], A is the area of the rupture and D is the average displacement during rupture. The seismic moment M_0 has the same units of energy and is often used to estimate the moment magnitude scale of an earthquake. $\mathbf{m}$ is symmetric and normalized such that $\sum_{ij} m_{ij}^2 = 1$.

Normally the incremental normal and shear stresses are applied directly on the corresponding grid points. However, in the staggered-grid FD approach, the normal stresses and shear stresses are not evaluated at the same position. Thus, simply applying incremental stresses directly on the stress components of the corresponding grid

[1]The source area is assumed to be isotropic.

points as the conventional modeling methods do (Pitarka, 1999, Narayan, 2001, Li et al., 2014) will not result in an exact moment tensor source. When implementing the moment tensor source in our staggered-grid FWM, in order to obtain a symmetrical moment tensor solution, we interpolate incremental shear stress on four adjacent shear stress grid points. Assuming a moment tensor point source acting at the grid position of the normal stress components, the location of the normal stress components will act as a central point. In order to obtain a symmetric moment tensor source, we evenly distribute the shear stress increments on the four adjacent shear stress grid points around the true moment tensor source location. Thus in total, there are twelve adjacent grid points around the true location of the moment tensor point source, which are numerically implemented with shear stress components (as shown by the blue grid points in Figure 2.1). The complete formulation for a moment tensor point source acting at the staggered-grid node i,j,k (i.e., the grid position of the normal stress components) is given by

$$
\begin{aligned}
\tau_{xx}(i,j,k) &= \tau_{xx}(i,j,k) - \frac{\Delta t}{V}\frac{\partial M_{xx}(t)}{\partial t},\\
\tau_{yy}(i,j,k) &= \tau_{yy}(i,j,k) - \frac{\Delta t}{V}\frac{\partial M_{yy}(t)}{\partial t},\\
\tau_{zz}(i,j,k) &= \tau_{zz}(i,j,k) - \frac{\Delta t}{V}\frac{\partial M_{zz}(t)}{\partial t},\\
\tau_{yz}(i,j+1/2,k+1/2) &= \tau_{yz}(i,j+1/2,k+1/2) - \frac{\Delta t}{4V}\frac{\partial M_{yz}(t)}{\partial t},\\
\tau_{yz}(i,j+1/2,k-1/2) &= \tau_{yz}(i,j+1/2,k-1/2) - \frac{\Delta t}{4V}\frac{\partial M_{yz}(t)}{\partial t},\\
\tau_{yz}(i,j-1/2,k+1/2) &= \tau_{yz}(i,j-1/2,k+1/2) - \frac{\Delta t}{4V}\frac{\partial M_{yz}(t)}{\partial t},\\
\tau_{yz}(i,j-1/2,k-1/2) &= \tau_{yz}(i,j-1/2,k-1/2) - \frac{\Delta t}{4V}\frac{\partial M_{yz}(t)}{\partial t},\\
\tau_{xz}(i+1/2,j,k+1/2) &= \tau_{xz}(i+1/2,j,k+1/2) - \frac{\Delta t}{4V}\frac{\partial M_{xz}(t)}{\partial t},\\
\tau_{xz}(i+1/2,j,k-1/2) &= \tau_{xz}(i+1/2,j,k-1/2) - \frac{\Delta t}{4V}\frac{\partial M_{xz}(t)}{\partial t},\\
\tau_{xz}(i-1/2,j,k+1/2) &= \tau_{xz}(i-1/2,j,k+1/2) - \frac{\Delta t}{4V}\frac{\partial M_{xz}(t)}{\partial t},\\
\tau_{xz}(i-1/2,j,k-1/2) &= \tau_{xz}(i-1/2,j,k-1/2) - \frac{\Delta t}{4V}\frac{\partial M_{xz}(t)}{\partial t},\\
\tau_{xy}(i+1/2,j+1/2,k) &= \tau_{xy}(i+1/2,j+1/2,k) - \frac{\Delta t}{4V}\frac{\partial M_{xy}(t)}{\partial t},\\
\tau_{xy}(i+1/2,j-1/2,k) &= \tau_{xy}(i+1/2,j-1/2,k) - \frac{\Delta t}{4V}\frac{\partial M_{xy}(t)}{\partial t},\\
\tau_{xy}(i-1/2,j+1/2,k) &= \tau_{xy}(i-1/2,j+1/2,k) - \frac{\Delta t}{4V}\frac{\partial M_{xy}(t)}{\partial t},\\
\tau_{xy}(i-1/2,j-1/2,k) &= \tau_{xy}(i-1/2,j-1/2,k) - \frac{\Delta t}{4V}\frac{\partial M_{xy}(t)}{\partial t},
\end{aligned}
\tag{2.6}
$$

where $V = \Delta x \cdot \Delta y \cdot \Delta z$ is the effective volume of the grid cell, and Δt is the time spacing of FD modeling. In the velocity-stress FD scheme (equation 2.1 and 2.2), the temporal derivative of the moment tensor is used, because the temporal derivatives of the stress components are used in the elastodynamic equations. However, for moment tensor source implementation in the displacement-stress FD scheme, the moment tensor itself is used instead of its temporal derivative. And the time spacing item in these equations also disappears.

2.2.5 Validation with Analytical Solutions

For microseismic monitoring where high-frequency data are often recorded, it is naturally favorable to consider only the far-field approximation. However, there are scenarios where the effect of near-field terms and intermediate-field terms cannot be ignored (Vidale, 1995). Full waveform FD modeling can provide a step improvement in accurately modeling all kinds of wave phenomena both in the near-field and far-field. We compare the synthetic displacement field in the Y direction using our FWM method with the analytical solutions (based on equation 2.15 in Appendix 2.4). The elastic parameters of the medium used are $v_p = 3500\ m/s$, $v_s = 2000\ m/s$ and $\rho = 2400\ kg/m^3$. The source time function is a Ricker wavelet with a peak frequency of 40 Hz and a time delay of $1.1/f_m$. (This source time function is also used in the remaining examples.) For generality, a non-double-couple moment tensor source is adopted in the simulation. The non-double-couple moment tensor is given by

$$\mathbf{m} = \begin{pmatrix} 0.4532 & 0.2789 & 0.1743 \\ 0.2789 & -0.5926 & 0.1046 \\ 0.1743 & 0.1046 & 0.4532 \end{pmatrix}. \tag{2.7}$$

This moment tensor comprises 11% isotropic (explosion), 45% double-couple and 44% compensated linear vector dipole components, and can well represent a general non-double-couple moment tensor. We choose this combination in order to jointly illustrate the effects of the major equivalent forces which are expected in microseismic settings. Figure 2.3 shows the far-field P-wave and S-wave radiation patterns of this non-double-couple moment tensor source. In Figure 2.3, the vectors exhibit the polarization direction of the P- and S-waves and the color and length of the vectors represent the polarization strength.

Figure 2.4 shows the simulated waveforms and modeling residuals. For the finite-difference simulation, the spatial and temporal intervals are 5 m and 0.1 ms, respectively. The source-receiver distances of the twelve receivers range from $0.5\lambda_s$ to $8\lambda_s$ with a 86.4° opening angle to account for both near-field and far-field scenarios (λ_s is the dominant S-wave wavelength, which is 50 m in this simulation experiment). The twelve receivers are deployed with azimuth angles varying from 0° to 85°. As shown in

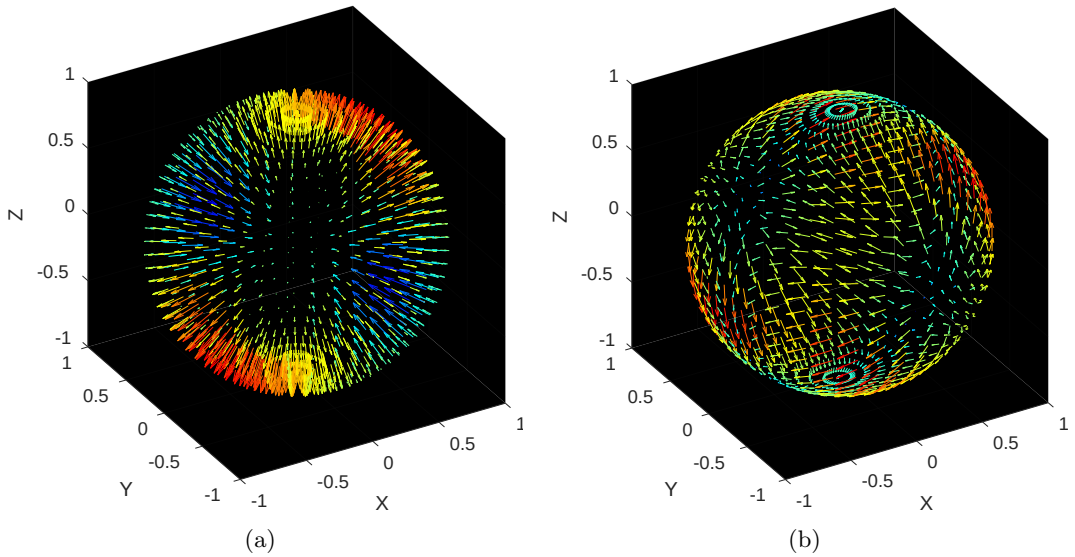

Figure 2.3: The far-field (a) P-wave and (b) S-wave radiation patterns of the non-double-couple moment tensor source (expressed in equation 2.7). The vectors exhibit the polarization direction of the P- and S-waves and the color and length of the vectors represent the polarization strength. Red color represents positive polarization, and blue color represents negative polarization. X, Y and Z axes show the 3D spatial coordinates which are normalized to 1

Figure 2.4(a), the waveform fidelity of the finite-difference results is in good agreement with the analytical solution at both the near-field and far-field, and there are no obvious amplitude differences or phase shifts with respect to the analytical solution. This is also verified by Figure 2.4(b) which shows the relative error of the peak amplitude with respect to the analytical solution. The relative errors of the tenth- and twelfth-order (in space domain) FD scheme are within 1% both in the near-field and far-field. The relative errors of the eighth-order FD scheme are greater than 2% in the near-field. As the tenth-order FD scheme provides sufficient modeling accuracy, we will adopt 10th-order as the default FD scheme in the following modeling examples. However, the relative errors of the far-field approximation are much larger than that of the finite-difference method, especially in the near-field. Considering the inevitable simulation error brought in by numerical discretization, the accuracy of this finite-difference simulation is sufficient. Therefore, the finite-difference modeling can provide full wavefield information and more accurate results than the far-field approximation.

2.3 Modeling Examples

2.3.1 Anisotropic Layered Model

The subsurface medium can range in complexity, both in terms of elastic heterogeneity and anisotropy. In order to inspect the influence of anisotropy on the wavefield from a microseismic event, a simple block velocity model with three layers is examined. The

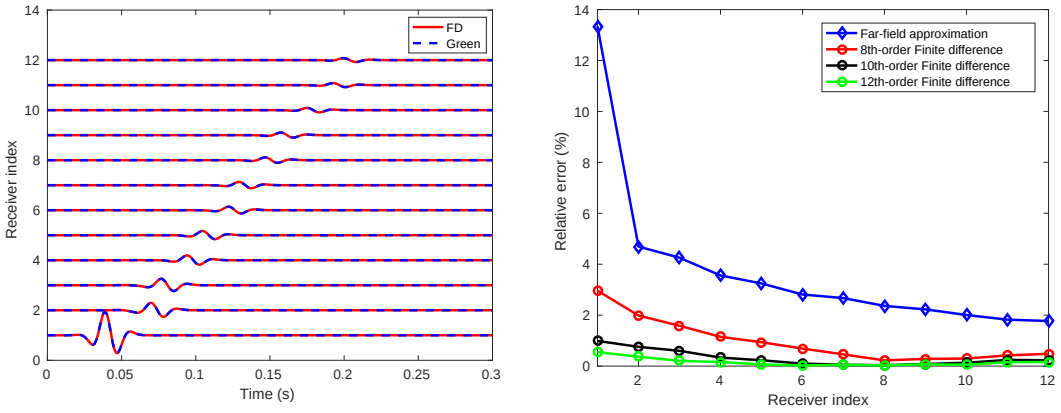

(a) (b)

Figure 2.4: (a) Synthetic seismograms (displacement in Y direction only) recorded by twelve receivers deployed in different directions and positions, with the FD results in solid red line overlaying the analytical solutions obtained by Green's function (equation 2.15 in Appendix 2.4) in dashed blue line. (b) Relative error of the peak amplitude of the FD modeling and far-field approximation with respect to analytical solutions for the twelve FD records, with eighth-, tenth- and twelfth-order FD modeling in red, black and green lines,respectively, and the far-field approximation in blue line

layered model is often used in microseismic interpretation and inversion. As shown in Figure 2.5 (a), a microseismic event is located in the middle of the model. Surface and downhole arrays are commonly used in microseismic monitoring. In the modeling experiment, both a surface array and a vertical downhole array are deployed to record the microseismic data. In order to comprehensively assess the influence of seismic anisotropy on travel-times and amplitudes of microseismic data, a dense surface array with full azimuth coverage is deployed. The surface array has 90000 geophones deployed uniformly along the free surface at 10 m intervals. The vertical downhole array is located at a horizontal distance of 283 m and an azimuth of 135° relative to the microseismic source (i.e., the middle of the model). The downhole array has 500 geophones with intervals of 5 m. In the second layer, where the microseismic event is located, we examine three submodels having three different types of anisotropy. In the first submodel, no anisotropy is introduced, which implies an isotropic layered setting. In the second submodel, the second layer is set to be VTI, which is used to simulate shale having horizontal stratification. In the third submodel, the second layer is set to be HTI, which is used to simulate rock with vertical fractures. For all the submodels, a vertical strike-slip event is used to simulate the microseismic source, which means only m_{xy} and m_{yx} are nonzero in the seismic moment tensor. The elastic parameters of the isotropic layered model are shown in Table 2.4. The velocity model used in the modeling is a simplified representation of geological structure typically encountered by hydraulic fracturing projects in the Barnett shale in Texas (Wong et al., 2011). The VTI medium in the second example has Thomsen parameters of $\varepsilon = 0.334$, $\gamma = 0.575$,

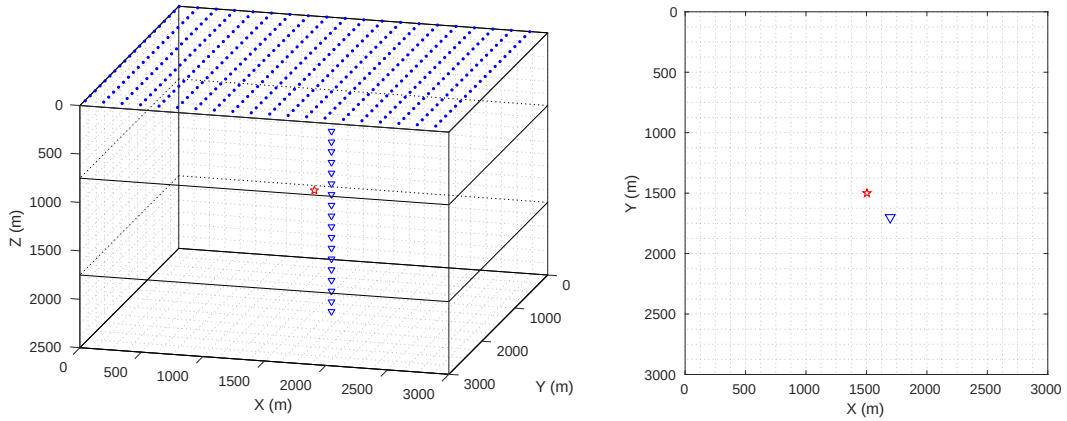

(a) (b)

Figure 2.5: (a) Schematic representation of the layered model and the recording arrays. The red star represents microseismic source, the blue points represent surface arrays, and the blue triangles represent downhole arrays. The microseismic source is placed in the middle of the model. (b) Surface projection of the source and downhole array

Table 2.4: Elastic parameters of layered isotropic model

Layer	Thickness (m)	Vp (m/s)	Vs (m/s)	Density (kg/m^3)
1	750	3724	1944	2450
2	1000	4640	2583	2490
3	750	5854	3251	2680

$\delta = 0.73$, which is a measured anisotropy in clayshale (Thomsen, 1986). The HTI medium in the third submodel is constructed by rotating the VTI medium of the second submodel anticlockwise along the Y-axis by 90°.

The P- and S-wave velocity anisotropy of the VTI and HTI media used in the second layer in the submodels is shown in Figure 2.6 (a-c) and Figure 2.6 (d-f), respectively. The relative variation for the P-, fast and slow S-wave velocity in the VTI medium is 29.2%, 46.6% and 28.4%, respectively. The velocity anisotropy of the HTI medium can be easily obtained by rotation.

Figure 2.7 (a-c) shows horizontal wavefield slices of particle velocity in the Y direction for the three submodels, where the wavefield is recorded at the depth of microseismic source. Different types of waves can be identified in these wavefield slices. For Figure 2.7(a), the isotropic case, only the P- and S-wave are identified in the wavefield slice. In the VTI example shown in Figure 2.7(b), S-wave splitting is clearly observed seen by the distinct fast S-wave (qS1-wave) and slow S-wave (qS2-wave) in the wavefield. As the second layer is transversely isotropic, the wavefront in the horizontal slice does not show anisotropic velocity variation in the different propagation directions. In the third example, where the second layer is HTI medium, a more complex wavefield is observed. Due to strong anisotropy, the wavefronts of the different types of waves show

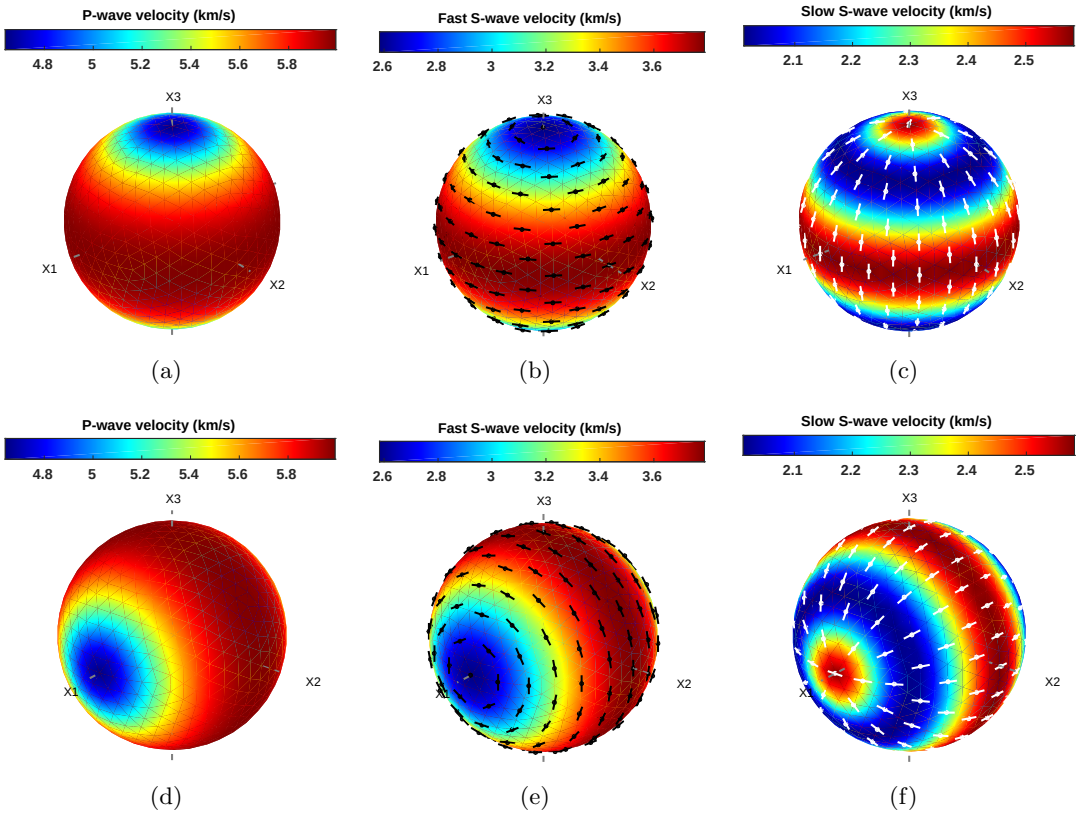

Figure 2.6: Variation of the (a) P-wave, (b) fast S-wave and (c) slow S-wave velocity in VTI medium along different propagation directions. Variation of the (d) P-wave, (e) fast S-wave and (f) slow S-wave velocity in HTI medium along different propagation directions. The black and white markers indicate the fast and slow S-wave polarization directions, respectively. Figures created using MSAT (Walker & Wookey, 2012)

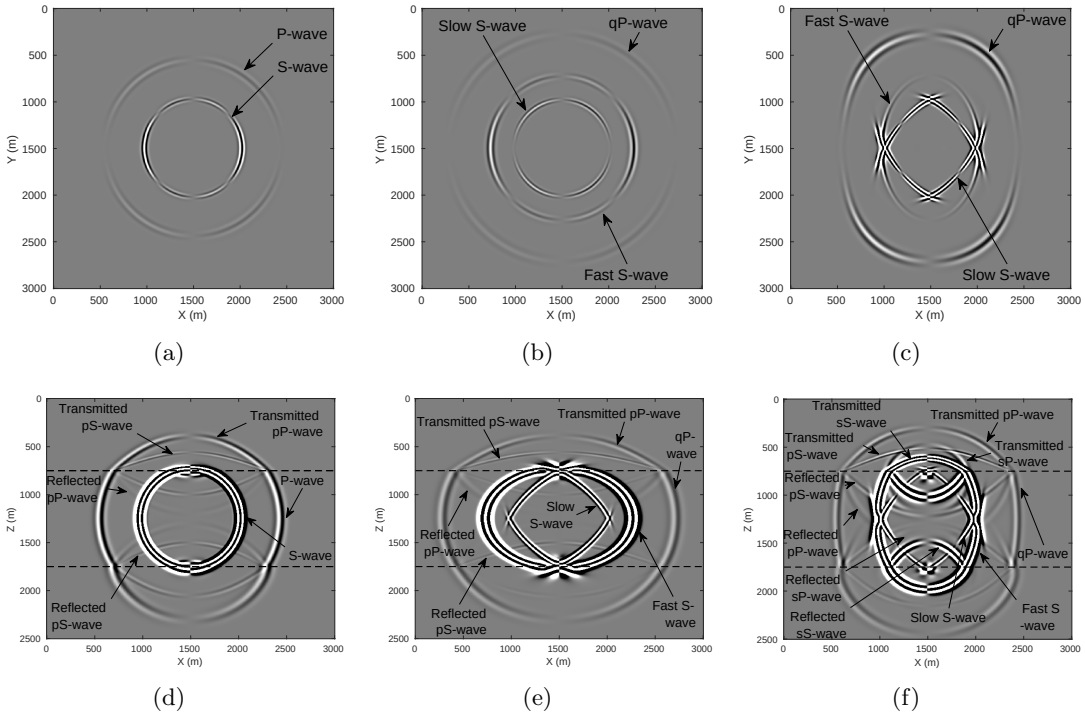

Figure 2.7: Horizontal slices of velocity component in Y direction for the (a) isotropic, (b) VTI and (c) HTI model. The horizontal slices are taken at time of 0.23 s and depth of microseismic source (z=1250 m). Vertical slices of velocity component in Y direction for the (d) isotropic, (e) VTI and (f) HTI model. The vertical slices are taken at a time of 0.23 s and lateral position of y=1500 m. Dashed lines show boundaries of different layers

strong anisotropy in the different propagation directions, and wavefront triplication is also observed in the slice.

Figure 2.7 (d-f) shows vertical wavefield slices of the particle velocity in the Y direction for the three submodels, where the vertical slice bisects the same Y-position of the microseismic source. Due to the existence of layer boundaries in these vertical slices, reflected waves, transmitted waves and mode-converted waves (e.g., converted PS-waves and converted SP-waves) appear in the wavefield slices, thus making the wavefield more complicated. For the VTI submodel, the vertical wavefield slice is not located in the transversely isotropic plane; thus, strong anisotropy can be observed in the shape of the wavefront (as shown in Figure 2.7(e)). For the HTI submodel, where the orientation of the HTI medium is oriented such that the transversely isotropic plane is parallel to the Y-axis, the vertical wavefield displays strong anisotropy in the wavefront (as shown in Figure 2.7(f)). The presence of seismic anisotropy has made the wavefield much more complex compared to the isotropic case, increasing the complexity of microseismic processing, such as event detection and travel-time picking.

Downhole Array

The recorded seismograms for the downhole array are shown in Figure 2.8. The recorded seismograms are the particle velocity component in the Y direction. The direct P- and S-wave are automatically picked in the recorded wavefields. Compared with the seismograms in the isotropic case, the seismograms for the anisotropic submodels are much more complicated. Due to S-wave splitting, more mode-converted and multi-reflected waves appear in the recorded data, thus making microseismic event detection and arrival-time picking more difficult. When many microseismic events are triggered in the target area within a short time, the extra complexity and interference in the wavefield introduced by the medium anisotropy will make microseismic location difficult.

To further study the influence of anisotropy on microseismic monitoring, travel-times and peak amplitudes of the direct P-wave in the three submodels are extracted and compared. As Figure 2.9 shows, when the subsurface medium shows strong anisotropy, the amplitudes and travel-times of the direct P-wave will be variable. The maximum relative differences in travel-time and peak amplitude are 16% and 86% for the VTI case, and 18% and 50% for the HTI case. The travel-time and amplitude differences between the anisotropic models and the isotropic model are not constant, and vary with wave propagation direction due to anisotropy. The amplitude of the recorded waveforms is mainly affected by the radiation pattern of the source, coupling between different phases and the elastic properties of the media such as impedance and attenuation. Because of seismic anisotropy, wave velocity varies with different propagation directions. Thus, the ray path and media elastic parameters in anisotropic cases are different from those in isotropic case. In this way, the seismic anisotropy has affected the travel-time and amplitude of the recorded waves and hence the observed radiation pattern of the microseismic source. Thus, without considering seismic anisotropy, the variation in travel-time and amplitude in the different directions will bias the final result, thus contributing to large errors in inverted source location and mechanism. As shown in Figure 2.9(b), when geophones are located in the anisotropic layer, the travel-time difference of the direct P-wave in the VTI and HTI models with respect to the isotropic model exhibit opposing trends. For the VTI model, the travel-time difference increases with the take-off angle of the seismic rays, whereas for the HTI model, the travel-time difference decreases with the take-off angle of the seismic rays. The travel-time difference can be expressed by

$$\Delta t = \frac{l_{ref}}{v_{ref}} - \frac{l_{ani}}{v_{ani}}, \tag{2.8}$$

where l represents the ray path in the isotropic reference medium or anisotropic medium; v_{ref} is the average group velocity along the ray path in the reference medium (which is the P-wave velocity of the isotropic model here); v_{ani} is the average group velocity along

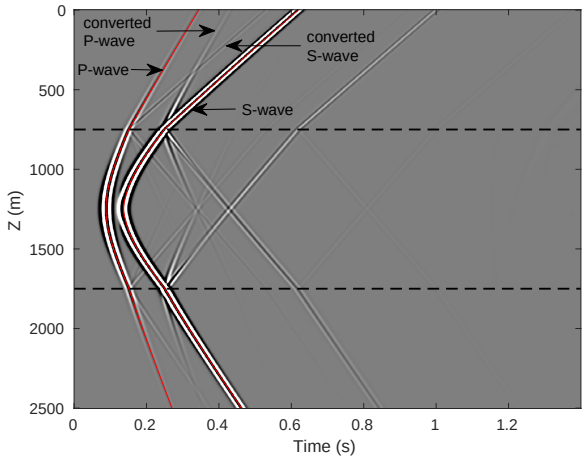

(a)

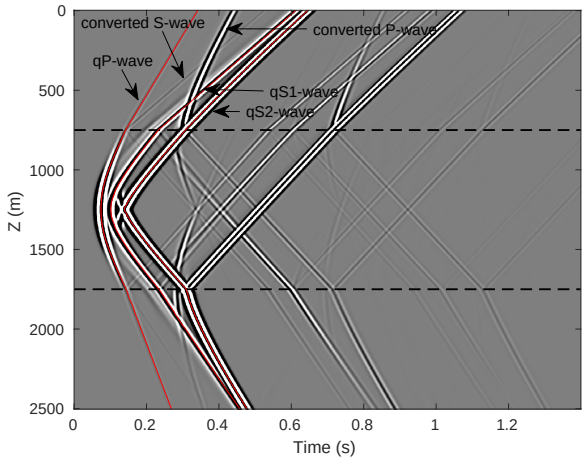

(b)

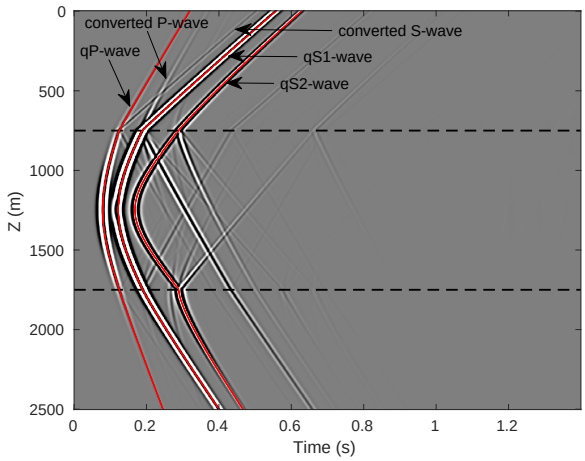

(c)

Figure 2.8: The recorded seismograms in downhole array for the (a) isotropic, (b) VTI and (c) HTI model. Vertical axis shows the position of geophones and horizontal axis shows recording time. Red dotted lines represent the automatically picked direct P- and S-wave wavefronts; dashed lines show boundaries of different layers

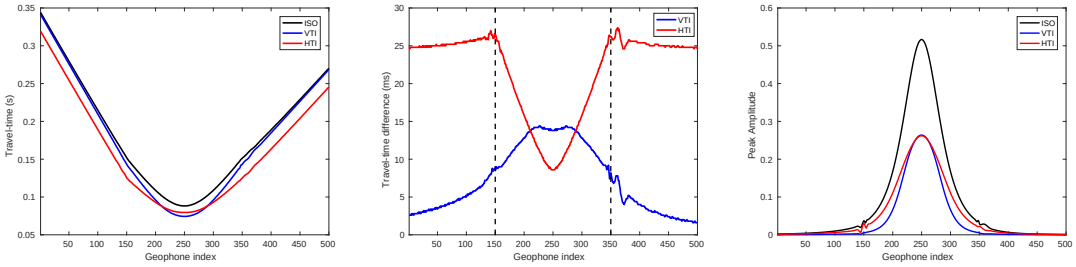

(a) (b) (c)

Figure 2.9: Comparison of travel-times and peak amplitudes of the direct P-wave for three modelings. Dark solid line represents value in the isotropic model; blue solid line represents value in the VTI model; red solid line represents value in the HTI model; dashed lines show boundaries of the layers (geophone 150 and geophone 350 are placed at layer boundary, geophone 250 is at the same depth of microseismic source). (a) Travel-times of the direct P-wave. (b) Travel-time differences with respect to the isotropic case. (c) Peak amplitudes of the direct P-wave

the ray path in the anisotropic medium. The average group velocity of the reference medium v_{ref} will only affect the sign of the travel-time difference and not the trend of the travel-time difference. In practice, the reference velocity can be determined by well logging data, which is an approximation for the velocity in the vertical direction. Due to the simplicity of the adopted anisotropic model, the ray path in the isotropic and anisotropic media could be considered approximately the same, which is often the case in the near-field and for smooth velocity models (Sadri & Riahi, 2010, Wang, 2013). Thus, the travel-time difference is proportional to the length of ray path and average group velocity of the anisotropic medium along the ray path. Under the current modeling geometry, the length of the ray path decreases with the take-off angle of the seismic rays. However, the downhole array is deployed near the source region and thus velocity variation of the anisotropic medium along different propagation directions is the main control factor for travel-time differences. When the recording array is deployed far enough away from the source region, such as surface arrays, the length of the ray path should be taken into consideration when analyzing travel-time differences.

As we have shown, the different types of velocity anisotropy can cause different trends in travel-time differences. The distribution of phase velocities of P-wave, slow S-wave and fast S-wave in 3D space domain forms the velocity surface corresponding to these three phases (Babuska & Cara, 1991). Figure 2.10 shows the velocity surfaces in the profile of the downhole array for the isotropic model, VTI model and HTI model. The P-wave velocity toward the directions of downhole geophones in the second layer is calculated and shown in Figure 2.11(b). For the VTI medium, the P-wave velocity increases with the take-off angle. However, for the HTI medium, the P-wave velocity decreases with the take-off angle at this particular azimuth. The normalized travel-time difference of the direct P-wave for the downhole geophones in the second layer is shown

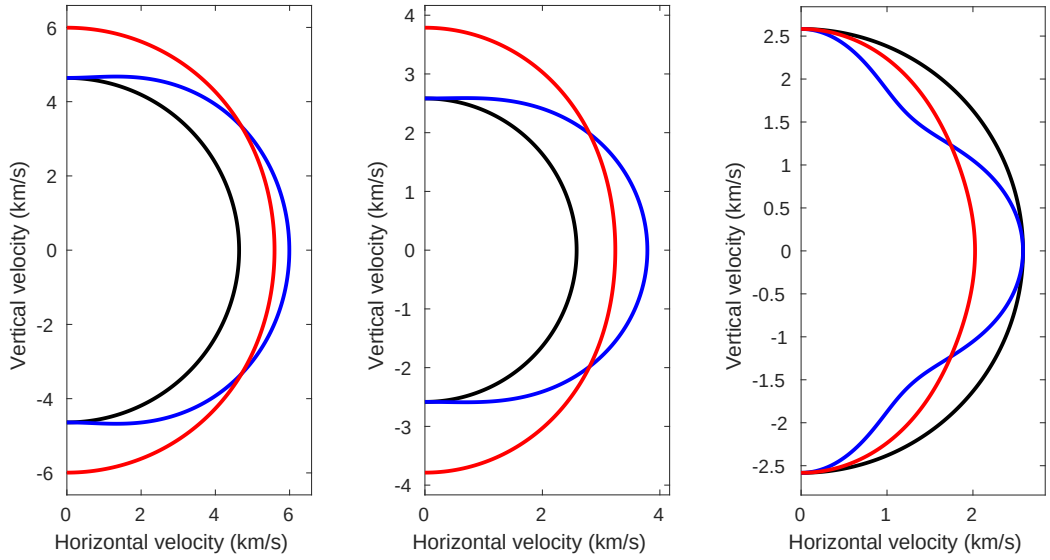

Figure 2.10: Velocity surfaces[a] of the P-, fast S- and slow S-waves, calculated in the same profile of the downhole array. The dark line represents the isotropic model; blue line represents the VTI model; red line represents the HTI model. For the isotropic model, there is only one S-wave mode, whose velocity is used in both fast and slow S-wave surface. (a) P-wave velocity surface; (b) fast S-wave velocity surface; (c) slow S-wave velocity surface. The velocity surface is the representation of directionally dependent body-wave phase velocities, and calculated using Christoffel equation

[a]Phase velocities are displayed in the figure.

in Figure 2.11(c). Because the receivers are placed at the same layer, ray path can be easily calculated. In Figure 2.11(c), the effect of the ray path has been considered and eliminated; thus, the travel-time differences are only influenced by the P-wave velocity. Figure 2.11(b) and 2.11(c) show strong similarity and potentially provides a way to estimate the anisotropy of the target zone in microseismic monitoring. The VTI and HTI media can be distinguished using a downhole array as well. For the TTI media, the travel-time difference will not monotonically increase or decrease with the take-off angle as for the VTI and HTI media.

The variation in travel-times and peak amplitudes for the fast S-wave (S-wave in isotropic case) in the different models is shown in Figure 2.12. In Figure 2.12(c), the peak amplitudes of the fast S-wave in the VTI model show a big difference from that for the isotropic and HTI models. From the recorded waveform in Figure 2.13 (a-b), we can clearly see that seismic anisotropy has completely changed the radiation pattern of the S-wave in the VTI model.

The velocity difference or travel-time difference between the fast S-wave and the slow S-wave can be used to describe the shear-wave anisotropy in an anisotropic medium. Large velocity differences between fast and slow shear-waves will cause strong shear-

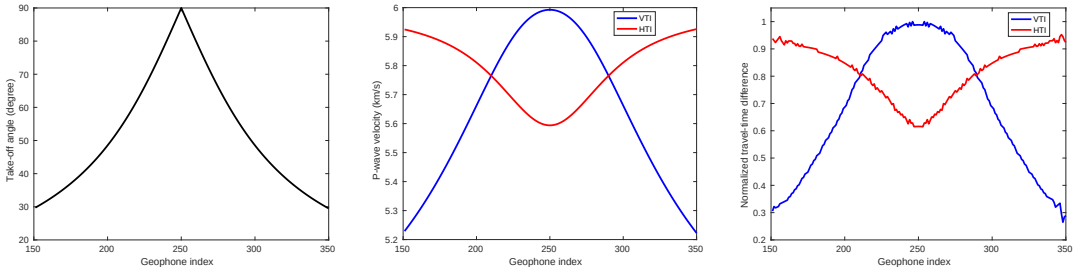

(a) (b) (c)

Figure 2.11: (a) Relationship between the take-off angle and geophone index. (b) Velocity variation of the P-wave for downhole geophones at the second layer. (c) Normalized travel-time differences of the direct P-wave for downhole geophones at the second layer. The effect of the ray path has been considered and eliminated. The small wiggles come from numerical artefacts of the automatic arrival time picking algorithm

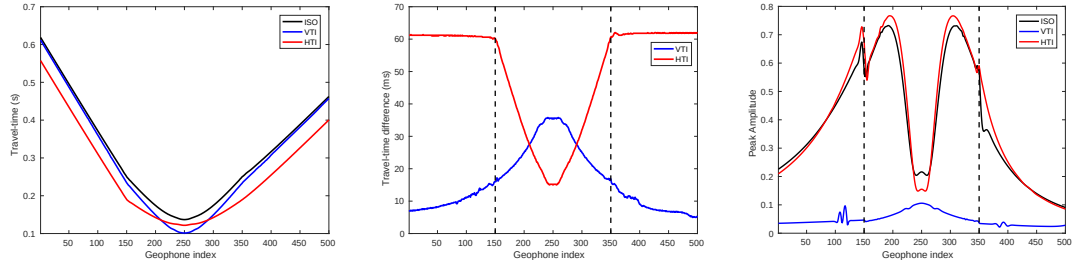

(a) (b) (c)

Figure 2.12: Comparison of travel-times and peak amplitudes of the direct fast S-wave (S-wave in the isotropic case) for three modeling examples. The figure description is analogous to figure 2.9. The small wiggles in the figure are caused by picking error introduced by interference of different waves. The sudden jump of peak amplitudes near the layer boundaries is caused by sudden change in elastic parameters or wave impedance between layers. (a) Travel-times of the direct S-wave or fast S-wave. (b) Travel-time differences with respect to isotropic case. (c) Peak amplitudes of the direct S-wave or fast S-wave

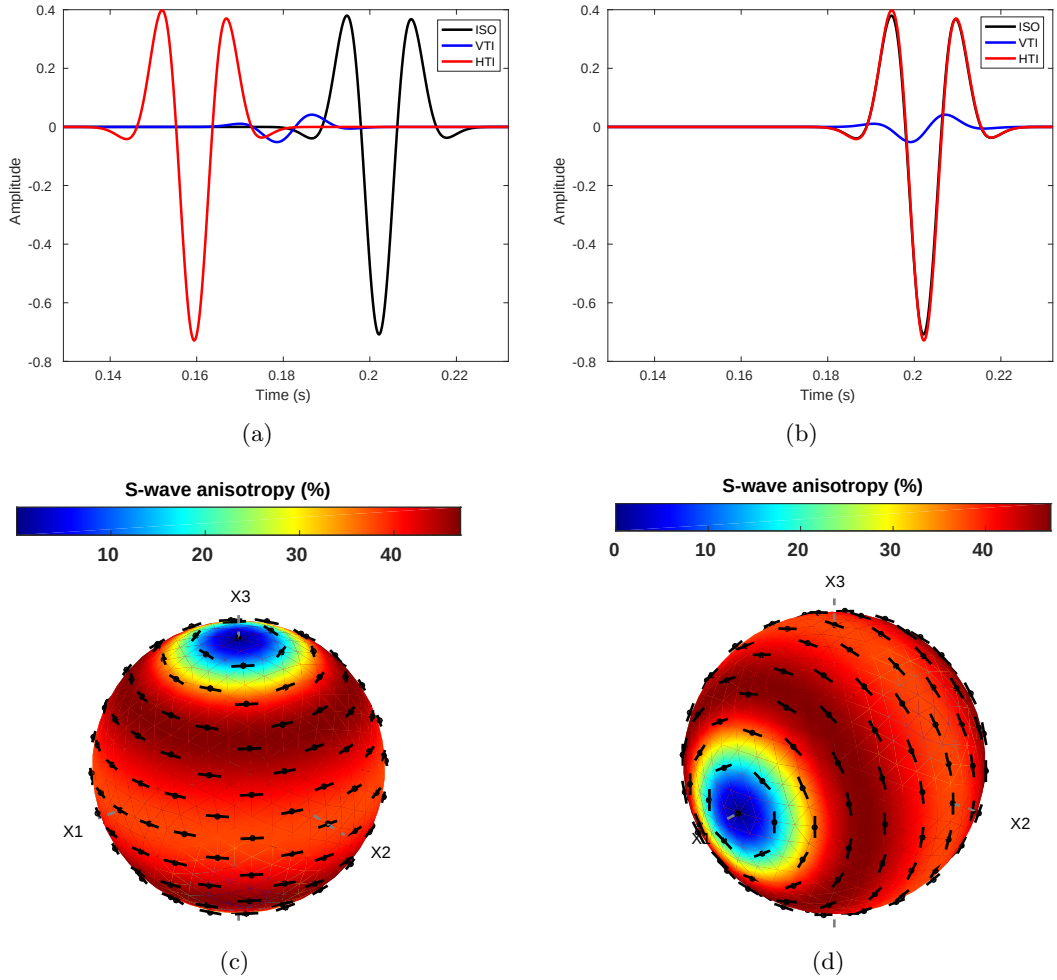

Figure 2.13: Waveform of the direct fast S-wave (S-wave in isotropic case) before (a) and after (b) time alignment at downhole geophone 180. Variation of S-wave anisotropy along different propagation directions in the (c) VTI and (d) HTI medium

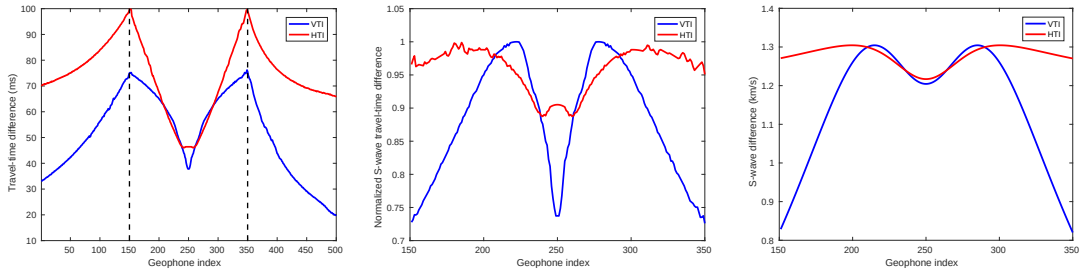

(a) (b) (c)

Figure 2.14: (a) Travel-time differences between the fast S-wave and slow S-wave in the VTI and HTI model. (b) Normalized travel-time differences between the fast S-wave and slow S-wave in the VTI and HTI model at the second layer. The effect of the ray path has been considered and eliminated. (c) Velocity difference between the fast S-wave and slow S-wave in the VTI and HTI model at the second layer

wave splitting (i.e., splitting time). Shear-wave anisotropy is used to describe shear-wave splitting strength. It is defined as the ratio between the difference and average of fast and slow shear-wave velocities ($aV_s = (V_{qS1} - V_{qS2})/0.5(V_{qS1} + V_{qS2})$) (Walker & Wookey, 2012). Figure 2.13 (c-d) shows the variation of shear-wave anisotropy in the VTI and HTI models. The travel-time difference between the fast S-wave and the slow S-wave are also extracted and displayed in Figure 2.14(a). The normalized travel-time difference after eliminating the influence of the ray path (Figure 2.14(b)) shows good consistency with the velocity difference (Figure 2.14(c)) suggesting that this is a feasible way to estimate the anisotropy of the subsurface in microseismic monitoring. The recorded fast and slow S-waves in anisotropic media can be identified and studied through shear-wave splitting analysis (Crampin & Peacock, 2008, Long & Silver, 2009). We note that inversion of shear-wave splitting data for anisotropy and fracture parameters is increasingly common (Wuestefeld et al., 2010, Verdon & Kendall, 2011). Our method enables the easy comparison of geomechanical models to these data by fully reproducing the wavefield in generally anisotropic media.

Surface Array

Figure 2.15 shows seismic profiles along the first line in the Y direction of the surface array. The direct P-wave arrivals are automatically picked in the recorded wavefields. Four traces in Figure 2.15 are extracted and shown in Figure 2.16. Due to the strong seismic anisotropy, the received seismic waveforms for the VTI and HTI submodels are quite different compared to the isotropic case. More phases can be observed in the anisotropic models because of shear-wave splitting. If care is not taken, these phases could be identified as true microseismic events having detrimental effect on microseismic interpretation.

Figure 2.17 shows the travel-times of the direct P-wave along the free surface. As

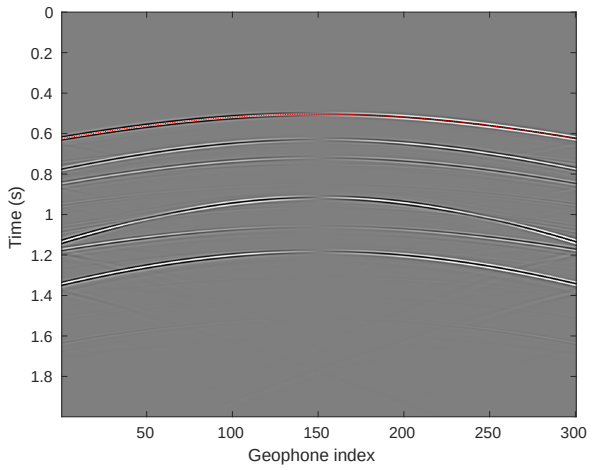

(a)

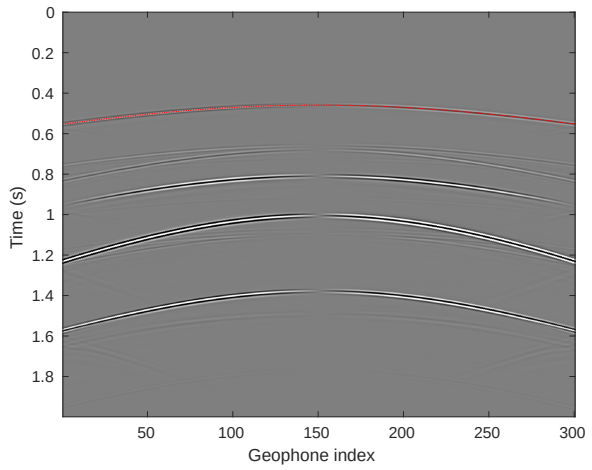

(b)

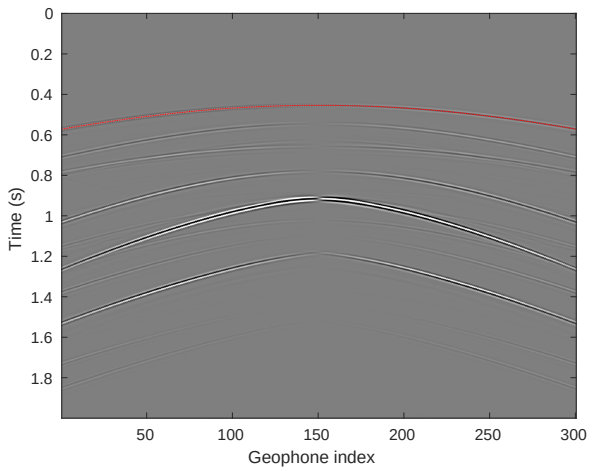

(c)

Figure 2.15: Recorded seismic profiles along the first line in the Y direction for the (a) isotropic, (b) VTI and (c) HTI models using surface array. These profiles are recorded at the first receiver line in Y direction. The direct P-wave has been automatically picked and annotated with red line in the figure

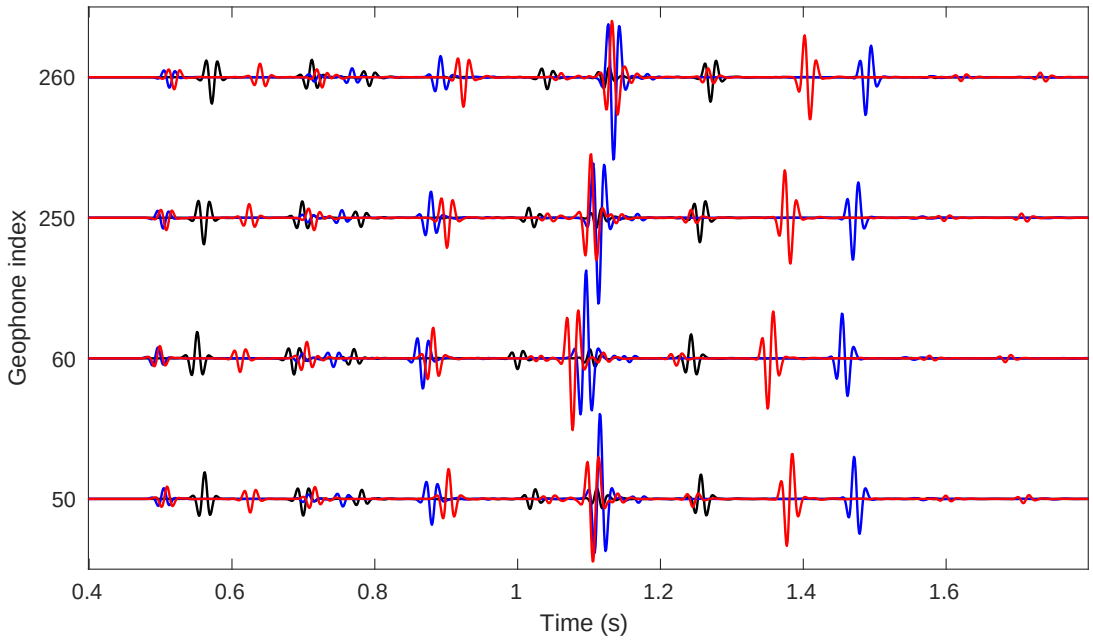

Figure 2.16: Shown are four traces extracted from figure 2.15 with the isotropic case in dark line, the VTI case in blue line and the HTI case in red line

the surface array is deployed uniformly on the free surface and the microseismic source is located just below the middle of the surface array, the travel-times of the seismic waves in the isotropic layered media should be symmetrical about the epicenter, as can be seen in Figure 2.17(a), where the travel-times of the direct P-wave are circular. In the VTI model, the transverse isotropic symmetry plane is in the horizontal plane, and so the travel-times of the direct P-wave are also circular (Figure 2.17(b)). The magnitude of travel-time differs from the isotropic case due to the presence of anisotropy. However, in HTI model, the transverse isotropic symmetry plane is vertical; thus, velocity anisotropy in the horizontal plane will contribute to an asymmetric distribution about the epicenter. As Figure 2.17(c) shows, travel-times of the direct P-wave are ellipses in the HTI model. The major axis of the ellipse is parallel to the isotropic plane of the HTI medium, which is along the orientation of the fracture planes. The ratio of the major and minor axes of the ellipse is proportional to the strength of anisotropy. Travel-time differences of the direct P-wave between the anisotropic models and the isotropic model are shown in Figure 2.18, which clearly exhibits the different characteristics of VTI and HTI media and the alteration of travel-times introduced by seismic anisotropy.

Figure 2.19 shows the peak amplitudes and also the polarization of the direct P-wave. The maximum relative difference of peak amplitude can be as large as 50% for VTI and HTI, which means seismic anisotropy can have a large influence on source mechanism characterization, such as moment tensor inversion. As shown in Figure 2.19, the peak amplitudes of the direct P-wave in anisotropic case are smaller than

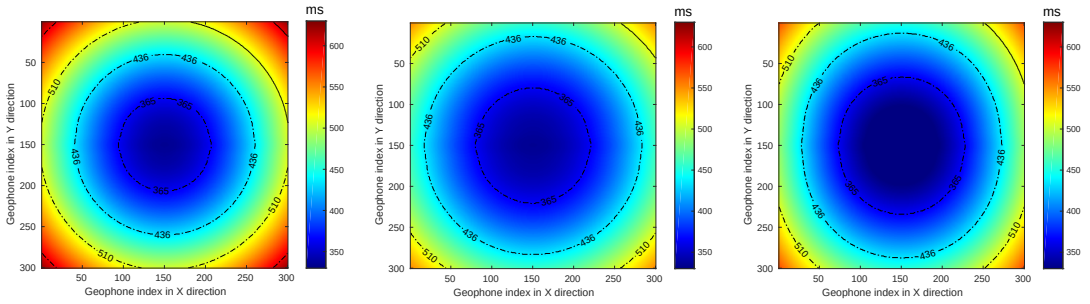

(a) (b) (c)

Figure 2.17: Travel-times of the direct P-wave in the (a) isotropic, (b) VTI and (c) HTI models for the surface array. The unit of time in these figures is millisecond. The contour lines of travel-times are also displayed in the figure

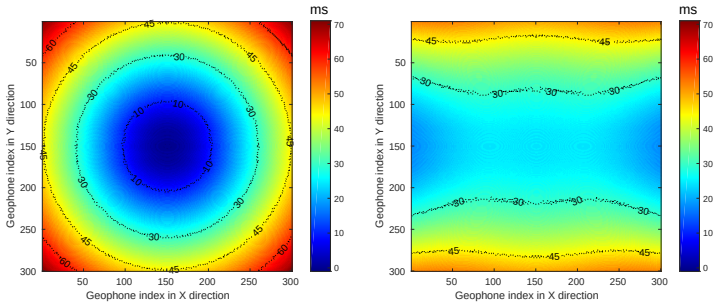

(a) (b)

Figure 2.18: Travel-time differences of the direct P-wave with respect to the isotropic case. (a) VTI model; (b) HTI model

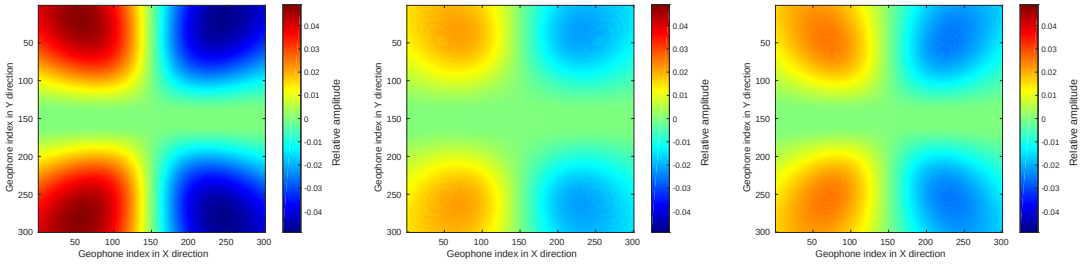

Figure 2.19: Peak amplitudes of the direct P-wave in the (a) isotropic, (b) VTI and (c) HTI models for the surface array

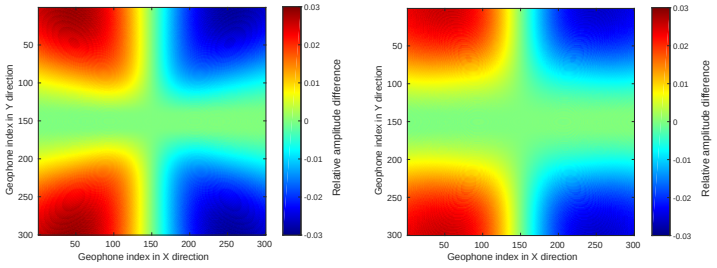

Figure 2.20: Peak amplitude differences of the direct P-wave with respect to the isotropic case. (a) VTI model; (b) HTI model

that in isotropic case. This will cause an underestimate of the seismic moment M_0 in the presence of anisotropy when only direct P-waves are used in the source magnitude estimation. In Figure 2.19, the polarizations of the direct P-wave have not been significantly affected by seismic anisotropy. The peak amplitude differences of the direct P-wave between the anisotropic models and the isotropic model are also shown in Figure 2.20, which clearly shows the alteration of amplitudes introduced by seismic anisotropy.

Source Location Error due to Seismic Anisotropy

If seismic anisotropy is ignored in microseismic event location, the location result will be biased (King & Talebi, 2007, Warpinski et al., 2009). Table 2.5 compares the event location results in the isotropic, VTI and HTI models using the recorded P-wave arrival times of the surface array. The microseismic event is located by minimizing the overall difference between the recorded arrival times and the calculated theoretical travel-times. The theoretical travel-times of direct P-waves are calculated at every discretized grid points based on the accurate isotropic velocity model. The event location results in Table 2.5 show the influence of different types of anisotropy. In the isotropic model, the microseismic event has been located accurately. In the VTI and HTI models, the located event is deeper than the correct event, with vertical deviations of 570 m and 190

Table 2.5: Source location results in isotropic, VTI and HTI media using surface array. The source location is determined by minimising the difference between the recorded arrival times and calculated traveltimes of a given velocity model. Δ means the difference between estimated and correct value. Cumulative residual is the overall cumulative residuals of arrival times for all receivers during source location

Medium	ΔX (m)	ΔY (m)	ΔZ (m)	ΔT_0 (s)	Cumulative residual (s)
ISO	0	0	0	0	0.0165
VTI	0	0	570	-0.1195	0.0246
HTI	0	0	190	-0.0614	0.2344

m respectively. Here, because the surface array is symmetric about the hypocenter of the microseismic event, the located event is well constrained in the horizontal direction. Therefore, no location deviations in X or Y directions are observed.

The seismic anisotropy has changed the curvature of the direct arrivals (see Figures 2.15 and 2.17), and therefore brings large errors for seismic location. The cumulative travel-time residual is used to evaluate the inversion error. It is defined as $\sqrt{\sum_i^N (t_i^a - t_i^c)^2}$, where t_i^a is the recorded arrival times, t_i^c is the calculated theoretical arrival times at the estimated event location, and N is the number of receivers. The cumulative travel-time residual in the isotropic model should be 0. However, due to some inevitable picking deviations of the direct P-waves, the cumulative travel-time residual in the isotropic model shows a very small value. In Table 2.5, the cumulative travel-time residual in the HTI model is much larger than for the VTI and isotropic models. This is because the arrival times of direct waves in the HTI model exhibit elliptical anisotropy for the surface array, which is different from the round distribution of arrival times in the VTI and isotropic models (as shown in Figure 2.17). Therefore, the calculated arrival times cannot match the recorded arrival times very well. Due to the trade-off between location depth and estimated origin time of seismic event, when the located event is deeper, the estimated origin time of the event is earlier than the correct origin time (as can be seen in our location results in the VTI and HTI models in Table 2.5). The location error in the VTI model is much larger than for the HTI model, and the estimated origin time is also much earlier. In microseismic monitoring, a few hundred meters deviation of event location can be fatal for assessing the fracturing effect or microseismic mapping. Therefore, seismic anisotropy needs to be accounted for in microseismic monitoring especially when many fractures have been stimulated by fracturing.

2.3.2 Anisotropic Overthrust Model

Based on the previous simple models, it is not surprising that microseismic imaging in complex media is a challenge. In complex media, the influence of seismic anisotropy could be further distorted due to the presence of elastic heterogeneity. In order to study

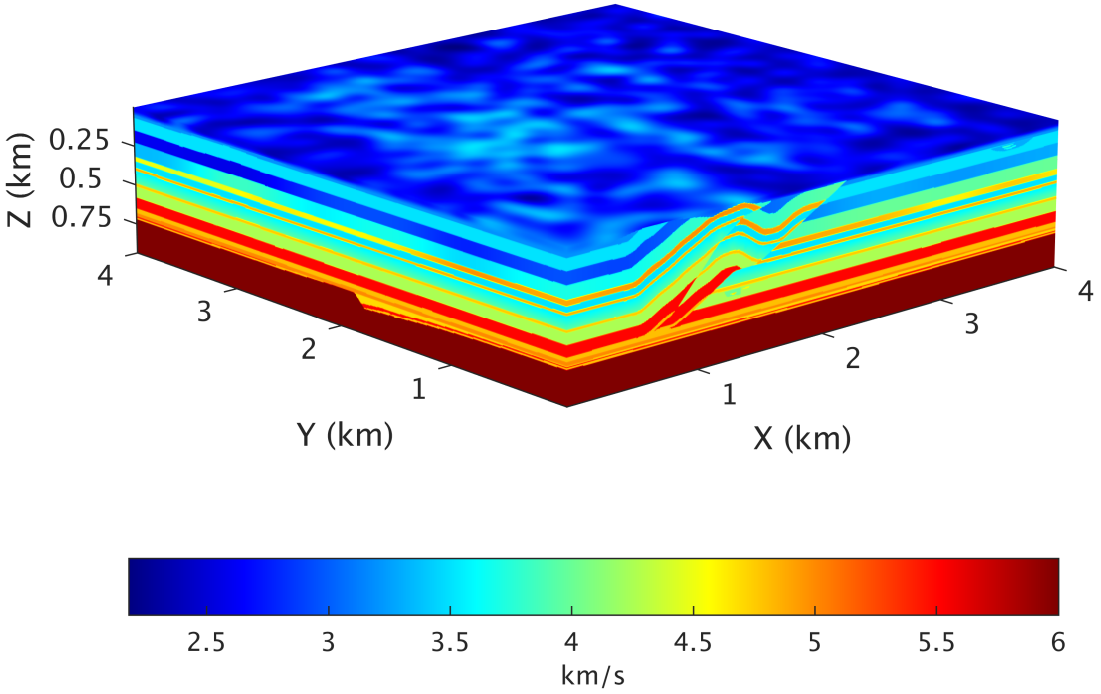

Figure 2.21: P-wave velocity of the 3D overthrust model

the influence of seismic anisotropy on microseismic monitoring in complex media, we apply full waveform modeling in the 3D isotropic and anisotropic SEG/EAGE overthrust model (Aminzadeh et al., 1997), which has been widely used in exploration geophysics (Virieux & Operto, 2009, Yuan et al., 2015). Three overthrust models with different types of anisotropy are used in the simulations. The P-wave velocity of the overthrust model is shown in Figure 2.21. The overthrust model has a size of $801 \times 801 \times 187$ cells in the X, Y and Z directions. The same double-couple source (vertical strike-slip) is placed in the middle of the 3D model, (i.e., grid coordinate 400, 400 and 93 in X, Y and Z directions). Around the source, an anisotropic region is set up (marked by the black lines in Figure 2.22). In the anisotropic region, different models are set to have different types of anisotropy, which are isotropy, VTI anisotropy and HTI anisotropy. The VTI anisotropy has the same Thomsen anisotropic parameters (i.e., $\varepsilon = 0.334$, $\gamma = 0.575$ and $\delta = 0.73$) as the former VTI modeling example. The HTI medium is constructed by rotating the VTI medium counter-clockwise along the Y-axis by 90°. Figure 2.22 shows three profiles of the overthrust model, in which the source location and anisotropic volume are clearly marked. As Figure 2.22 shows, the 3D SEG/EAGE overthrust model contains lots of faults (Figure 2.22(b) and 2.22(c)) and fluvial deposits (Figure 2.22(a)), which are suitable for studying the influence of anisotropy in complex heterogeneous media. Both a surface array (149×149 geophones at 25 m intervals) and a vertical downhole array (127 geophones at 5 m intervals) are used to record the microseismic data in the simulations.

Figure 2.23 shows the wavefield snapshots of these three modelings. Compared with

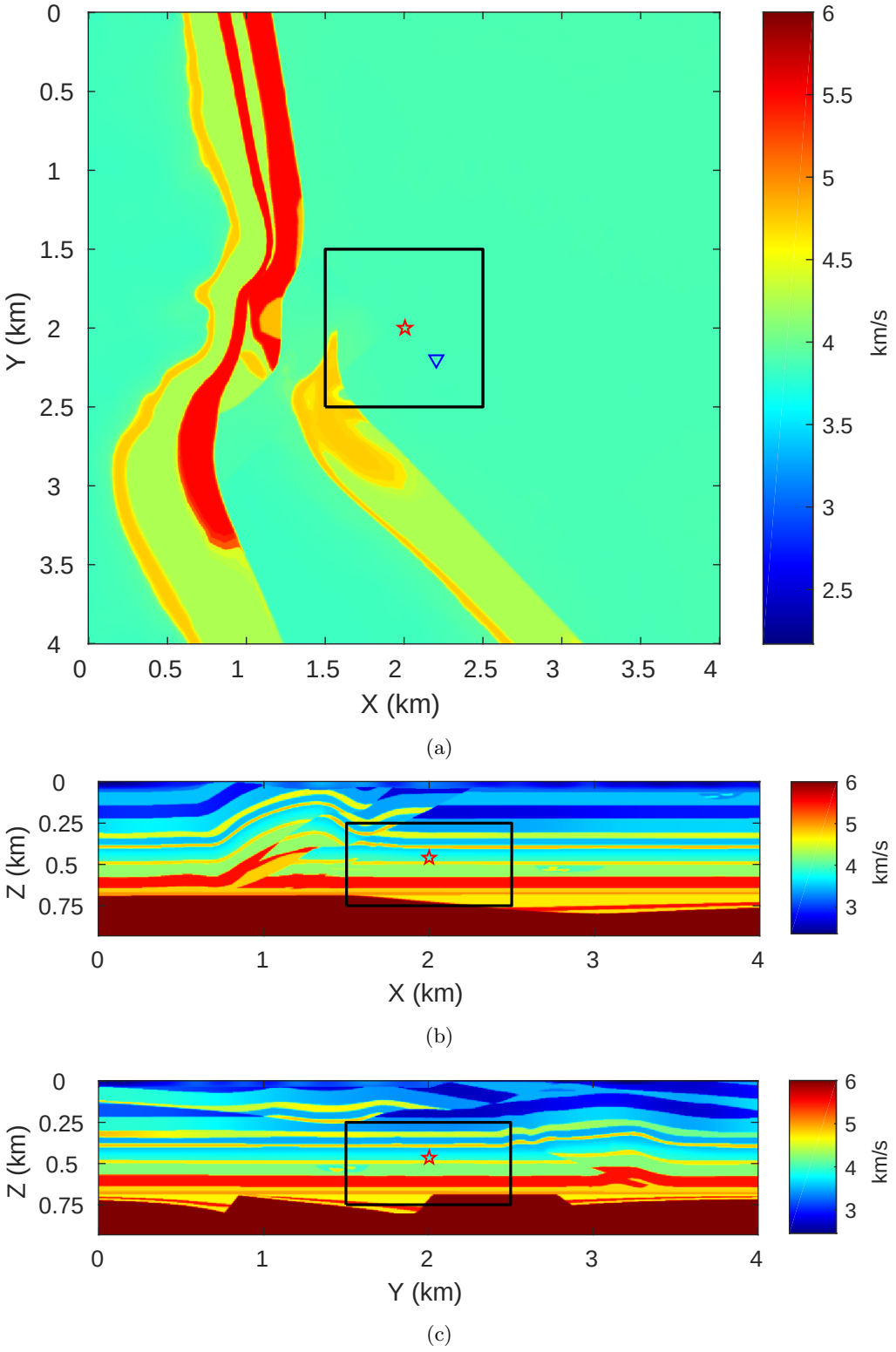

Figure 2.22: Shown are P-wave velocity profiles of the 3D overthrust model. The red star represents source position; the black line exhibits the anisotropic region in the model; the blue triangle represents the horizontal projection of the vertical downhole array. (a) Velocity profile at the depth of microseismic source (0.46 km). (b) Velocity profile at 2 km in the Y direction. (c) Velocity profile at 2 km in the X direction

the wavefield in the isotropic model, the wavefield in the anisotropic models is much more complex due to seismic anisotropy, especially in the anisotropic region. This complexity arises from the shear-wave splitting and velocity contrast between isotropic region and anisotropic region.

Figure 2.24 shows the recorded seismograms of the downhole array in different models. The strong heterogeneity has made the wavefields very complex, where abundant reflected and multiple waves can be seen in the recorded seismograms. In the presence of anisotropy, the model complexity has added to the general complexity of anisotropic phenomena. Significant differences of the recorded seismograms between the anisotropic models and the isotropic model can be seen in Figure 2.24.

The travel-times and peak amplitudes of the direct P-wave have been automatically picked and displayed in Figure 2.25. As with the previous analysis in the layered model, the travel-time differences of the direct P-wave in the VTI model increases with take-off angle of the rays and exhibits an upside down U shape pattern in the downhole array. On the contrary, the travel-time differences of the direct P-wave in the HTI model exhibit an opposite trend in the downhole array. The amplitudes of the direct P-waves are also different in the anisotropic scenarios. The maximum relative differences for travel-times and amplitudes are 17% and 80%, respectively, in the anisotropic models.

The seismic profiles recorded by surface array are shown in Figure 2.26. Significant differences in the recorded wavefields can be observed between the isotropic, VTI and HTI models. The direct P-waves recorded by the surface array are automatically picked. The picked travel-times and peak amplitudes of the direct P-wave are shown in Figures 2.27 and 2.28. Because of the complexity of the recorded wavefields and the weak strength of the direct P-wave, the automatic picking is not perfect. Some picking errors can be seen in the figures and the picked peak amplitudes are blurred. However, the radiation pattern of the direct P-wave can be recognized both in the isotropic and the VTI models. The radiation pattern of the direct P-wave in HTI model is affected by picking error and cannot be recognized easily. In this situation, manual picking is required. The surface array is symmetrical about the epicenter of the source. The travel-times of the direct P-wave in VTI model maintain the circular distribution as in the isotropic model because the transverse isotropic symmetry plane is in the horizontal plane. However, the travel-times of the direct P-wave in HTI model exhibit an elliptical distribution because of the anisotropy in the horizontal plane. The major axis of the ellipse is parallel to the direction of the isotropic plane of the HTI media, and the minor axis of the ellipse is parallel to the direction of the symmetry axis of the HTI media. And the ratio of the major axis to the minor axis is proportional to the strength of anisotropy. In reality, if a microseismic source is located, we can pick out the same phases with the same offset but at different azimuth angles in the surface array and compare the travel-time of these phases. As dense surface array

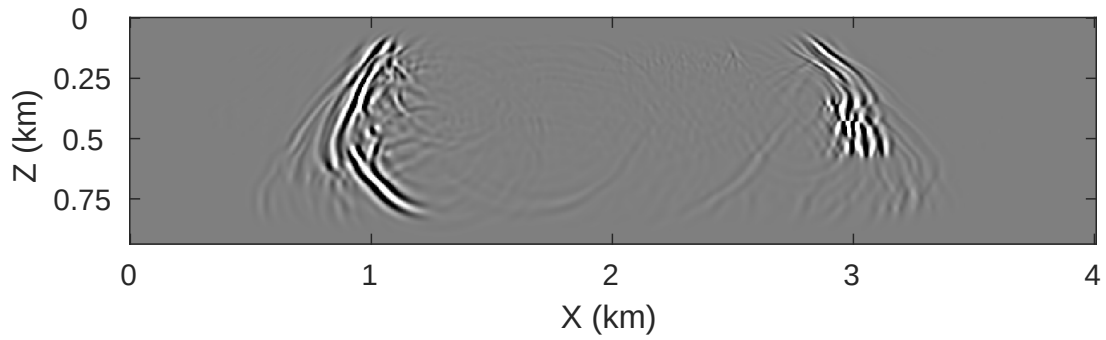

(a)

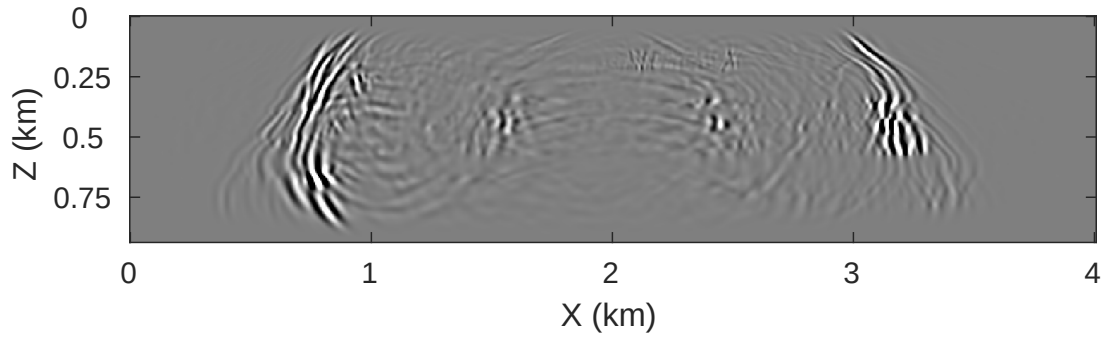

(b)

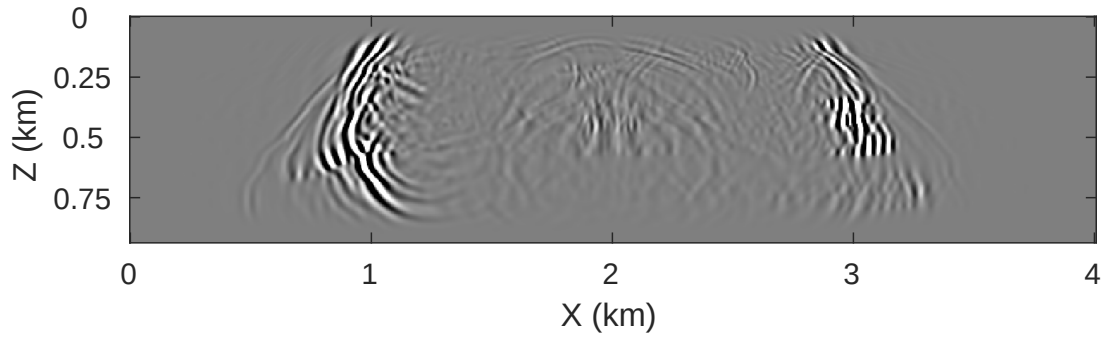

(c)

Figure 2.23: Wavefield snapshots of velocity component in Y direction at 0.49 s and y=2 km. (a) Isotropic case. (b) VTI case. (c) HTI case

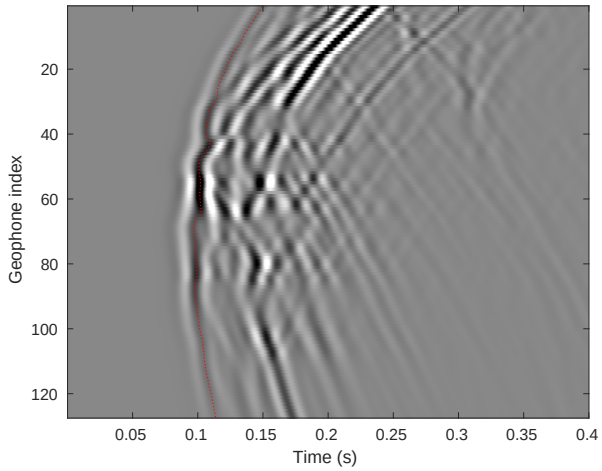

(a)

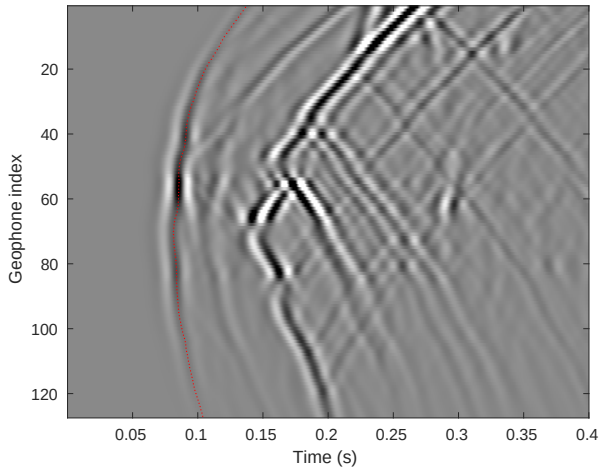

(b)

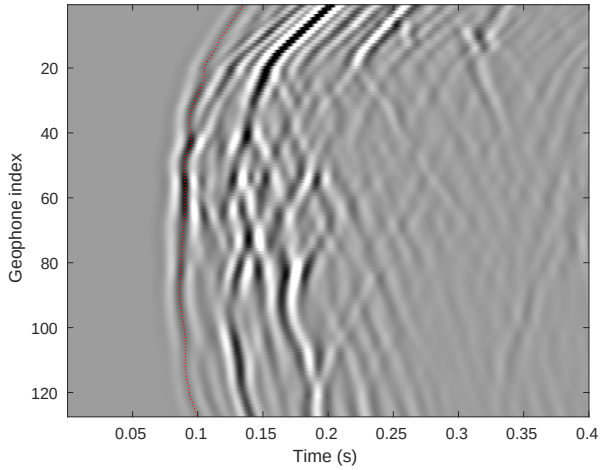

(c)

Figure 2.24: The recorded seismograms in the downhole array for the (a) isotropic, (b) VTI and (c) HTI model. Red dotted lines represent the automatically picked direct P-wave wavefronts

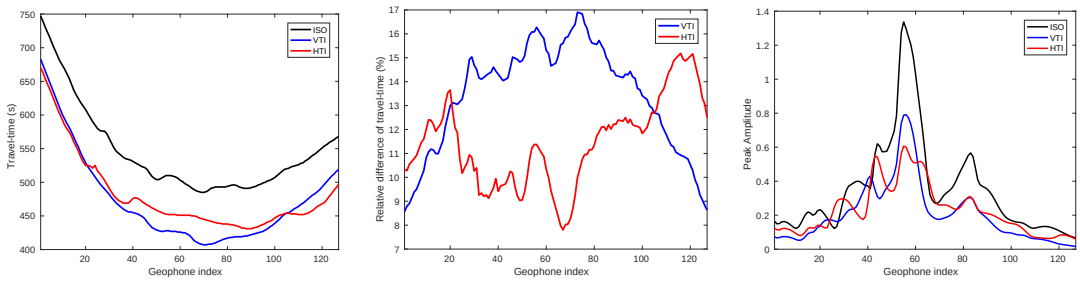

(a) (b) (c)

Figure 2.25: Comparisons of travel-times and peak amplitudes of the direct P-wave for the isotropic, VTI and HTI model. Dark solid line represents value in the isotropic model; blue solid line represents value in the VTI model; red solid line represents value in the HTI model. (a) Travel-times of the direct P-wave. (b) Relative travel-time differences of the VTI and HTI model with respect to the isotropic model. (c) Peak amplitudes of the direct P-wave

with wide-azimuth is increasingly used in the microseismic monitoring, it is not hard to find receivers which have the same offset but different azimuth angles. Thus in this way, we can estimate the orientation and density of the fractures using surface array in microseismic monitoring when the seismic anisotropy is caused by the vertical cracks induced by hydraulic fracturing. Through analyzing anisotropy using surface array data of different events during hydraulic fracturing, we can also evaluate the fracturing effect and gain more knowledge about the fracturing process. Even though the ray path in different azimuth is different due to horizontal heterogeneity, the travel-time is not affected too much by the ray path. The influence of seismic anisotropy in travel-times is still observable and is more significant at relatively large offsets. This demonstrates it is feasible to estimate the seismic anisotropy of complex subsurface media using surface arrays. Seismic anisotropy obtained using surface array has been extensively used for fracture detection in exploration geophysics (Bakulin et al., 2000, Wang et al., 2007, Bachrach et al., 2009). Effective anisotropy parameters and fracture characteristics can also be extracted from the microseismic surface monitoring (Wuestefeld et al., 2010, Zhang et al., 2013). The polarization of the direct P-wave is not seriously affected by anisotropy. However, the variation in amplitude caused by anisotropy could introduce biases in moment tensor inversion.

2.4 Discussions and Conclusion

The primary focus of this study was to develop an efficient FD forward modeling tool with arbitrary moment tensor source, which can be used for simulating wave propagation in anisotropic media for microseismic monitoring. We have shown how to implement an symmetrical moment tensor source into the staggered-grid FD modeling scheme. We simulated and analyzed the wavefields in both a 3D layered and a 3D overthrust anisotropic model using surface and downhole arrays. Because both VTI and

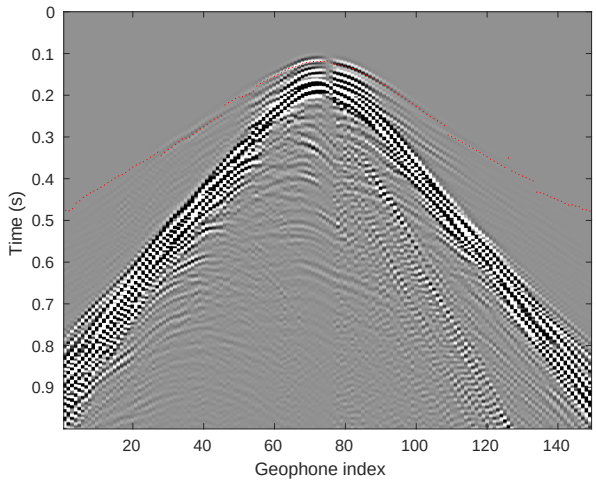

(a)

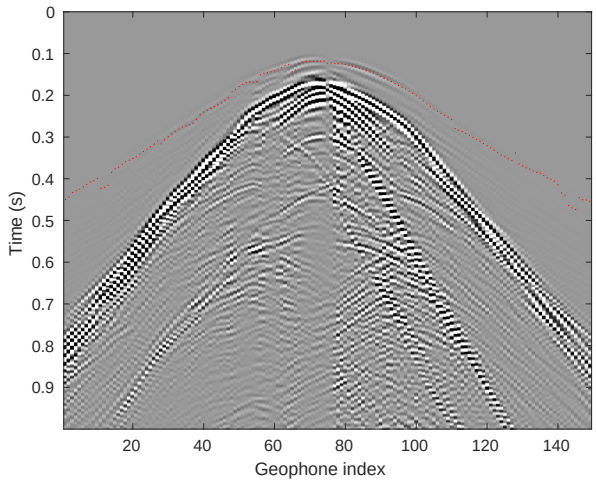

(b)

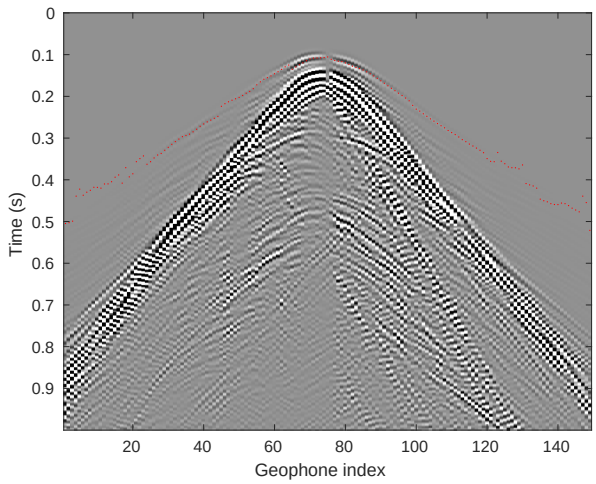

(c)

Figure 2.26: The recorded seismic profiles in the surface array for the (a) isotropic, (b) VTI and (c) HTI model at the 70th receiver line in Y direction. Red dotted lines represent the automatically picked direct P-wave wavefronts

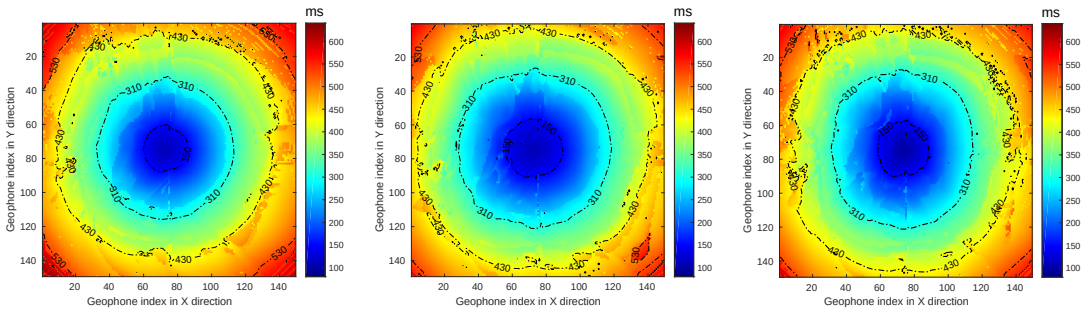

Figure 2.27: Travel-times of the direct P-wave in the (a) isotropic, (b) VTI and (c) HTI model for the surface array. The contour lines of travel-times are also displayed in the figure. The unit of time in these figures is millisecond

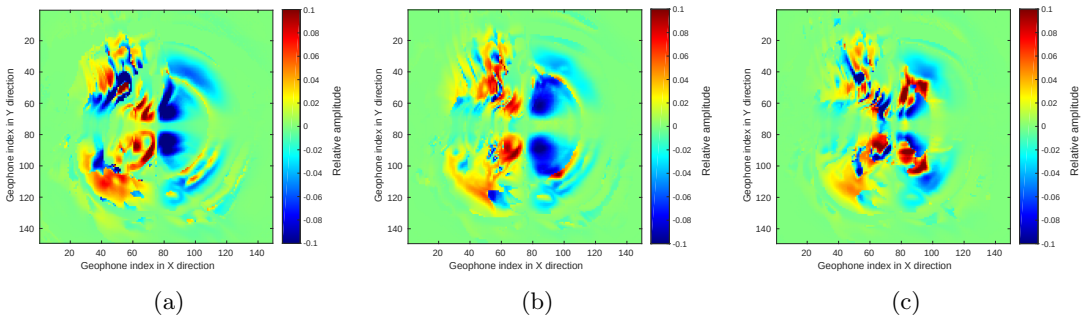

Figure 2.28: Peak amplitudes of the direct P-wave in the (a) isotropic, (b) VTI and (c) HTI model for the surface array

HTI anisotropy are common in shale or fractured media, we focused only on wavefields in VTI, HTI and orthorhombic media.

Seismic anisotropy will make the recorded wavefield more complex and distort the amplitudes and arrival times of the P- and S-waves, thus making microseismic imaging difficult. The retrieval of seismic anisotropy from microseismic data is very helpful for characterizing the stimulated fracture properties in hydraulic fracturing. In practice, the effect of seismic anisotropy, source radiation pattern and geological structure on recorded wavefields may be difficult to separate. Therefore, trade-off among these effects may exist when analyzing real microseismic data. In practice, the sensitivity and trade-off analysis should be performed on a case-by-case basis at each monitoring operation. An accurate velocity model is favorable for anisotropy analysis and moment tensor inversion. Many methods have been put forward to obtain a highly accurate velocity model, such as full waveform inversion (Tarantola, 2005), but on the basis of accurate forward modeling. The joint source location, mechanism determination and velocity inversion is also a promising way to obtain more practical solutions. By simultaneously using source location, mechanism and velocity information to minimize the misfit relative to recorded wavefields, a better solution can be found with less trade-off among these properties. All these methods require the kind of anisotropic FWM we demonstrate here.

Most shale reservoirs in which hydraulic fracturing is often implemented have sub-horizontal bedding, where the beds also show sub-horizontal fabrics. Therefore, VTI can be a good approximation for this kind of anisotropy (Helbig & Thomsen, 2005, Kendall et al., 2007, Sone & Zoback, 2013). Reflection seismic and borehole data can give a good control on the dips of beds, and also fracture orientations, which tend to be sub-vertical. Therefore, although we only simulate and analyze full wavefields in VTI and HTI media, both of these cases are often quite well constrained in practice. However, the combination of bedding/lattice-preferred-orientation (LPO) and fractures gives a lower symmetry to the anisotropy (orthorhombic), which can also be well simulated using our modeling tool. Apart from HTI, VTI and orthorhombic anisotropy, the subsurface can be more complex, such as TTI, monoclinic and general anisotropy. The wave propagation phenomena in these complex media will be more complicated. However, our FWM tool can be easily expanded to incorporate the general anisotropy, which can help promote the full anisotropic interpretation and inversion of field data. In addition, seismic anisotropy in combination with complex velocity heterogeneity will also make the interpretation and inversion of realistic data more difficult. Therefore, the full anisotropy interpretation and inversion of field data still need further development. Shear-wave splitting analysis (Crampin & Peacock, 2008, Verdon et al., 2009) is a powerful way to separate the shear-waves and provide anisotropic information of the subsurface, such as fracture alignment, density and aspect-ratio.

Panza & Saraò (2000) pointed out that poor station coverage, mislocation of the

hypocenter, noise and inadequate structural model can cause spurious non-double-couple mechanisms. When conducting real data analysis, error analysis based on synthetic full waveform tests must be performed to estimate the reliability of the source mechanism solutions. In addition, Vavryčuk (2004) proposed an inversion method to retrieve seismic anisotropy from non-double-couple components of seismic moment tensors. Unlike most anisotropy analysis methods which retrieve an overall anisotropy along a whole ray path, this inversion method can obtain the anisotropy just in the focal area. However, this inversion method requires obtaining highly accurate source moment tensor in anisotropic media. Therefore, it is necessary and important to develop an anisotropic modeling tool with arbitrary moment tensor source for testing, analyzing and benchmarking. Our FWM method provides an efficient modeling tool to generate and analyze the microseismic full wavefield with full moment tensor source in anisotropic media. The modeling feature in seismic anisotropy and arbitrary moment tensor source can help to conduct anisotropic full waveform inversion, anisotropy analysis and full moment tensor inversion.

In the complex overthrust model, when analyzing travel-time differences, we did not eliminate the influence of ray path differences as we did in the layered model. However, the variation trends of travel-time differences with respect to take-off angle in VTI and HTI anisotropic scenarios are still established in the downhole array. And the variation of travel-time in the surface array also exhibits the same phenomenon as with the layered model. This is because the anisotropy is strong enough (as is often the case in shale or fracture-enriched layer) that the influence of velocity variation surmounts that of ray path differences in travel-time. However, when the variation of ray path is significant or the anisotropy is weak, the influence of ray path must be considered and eliminated in order to correctly evaluate the anisotropy. This will involve ray tracing in heterogeneous and/or anisotropic media.

Seismic anisotropy is an important property of shale rocks, where most hydraulic fracturing is implemented. The fracture networks induced by hydraulic fracturing are also responsible for seismic anisotropy in the subsurface. We have shown that seismic anisotropy can have a significant influence on travel-time and amplitude of the recorded seismic waves, thus contributing to larger deviations in source location and moment tensor inversion in microseismic monitoring. These variations in travel-time and amplitude caused by seismic anisotropy can also be used to evaluate the anisotropy of the subsurface, especially for estimating the strength of anisotropy in HTI media using surface array. In vertical downhole array, the travel-time differences of direct P-waves will normally increase with the take-off angle of the seismic rays in VTI media, while the travel-time differences of direct P-waves will normally decrease with the take-off angle of the seismic rays in HTI media. In surface array, the travel-times of direct P-wave exhibit a circular distribution in isotropic and VTI media, while the travel-times of direct P-wave exhibit an elliptical distribution in HTI media. The strength of seismic

anisotropy can be estimated by calculating the ratio of the major axis of the ellipse to the minor axis of the ellipse. The direction of the symmetry axis of the HTI media (i.e., the orientation of fracture planes) can also be estimated through identifying the direction of the major axis of the ellipse. The fracturing effect can also be evaluated through anisotropy analysis of different events in hydraulic fracturing. Although the polarization of direct waves is less affected by anisotropy, the deviation in source location will be accumulated into the source mechanism determination and make source mechanism determination problematic. Since we have focused on full waveform modeling in heterogeneous and anisotropic media in this paper, a quantitative analysis of the influence of anisotropy on microseismic source location is not robustly studied.

Compared with surface array, downhole array is more vulnerable to seismic anisotropy. Thus extra care should be taken when conducting microseismic monitoring in anisotropic media using downhole array. Analyzing seismic anisotropy of the recorded microseismic data provides a feasible way to evaluate the fracture networks induced by hydraulic fracturing, and can also improve the accuracy of microseismic source location and mechanism characterization.

Acknowledgements

We are grateful to the anonymous reviewers who have provided many constructive comments to improve the manuscript. We also wish to thank Institute of Applied Geoscience and Institute of Geophysics and Tectonics, University of Leeds for supporting this work. The work of P. Shi is supported by a China Scholarship Council/University of Leeds scholarship. A. Nowacki is supported by a Leverhulme Early Career Fellowship.

Appendix 1: Moment Tensor Source Radiation Pattern

A seismic moment tensor is the combination of nine generalized couple forces which have three possible directions and act on three possible arms. It can be used to simulate seismic sources which have body-force equivalent given by pairs of forces. The seismic moment tensor source equivalent has been verified by the radiation patterns of teleseismic data and also seismic data obtained very close to the source region (Aki & Richards, 2002). A common seismic moment tensor can be expressed as

$$\mathbf{m} = \begin{pmatrix} m_{xx} & m_{xy} & m_{xz} \\ m_{yx} & m_{yy} & m_{yz} \\ m_{zx} & m_{zy} & m_{zz} \end{pmatrix}. \tag{2.9}$$

The source radiation pattern of P- and S-waves can be derived from the Green's function in an isotropic elastic medium (Aki & Richards, 2002). For far-field P-waves,

the radiation pattern is given by

$$R_n^p = \gamma_n \gamma_p \gamma_q m_{pq}. \tag{2.10}$$

For far-field S-waves, the radiation pattern is given by

$$R_n^s = -(\gamma_n \gamma_p - \delta_{np}) \gamma_q m_{pq}. \tag{2.11}$$

In these equations, R_n represents the nth component of the radiation pattern vector for P- or S-wave, γ_p is the direction cosine of the source-receiver unit direction vector, m_{pq} is the moment tensor component. Implicit summation over the repeated index is applied in these equations.

If using the unit basis vectors in spherical coordinates, then we can further obtain the radiation pattern for P-waves (Chapman, 2004)

$$\begin{aligned} R^p = &\left(m_{xx}\cos^2\phi + m_{yy}\sin^2\phi + m_{xy}\sin 2\phi\right)\sin^2\theta \\ &+ m_{zz}\cos^2\theta + (m_{zx}\cos\phi + m_{yz}\sin\phi)\sin 2\theta, \end{aligned} \tag{2.12}$$

for SV-waves

$$\begin{aligned} R^{sv} = \frac{1}{2}&\left(m_{xx}\cos^2\phi + m_{yy}\sin^2\phi - m_{zz} + m_{xy}\sin 2\phi\right)\sin 2\theta \\ &+ (m_{zx}\cos\phi + m_{yz}\sin\phi)\cos 2\theta, \end{aligned} \tag{2.13}$$

for SH-waves

$$R^{sh} = \left(\frac{1}{2}(m_{yy} - m_{xx})\sin 2\phi + m_{xy}\cos 2\phi\right)\sin\theta + (m_{yz}\cos\phi - m_{zx}\sin\phi)\cos\theta, \tag{2.14}$$

in which θ and ϕ represent the coordinate components (polar angle and azimuth angle) in the spherical coordinates, respectively.

Appendix 2: Analytical Solutions in Homogeneous Isotropic Medium

The displacement field in a homogeneous isotropic medium can be obtained by convolving the Green's function with the seismic moment tensor (Aki & Richards, 2002, Equation 4.29)

$$\begin{aligned} u_n = M_{pq} * G_{np,q} = R_n^{ne}\frac{M_0}{4\pi\rho r^4}\int_{r/v_p}^{r/v_s} \tau S(t-\tau)d\tau + R_n^{ip}\frac{M_0}{4\pi\rho v_p^2 r^2}S\left(t - r/v_p\right) \\ + R_n^{is}\frac{M_0}{4\pi\rho v_s^2 r^2}S\left(t - r/v_s\right) + R_n^{fp}\frac{M_0}{4\pi\rho v_p^3 r}\dot{S}\left(t - r/v_p\right) + R_n^{fs}\frac{M_0}{4\pi\rho v_s^3 r}\dot{S}\left(t - r/v_s\right), \end{aligned} \tag{2.15}$$

where u_n is the nth component of displacement field, r is the distance between source point and receiver point, $G_{np,q}$ is the Green's function describing the wave propagation between source and receiver, R_n^{ne}, R_n^{ip}, R_n^{is}, R_n^{fp}, R_n^{fs} are near-field, intermediate-field P-wave, intermediate-field S-wave, far-field P-wave, far-field S-wave radiation pattern, respectively. The comma indicates the spatial derivative with respect to the coordinate after the comma (e.g., $G_{np,q} = \partial G_{np}/\partial q$), and the dot above the source time function $S(t)$ indicates the time derivative. Thus, the displacement field in the far-field is proportional to particle velocities at the source. The elastic properties of the medium are described by density ρ, P-wave velocity v_p and S-wave velocity v_s.

The first term in equation 2.15 is called the near-field term, which is proportional to $r^{-4}\int_{r/v_p}^{r/v_s}\tau S(t-\tau)d\tau$ (hereafter referred to as the proportional part of near-field term). The two middle terms are called the intermediate-field terms, which are proportional to $(vr)^{-2}S(t-r/v)$. The last two terms are called the far-field terms, which are proportional to $v^{-3}r^{-1}\dot{S}(t-r/v)$. Since there is no intermediate-field region where only the intermediate-field terms dominate, it is common to combine the intermediate-field and near-field terms. If a Ricker wavelet $S(t) = (1-2\pi^2 f_m^2 t^2)e^{-\pi^2 f_m^2 t^2}$ (f_m is the peak frequency of the wavelet) is used as the source time function, the integration in the near-field term is very small and its peak amplitude is approximately proportional to r/f_m with ratio often smaller than 10^{-6} in SI units. The derivative term of the source time function in the far-field terms is much larger than the Ricker wavelet and its integration, and its peak amplitude is approximately proportional to f_m with an approximate ratio of 6.135 for Ricker wavelet.

Appendix 3: Distortion of Near- and Far-Field Due to Source Radiation Pattern

Normally, the near- and far-field are just defined using source-receiver distance and seismic wavelength. However, through examining equation 2.15 and numerical experiments, we find that the near- and far-field are also influenced by source radiation patters. Figure 2.29(a) shows the relative magnitude of peak amplitude of the proportional part of the near-field term, intermediate-field terms and far-field terms at different source-receiver distances. The elastic parameters of the medium used are $v_p = 3500\ m/s$, $v_s = 2000\ m/s$ and $\rho = 2400\ kg/m^3$. The source time function is a Ricker wavelet with a peak frequency of 40 Hz and a time delay of $1.1/f_m$. The X-axis of Figure 2.29(a) is the ratio of the source-receiver distance to the dominant S-wave wavelength. It is obvious that at a distance larger than three or four dominant S-wave wavelengths, the far-field term dominates the wavefield (with a proportion higher than 95%). This far-field approximation is quite pervasive in microseismic monitoring because of the widely used ray-based methods and relatively high dominant frequencies of the recorded data. Furthermore, most focal mechanism inversion methods are also

based on the far-field approximation. However, at a distance less than two dominant S-wave wavelengths, the near-field terms and intermediate-field terms will have a non-negligible effect on the whole wavefield and may even dominate the wavefield, especially when very close to the source region (less than one half the dominant S-wave wavelength). For microseismic downhole monitoring arrays, which are deployed close to the microseismic source area, larger errors may occur due to the significant contribution of the near-field and intermediate-field terms.

The far-field approximation is not only related to the source-receiver distance but also the radiation patterns of the near-field terms (including intermediate-terms hereafter) and far-field terms. In directions where the strength of the far-field radiation pattern is weaker than the strength of the near-field radiation pattern, the contribution of near-field terms may bias the far-field approximation in the "far" field. Figure 2.29(b) is a 3D map which shows the far-field distance of a 45° dip-slip double-couple source ($m_{xx} = -m_{zz}$ and other components are 0) in different directions. The elastic property of the medium is the same as before. The far-field distance is expressed in terms of S-wave wavelength. The color and shape in the figure shows the distance where the far-field terms will occupy 80% energy in the whole wavefield. Beyond this distance, we can consider that the far-field terms dominate the wavefield. Figure 2.29(b) reveals an obvious directional feature. If there were no difference in radiation pattern between the far-field and near-field terms, Figure 2.29(b) would show an uniform spherical distribution in different directions. However the difference in radiation patterns has distorted the scope where the near-field could exert influence on the wavefield. In directions where the near-field radiation pattern is strong and the far-field radiation is weak, the distance in which the near-field terms have a non-negligible influence on the whole wavefield has been extended. The far-field distance in different directions in Figure 2.29(b) ranges from about 2 times the dominant S-wave wavelength to 12 times the dominant S-wave wavelength. Thus, great care must be taken when receivers have been deployed in these directions. Figure 2.29(c) shows the variation of relative magnitude in two specific directions for the same double-couple source. The radiation patterns of the near-, intermediate- and far-field terms have been taken into consideration. When considering the source radiation pattern, the far-field distance shows strong dependence on directions. The far-field distance has been extended to 12 times the dominant S-wave wavelength in direction of 5° zenith angle and 0° azimuth angle (shown as the dashed lines). The far-field terms need a farther distance to dominate in the whole wavefield. This example demonstrates that the far-field distance is changed and is also affected by source radiation patterns. For microseismic monitoring, the receivers are normally deployed near microseismic events, especially for the downhole array. Therefore, the influence of source radiation patterns to far-field distance must be taken into consideration. When source-receiver geometry, source moment tensor and media elastic parameters are defined, the far-field distance in different directions where

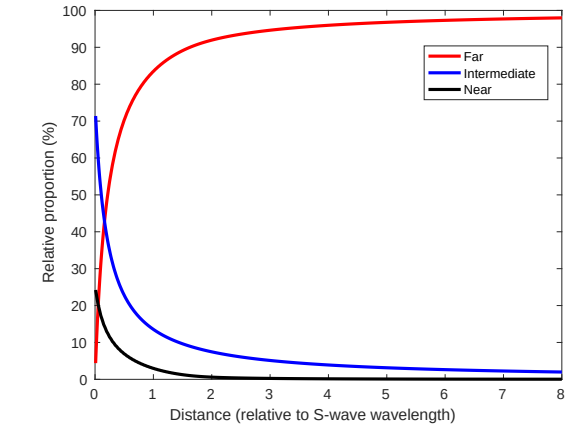

(a)

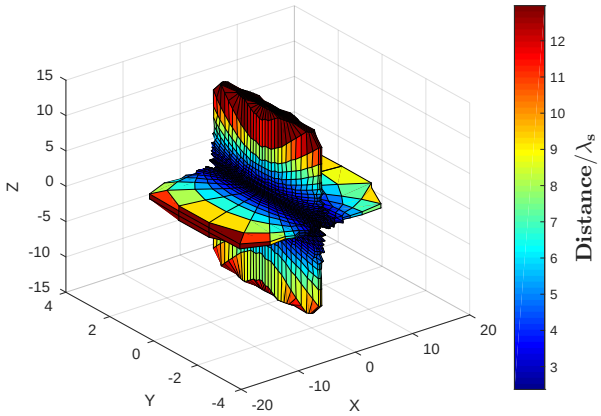

(b)

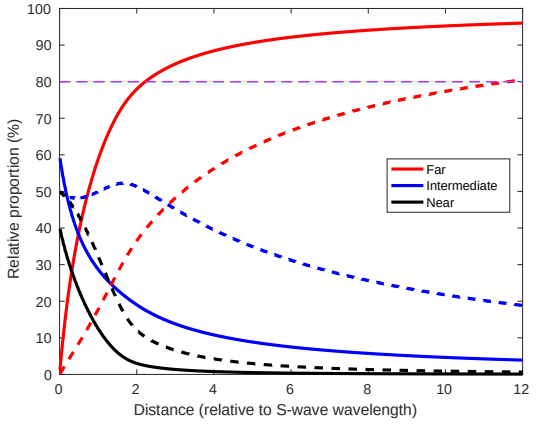

(c)

Figure 2.29: (a) Relative magnitude of peak amplitude of the proportional part for near-field term, intermediate-field terms and far-field terms under certain parameters. (b) 3D map which shows the far-field distance in terms of S-wave wavelength in different directions for a 45° dip-slip double-couple source. Beyond this far-field distance, the far-field terms will occupy more than 80% energy in the whole wavefield. (c) Relative magnitude of wavefields for near-field term, intermediate-field S-wave term and far-field S-wave term for a double-couple source in different directions. The solid lines show the scenario in direction which has a zenith angle of 45° and azimuth angle of 0°. The dashed lines show the scenario in direction which has a zenith angle of 5° and azimuth angle of 0°

the far-field approximation is acceptable can be quantitatively evaluated. This will be very helpful for array deployment and data interpretation in microseismic monitoring.

References

Aboudi, J., 1971. Numerical simulation of seismic sources, *Geophysics*, **36**(5), 810–821. 2.2.4

Aki, K. & Richards, P. G., 2002. *Quantitative seismology*, vol. 1, University Science Books. 2.1, 2.4, 2.4, 2.4

Al-Harrasi, O., Al-Anboori, A., Wüstefeld, A., & Kendall, J.-M., 2011. Seismic anisotropy in a hydrocarbon field estimated from microseismic data, *Geophys. Prospect.*, **59**(2), 227–243. 2.1

Alterman, Z. & Karal, F., 1968. Propagation of elastic waves in layered media by finite difference methods, *Bull. Seismol. Soc. Am.*, **58**(1), 367–398. 2.1

Aminzadeh, F., Jean, B., & Kunz, T., 1997. *3-D salt and overthrust models*, Society of Exploration Geophysicists. 2.3.2

Angus, D., Aljaafari, A., Usher, P., & Verdon, J., 2014. Seismic waveforms and velocity model heterogeneity: Towards a full-waveform microseismic location algorithm, *J. Appl. Geophys.*, **111**, 228–233. 2.1

Artman, B., Podladtchikov, I., & Witten, B., 2010. Source location using time-reverse imaging, *Geophys. Prospect.*, **58**(5), 861–873. 2.1

Babuska, V. & Cara, M., 1991. *Seismic anisotropy in the Earth*, vol. 10, Springer Science & Business Media. 2.3.1

Bachrach, R., Sengupta, M., Salama, A., & Miller, P., 2009. Reconstruction of the layer anisotropic elastic parameters and high-resolution fracture characterization from P-wave data: a case study using seismic inversion and Bayesian rock physics parameter estimation, *Geophys. Prospect.*, **57**(2), 253–262. 2.3.2

Bakulin, A., Grechka, V., & Tsvankin, I., 2000. Estimation of fracture parameters from reflection seismic dataPart I: HTI model due to a single fracture set, *Geophysics*, **65**(6), 1788–1802. 2.3.2

Baysal, E., Kosloff, D. D., & Sherwood, J. W., 1983. Reverse time migration, *Geophysics*, **48**(11), 1514–1524. 2.1

Bohlen, T., 2002. Parallel 3-D viscoelastic finite difference seismic modelling, *Comput. Geosci.*, **28**(8), 887–899. 2.1

Boyd, O. S., 2006. An efficient Matlab script to calculate heterogeneous anisotropically elastic wave propagation in three dimensions, *Comput. Geosci.*, **32**(2), 259–264. 2.1

Brzak, K., Gu, Y. J., Ökeler, A., Steckler, M., & Lerner-Lam, A., 2009. Migration imaging and forward modeling of microseismic noise sources near southern Italy, *Geochem. Geophys. Geosyst.*, **10**(1). 2.1

Cesca, S., Rohr, A., & Dahm, T., 2013. Discrimination of induced seismicity by full moment tensor inversion and decomposition, *J. Seismol.*, **17**(1), 147–163. 2.1

Chambers, K., Dando, B. D., Jones, G. A., Velasco, R., & Wilson, S. A., 2014. Moment tensor migration imaging, *Geophys. Prospect.*, **62**(4), 879–896. 2.1

Chapman, C., 2004. *Fundamentals of seismic wave propagation*, Cambridge university press. 2.4

Coutant, O., Virieux, J., & Zollo, A., 1995. Numerical source implementation in a 2D finite difference scheme for wave propagation, *Bull. Seismol. Soc. Am.*, **85**(5), 1507–1512. 2.2.4

Crampin, S. & Peacock, S., 2008. A review of the current understanding of seismic shear-wave splitting in the Earths crust and common fallacies in interpretation, *Wave Motion*, **45**(6), 675–722. 2.3.1, 2.4

Dong, Z. & McMechan, G. A., 1995. 3-D viscoelastic anisotropic modeling of data from a multicomponent, multiazimuth seismic experiment in northeast Texas, *Geophysics*, **60**(4), 1128–1138. 2.2.2

Foulger, G., Julian, B., Hill, D., Pitt, A., Malin, P., & Shalev, E., 2004. Non-double-couple microearthquakes at Long Valley caldera, California, provide evidence for hydraulic fracturing, *J. Volcanol. Geotherm. Res.*, **132**(1), 45–71. 2.1

Gajewski, D. & Tessmer, E., 2005. Reverse modelling for seismic event characterization, *Geophys. J. Int.*, **163**(1), 276–284. 2.1

Graves, R. W., 1996. Simulating seismic wave propagation in 3D elastic media using staggered-grid finite differences, *Bull. Seismol. Soc. Am.*, **86**(4), 1091–1106. 2.2.4

Grechka, V. & Yaskevich, S., 2013a. Azimuthal anisotropy in microseismic monitoring: A Bakken case study, *Geophysics*, **79**(1), KS1–KS12. 2.1

Grechka, V. & Yaskevich, S., 2013b. Inversion of microseismic data for triclinic velocity models, *Geophys. Prospect.*, **61**(6), 1159–1170. 2.1

Grechka, V., Singh, P., & Das, I., 2011. Estimation of effective anisotropy simultaneously with locations of microseismic events, *Geophysics*, **76**(6), WC143–WC155. 2.1

Helbig, K. & Thomsen, L., 2005. 75-plus years of anisotropy in exploration and reservoir seismics: A historical review of concepts and methods, *Geophysics*. 2.4

Hobro, J., Williams, M., & Calvez, J. L., 2016. The finite-difference method in microseismic modeling: Fundamentals, implementation, and applications, *The Leading Edge*, **35**(4), 362–366. 2.1

Holberg, O., 1987. Computational aspects of the choice of operator and sampling interval for numerical differentiation in large-scale simulation of wave phenomena, *Geophys. Prospect.*, **35**(6), 629–655. 2.2.2

Jin, S., Jiang, F., & Zhu, X., 2013. Viscoelastic modeling with simultaneous microseismic sources, in *SEG Technical Program Expanded Abstracts 2013*, pp. 3355–3359, Society of Exploration Geophysicists. 2.1

Johnston, J. E. & Christensen, N. I., 1995. Seismic anisotropy of shales, *J. Geophys. Res.*, **100**(B4), 5991–6003. 2.1

Jost, M. u. & Herrmann, R., 1989. A students guide to and review of moment tensors, *Seismol. Res. Lett.*, **60**(2), 37–57. 2.1

Julian, B. R., Miller, A. D., & Foulger, G., 1998. Non-double-couple earthquakes 1. Theory, *Rev. Geophys.*, **36**(4), 525–549. 2.1

Kawakatsu, H. & Montagner, J.-P., 2008. Time-reversal seismic-source imaging and moment-tensor inversion, *Geophys. J. Int.*, **175**(2), 686–688. 2.1

Kelly, K., Ward, R., Treitel, S., & Alford, R., 1976. Synthetic seismograms: A finite-difference approach, *Geophysics*, **41**(1), 2–27. 2.1

Kendall, J.-M., Fisher, Q., Crump, S. C., Maddock, J., Carter, A., Hall, S., Wookey, J., Valcke, S., Casey, M., Lloyd, G., et al., 2007. Seismic anisotropy as an indicator of reservoir quality in siliciclastic rocks, *Geol. Soc. London Spec. Publ.*, **292**(1), 123–136. 2.4

King, A. & Talebi, S., 2007. Anisotropy effects on microseismic event location, *Pure Appl. Geophys.*, **164**(11), 2141–2156. 2.3.1

Kosloff, D., Queiroz Filho, A., Tessmer, E., & Behle, A., 1989. Numerical solution of the acoustic and elastic wave equations by a new rapid expansion method, *Geophys. Prospect.*, **37**(4), 383–394. 2.2.4

Lele, S. K., 1992. Compact finite difference schemes with spectral-like resolution, *J. Comput. Phys.*, **103**(1), 16–42. 2.2.2

Li, D., Helmberger, D., Clayton, R. W., & Sun, D., 2014. Global synthetic seismograms using a 2-D finite-difference method, *Geophys. J. Int.*, **197**(2), 1166–1183. 2.2.4, 2.2.4

Li, H., Wang, R., & Cao, S., 2015. Microseismic forward modeling based on different focal mechanisms used by the seismic moment tensor and elastic wave equation, *J. Geophys. Eng.*, **12**(2), 155. 2.1

Li, J., Sadi Kuleli, H., Zhang, H., & Nafi Toksöz, M., 2011. Focal mechanism determination of induced microearthquakes in an oil field using full waveforms from shallow and deep seismic networks, *Geophysics*, **76**(6), WC87–WC101. 2.1

Linzer, L., Mhamdi, L., & Schumacher, T., 2015. Application of a moment tensor inversion code developed for mining-induced seismicity to fracture monitoring of civil engineering materials, *J. Appl. Geophys.*, **112**, 256–267. 2.1

Lisitsa, V. & Vishnevskiy, D., 2010. Lebedev scheme for the numerical simulation of wave propagation in 3D anisotropic elasticity, *Geophys. Prospect.*, **58**(4), 619–635. 2.2.2

Liu, Y. & Sen, M. K., 2009. An implicit staggered-grid finite-difference method for seismic modelling, *Geophys. J. Int.*, **179**(1), 459–474. 2.2.2

Long, M. D. & Silver, P. G., 2009. Shear wave splitting and mantle anisotropy: measurements, interpretations, and new directions, *Surv. Geophys.*, **30**(4-5), 407–461. 2.3.1

Michéa, D. & Komatitsch, D., 2010. Accelerating a three-dimensional finite-difference wave propagation code using GPU graphics cards, *Geophys. J. Int.*, **182**(1), 389–402. 2.1

Miller, A. D., Foulger, G., & Julian, B. R., 1998. Non-double-couple earthquakes 2. Observations, *Rev. Geophys.*, **36**(4), 551–568. 2.1

Moczo, P., Kristek, J., Vavryčuk, V., Archuleta, R. J., & Halada, L., 2002. 3D heterogeneous staggered-grid finite-difference modeling of seismic motion with volume harmonic and arithmetic averaging of elastic moduli and densities, *Bull. Seismol. Soc. Am.*, **92**(8), 3042–3066. 2.1

Moczo, P., Kristek, J., & Gális, M., 2014. *The finite-difference modelling of earthquake motions: Waves and ruptures*, Cambridge University Press. 2.1

Montagner, J.-P., 1998. Where can seismic anisotropy be detected in the Earth's mantle? In boundary layers..., *Pure Appl. Geophys.*, **151**(2-4), 223. 2.2.1

Nakata, N. & Beroza, G. C., 2016. Reverse time migration for microseismic sources using the geometric mean as an imaging condition, *Geophysics*, **81**(2), KS51–KS60. 2.1

Narayan, J., 2001. Site-specific strong ground motion prediction using 2.5-D modelling, *Geophys. J. Int.*, **146**(2), 269–281. 2.2.4, 2.2.4

Nowacki, A., Wookey, J., & Kendall, J.-M., 2011. New advances in using seismic anisotropy, mineral physics and geodynamics to understand deformation in the lowermost mantle, *J. Geodyn.*, **52**(3), 205–228. 2.2.1

O'Brien, G., Lokmer, I., De Barros, L., Bean, C. J., Saccorotti, G., Metaxian, J.-P., & Patané, D., 2011. Time reverse location of seismic long-period events recorded on Mt Etna, *Geophys. J. Int.*, **184**(1), 452–462. 2.1

Panza, G. F. & Saraò, A., 2000. Monitoring volcanic and geothermal areas by full seismic moment tensor inversion: Are non-double-couple components always artefacts of modelling?, *Geophys. J. Int.*, **143**(2), 353–364. 2.4

Pitarka, A., 1999. 3D elastic finite-difference modeling of seismic motion using staggered grids with nonuniform spacing, *Bull. Seismol. Soc. Am.*, **89**(1), 54–68. 2.2.4, 2.2.4

Robertsson, J. O., van Manen, D.-J., Schmelzbach, C., Van Renterghem, C., & Amundsen, L., 2015. Finite-difference modelling of wavefield constituents, *Geophys. J. Int.*, **203**(2), 1334–1342. 2.1

Rössler, D., Rümpker, G., & Krüger, F., 2004. Ambiguous moment tensors and radiation patterns in anisotropic media with applications to the modeling of earthquake mechanisms in W-Bohemia, *Stud. Geophys. Geod.*, **48**(1), 233–250. 2.1

Rüger, A., 1997. P-wave reflection coefficients for transversely isotropic models with vertical and horizontal axis of symmetry, *Geophysics*, **62**(3), 713–722. 2.2.1

Sadri, M. & Riahi, M., 2010. Ray tracing and amplitude calculation in anisotropic layered media, *Geophys. J. Int.*, **180**(3), 1170–1180. 2.3.1

Saenger, E. H., Gold, N., & Shapiro, S. A., 2000. Modeling the propagation of elastic waves using a modified finite-difference grid, *Wave Motion*, **31**(1), 77–92. 2.1, 2.2.2

Saenger, E. H., Kocur, G. K., Jud, R., & Torrilhon, M., 2011. Application of time reverse modeling on ultrasonic non-destructive testing of concrete, *Appl. Math. Model.*, **35**(2), 807–816. 2.1

Sayers, C. M., 1998. Misalignment of the orientation of fractures and the principal axes for P and S waves in rocks containing multiple non-orthogonal fracture sets, *Geophys. J. Int.*, **133**(2), 459–466. 2.2.1

Schoenberg, M. & Sayers, C. M., 1995. Seismic anisotropy of fractured rock, *Geophysics*, **60**(1), 204–211. 2.1

Sheriff, R. E. & Geldart, L. P., 1995. *Exploration seismology*, Cambridge university press. 2.1, 2.2.1

Šílenỳ, J. & Milev, A., 2008. Source mechanism of mining induced seismic eventsresolution of double couple and non double couple models, *Tectonophysics*, **456**(1), 3–15. 2.1

Šílenỳ, J., Hill, D. P., Eisner, L., & Cornet, F. H., 2009. Non–double-couple mechanisms of microearthquakes induced by hydraulic fracturing, *J. Geophys. Res.*, **114**(B8). 2.1

Sone, H. & Zoback, M. D., 2013. Mechanical properties of shale-gas reservoir rocksPart 1: Static and dynamic elastic properties and anisotropy, *Geophysics*. 2.4

Song, F. & Toksöz, M. N., 2011. Full-waveform based complete moment tensor inversion and source parameter estimation from downhole microseismic data for hydrofracture monitoring, *Geophysics*, **76**(6), WC103–WC116. 2.1

Steiner, B., Saenger, E. H., & Schmalholz, S. M., 2008. Time reverse modeling of low-frequency microtremors: Application to hydrocarbon reservoir localization, *Geophys. Res. Lett.*, **35**(3). 2.1

Stierle, E., Vavryčuk, V., Kwiatek, G., Charalampidou, E.-M., & Bohnhoff, M., 2016. Seismic moment tensors of acoustic emissions recorded during laboratory rock deformation experiments: sensitivity to attenuation and anisotropy, *Geophys. J. Int.*, **205**(1), 38–50. 2.1

Tarantola, A., 2005. *Inverse problem theory and methods for model parameter estimation*, SIAM. 2.4

Teanby, N., Kendall, J.-M., Jones, R., & Barkved, O., 2004. Stress-induced temporal variations in seismic anisotropy observed in microseismic data, *Geophys. J. Int.*, **156**(3), 459–466. 2.1

Thomsen, L., 1986. Weak elastic anisotropy, *Geophysics*, **51**(10), 1954–1966. 2.2.1, 2.2.1, 2.3.1

Tromp, J., Komattisch, D., & Liu, Q., 2008. Spectral-element and adjoint methods in seismology, *Commun. Comput. Phys.*, **3**(1), 1–32. 2.1

Tsvankin, I., 1997. Anisotropic parameters and P-wave velocity for orthorhombic media, *Geophysics*, **62**(4), 1292–1309. 2.2.1

Usher, P., Angus, D., & Verdon, J., 2013. Influence of a velocity model and source frequency on microseismic waveforms: some implications for microseismic locations, *Geophys. Prospect.*, **61**(s1), 334–345. 2.1

Vavryčuk, V., 2004. Inversion for anisotropy from non-double-couple components of moment tensors, *J. Geophys. Res.*, **109**(B7). 2.4

Vavryčuk, V., 2005. Focal mechanisms in anisotropic media, *Geophys. J. Int.*, **161**(2), 334–346. 2.1

Vavryčuk, V., 2007. On the retrieval of moment tensors from borehole data, *Geophys. Prospect.*, **55**(3), 381–391. 2.1

Verdon, J., Kendall, J.-M., & Wüstefeld, A., 2009. Imaging fractures and sedimentary fabrics using shear wave splitting measurements made on passive seismic data, *Geophys. J. Int.*, **179**(2), 1245–1254. 2.1, 2.4

Verdon, J. P. & Kendall, J., 2011. Detection of multiple fracture sets using observations of shear-wave splitting in microseismic data, *Geophys. Prospect.*, **59**(4), 593–608. 2.3.1

Vernik, L. & Liu, X., 1997. Velocity anisotropy in shales: A petrophysical study, *Geophysics*, **62**(2), 521–532. 2.1

Vidale, J. E., 1995. Near-field deformation seen on distant broadband, *Geophys. Res. Lett.*, **22**(1), 1–4. 2.2.5

Virieux, J., 1984. SH-wave propagation in heterogeneous media: Velocity-stress finite-difference method, *Geophysics*, **49**(11), 1933–1942. 2.2.2

Virieux, J., 1986. P-SV wave propagation in heterogeneous media: Velocity-stress finite-difference method, *Geophysics*, **51**(4), 889–901. 2.2.2, 2.2.4

Virieux, J. & Operto, S., 2009. An overview of full-waveform inversion in exploration geophysics, *Geophysics*, **74**(6), WCC1–WCC26. 2.1, 2.3.2

Walker, A. M. & Wookey, J., 2012. MSAT-A new toolkit for the analysis of elastic and seismic anisotropy, *Comput. Geosci.*, **49**, 81–90. 2.6, 2.3.1

Wang, S., Li, X.-Y., Qian, Z., Di, B., & Wei, J., 2007. Physical modelling studies of 3-D P-wave seismic for fracture detection, *Geophys. J. Int.*, **168**(2), 745–756. 2.1, 2.3.2

Wang, Y., 2013. Seismic ray tracing in anisotropic media: A modified Newton algorithm for solving highly nonlinear systems, *Geophysics*, **79**(1), T1–T7. 2.3.1

Wang, Z., 2002. Seismic anisotropy in sedimentary rocks, part 2: Laboratory data, *Geophysics*, **67**(5), 1423–1440. 2.1

Warpinski, N. R., Waltman, C. K., Du, J., & Ma, Q., 2009. Anisotropy effects in microseismic monitoring, in *SPE Annual Technical Conference and Exhibition*, Society of Petroleum Engineers. 2.1, 2.3.1

Wong, J., Manning, P. M., Han, L., & Bancroft, J. C., 2011. Synthetic microseismic datasets, *CSEG RECORDER*. 2.3.1

Wuestefeld, A., Al-Harrasi, O., Verdon, J. P., Wookey, J., & Kendall, J. M., 2010. A strategy for automated analysis of passive microseismic data to image seismic anisotropy and fracture characteristics, *Geophys. Prospect.*, **58**(5), 755–773. 2.1, 2.3.1, 2.3.2

Xu, Y., 2012. *Analysis of P-wave seismic response for fracture detection: Modelling and case studies*, Ph.D. thesis, The University of Edinburgh. 2.2.2

Xuan, R. & Sava, P., 2010. Probabilistic microearthquake location for reservoir monitoring, *Geophysics*, **75**(3), MA9–MA26. 2.1

Yan, B., Yuan, S., Wang, S., OuYang, Y., Wang, T., & Shi, P., 2016. Improved eigenvalue-based coherence algorithm with dip scanning, *Geophysics*, **82**(2), V95–V103. 2.1

Yao, G., Wu, D., & Debens, H. A., 2016. Adaptive finite difference for seismic wavefield modelling in acoustic media, *Sci. Rep.*, **6**, 30302. 2.1

Yomogida, K. & Etgen, J. T., 1993. 3-D wave propagation in the Los Angeles basin for the Whittier-Narrows earthquake, *Bull. Seismol. Soc. Am.*, **83**(5), 1325–1344. 2.2.4

Yuan, S., Wang, S., Sun, W., Miao, L., & Li, Z., 2014. Perfectly matched layer on curvilinear grid for the second-order seismic acoustic wave equation, *Explor. Geophys.*, **45**(2), 94–104. 2.1

Yuan, S., Wang, S., Luo, C., & He, Y., 2015. Simultaneous multitrace impedance inversion with transform-domain sparsity promotion, *Geophysics*, **80**(2), R71–R80. 2.3.2

Zhang, J.-H. & Yao, Z.-X., 2013. Optimized explicit finite-difference schemes for spatial derivatives using maximum norm, *J. Comput. Phys.*, **250**, 511–526. 2.1, 2.2.2

Zhang, Y., Eisner, L., Barker, W., Mueller, M. C., & Smith, K. L., 2013. Effective anisotropic velocity model from surface monitoring of microseismic events, *Geophys. Prospect.*, **61**(5), 919–930. 2.1, 2.3.2

Zienkiewicz, O. C., Taylor, R. L., & Taylor, R. L., 1977. *The finite element method*, vol. 3, McGraw-hill London. 2.1

Chapter 3

Automated seismic waveform location using Multichannel Coherency Migration (MCM)–I. Theory

P. Shi[1], D. Angus[2], S. Rost[1], A. Nowacki[1] and S. Yuan[3]

[1] *School of Earth and Environment, University of Leeds, Leeds, United Kingdom*
[2] *ESG Solutions, Kingston, ON K7K 7K2, Canada*
[3] *College of Geophysics, China University of Petroleum, Beijing, 102249, China*

Abstract

With the proliferation of dense seismic networks sampling the full seismic wavefield, recorded seismic data volumes are getting bigger and automated analysis tools to locate seismic events are essential. Here, we propose a novel Multichannel Coherency Migration (MCM) method to locate earthquakes in continuous seismic data and reveal the location and origin time of seismic events directly from recorded waveforms. By continuously calculating the coherency between waveforms from different receiver pairs, MCM greatly expands the available information which can be used for event location. MCM does not require phase picking or phase identification, which allows fully automated waveform analysis. By migrating the coherency between waveforms, MCM leads to improved source energy focusing. We have tested and compared MCM to other migration-based methods in noise-free and noisy synthetic data. The tests and analysis show that MCM is noise resistant and can achieve more accurate results compared with other migration-based methods. MCM is able to suppress strong interference from other seismic sources occurring at a similar time and location. It can

be used with arbitrary 3D velocity models and is able to obtain reasonable location results with smooth but inaccurate velocity models. MCM exhibits excellent location performance and can be easily parallelized giving it large potential to be developed as a real-time location method for very large datasets.

3.1 Introduction

With the routine deployment of large monitoring arrays, significant quantities of waveform data have and are being recorded by various types of seismometers and geophones around the world. The increasing volume of real-time seismic data and the necessity to seismically monitor natural and man-made seismic hazard require the development of fully automated seismic analysis methods. Conventional arrival time based source location methods require accurate picking of the P- and/or S-wave arrivals. However, even though automatic picking algorithms are being used increasingly (Allen, 1982, Bai & Kennett, 2000, Saragiotis et al., 2002, Yuan et al., 2018), manual picking is still usually needed to increase location accuracy as well as quality control. This kind of user interactivity is expensive, time consuming and cannot handle the increasingly larger datasets resulting from full wavefield experiments. Furthermore, picking algorithms do not work well when the signal-to-noise ratio is too low and/or the phase arrivals of different seismic events overlap. Therefore arrival time based location methods are more suitable for locating global and regional earthquakes with recognisable phase arrivals. Conversely, microseismicity such as small tremors during volcanic activity, induced seismicity during fluid injection and triggered/induced seismicity during reservoir depletion have relatively smaller magnitudes. The recorded amplitudes of these microseismic events are weak and often inundated by noise. Additionally for hydraulic fracturing, a large number of microseismic events can occur in a limited spatial and temporal window, which often causes interference of the recorded waveforms. As such, the detection and location of microseismic events can be extremely difficult, making conventional arrival time based location methods not ideal for locating microseismic events.

The conventional picking and arrival time based methods only utilize the travel-time information while valuable information in the data such as recorded waveforms are omitted. Furthermore, effectively utilizing the available waveforms and extracting useful information from the recorded data are important to comprehensively evaluate the seismic source. In order to make full use of the recorded wavefield, waveform-based methods are increasingly used to automatically locate the microseismicity and characterize the source mechanism. Cesca & Grigoli (2015) reviewed the recent application of full waveform methods in microseismic location, source mechanism characterization and microseismicity waveform classification. Phase picking and identification are not required in the waveform-based location methods, which enable their application on

data with low signal-to-noise ratio. Waveform-based location methods can be divided into two main categories: migration-based location methods and full waveform inversion methods. Full waveform inversion approaches are often used to determine the velocity model of the subsurface (Tarantola, 1984) and can also be used to characterize source parameters (Wu & McMechan, 1996, Ramos-Martínez & McMechan, 2001, Kaderli et al., 2015). However due to the high computational cost, it is not extensively used in seismic source characterization. The migration-based methods can be divided into reverse time imaging and diffraction stack imaging (DSI) approaches (McMechan, 1982, Fink et al., 2000, Larmat et al., 2006, Kao & Shan, 2004, Liao et al., 2012, Drew et al., 2013, Grigoli et al., 2013a). Reverse time imaging approach utilizes the reversibility of the wave equation and propagates the recorded seismograms backward in time to resolve the source parameters (Steiner et al., 2008, Larmat et al., 2009, Artman et al., 2010); it involves solving the wave equation and thus is computationally intensive. Constructing an appropriate imaging condition and imaging seismic sources having different radiation patterns are also challenges for reverse time imaging. DSI approaches use delayed and summed coherent phases from different station recordings according to traveltimes of P- and/or S-phases for a specific velocity model to focus the source energy at the estimated source location. It is computationally faster and can be applied to arbitrarily complex media. However the DSI approach cannot effectively utilize the whole wavefield, and reflections, multiples and mode conversions often make this method unsuitable.

For the DSI method, Kao & Shan (2004) first proposed a source scanning algorithm (SSA) in which the absolute amplitudes of normalized seismograms in a selected time window are stacked to image the seismic sources with emergent arrivals in both space and time. At the correct source position and origin time, the waveform will add coherently, which will lead to maximum energy focusing. Through identifying the maximum value in the stacked data volume, both the location and origin time of the source can be determined. For a pure shear source, the source radiation pattern will cause difficulty in imaging the source directly from original waveform data. The maximum value of the stacked data will not appear at the true source location due to the radiation pattern of seismic source and thus influencing the accuracy of the location (Artman et al., 2010, Zhebel & Eisner, 2014). Thus varieties of modified DSI methods have been proposed to eliminate the influence of the source radiation pattern. Kao & Shan (2007) further modified the SSA by stacking the P-wave envelopes to rapidly image the rupture pattern of an earthquake. Grigoli et al. (2013b) stacked the short-term-average/long-term-average (STA/LTA) traces to locate mining induced seismicity and also estimated the location uncertainties. As an estimated velocity model is required to migrate recorded waveforms in the DSI, the location performance of the DSI approach often strongly depends on our knowledge of the subsurface velocity model. To overcome the difficulty of obtaining an accurate velocity model, Grigoli et al. (2016) proposed the

master-event waveform stacking to reduce the dependency of DSI on velocity model. However for DSI, to further utilize the waveform information and obtain high-quality imaging results on extremely low signal-to-noise data the method still requires improvements.

In seismology, cross-correlation is often used to evaluate the coherency between waveforms from different stations (Wang et al., 2016). It has been widely used to estimate signal delay times (VanDecar & Crosson, 1990) and in seismic interferometry (Halliday & Curtis, 2008, Wapenaar et al., 2011). Wassermann & Ohrnberger (2001) utilized the wavefield coherency to determine the hypocenter of volcano induced seismic transients. Recently Ruigrok et al. (2016) performed beamforming based on cross-correlated data. Here, we propose a Multichannel Coherency Migration (MCM) method to determine the location and origin time of seismicity. In the MCM method the coherency between different receiver pairs are stacked to focus the source energy. The coherency between all possible receiver pairs are calculated simultaneously through normalizing the covariance matrix of the recorded waveforms. We will first introduce the theory of the new proposed location method. Then we compare the MCM method with different migration-based location methods in the presence of strong random noise for a synthetic full waveform dataset. The location results demonstrate that the MCM can achieve a better imaging resolution under varying noise levels. Finally, we show that the MCM can obtain more stable and reasonable location results compared with other migration-based location methods when the velocity model is not accurate or strong interference exists. The applications of MCM on real datasets and practical situations can be found in Shi et al. (2019).

3.2 Method

In this section, we will first describe previously used migration techniques and then introduce our new location method. Migration-based location methods often consist of four components: (1) traveltime calculation, (2) characteristic function calculation, (3) migration and (4) source event identification.

3.2.1 Constructing the traveltime table

The rupture lengths of microseismic events are significantly smaller compared to the dominant wavelength of seismic waves, especially for surface monitoring. Thus microseismic sources can be well approximated as point sources. In the potential source location region, the volume can be discretized into image points according to the required spatial resolution. The spatial interval should be less than one half-wavelength to ensure a sufficient spatial sampling rate. Once the source and receiver geometry is determined, a look-up table of traveltimes is constructed for both P- and S-waves given

the seismic velocity model. The look-up table only needs to be calculated once in the whole location process, thus accelerating the migration of waveforms later.

The traveltime calculation of direct P- and S-wave can be expressed as $t^P(x, y, z) = f(v_P, G)$ and $t^S(x, y, z) = f(v_S, G)$ respectively, where v_P, v_S represent the P- and S-wave velocity fields, G represents the geometry of potential source locations and receiver array and x, y, z are 3D spatial coordinates of the source point. The traveltime table can be built upon any known velocity model of arbitrary complexity and seismic traveltimes can be calculated using the seismic wave equation in a variety of ways. In homogeneous medium, the traveltimes can be calculated using analytical solutions; in 1D layered media, the traveltimes can be calculated e.g. using ray-tracing or the reflectivity method; in 2D and 3D heterogeneous media, the traveltimes can be calculated e.g. using an Eikonal solver (Podvin & Lecomte, 1991).

3.2.2 Calculating the characteristic function

Unlike exploration seismology, where explosive sources are extensively used, tectonic events show complex rupture patterns and therefore show different radiation patterns for the seismic energy. Due to the radiation pattern, the polarization of the P- and S-waves vary dependent on the take-off and azimuth angles of the seismic energy, which means the polarization of these recorded phases may vary in amplitude and sign for different receivers along the array. Thus simply stacking the amplitude of recorded waveforms may contribute to an inaccurate imaging result, leading to several maxima around the true source position. This is especially significant when imaging pure double-couple sources using only single phase and single component data (Artman et al., 2010, Zhebel & Eisner, 2014). The polarization needs to be taken into account when migrating energy back to the source location to avoid ambiguous imaging results. In order to remove the influence of the source radiation pattern, various characteristic functions have been used to perform waveform migration, e.g. the absolute value (Kao & Shan, 2004), the envelope (Kao & Shan, 2007, Gharti et al., 2010), the STA/LTA (Drew et al., 2013, Grigoli et al., 2013b) and the kurtosis of the waveforms (Langet et al., 2014).

The characteristic function is actually a transformation of the recorded original waveforms in order to obtain non-negative stacking traces. The transformation can be expressed as $S(t) = \mathcal{T}(d(t))$, where $d(t)$ represents the recorded original data, $\mathcal{T}$ corresponds to different kinds of transformations, $S(t)$ represents the characteristic function after transformation. Stacking the envelope or the absolute value of the waveforms cannot effectively utilize the non-correlation of the random noise and so often fails to suppress random noise. Thus these kinds of characteristic functions only work well on data with high signal-to-noise ratio. The STA/LTA or kurtosis of the waveforms utilizes the statistical characteristics of the data and is often used to detect and pick weak signals (Allen, 1982, Saragiotis et al., 2002). Thus the STA/LTA and kurtosis characteristic functions have the ability to suppress random noise in the data. However

the performance of the STA/LTA or kurtosis transforms are often subject to the choice of time window and are often unsatisfactory in low signal-to-noise ratio situations. The STA/LTA and kurtosis transforms can highlight weak signals against background noise, but at the expense of losing accurate estimation of the source magnitude.

3.2.3 Migration

Conventional migration

After the traveltime table and characteristic function have been calculated, traditional waveform migration can then be performed upon each potential source location and estimated origin time. At each potential source location, migration is performed by summing the windowed characteristic functions according to the traveltime table and estimated origin time. By stacking the characteristic function, the source energy will focus at the true source location and correct source origin time. Thus a 4D imaging function $W(x, y, z, t_0)$ is obtained, where the maximum corresponds to the estimated source location and origin time:

$$W(x, y, z, t_0) = \sum_{i}^{N} \sum^{R} |S_i(\tau_R^P)| + \sum_{i}^{N} \sum^{R} |S_i(\tau_R^S)|, \tag{3.1}$$

where i represents the ith component of the recorded data, $W(x, y, z, t_0)$ is the 4D imaging function that corresponds to the spatial location and origin time of the source, τ_R^P and τ_R^S represent the delayed P- and S-wave traveltimes from a specified image point (x, y, z) to the receiver R. τ^P and τ^S can be explicitly expressed as

$$\tau^P(x, y, z, t_0) = t^P(x, y, z) + t_0 \quad \text{and} \quad \tau^S(x, y, z, t_0) = t^S(x, y, z) + t_0, \tag{3.2}$$

where t_0 is the delay time which accounts for the origin time of the source. The P and S phases are simultaneously used in the migration method to better constrain the source location (Gharti et al., 2010). It is feasible to include multiple phases into the migration, which might significantly improve the resolution of the source location. However the accuracy of the traveltimes for reflected and converted phases depends more heavily on the velocity model than the primary phases. If an accurate velocity model is available, reflections and conversions could be incorporated into the migration method to improve the imaging quality. Usually the P-waves will have a distinct arrival on the vertical component record while the S-waves tend to have a distinct arrival on the horizontal component record. Thus, jointly utilizing multi-component data in migration is also recommended, as it can provide more information and constraints for source location.

Multichannel Coherency Migration

Unlike conventional migration methods which directly migrate the waveforms of the original data or the characteristic functions of recorded waveforms, our MCM first calculates the Pearson correlation coefficients (Ezekiel & Fox, 1959) of time windowed records for all possible combinations of two or more stations and then stacks the calculated correlation coefficients. The time window used for coherency analysis is determined according to the length of the source time function and thus will include both the direct P- and S-phases at the correct source position and origin time. The approach works with imaging either P or S arrivals or a combination of both. The Pearson correlation coefficient describes the linear dependence between two or more traces, and can be calculated based on two-channel or multichannel (which can be interpreted as multidimensional cross-correlation Arfken & Weber (1999)) as

$$r_m = \frac{\sum_t \left[w_{i_1}(d_{i_1}(t) - \overline{d_{i_1}(t)})\right] \left[w_{i_2}(d_{i_2}(t) - \overline{d_{i_2}(t)})\right] \cdots \left[w_{i_n}(d_{i_n}(t) - \overline{d_{i_n}(t)})\right]}{(N_t - 1)\,\sigma_{i_1}\sigma_{i_2}\cdots\sigma_{i_n}}, \quad (3.3)$$

where r_m is the m-th multidimensional waveform coherency (n-dimension) among different stations $i_1, i_2, \cdots i_n$ ($i_j \in [1, 2, \cdots, N]$ and N is the total number of all stations, $m \in [1, 2, \cdots, M]$ and M is the total number of n-wise groups of stations), $d_{i_j}(t)$ is the time windowed signal of the i_j-th station according to the pre-calculated traveltime table and estimated origin time, w_{i_j} is weighting factor for the i_j-th station, N_t is the number of time samples, σ is the standard deviation of the corresponding signal and the overlines denote averages. When the data quality of a trace is good, the weighting factor w_{i_j} is set to 1; whereas when a trace is highly contaminated by noise, the weighting factor w_{i_j} is set to 0. The weighting factors can be adjusted but in our test we retain with these binary weightings. By exploiting weighting factors, known-good or known-bad traces can be up-/down-weighted. The correlation coefficient of two input signals is equal to the covariance of the two signals normalized by the product of their standard deviations. The correlation coefficient evaluates the waveform similarity among the traces and has a value between $+1$ and -1, where ± 1 represents a total positive/negative linear correlation between the two traces, whilst 0 represents no linear correlation between two traces. If the waveforms of the two traces within the selected time window are similar, such as for coherent P arrivals, the absolute value of the correlation coefficient will be high towards 1. If the waveforms of the two traces within the selected time window are not coherent, such as for random noise, the absolute value of the correlation coefficient will be low towards 0. Fig. 3.1 shows the corresponding waveform coherency within a time window at the true source location and an incorrect position respectively. At a particular imaging point, by the utilization of multidimensional waveform coherency, the total number of effective information available for migration is improved from N to $M = \frac{N!}{L!(N-L)!}$ ($L = \sum_{i_j} w_{i_j}$ and ! denotes

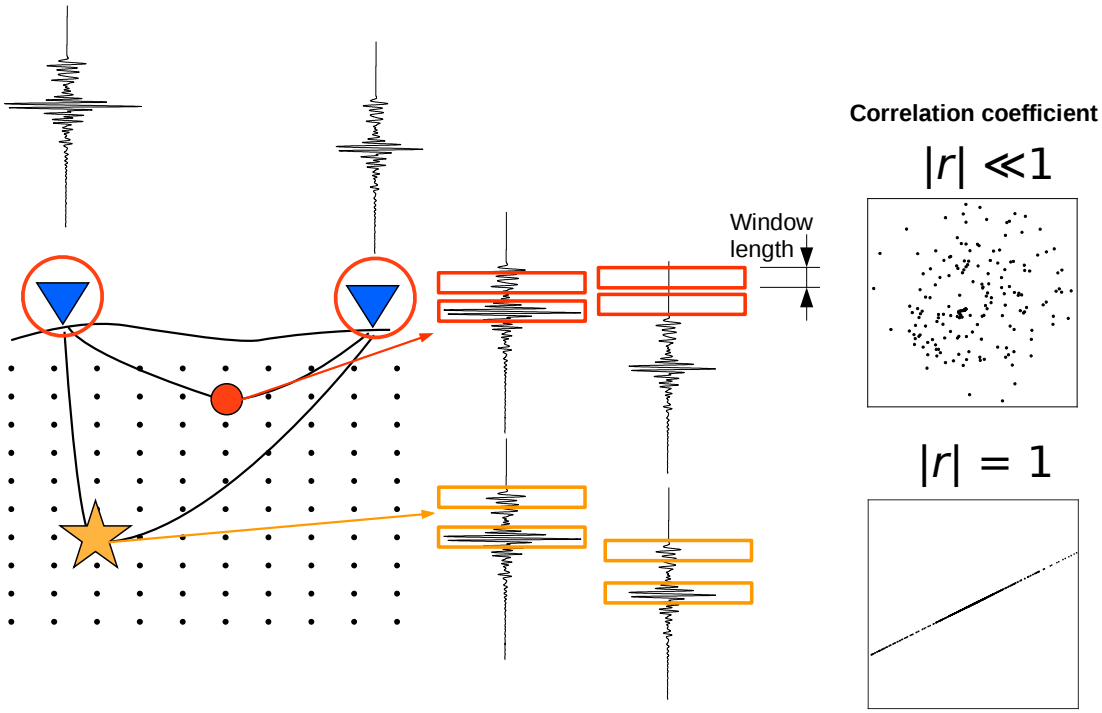

Figure 3.1: Schematic diagram showing the waveform coherency for different imaging points. Black dots show subsurface imaging points. Blue triangles show surface receivers. Orange star represents the true source point which has a high waveform coherency and red circle represents an incorrect imaging point which has a very low waveform coherency.

factorial).

When calculating the coherency between waveforms, the cross-correlation method is extensively used (such as the cross-correlation beamforming method proposed by Ruigrok et al. (2016)). The zero-lag normalized cross-correlation can be expressed as

$$r_{ij} = \frac{\sum_t (d_i(t) d_j(t))}{|d_i(t)||d_j(t)|}, \tag{3.4}$$

where $|\cdot|$ represents the norm of the waveform vector. The normalized cross-correlation can achieve similar results to the standard correlation coefficient when the input waveforms all have zero mean values. However, when the recorded waveforms of some stations are biased (e.g. due to different instrument responses or different waveform processing), the normalized cross-correlation will not effectively evaluate the coherency between waveforms, while the correlation coefficient may still calculate the coherency accurately as the mean values have been removed from the input waveform data and the covariance is normalized by the standard deviation of the input data.

Next the absolute value of the correlation coefficients of the traces are stacked to image the source location and origin time. The influence of the source radiation pattern can be eliminated by stacking the absolute value of the correlation coefficients. The

stacked traces (referred to as stacking function hereafter) can be expressed as

$$p(x,y,z,t_0) = \frac{1}{2M}\left(\sum_{m=1}^{M}|r_m^P| + \sum_{m=1}^{M}|r_m^S|\right), \tag{3.5}$$

where r_m^P and r_m^S represent the waveform coherency of P- and S-phases respectively, M is the total number of unique multichannel receiver groups, $p(x,y,z,t_0)$ is the final 4D imaging function and stores the stacked waveform coherency at position (x,y,z) and origin time t_0. The imaging function $p(x,y,z,t_0)$ is a bounded function, with values between 0 and 1. The stacked correlation coefficients are normalized by the total number of unique multichannel receiver groups given by M. Here, because both P- and S-phase coherency are used, the stacked correlation coefficients are thus normalized by $2M$. If the waveforms of all the traces in the selected time window are completely linearly coherent (positive or negative correlation), then the correlation coefficients are all 1 and the final imaging value for this point and origin time is $p = 1$. With seismic data, because of noise and heterogeneity of the medium, the stacked coherency of the source may rather have a high value approaching 1.

Two-dimensional MCM

In equation 3.3, if n is chosen to be 2, we can obtain the most concise form of MCM, i.e. two-dimensional MCM. The Pearson correlation coefficient between two traces is calculated by

$$r_{ij} = \frac{\sum_t w_i w_j \left[d_i(t) - \overline{d_i(t)}\right]\left[d_j(t) - \overline{d_j(t)}\right]}{(N_t - 1)\,\sigma_i \sigma_j}, \tag{3.6}$$

where r_{ij} is the correlation coefficient (i.e. coherency) between waveforms from station i and j, $d_i(t)$ and $d_j(t)$ are the two input waveforms within the selected time window. Correspondingly, the stacking function can be expressed as

$$p(x,y,z,t_0) = \frac{1}{N(N-1)}\left(\sum_{i<j}^{N}|r_{ij}^P| + \sum_{i<j}^{N}|r_{ij}^S|\right). \tag{3.7}$$

In equation 4.2, because both P- and S-phase coherency are used, the stacked correlation coefficients are normalized by twice the total number of unique receiver pairs which is $N(N-1)/2$.

The calculation of the two-dimensional MCM can be expressed in matrix form yielding an efficient computational algorithm. The coherency does not need to be calculated based on each receiver pair separately. In other words, the correlation coefficients between all possible receiver pairs can be calculated simultaneously through forming a covariance matrix. At each imaging point a data matrix $\mathbf{D}$ can be constructed from the recorded data according to the pre-calculated traveltime table and estimated origin

time. The data matrix $\mathbf{D}$ has the dimensions $[N_t \times N]$ (N_t is the length of the time window):

$$\mathbf{D} = [\mathbf{d}_1 \mathbf{d}_2 \cdots \mathbf{d}_N], \tag{3.8}$$

where $\mathbf{d}_i$ is a column vector and represents the windowed signal of the ith trace. The covariance matrix $\mathbf{C}$ is then calculated through

$$\mathbf{C} = \widehat{\mathbf{D}}^T \widehat{\mathbf{D}}/(N_t - 1), \tag{3.9}$$

where $\widehat{\mathbf{D}} = \mathbf{D} - \mathbf{E}\mathbf{D}/N_t$ represents the signal deviations from their individual expected values ($\mathbf{E}$ is a $N_t \times N_t$ square matrix with all elements equal to 1) and T represents transpose. The correlation coefficient matrix can be obtained through

$$\mathbf{R} = \frac{\mathbf{C}}{\boldsymbol{\sigma}\boldsymbol{\sigma}^T}, \tag{3.10}$$

where $\boldsymbol{\sigma}$ is the standard deviation vector (i.e. $\boldsymbol{\sigma} = [\sigma_1 \sigma_2 \cdots \sigma_N]^T$). Here the division in equation 3.10 means element-wise division not matrix division. Finally the stacking coherency at this imaging point and origin time is

$$p = \frac{\sum_{i<j}^{N} (|\mathbf{R}_P| + |\mathbf{R}_S|)}{N(N-1)}, \tag{3.11}$$

where $\mathbf{R}_P$ and $\mathbf{R}_S$ represent the correlation coefficient matrix of the P- and S-waves respectively. The summation in equation 3.11 is performed over the upper-triangular elements of the correlation coefficient matrix to exclude the auto-correlation of the signals.

The application of the MCM can be quite flexible. The waveform coherency can be easily calculated based on two or more traces. Using the coherency of multiple traces, the source coherency can be further strengthened. The selected time window can also be altered adaptively during the coherence analysis. The MCM can be applied to the original waveform data as well as any kind of the characteristic functions of the original data. As the original waveform data normally contain the most abundant information, applying MCM directly to the waveform data is recommended. In this paper, our MCM results and analysis are all based on the coherency of the original waveform data for two stations.

3.2.4 Identifying the source location and origin time

Once the migration process is done, a 4D migration volume is finally generated, which contains the information about source location and origin time. If there is only one seismic event recorded in a certain monitoring time period, the location (x_s, y_s, z_s) and origin time t_{0s} of this event can be identified through finding the maximum value in

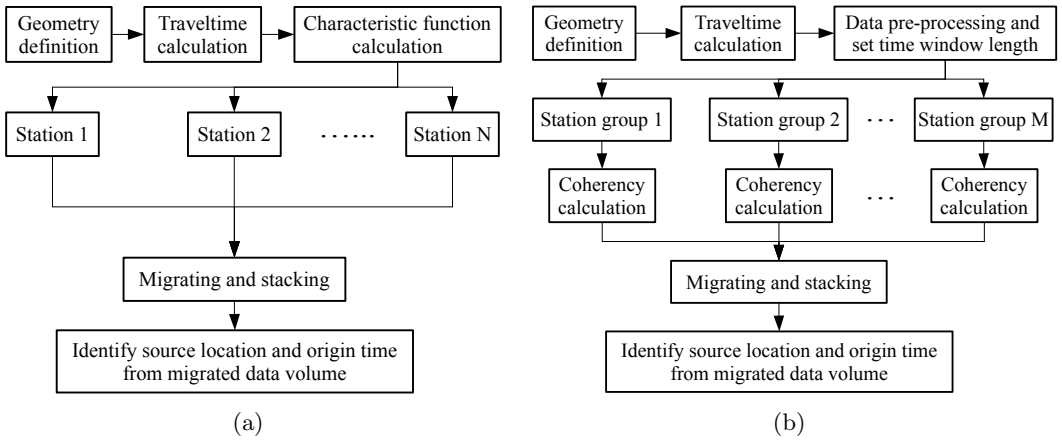

Figure 3.2: (a) Workflow of the traditional migration-based location method. (b) Workflow of the MCM method.

the 4D image volume $p(x_s, y_s, z_s, t_{0s}) = max\{p(x, y, z, t_0)\}$. If multiple events exist, events can be identified by setting a coherency threshold. The coherence threshold is determined through investigating the stacking coherency of the background noise. Any stacking coherency above the threshold can be viewed as a seismic event. However, when the imaging point and estimated origin time are close to the true source location and origin time, high coherency will also appear in the imaging domain. In order to avoid mis-identification of non-physical sources, only one seismic event with the highest coherency will be identified within a specific space zone and time period. Fig. 3.2 shows the workflow for the conventional migration-based location method and the MCM location method.

In theory, the origin time of the source corresponds to the time of maximum stacking energy. The stacking energy rises above the coherency level of background noise as the coherency analysis time window approaches the origin time of the source (a coherency analysis time window earlier than the origin time), reaches a maximum value around the origin time and then decreases to the coherency noise level as the window passes the end time of the source wavelet. Fig. 3.3 shows two signals with random noise and the calculated coherency between the two noisy signals using a sliding time window. In this example, the two signals are negatively correlated. A constant shift in amplitude is added to one signal. Random noise is added to the two signals separately. Fig. 3.3(b) displays the coherency of the two signals calculated through the Pearson correlation coefficient method expressed in equation 3.3. Fig. 3.3(c) displays the coherency of the two signals calculated through the normalized cross-correlation method expressed in equation 3.4. We can see the coherency is better evaluated by the Pearson correlation coefficient method when the waveforms have differing means.

We can see that the coherency functions of the synthetic data have a flat maximum (Fig. 3.3(b)). The flat maximum lasts one period of the source time function plus

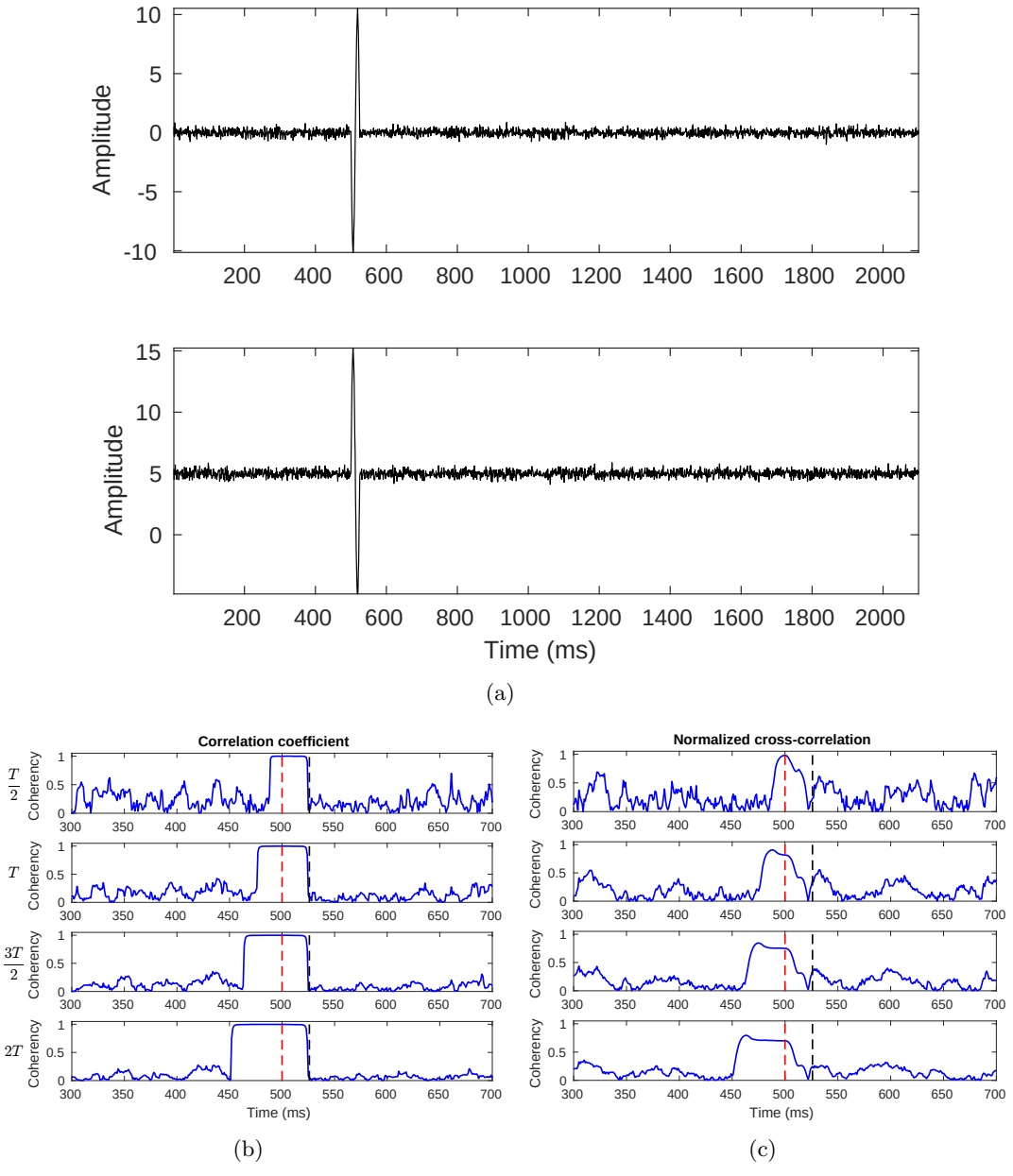

Figure 3.3: Coherency of two sinusoidal signals with random noise obtained by a sliding time window of different size. The period (T) of the sinusoidal signal is 25 ms. The top row of figure (b) and (c) shows the case with a time window of 13 ms (T/2), the second row with a time window of 25 ms (T), the third row with a time window of 38 ms (3T/2), the bottom row with a time window of 50 ms (2T). The red dashed line exhibits the origin time of the sinusoidal signal at 500 ms. The black dashed line exhibits the end time of the sinusoidal signal at 526 ms. (a) The two sinusoidal signals with random noise. The signal-to-noise ratio is 10. (b) The coherency obtained by the Pearson correlation coefficient method using equation 3.3. (c) The coherency obtained by normalized cross-correlation method using equation 3.4.

the length of the coherency analysis time window. Thus the determination of the origin time from the stacking function needs to be calibrated based on the coherency analysis time window. If the length of the time window is chosen to be the same as the period of the signal, the flat maximum is symmetrical about the origin time (second row in Fig. 3.3(b)). The length of the time window influences the performance of the coherency function in the presence of noise. A longer time window suppresses noise well since more samples are used in calculating the coherency between different traces (see Fig. 3.3(b)). However a longer time window will reduce the spatial and temporal resolution of the imaging result, as interference easily happens when more data are incorporated into coherency analysis. And the coherency value of the windowed data will also decrease due to the longer time window, as more non-coherent samples are taken into the coherency analysis. Thus when choosing the time window, the trade-off between noise suppression and imaging resolution needs to be considered. In practice, a time window which equals the length of the source wavelet is suggested as it can keep a balance between the noise suppression and imaging resolution. However, when the noise is very strong in the recorded data, a longer time window is expected to be more appropriate. In the following sections, we will use approximately one period of the recorded signals as the time window since it will provide the optimal temporal resolution of the origin time.

3.3 Noise resistance

For microseismic monitoring, locating weak seismic events is challenging. The signals from weak or small events are more likely to have lower signal-to-noise ratios. In contrast to traditional single-channel based migration methods, the two-dimensional MCM method utilizes the resemblance between different receiver pairs and increases the number of available data from N to $N(N-1)/2$ (N is the total number of traces). Thus the MCM method is more resistant to noise and hence able to identify weak events, which is critical for enhancing microseismic monitoring. In order to evaluate the performance of different migration-based location methods in the presence of noise, we compare the stacking functions of different migration methods at the source position using different noise-to-signal ratios (as shown in Fig. 3.4). The noise-to-signal ratio (NSR) is defined by the ratio of the maximum amplitude between noise and signal, which is used to highlight the noise level more intuitively. Here four migration-based location methods are compared, i.e. using the waveform envelope, STA/LTA and kurtosis as characteristic functions and our MCM method as defined in section 3.2.3.

Source prominence (S_{pro}) is used to evaluate the performance of the different methods in source identification. The source prominence is defined as the ratio of the stacked energy of the source to the average stacked energy of the noise, and is a unitless metric that characterises how strong the source coherency is with respect to the background

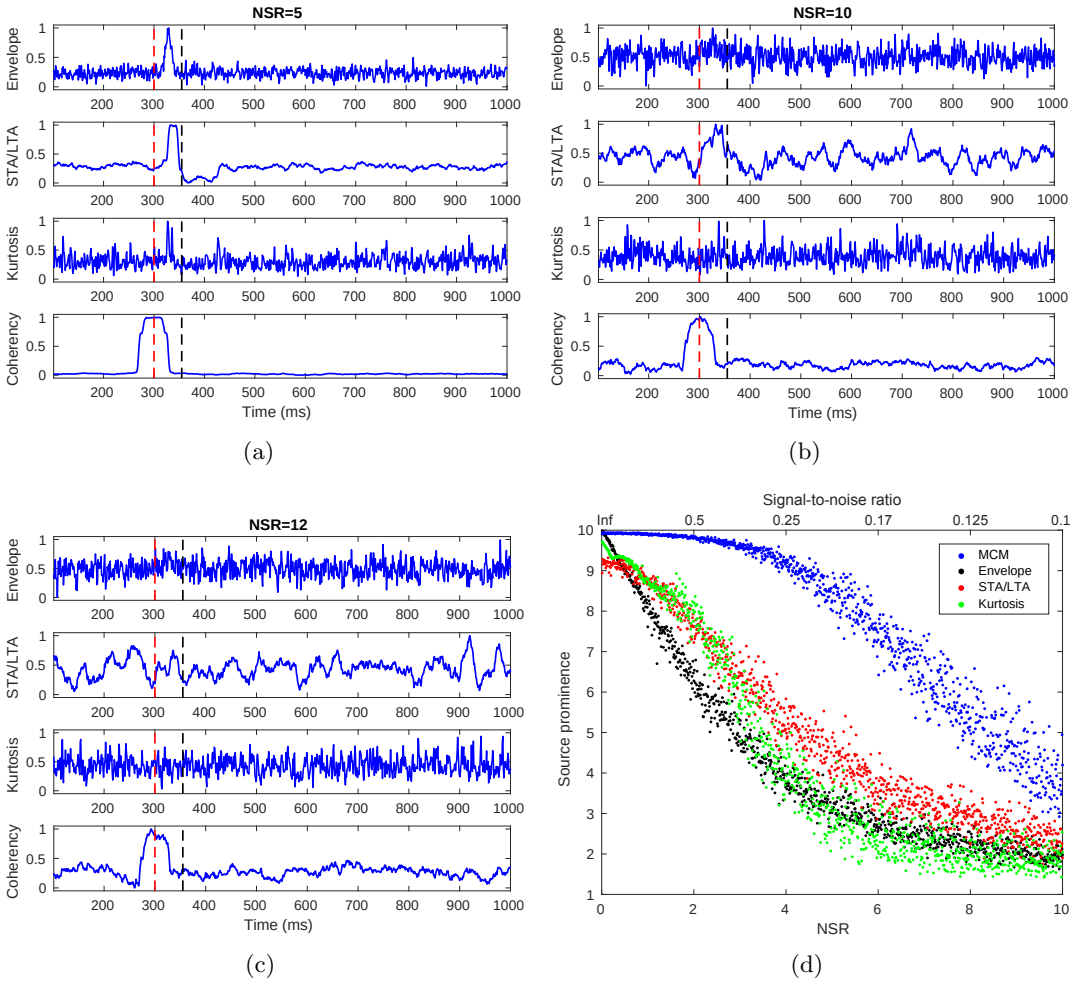

Figure 3.4: Stacking functions and source prominence (S_{pro}) at the correct source position under different NSRs for four different migration methods (envelope, STA/LTA, kurtosis and MCM). Total number of available traces is 441. Red and black dashed lines show the origin and end time of the source respectively. The stacking functions for the four different migration methods when NSR is (a) 5, (b) 10, (c) 12. (d) The variation of source prominence with different NSRs. The results are obtained through Monte Carlo simulation with black points showing the envelope method, STA/LTA method (red points), kurtosis method (green points) and MCM method (blue points). Because the stacking energy is not at the same scale for different migration methods, the source prominence is calculated after normalizing the stacking functions between 1 and 10. MCM performs best in the presence of strong random noise.

noise. The higher the source prominence is, the greater the certainty in the source location and origin time estimates. As the NSR increases, the stacked energy of the background noise also increases, and so source identification is more difficult. When the NSR reaches approximately 12, only the MCM method can accurately locate the source, while all the other methods fail (Fig. 3.4(c)). As shown in Fig. 3.4(d), the source prominences of the MCM are larger and also decrease more slowly with increasing NSRs compared to the other methods, which confirms the improved noise resistance of the MCM method. As statistic-based migration methods, the STA/LTA and kurtosis methods show better performance than the envelope method and their source prominences are higher than the envelope method. However, when NSR is higher than 3, the source prominence of kurtosis method decreases rapidly. And when NSR is higher than 4, the performance of the kurtosis method is not as good as the STA/LTA method and even inferior to the envelope method. Compared to the other methods, the kurtosis method is more sensitive to strong noise.

Source prominence is sensitive to the NSR. High NSR will lead to a high background noise level, thus contributing to a low source prominence. As indicated in Fig. 3.4, source prominence could be used to evaluate the noise resistance ability of a source location method. Fig. 3.5 exhibits the source prominence of the MCM method under different NSRs. We can see that the source prominence decreases gradually with increasing NSR. The source prominence eventually approaches 1 with extremely high NSR, which means the source energy is completely inundated by the background noise. We use a Monte Carlo simulation to obtain the variation of the source prominence with different NSRs. For every different NSR, the source prominence is obtained by calculating the average prominence of 10 separate data with independent random noise. From Fig. 3.5(d), we can infer a relation between the source prominence and the NSR, which can be expressed as $S_{pro} = \alpha * \exp(\beta * NSR) + 1$. The scale factor α and β will depend on the radiation pattern of the source, time window length of the coherency calculation and the frequency content of the signal and noise. Since increasing the total number of traces only contributes to increasing the number of available coherency information having the same coherency level, in theory the source prominence is not affected by the total trace number (N).

Another important property to evaluate the noise resistance ability of a migration-based location method is the variation of the stacked energy of the background noise (σ^2_{noise}). When the source prominence is low, the variation of the noise energy will be extremely important for determining the correct source location. The stacked noise energy could form several local maxima in the stacking function, which will hinder precise source identification. The lower the variance of the stacked noise energy, the easier it will be to identify the source. Fig. 3.6 shows the stacking functions and variance of noise energy at the source position for different number of traces (N) and the different methods. The available trace number ranges from 10 to 100. We can see

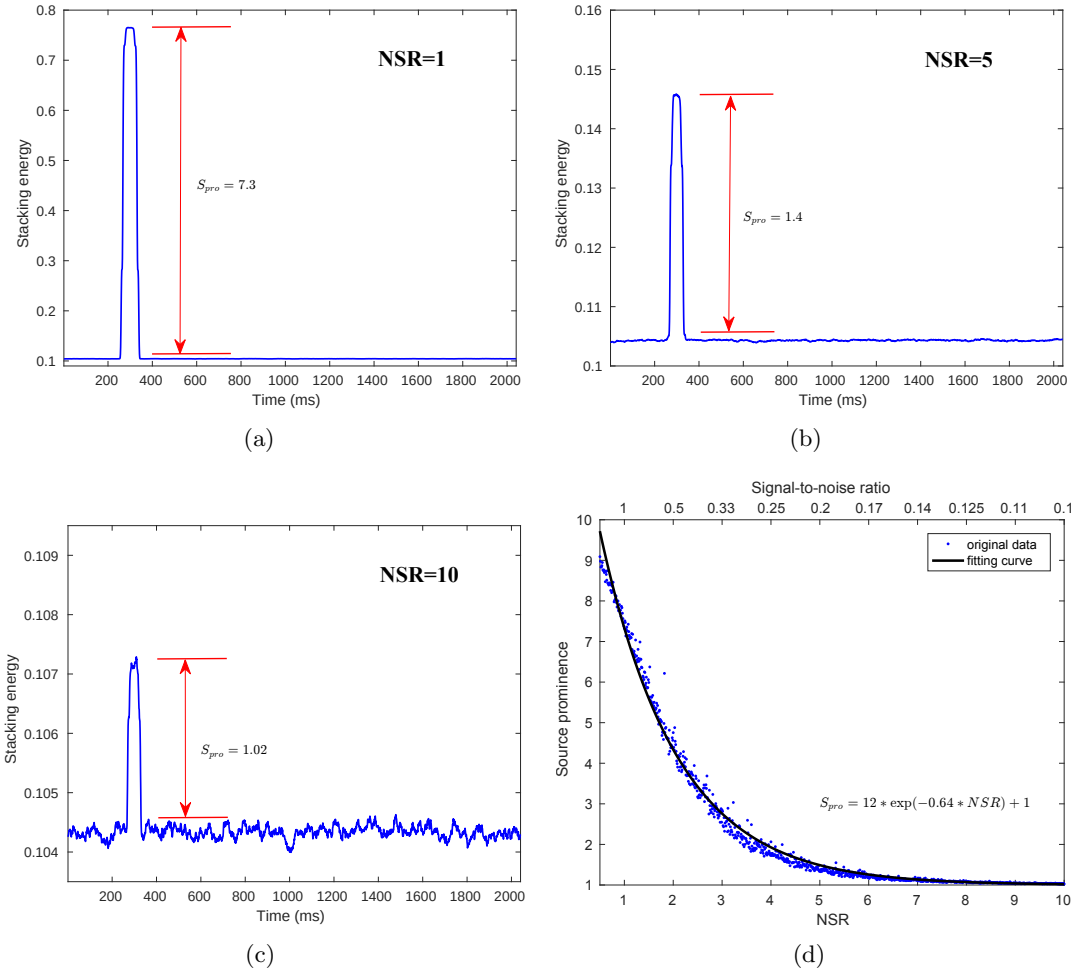

Figure 3.5: Stacking functions at the source position when NSR is (a) 1, (b) 5 and (c) 10 for the MCM method. (d) Variation of source prominence with different NSRs at the source position for the MCM method. Results are obtained through Monte Carlo simulation. Blue points represent the calculated source prominences, and the black line shows the fit to the data. The fitting formula is also shown in the figure. The source prominence is calculated using the simulation results directly without normalization. The total number of available traces is 1000.

the variance of the noise decrease gradually with increasing number of traces for all four methods. The MCM method has the lowest variance of noise energy for all trace numbers N, indicating better performance of the MCM method on source location and origin time estimation. The noise variance of STA/LTA and kurtosis methods fall between the MCM and envelope methods.

The variance of the stacked noise energy is sensitive to the total number of available traces N. For N receivers, there are $N(N-1)/2$ unique receiver pairs, which can provide effective coherency information. Increasing the number of receivers could effectively reduce the variance of noise energy in the stacking function. Fig. 3.7 shows that the variance of noise energy decreases rapidly with an increasing number of traces. A low variance of noise energy makes it much easier to identify the source location and origin time. From Fig. 3.7(d), we can estimate the relationship between the variance of noise energy and the number of traces, which is $\sigma^2_{noise} = a/(N(N-1))$. This means the variance of noise energy is inversely proportional to the number of unique receiver pairs. The scale factor a is related to the statistical characteristics and frequency content of the noise.

In order to test the performance of different methods in the presence of strong noise, we use a synthetic full waveform microseismic dataset. Fig. 3.8 shows the velocity model and the geometry of the surface array. A pure dip-slip source is located in the middle of the layered earth model, with coordinates of 2.0, 2.0 and 2.85 km in the X, Y and Z directions, respectively. The receivers are uniformly distributed on the free surface with a constant spacing of 0.2 km and are symmetrical about the epicenter of the source. The synthetic data for this model and source-receiver geometry are shown in Fig. 3.9. Gaussian random noise has been added to the synthetic data. A NSR of 6 is used and represents a relatively high noise level. From Figs 3.9(a) and 3.9(c), we can see that the effective signals have been completely masked by the random noise, and hence we cannot identify the direct P- and S-waves within the waveform data. Manual picking of the direct P- and S-wave arrivals is impossible with such a high noise level.

The coordinates of the target area are set between 1 to 3 km in the X and Y directions, and between 2.2 to 3.5 km in the Z direction. This target volume is discretized with 45387 potential source positions with 50 m grid interval in the X, Y and Z directions. A total of 1001 origin times are scanned with a time interval of 1 ms. Fig. 3.10 shows the vertical and horizontal slices through the stacking functions at the maximum for the four migration-based location methods. The color in the figures exhibits the maximum-likelihood location of the source. As shown in Fig. 3.10, only the MCM can identify the true source location in the presence of the high noise level. The STA/LTA method locates the source correctly in the X and Z directions, but deviates 50 m in the Y direction. Both the envelope and kurtosis methods have very large deviations and fail to locate the correct source location in this situation. 3D profiles of the STA/LTA and MCM migration results are further displayed in Fig. 3.11. Compared with the

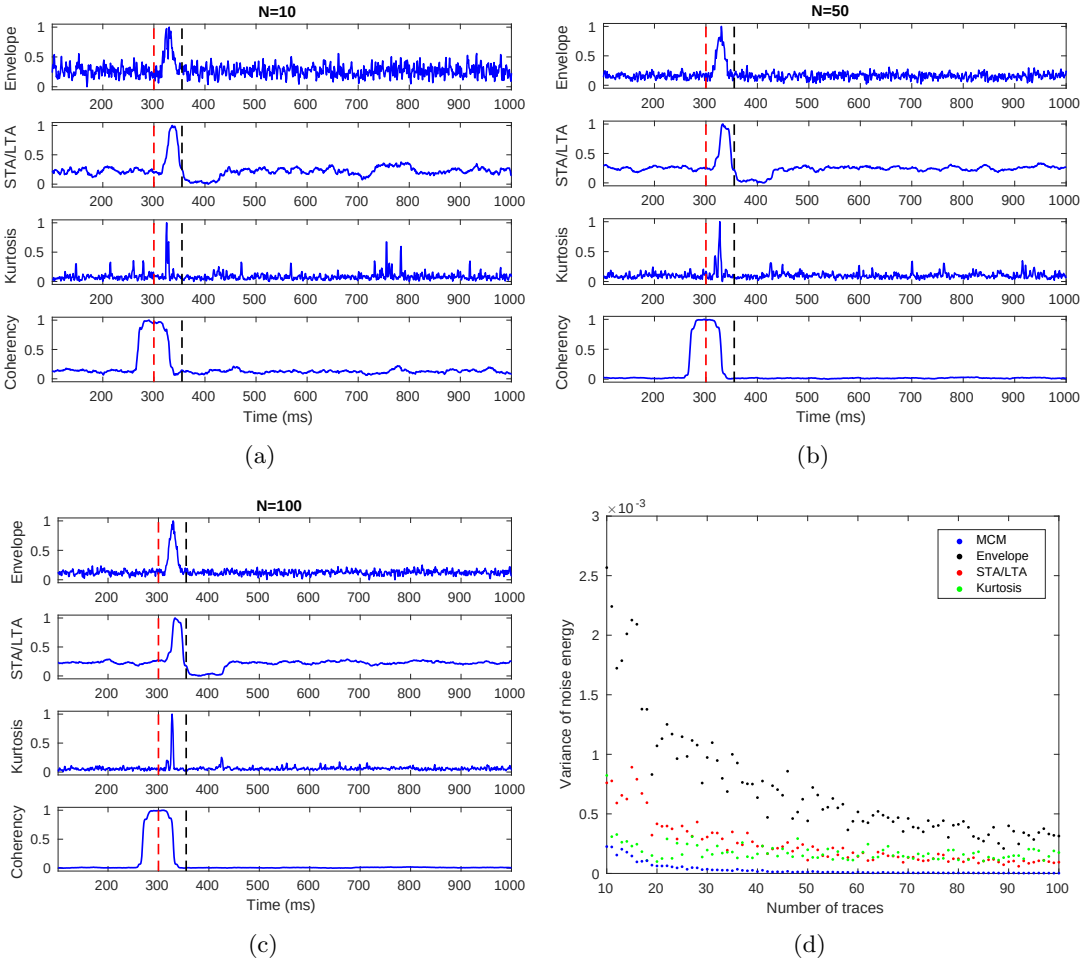

Figure 3.6: Stacking functions and variance of noise energy at the source position under different number of traces (N) for the four different migration methods (envelope, STA/LTA, kurtosis and MCM). NSR is 2 for all the figures. Red and black dashed lines show the origin and end time of the source respectively. Stacking functions when N is (a) 10, (b) 50 and (c) 100. (d) Variation of noise variances with different N. The results are obtained through Monte Carlo simulation. Black points show the envelope method, red points show STA/LTA method, green points show kurtosis method and blue points show the MCM method. Because the stacking energy is not at the same scale for different migration methods, the source prominence is calculated after normalizing the stacking functions between 0 and 1.

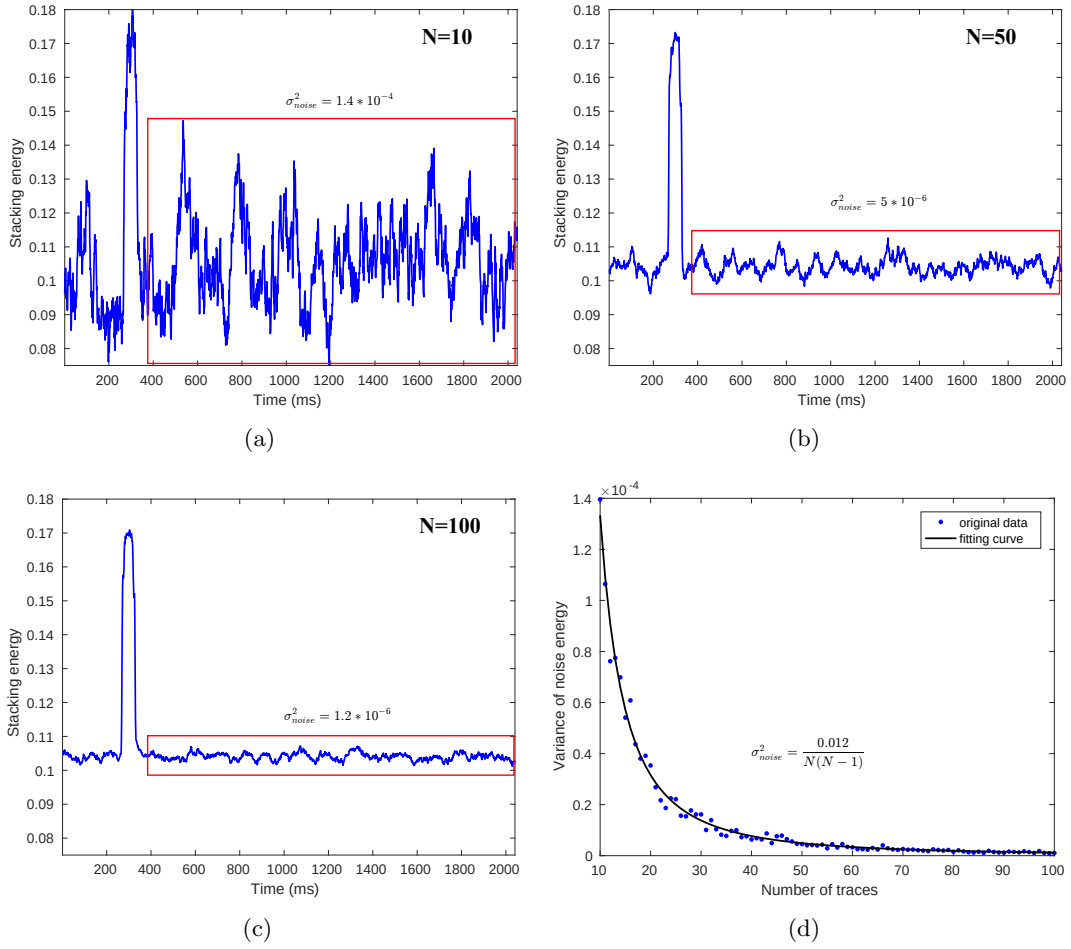

Figure 3.7: Stacking functions at the source position when the trace number (N) is (a) 10, (b) 50 and (c) 100 for the MCM method. (d) Variation of the variance of noise energy with different trace numbers at the source position for the MCM method. The results are obtained through Monte Carlo simulation. Blue points represent the calculated variance of noise energy, and the black line shows the fit to the variance data points. The fitting formula is also shown in the figure. The NSR is 4 for all the figures.

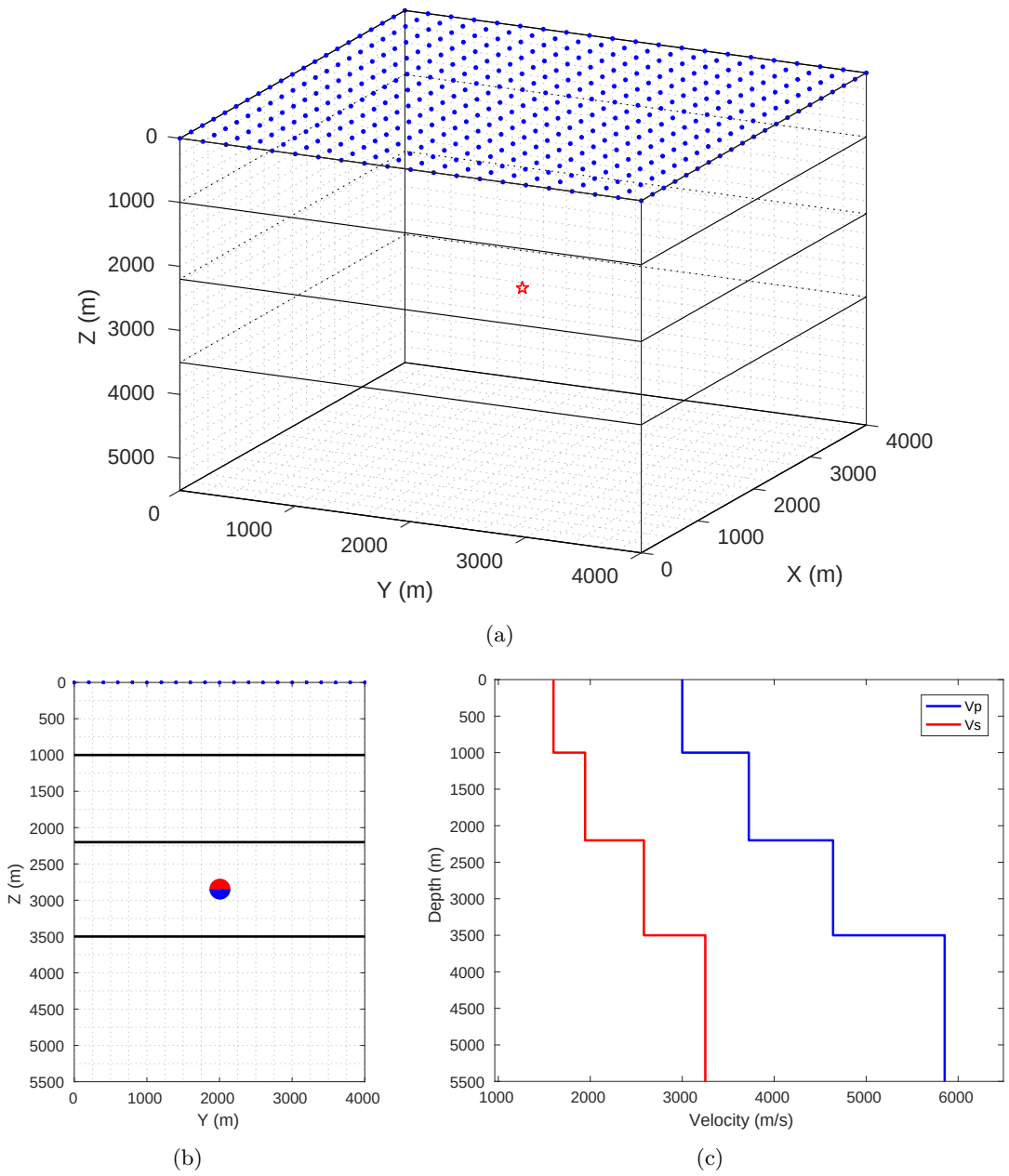

Figure 3.8: The velocity model and receiver geometry for the microseismic monitoring. (a) Layered model showing the velocity and surface array. The red star represents the vertical dip-slip source, blue points represent the surface receivers. 441 receivers are uniformly distributed on the free surface with 21 receiver lines in X direction, 21 receiver lines in Y direction and a lateral interval of 200 m. (b) Vertical profile of the layered model with a beach ball showing the moment tensor source. (c) P- and S-wave velocities used for the migration.

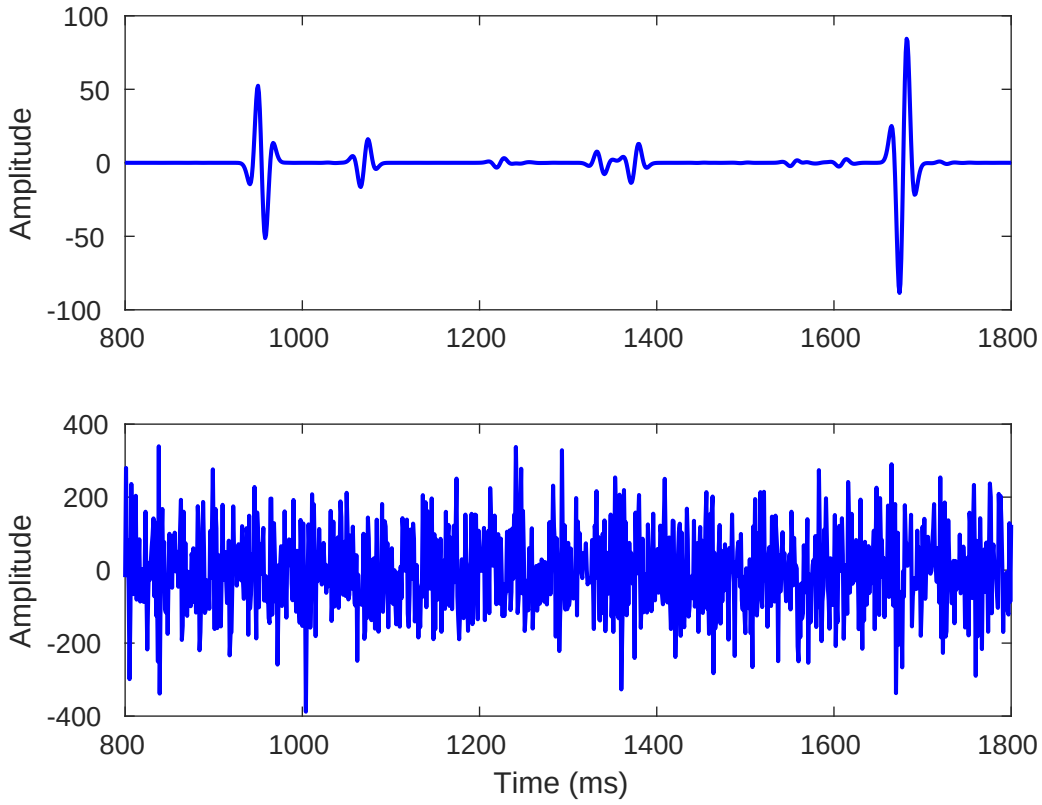

(a)

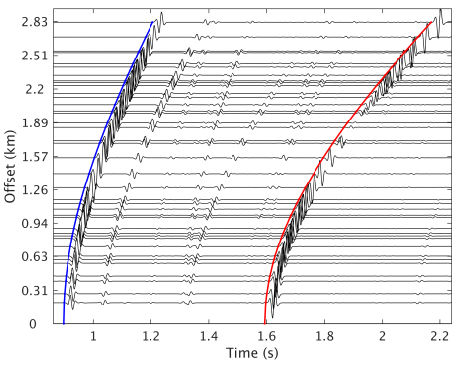

(b)

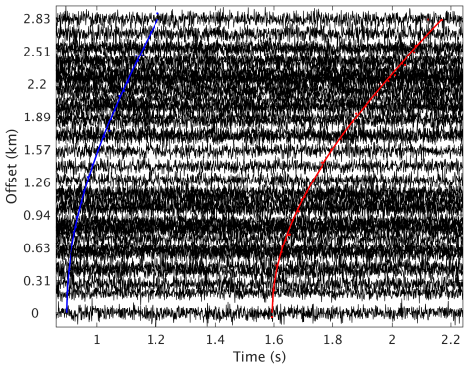

(c)

Figure 3.9: The synthetic noise free data (vertical component) and the data after adding noise. The NSR is 6. (a) Synthetic seismogram at trace number 305 (upper) and the same seismogram after adding noise (lower). (b) The record section of the synthetic noise free data. (c) The record section of the noisy data. Blue line shows the arrivals of the direct P-waves. Red line shows the arrivals of the direct S-waves.

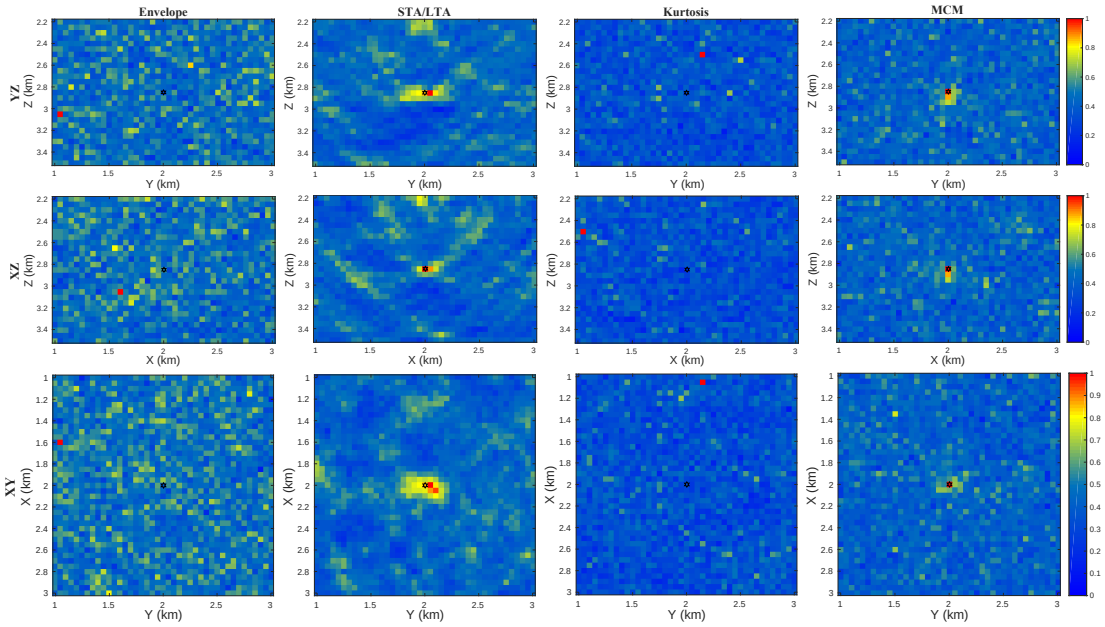

Figure 3.10: Profiles of the migration results through the normalized stacking functions at the stacking maximum for the four migration methods. NSR = 6. For better comparison of different migration results, all the stacking functions have been linearly normalized to the range between 0 and 1. Black hexagrams in the middle of the target area represent the true source location. The first column shows results of envelope, second column for STA/LTA, third column for kurtosis, fourth column for MCM. The first row shows YZ (vertical) profiles, second row shows XZ (vertical) profiles, third row shows XY (horizontal) profiles.

STA/LTA migration results, migration results of the MCM method have a more distinguishable source imaging effect with better source prominence and no location errors.

Fig. 3.12 shows the stacking functions at the correct source location for all the methods. Only the MCM and the STA/LTA methods have a recognisable stacked energy around the origin time of the source. The MCM method has a better source prominence compared with the other methods. Table 3.1 shows the location error of the different methods, and demonstrates the robustness of the MCM method over the other methods in terms of noise resistance.

3.4 Robustness and imaging weak events

Given the complexity of the fracturing process as well as geological heterogeneity, it is quite common that weak seismic events occur spatially with strong events within roughly the same time period (e.g. GutenbergRichter law). Imaging extremely weak events in the presence of larger events is difficult, because the signals of the large events have much larger amplitude and signal-to-noise ratio than the weak events. Furthermore, the reflected waves, multiples and coda waves of the large events potentially interfere with weak events, especially in complex geological structures. The robustness

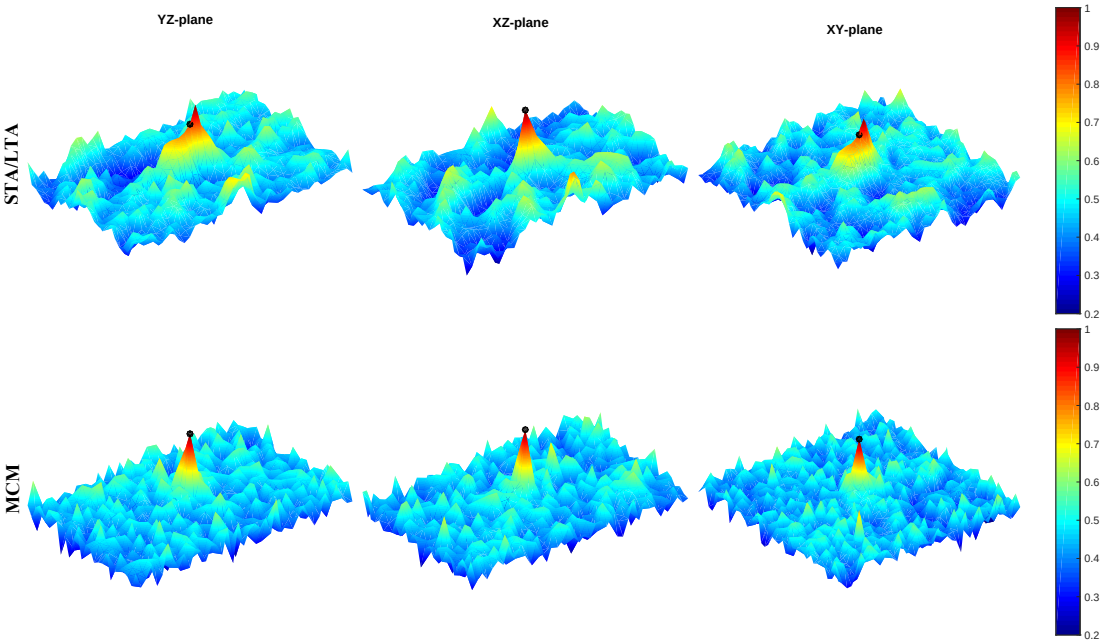

Figure 3.11: 3D profiles of the migration results through the maximum migrated value of normalized stacking functions for the STA/LTA and MCM methods. Black balls show the location of the source event. The first column shows YZ profiles, second column shows XZ profiles, third column shows XY profiles. The first row shows results of the STA/LTA method, second row for MCM.

Table 3.1: Location results of different methods and comparison with true source location.

	Source location				Location error			
	X (km)	Y (km)	Z (km)	T_0 (s)	ΔX (m)	ΔY (m)	ΔZ (m)	ΔT_0 (s)
True	2.00	2.00	2.85	0.100	-	-	-	-
Envelope	1.60	1.05	3.05	0.565	400	950	200	0.465
STA/LTA	2.00	2.05	2.85	0.136	0	50	0	0.036
Kurtosis	1.05	2.15	2.50	0.199	950	150	350	0.099
Coherency	2.00	2.00	2.85	0.081	0	0	0	-0.019

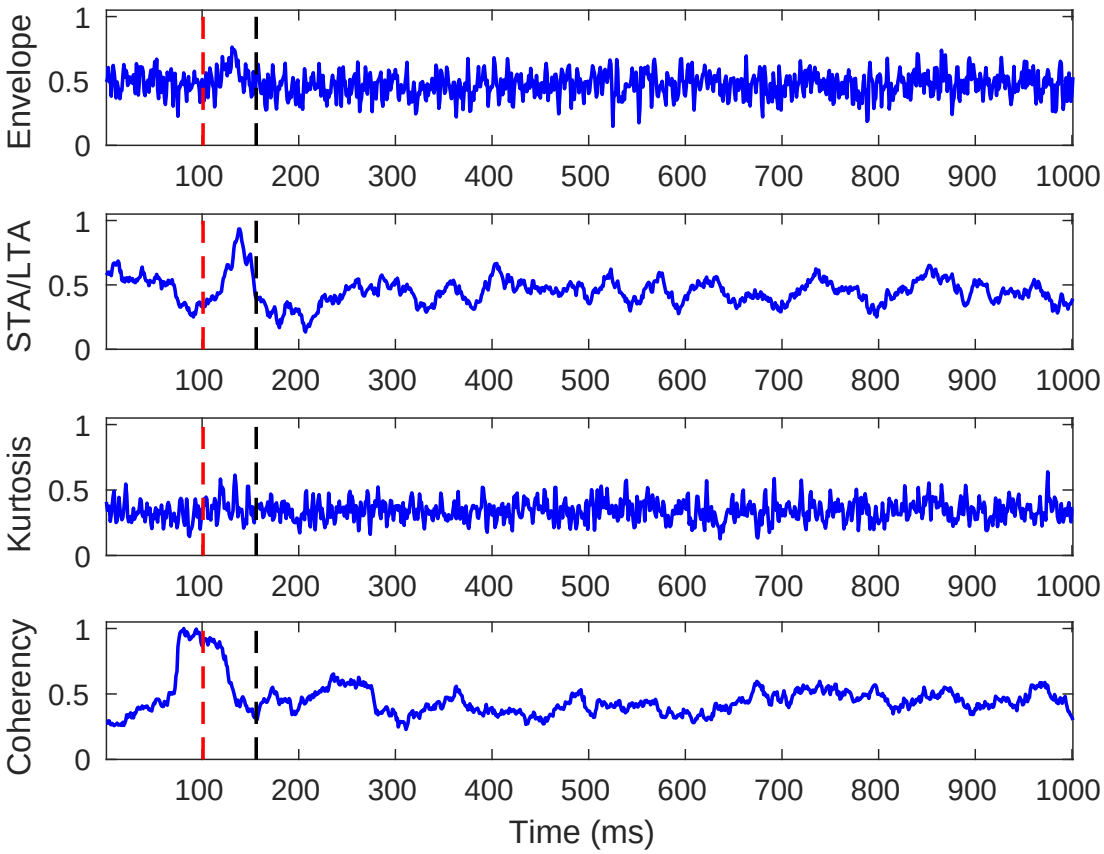

Figure 3.12: The stacking functions at the true source location for the four methods. The red and black dashed line shows the origin time and end time of the source respectively.

against interfering signals is critical for imaging weak events. In this section we test and compare the ability to image extremely weak events using different migration methods.

For pure amplitude-based migration methods, such as migration using amplitude, envelope and energy of the traces, the imaging results are often dominated by strong amplitude signals. From equation (3.3), we can see that the covariance between traces is normalized by the standard deviation of the traces. Thus the coherency between traces is not affected by the absolute amplitude of the recorded phases, and rather only affected by the resemblance of the waveforms. In this way, the MCM can resist interference from large events and balance the imaging results between strong and weak events. In fact the imaging quality of the events in the MCM method is not affected by the absolute amplitude of the events, but mainly influenced by the signal-to-noise ratio of the signals of the corresponding events. Even though the signal of large events have higher signal-to-noise ratios, they are not largely coherent at the true locations of other weak events. Thus the overall coherency of the large event interference is not comparable with respect to the local coherency of the weak signals. For the statistic-based migration methods based on characteristic functions of a single trace, such as the STA/LTA and kurtosis methods, strong interference signals over large scales can lead to non-physical source images. However, for the MCM method, as long as the interference signals are not coherent over a large scale between traces, the interference will not locally focus in the imaging domain.

The robustness of the different migration methods in resisting strong interference is tested using synthetic waveform traces. Fig. 3.13 shows the time aligned traces and the stacking functions at the correct source location. We have added large coherent interference signals into 23 of the traces (Fig. 3.13(b)). The amplitude of the interference signals is 32768 times the amplitude of the weak signals to be detected, chosen to make the seismic magnitude of the events 3 times larger. With such an extremely strong energy contrast, only the MCM method correctly locates the weak signals and suppress the large interference signals at the same time (Fig. 3.13(c)). The results of the other methods are dominated by the large interference signals. The STA/LTA method can successfully detect the weak signals, however shows an even stronger indication of the large interference signals. Here we have added coherent interference signals, but if the interference signals in different traces are not coherent, even more significant interference suppression can be expected for the MCM method.

Fig. 3.14 shows the same velocity and geometry model as used in Fig. 3.8 but with two double-couple sources placed at depths of 2.55 and 3.15 km, respectively. Event 1 is a vertical dip-slip source with an origin time of 0 s and event 2 is a 45 degree dip-slip source with an origin time of 0.1 s. Event 1 and event 2 have the same source time function, which means the recorded signals of event 1 and 2 are coherent. In this situation, imaging the source events will be more difficult for the MCM. The seismic moment of event 1 is 1024 times that of event 2, such that the magnitude of event 1

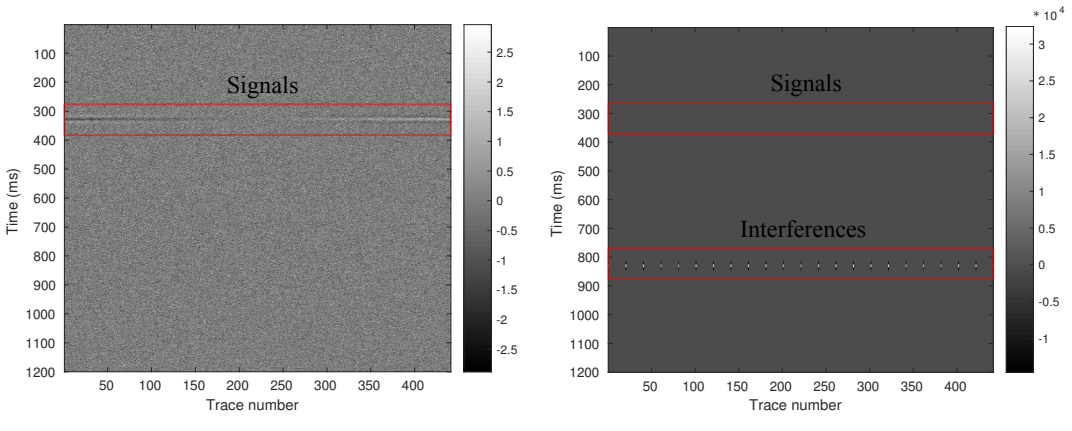

(a) (b)

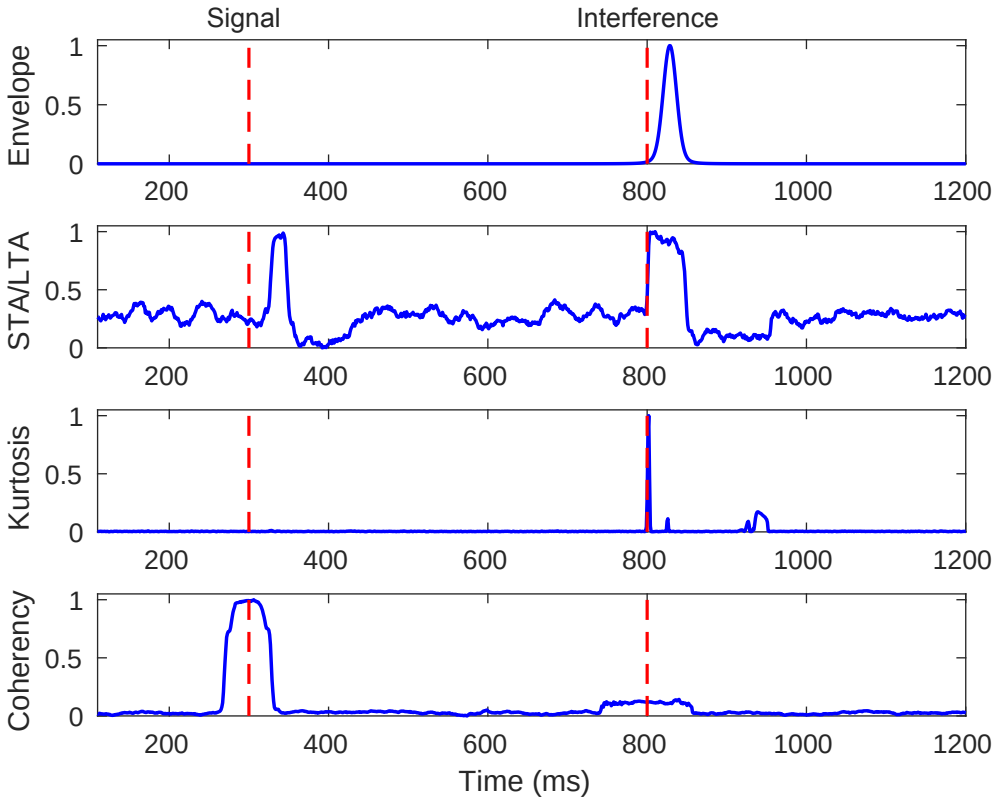

(c)

Figure 3.13: (a) The time aligned traces with NSR = 3. The origin time for the weak signals to be detected is 300 ms. (b) The time aligned traces after adding strong coherent interference signals into 23 of the traces in (a). The amplitude of the interference signals is 32768 times the amplitude of the weak effective signals. After adding interferences, the effective signals are invisible because of the enormous amplitude differences between the signals and the interferences. The origin time of the interference signals is 800 ms. Signals and interferences are annotated in the figure, respectively. (c) Stacking functions of the four different methods with red dashed lines showing the origin times of the weak signals and interference signals.

is twice as large. In Fig. 3.14(b), the amplitudes of the P- and S-waves from event 1 are so large that we can hardly identify the P- and S-wave arrivals of event 2. The multiples and reflected waves from event 1 have much larger amplitude than the direct waves of event 2.

Fig. 3.15 shows the vertical and horizontal slices through the true location of event 1 for the four migration-based location methods. Because event 1 has a much larger magnitude, we obtain very good energy focusing of event 1 for all four methods. The vertical profiles of the envelope, STA/LTA and kurtosis methods show a similar pattern around the location of event 1, which is related to the source-receiver geometry. The resolution of STA/LTA is lower compared with the other methods. It is worth noting that for the STA/LTA method, the maximum stacking value is not at the correct location of event 1, and is 1 grid point deeper. This leads to a 50 m location deviation for event 1, while the other methods all locate accurately. The poor performance of the STA/LTA method is likely due to the relatively lower resolution in the vertical direction, which results from the inaccurate estimation of the origin time of the event.

Fig. 3.16 shows vertical and horizontal slices through the true location of event 2 for the four migration-based location methods. Due to strong interference from event 1 and the weak amplitudes of event 2, the energy focusing of event 2 is not as good as event 1. The interfering energy from event 1 can be seen in the migrated profiles, and significantly influences the correct location of event 2. Compared to other methods, the MCM method is better at suppressing the strong interference from event 1 and so results in good imaging results for the vertical profiles. In the horizontal section (the bottom right one in Fig. 3.16), it is apparent that the MCM methods suffers strong interference from event 1. However the energy focusing for event 2 is still recognisable. In this situation, a well-designed source identification algorithm is needed to correctly identify the weak event. We can see it is very hard to simultaneously image seismic events whose signals are interfering and which have magnitude differences larger than 2. Here the signals of event 1 and 2 are coherent. If they are not coherent, a better imaging result of event 2 can be achieved using the MCM method.

Fig. 3.17 shows the stacking functions at the true locations of event 1 and 2. The four methods all exhibit very good migration results for the strong event 1. However for the weak event 2, only the MCM method indicates good energy focusing at the correct origin time. The envelope, STA/LTA and kurtosis methods fail to suppress the interfering energy from event 1. The kurtosis method exhibits severe oscillation in the stacking functions and the STA/LTA method shows multiple-peaks in the stacking functions, which are detrimental to the correct identification of event 2.

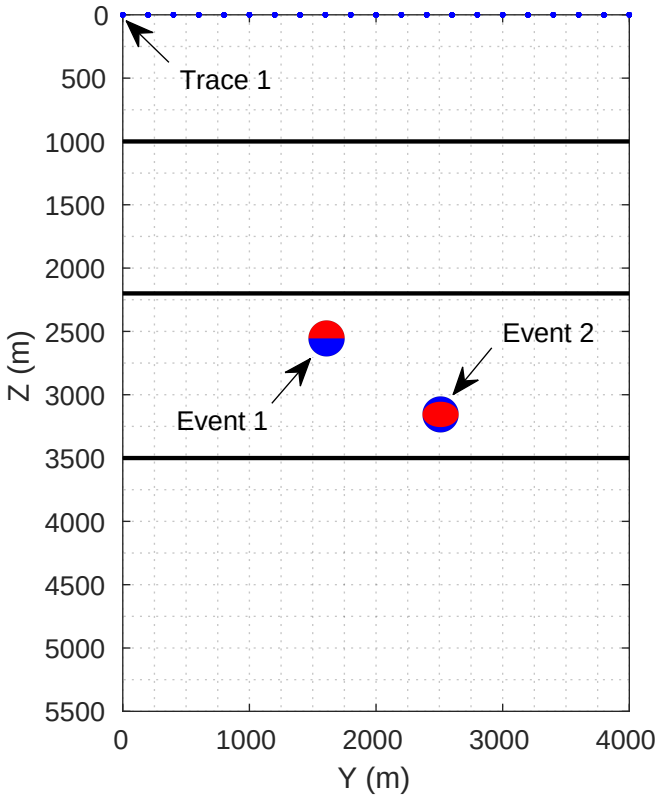

(a)

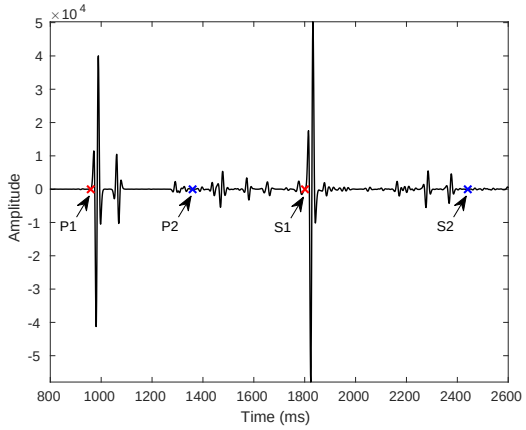

(b)

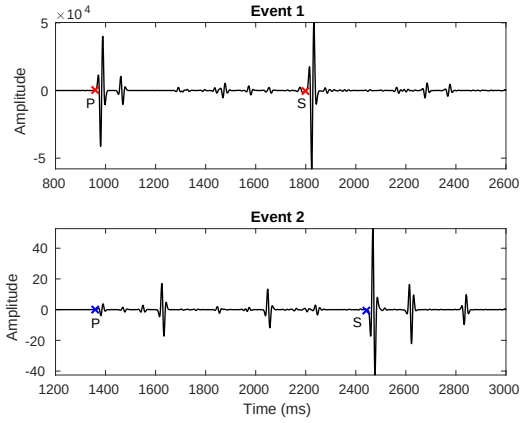

(c)

Figure 3.14: (a) Model profile which shows the positions of two events. Event 1 is a vertical dip-slip source and event 2 is a 45 degree dip-slip source. Beach balls are used to show the radiation pattern of the moment tensor sources. (b) The recorded seismogram in trace 1. The red crosses show the P- and S-wave arrivals of event 1. The blue crosses show the P- and S-wave arrivals of event 2. (c) Separate wavefields of event 1 and 2.

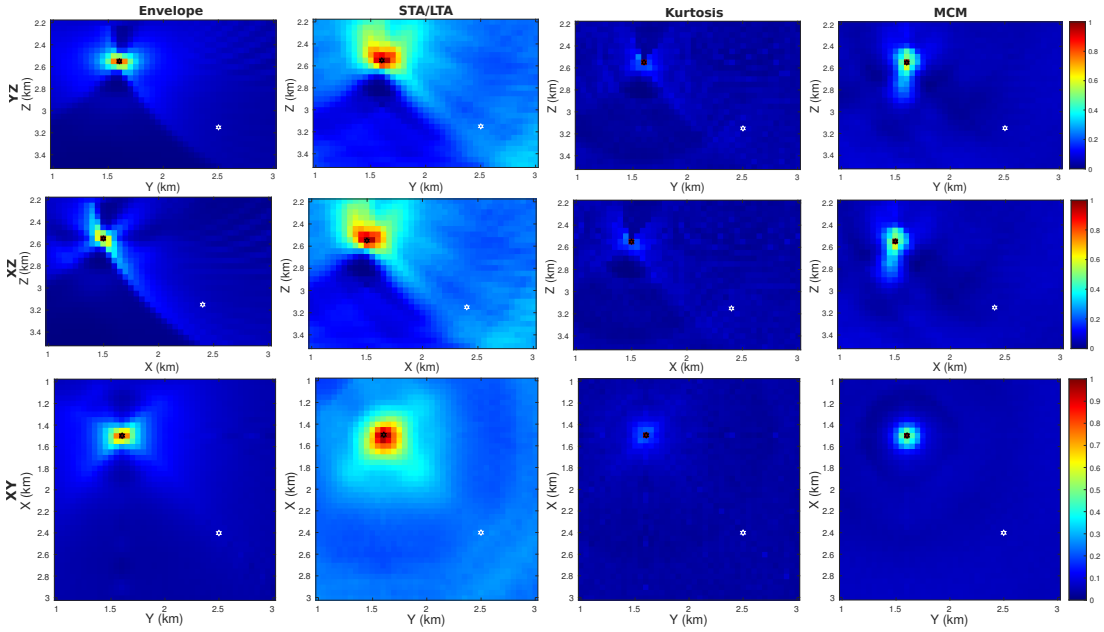

Figure 3.15: Profiles of the migration results through the true location of event 1 for the four migration methods. The slices are taken at the time of maximum stacking value for event 1. The stacking functions have been linearly normalized between 0 and 1. The black hexagram in the upper left part of the model represents the true location of event 1. Event 2 is also projected on the profile, shown as the white hexagram in the lower right part of the model. The first column shows results of envelope, second column for STA/LTA, third column for kurtosis, fourth column for MCM. The first row shows YZ (vertical) profiles, second row shows XZ (vertical) profiles, and third row shows XY (horizontal) profiles.

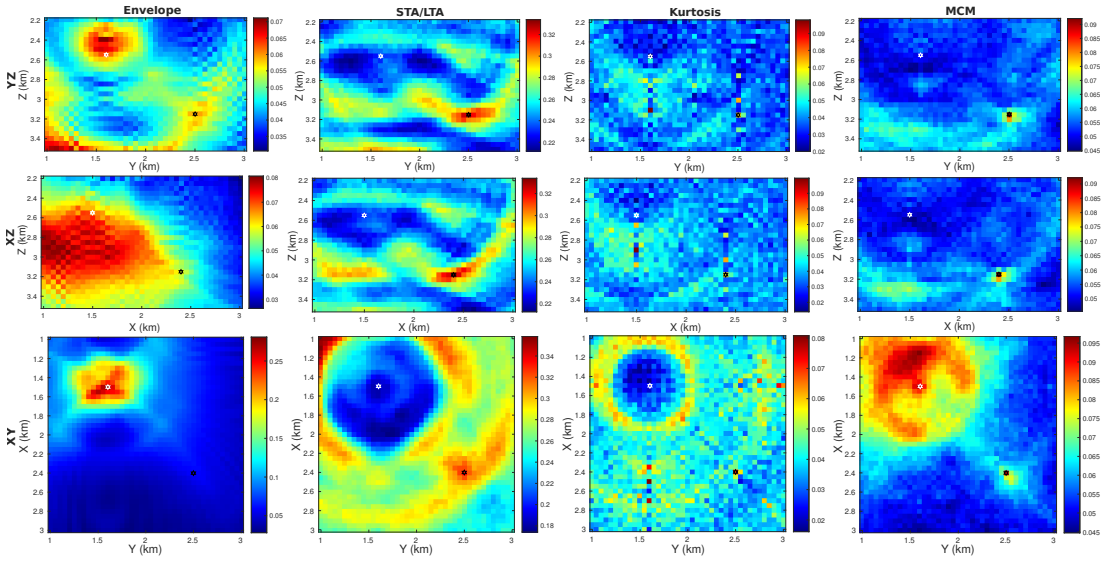

Figure 3.16: Profiles of the migration results through the true location of event 2 for the four migration methods. The slices are taken at the time of maximum stacking value for event 2. The black hexagram in the lower right part of the model represents the true location of event 2. Event 1 is also projected on the profile, shown as the white hexagram in the upper left. The first column shows results of Envelope, second column for STA/LTA, third column for kurtosis, fourth column for MCM. The first row shows YZ (vertical) profiles, second row shows XZ (vertical) profiles, third row shows XY (horizontal) profiles.

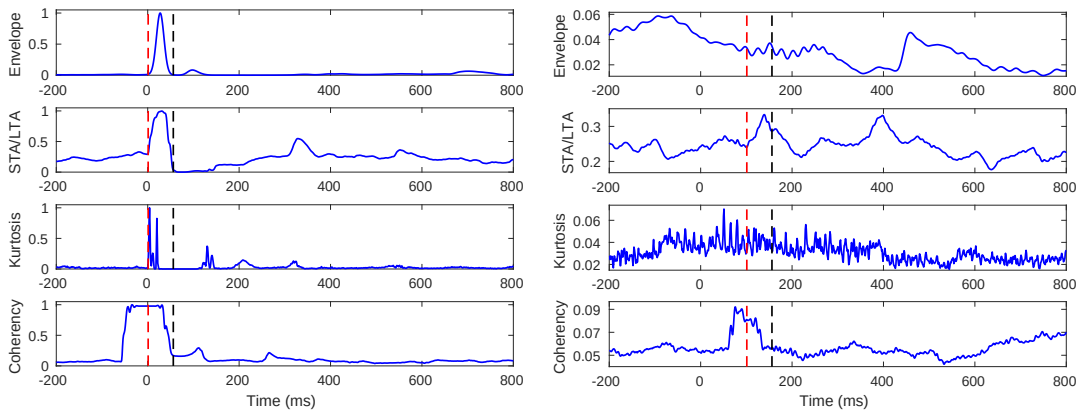

Figure 3.17: The stacking functions at the true source locations of (a) event 1 and (b) event 2 for the four methods. The red and black dashed line shows the origin time and end time of the event 1 and 2 respectively.

3.5 Influence of velocity model

Our MCM location method is applicable to different velocity models, including anisotropy, as long as a sufficiently accurate traveltime table can be built. However in practice, an accurate velocity model is not always possible to obtain. Typically an inaccurate velocity structure may cause large deviation in source location (Usher et al., 2013). The deviation in source location will lead to an accumulated error in the source mechanism determination and make source mechanism characterization difficult (Grigoli et al., 2016). In this section, we will discuss the influence of uncertainties in velocity model on source location.

In order to test the influence of the velocity model on source location, we use three different velocity models to generate the traveltime table for migration. One is the true layered velocity model, which will produce the correct traveltime table for the P- and S-waves. The other two are homogeneous velocity models, representing the simplest possible models. For the two homogeneous models, the first is obtained by calculating the root-mean-square (RMS) velocity of the top three layers, and leads to a model with velocity too fast for calculating the correct traveltime table compared with the true velocity model. Using a high velocity model, the arrival times of the P- and S-waves are shifted earlier. The second homogeneous model is relatively slow compared to the real model, which will delay the arrival times of the P- and S-waves. The P- and S-wave velocities of the high velocity model are 3.7984 km/s and 2.0437 km/s, respectively, which are the RMS velocities of the true model. The P- and S-wave velocities of the low velocity model are 3.362 km/s and 1.772 km/s, respectively, which are the arithmetic mean velocities of the first two layers of the true model. These two velocity models have different Vp/Vs ratios which adds a further element of variability.

If a homogeneous model instead of a true layered model is used in the migration, the migration results will tend to have deviations in vertical direction (Figs 3.18-3.19) because the receivers are at the surface. The location deviations depend on the amount of over/under prediction of the true velocity model. Here the recording array is symmetrical about the epicenter, thus the event is well constrained in the horizontal direction. If the array were not symmetrical about the epicenter, horizontal deviations in location would also be expected. The different migration methods exhibit different patterns in the imaging results (as shown in Figs 3.18-3.19). The kurtosis and MCM methods have higher resolution compared to the envelope and STA/LTA methods. For all four methods, if an inaccurate velocity model is used, there will be energy focused at both shallower and larger depth than the true source location. The inaccurate velocity model singularizes the trade-off between location depth and estimated origin time for surface array. In the shallower part, the energy tends to focus at a later time compared to the true origin time of the event, while in the deeper part, the energy tends to focus earlier. The location results using different velocity models are shown in Table 3.2. If a low velocity model is used (Fig. 3.18), the located event is deeper than the true source location (except STA/LTA method). While if a high velocity model is used (Fig. 3.19), the located event is shallower than the true source location (except envelope method). The unusual behaviour of STA/LTA and envelope methods probably comes from the relatively low resolution in source location and more severe trade-off between location depth and estimated origin time for the two methods (see Figs 3.18 and 3.19). The location results of the MCM and kurtosis methods in the high velocity model only have a deviation of a single grid point (50 m). Here, because the RMS velocity is used to construct the high velocity model, location results in the high velocity model are better (except for STA/LTA). Compared with other methods, the MCM and kurtosis methods are less sensitive to the velocity model (especially when overpredicting the model velocities) and have higher imaging resolution.

3.6 Source location in complex models

Subsurface heterogeneity can affect the recorded waveforms at different stations. In order to test the performance of our MCM method in the presence of strong heterogeneity, we compare the location performance of the MCM with other migration-based methods on a complex 3D overthrust model (Aminzadeh et al., 1997). The P-wave velocity of the overthrust model are shown in Figs 3.20 and 3.21, which are widely used to test and verify various geophysical algorithms (Virieux & Operto, 2009, Yuan et al., 2015, Shi et al., 2018). The adopted overthrust model has a size of 4 km $\times$ 4 km $\times$ 0.93 km in the X, Y and Z directions. As shown in Fig. 3.21, the overthrust model shows many complex structures including numerous thrust faults and fluvial deposits, which allows us to study the influence of heterogeneity on waveform coherency and

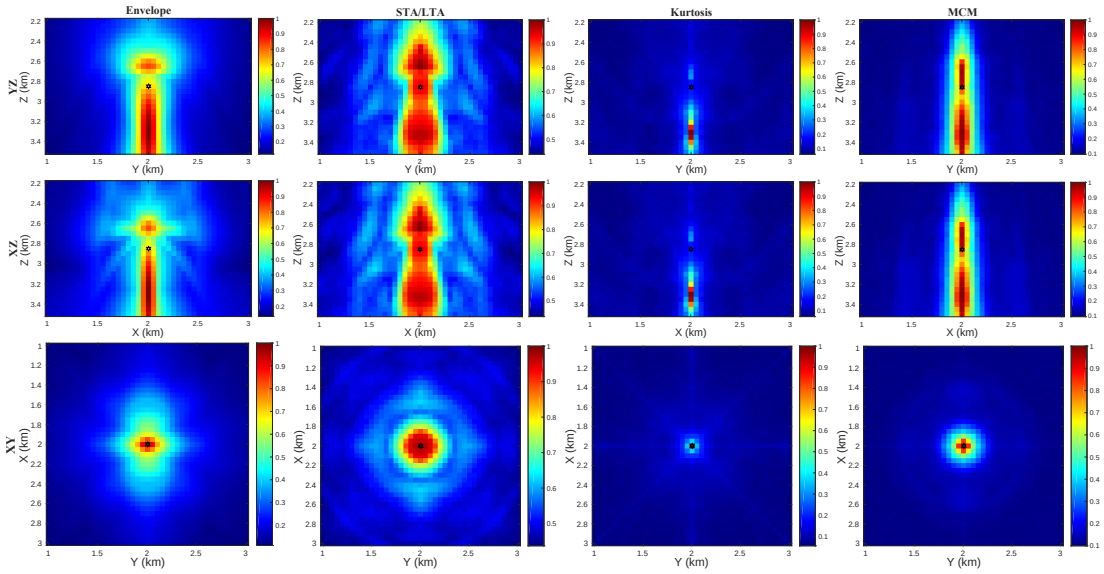

Figure 3.18: Profiles of the migration results using the low velocity model for the four methods. The profiles are obtained by projecting the maximum values along the time domain and the corresponding directions (i.e. for YZ profiles, projecting along the X direction; for XZ profiles, projecting along the Y direction; for XY profiles, projecting along the Z direction). The black hexagram in the middle of the figures represents the true source location. The first column shows results of envelope, second column for STA/LTA, third column for kurtosis, fourth column for MCM. The first row shows YZ (vertical) profiles, second row shows XZ (vertical) profiles, third row shows XY (horizontal) profiles.

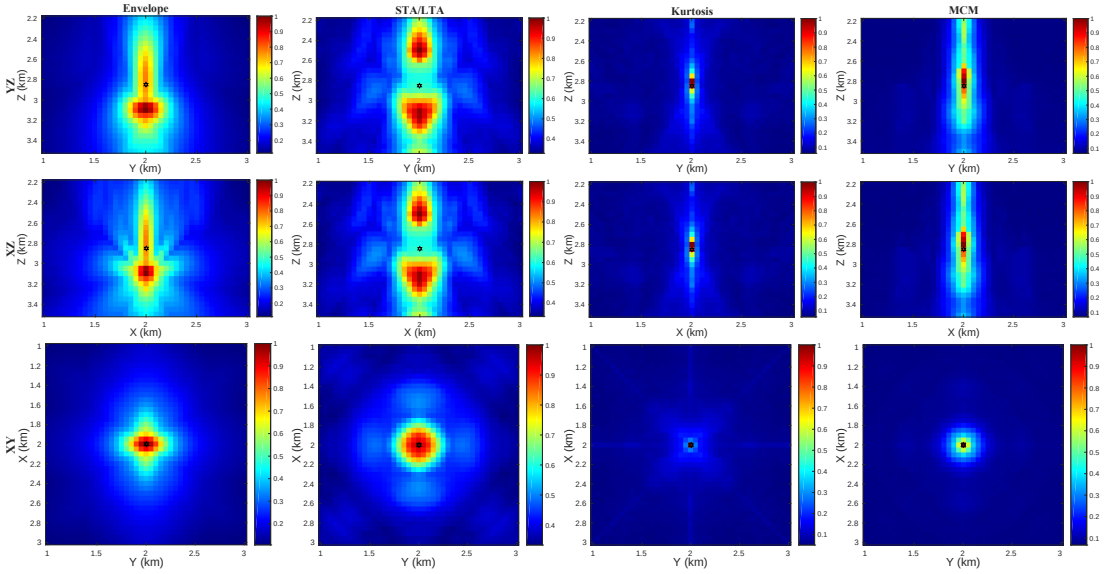

Figure 3.19: Profiles of the migration results using the high velocity model for the four methods. The profiles are obtained by projecting the maximum values along the time domain and the corresponding directions (i.e. for YZ profiles, projecting along the X direction; for XZ profiles, projecting along the Y direction; for XY profiles, projecting along the Z direction). The black hexagram in the middle of the figures represents the true source location. The first column shows results of envelope, second column for STA/LTA, third column for kurtosis, fourth column for MCM. The first row shows YZ (vertical) profiles, second row shows XZ (vertical) profiles, third row shows XY (horizontal) profiles.

Table 3.2: Location results of different methods and comparison with true source location using the low and high velocity models.

		Source location				Location error			
		X (km)	Y (km)	Z (km)	T_0 (s)	ΔX (m)	ΔY (m)	ΔZ (m)	ΔT_0 (s)
	True	2.00	2.00	2.85	0.100	-	-	-	-
Low	Envelope	2.00	2.00	3.30	-0.056	0	0	450	-0.156
	STA/LTA	2.00	2.00	2.65	0.105	0	0	200	0.005
	Kurtosis	2.00	2.00	3.30	-0.081	0	0	450	-0.181
	Coherency	2.00	2.00	3.30	-0.135	0	0	450	-0.235
High	Envelope	2.00	2.00	3.10	0.118	0	0	250	0.018
	STA/LTA	2.00	2.00	2.50	0.379	0	0	350	0.279
	Kurtosis	2.00	2.00	2.80	0.161	0	0	50	0.061
	Coherency	2.00	2.00	2.80	0.182	0	0	50	0.082

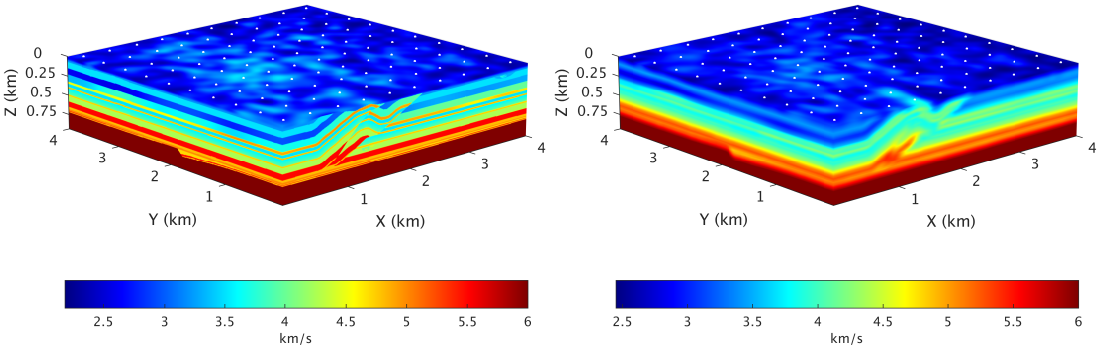

Figure 3.20: P-wave velocity model of the 3D overthrust model (Aminzadeh et al., 1997). White dots show the surface projection of the monitoring arrays. Left: original velocity model used for full wavefield modeling. Right: smoothed velocity model used for source location.

source location. Full wavefields for this model are generated using the finite difference modeling technique of Shi et al. (2018). A vertical strike-slip source is placed in the middle of the model, which has coordinates of (1.995, 1.995, 0.46) km in the X, Y and Z directions (Fig. 3.21). A Ricker wavelet with a peak frequency f_m of 40 Hz and a time delay of $1.1/f_m$ is used as the source time function in the simulation.

A monitoring array consisting of 100 receivers (10 $\times$ 10 receiver lines at an average horizontal interval of 400 m and at depth of 150 m) is used to record the three component particle velocities with a sampling rate of 5000 samples/s in the simulation (Fig. 3.20). The receivers lie in different geological units and the geological structures beneath the receivers are also different. The thicknesses of most layers in the overthrust model are about 15 - 90 m, which are comparable to the average wavelengths of P-wave (100 m) and S-wave (59 m). Therefore, due to complex structures of the model and the velocity heterogeneity, scattering is strong in the simulation. As can be seen in the record section shown in Fig. 3.22, the recorded wavefields are very complex with

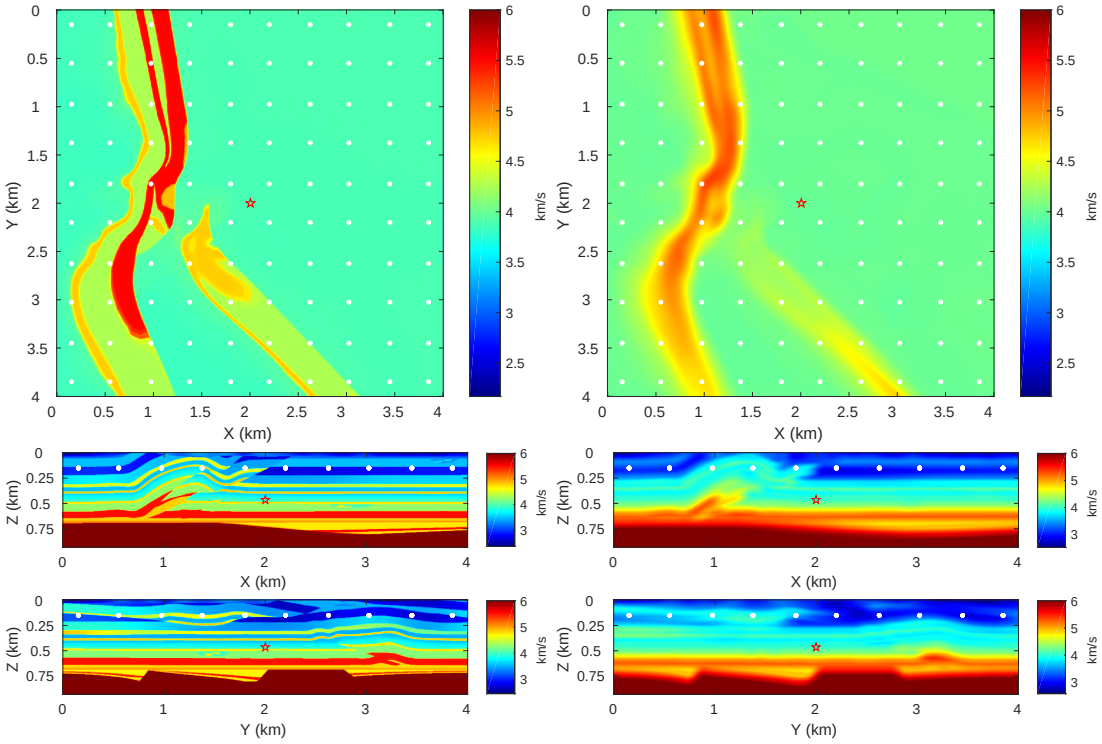

Figure 3.21: P-wave velocity profiles of the 3D overthrust model through the source point. Red star shows the location of the source and white dots show the projection of receivers. First row: horizontal profiles at the depth of 0.46 km. Second row: vertical profiles at 1.995 km in the Y direction. Third row: vertical profiles at 1.995 km in the X direction. Left: original velocity model used for full wavefield modeling. Right: smoothed velocity model used for source location.

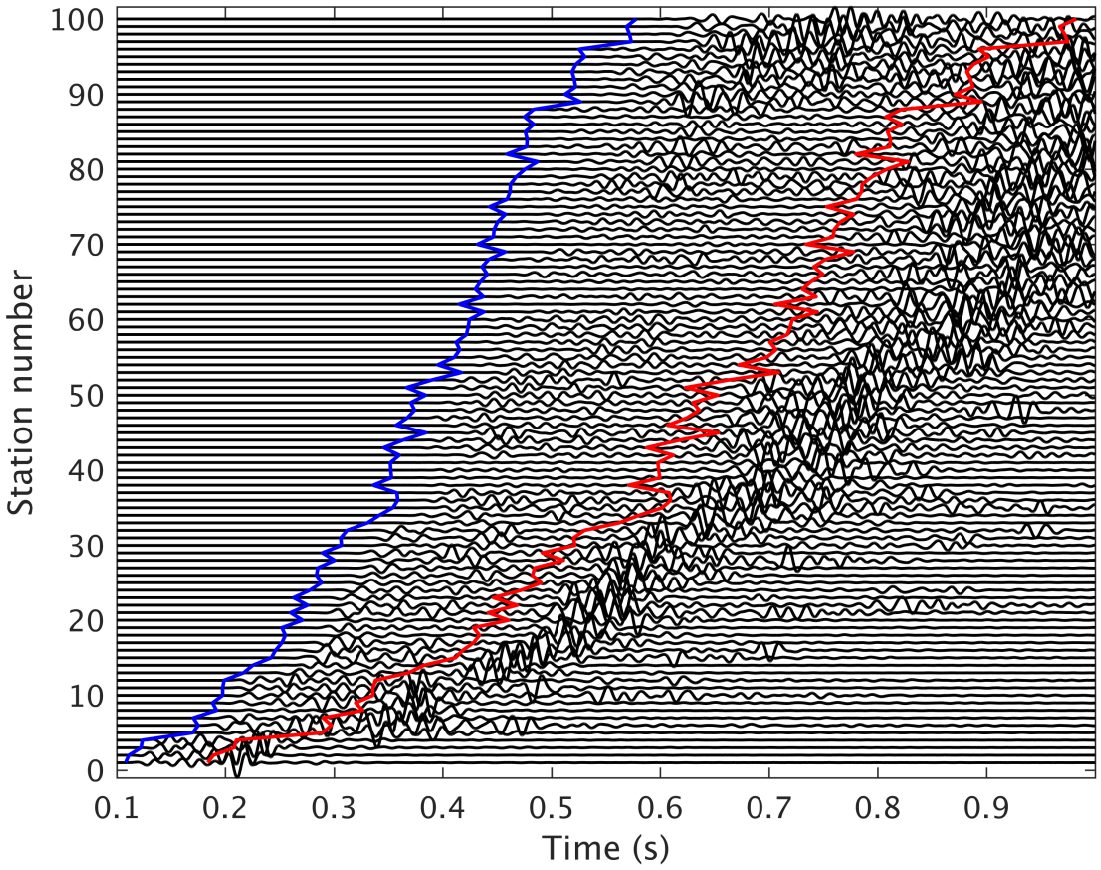

Figure 3.22: Record section of particle velocities in the Z direction for the 3D overthrust model. Blue line shows the calculated arrival times for the direct P-waves and red line shows the calculated arrival times for the direct S-waves. The recorded traces are numbered and aligned vertically according to horizontal offsets. Note that the calculated arrival times of the direct P- and S-waves are not smooth (zigzagged) because of strong 3D heterogeneity of the model.

strong evidence of scattering and coda waves. Because of the strong 3D heterogeneity and complex structures of the model, the calculated arrival times of the direct P- and S-waves are not smooth (Fig. 3.22).

Waveform migration is performed on 102400 potential source positions (80×80×16 in the X, Y and Z directions respectively) with 50 m interval. Origin times from -0.3 s to 0.3 s with an interval of 1 ms are scanned. In practice, it is almost impossible to obtain an exact velocity model. Therefore waveform migrations are conducted on a smoothed velocity model which is obtained by using a box convolution kernel with a size of 21 grid points (Figs 3.20 and 3.21). Fig. 3.23 shows the migration results using the smoothed velocity model for the four methods, i.e. envelope, STA/LTA, Kurtosis migration and the MCM. The black ball shows the correct source position. Apart from the envelope migration, the other three methods can all correctly locate the source position. MCM and STA/LTA migration perform the best. Kurtosis migration has relatively higher imaging resolution. However the stacking results of kurtosis migration

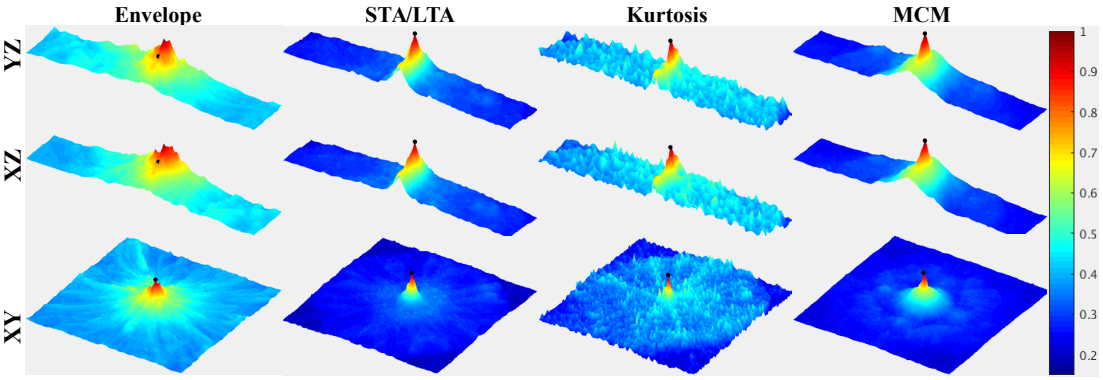

Figure 3.23: 3D profiles of the migration results using the smoothed overthrust velocity model for the four methods. The profiles are obtained by projecting the maximum stacking values along the time domain and the corresponding directions (i.e. for YZ profiles, projecting along the X direction; for XZ profiles, projecting along the Y direction; for XY profiles, projecting along the Z direction). Black balls show the true position of the source event. The migrated volumes of different methods are all linearly normalized to 0 - 1. The first column shows results of envelope, second column for STA/LTA, third column for kurtosis, fourth column for MCM. The first row shows YZ (vertical) 3D profiles, second row shows XZ (vertical) 3D profiles, third row shows XY (horizontal) 3D profiles.

exhibit much more oscillations than the other results, which might come from interferences of the scattering waves and multiples. Therefore compared to the other three methods, kurtosis migration tend to be more unstable. Because of the influence of scattering waves and model heterogeneity, waveform coherency between different stations decreases. The stacked waveform coherency at the correct source location is 0.64. The decreased waveform coherency will weaken the noise resistance of the MCM method, however MCM can still obtain stable and accurate location results if the coherency of recorded waveforms are not completely destroyed by the model heterogeneity or noise. Therefore MCM can be applied to complex models where scattering and coda waves are generated and obtain reliable and accurate location results using a smoothed version of the complex velocity model.

3.7 Discussion

The calculation of multichannel coherency also brings extra computations for the MCM method. With precalculated characteristic functions, the calculation of conventional migration-based method is proportional to $N_s * N_t * N$ (N_s is the number of image points, N_t is the number of searching origin time points, N is the number of stations). With the two channel-based coherency (equation (3.3)), the calculation of the MCM method is proportional to $N_s * N_t * (N * (N-1)/2) * 10M_t$ (M_t is the length of the coherency analysis time window). Compared with conventional migration method, the calculation burden of the MCM method is increased greatly. However, the MCM location method can be implemented quite efficiently. At every imaging point, the calculation of the correlation

coefficient matrix (equation (3.10)) and the stacking coherency (equation (3.11)) are independent of all other imaging points. The coherency calculation is also independent of the various origin times. Thus the whole calculation of the MCM method is highly parallelizable on distributed computing architectures. Specifically, the MCM location algorithm can be parallelized on a large scale according to image points and/or origin times using graphics processing unit (GPU). Implementation of a parallelized MCM location algorithm over a large amount of calculation nodes or GPUs would make the method a suitable real time monitoring method.

For MCM using surface arrays, the horizontal resolution of the imaging results is higher than the vertical resolution (Fig. 3.10) and this is due to the adopted time window in the coherency analysis. When moving the image point slightly in the vertical direction from the true source location, the arrival times of the P- and S-phases for all the traces will increase or decrease simultaneously. However, due to the use of a coherency analysis window, the P- and/or S-phases arrivals can still be incorporated into the time window of the coherency analysis, which contributes to a high coherence value. When moving the image point slightly in the horizontal direction from the true source location, the arrival times for different traces will increase or decrease differently according to the relative position of the source and receivers. Thus only a small part of P- and/or S-phases arrivals in the received data will fall into the coherency analysis window. Thus the stacking of the coherence value decreases more rapidly in the horizontal direction than in the vertical direction. Thus the sensitivity of the stacking function in the horizontal direction contributes to the higher horizontal resolution. It is feasible to increase the imaging resolution by using a smaller coherency analysis window. However, a smaller time window is detrimental for noise suppression. In practice, an optimum trade-off between the imaging resolution and noise suppression is required. Adaptively adjusting the coherency analysis window according to the noise level of the data could be a good way to give consideration to the imaging resolution and noise suppression.

For the envelope and STA/LTA migration, large deviations in the vertical direction are often observed especially when the adopted velocity model for migration is inaccurate (as shown in Figs 3.18 and 3.19). The characteristic functions of the envelope and STA/LTA migration cannot accurately identify the arrival of P- and S-waves. The local maximum values in the characteristic functions of the envelope and STA/LTA methods often appears slightly later than the exact arrival times of direct P- and S-waves. Due to the inaccurate estimation of the arrival times of direct P- and S-waves, the envelope and STA/LTA migration suffer more severe trade-off between location depth and estimated event origin time compared with other methods. The spatial imaging resolution of the envelope and STA/LTA methods is lower compared to the MCM and kurtosis method. For conventional migration-based location methods, the spatial and temporal imaging resolution is related to the local shape of the characteristic functions

nearby the arrivals of direct P- and S-waves. The sharper the characteristic function, the higher the imaging resolution. A wide waveform bandwidth in characteristic functions nearby the arrivals of direct P- and S-waves will make it hard to distinguish the traveltime difference between adjacent image points. The characteristic functions of the envelope and STA/LTA method have a wide waveform bandwidth nearby the direct P- and S-wave arrivals, thus lead to a relatively low imaging resolution. The waveform bandwidth nearby the direct P- and S-wave in the characteristic function arrivals can be used to estimate the location uncertainties in the migration-based location method. In contrast, due to the application of derivatives in the kurtosis migration method (Langet et al., 2014), the characteristic function shows more accurate representation for the arrival times of direct P- and S-waves and has a narrower waveform bandwidth nearby the direct P- and S-wave arrivals. Thus for the kurtosis method, the location depth has less uncertainties and trade-off with estimated origin time, and the imaging resolution is higher compared to envelope and STA/LTA methods. MCM is applied directly to original seismic waveforms, and the stacked pairwise waveform coherency decreases rapidly when imaging points deviate from the true source location. Therefore, MCM has high imaging resolution and less location uncertainty compared to conventional migration methods.

In the MCM method, the length of coherency analysis time window is the only parameter that need to be adjusted. Because the imaging result of the MCM method is not very sensitive to the length of the coherency analysis time window, the time window length can be easily determined according to the length of the source time function, frequency band of the data and noise level. Normally the noise level is the major factor that influences the choice of time window. In contrast, the STA/LTA and kurtosis methods have several parameters to adjust, such as time window and frequency band. The migration performance is often highly depend on the choice of these parameters. In practice, it is difficult to obtain a set of optimum parameters that are suitable for all seismic events in the dataset.

In practice, seismic data recorded by local stations might be contaminated by coherent noise such as injection noise and meteorological noise (Birnie et al., 2016). This coherent noise can form severe challenges for migration-based location methods as the coherent noise may be continuous in space and time (Shi et al., 2019). In these cases, additional measures such as automatic quality control are needed to obtain a stable and reliable location results (Shi et al., 2019). In addition, scattering together with medium heterogeneity can degrade the waveform coherency, and thus affect the location performance of MCM. However as long as the waveform coherency among stations are not completely undermined by heterogeneity of the subsurface, the MCM method could still achieve a reliable and accurate location result. In the situation of severe decorrelation because of heterogeneity, measures e.g. deconvoluting with empirical Green's functions to remove the effects of media heterogeneity and recover waveform coherency

among receivers can help improve the location performance for MCM.

Compared to downhole arrays, surface arrays used in microseismic monitoring often have larger recording aperture and have a large station density, which are particularly conducive to the migration-based location methods. Through utilizing the coherency of waveforms, the migration-based location method can resist noise and obtain a high quality imaging result. By calculating the pairwise coherency of the recorded waveform data, our MCM method further extends the available information used for migration and obtains better imaging resolution and noise resistance. Compared with downhole array, a surface array of microseismic monitoring has much better horizontal imaging resolution but shows high uncertainties in depth location due to the trade-off with the estimated origin time. Whereas downhole arrays are better at depth location, but have poor horizontal imaging resolution. Migration using a combination of surface and downhole array data might contribute to a better imaging result both in the vertical and horizontal directions.

3.8 Conclusions

In this paper we have proposed a novel migration-based method for locating seismic sources. This new method utilizes the coherency among traces and greatly expands the available information used for source location. The MCM location method provides an automated seismic location tool, which is suitable for dealing with large data volume or abundant seismic events. The computational cost of the MCM method does not depend on the number of seismic events, yet is dependant on the recording times and the number of imaging grid points. As the MCM is highly parallelizable, it has the potential to be developed as a real-time location method for natural or induced seismic monitoring. We have shown that the MCM has the ability to resist strong random noise, where the random noise analysis has exhibited excellent imaging performance for the MCM method in the presence of strong noise. Compared to other methods, the location results of the MCM have higher resolution and are more stable. Robustness tests with an extremely weak event have shown that the MCM can suppress strong interference and obtain a robust imaging result. The MCM method can still achieve a better imaging result compared to other methods when using incorrect velocity models for the migration. This new method is very suitable for locating local seismic events with dense monitoring networks, where the waveform coherency is generally preserved.

Acknowledgements

We would like to thank the editors and reviewers for constructive comments. P. Shi is funded by a China Scholarship Council/University of Leeds scholarship. A. Nowacki is supported by a Leverhulme Early Career Fellowship.

References

Allen, R., 1982. Automatic phase pickers: Their present use and future prospects, *Bull. Seismol. Soc. Am.*, **72**(6B), S225–S242. 3.1, 3.2.2

Aminzadeh, F., Jean, B., & Kunz, T., 1997. *3-D salt and overthrust models*, Society of Exploration Geophysicists. 3.6, 3.20

Arfken, G. B. & Weber, H. J., 1999. Mathematical methods for physicists. 3.2.3

Artman, B., Podladtchikov, I., & Witten, B., 2010. Source location using time-reverse imaging, *Geophys. Prospect.*, **58**(5), 861–873. 3.1, 3.2.2

Bai, C.-y. & Kennett, B., 2000. Automatic phase-detection and identification by full use of a single three-component broadband seismogram, *Bull. Seismol. Soc. Am.*, **90**(1), 187–198. 3.1

Birnie, C., Chambers, K., Angus, D., & Stork, A. L., 2016. Analysis and models of pre-injection surface seismic array noise recorded at the Aquistore carbon storage site, *Geophys. J. Int.*, **206**(2), 1246–1260. 3.7

Cesca, S. & Grigoli, F., 2015. Chapter two-full waveform seismological advances for microseismic monitoring, *Adv. Geophys.*, **56**, 169–228. 3.1

Drew, J., White, R. S., Tilmann, F., & Tarasewicz, J., 2013. Coalescence microseismic mapping, *Geophys. J. Int.*, **195**(3), 1773–1785. 3.1, 3.2.2

Ezekiel, M. & Fox, K. A., 1959. Methods of correlation and regression analysis: linear and curvilinear. 3.2.3

Fink, M., Cassereau, D., Derode, A., Prada, C., Roux, P., Tanter, M., Thomas, J.-L., & Wu, F., 2000. Time-reversed acoustics, *Rep. Prog. Phys.*, **63**(12), 1933. 3.1

Gharti, H. N., Oye, V., Roth, M., & Kühn, D., 2010. Automated microearthquake location using envelope stacking and robust global optimization, *Geophysics*, **75**(4), MA27–MA46. 3.2.2, 3.2.3

Grigoli, F., Cesca, S., Amoroso, O., Emolo, A., Zollo, A., & Dahm, T., 2013a. Automated seismic event location by waveform coherence analysis, *Geophys. J. Int.*, **196**(3), 1742–1753. 3.1

Grigoli, F., Cesca, S., Vassallo, M., & Dahm, T., 2013b. Automated seismic event location by travel-time stacking: An application to mining induced seismicity, *Seismol. Res. Lett.*, **84**(4), 666–677. 3.1, 3.2.2

Grigoli, F., Cesca, S., Krieger, L., Kriegerowski, M., Gammaldi, S., Horalek, J., Priolo, E., & Dahm, T., 2016. Automated microseismic event location using master-event waveform stacking, *Sci. Rep.*, **6**, 25744. 3.1, 3.5

Halliday, D. & Curtis, A., 2008. Seismic interferometry, surface waves and source distribution, *Geophys. J. Int.*, **175**(3), 1067–1087. 3.1

Kaderli, J., McChesney, M. D., & Minkoff, S. E., 2015. Microseismic event estimation in noisy data via full waveform inversion, in *SEG Technical Program Expanded Abstracts 2015*, pp. 1159–1164, Society of Exploration Geophysicists. 3.1

Kao, H. & Shan, S.-J., 2004. The source-scanning algorithm: Mapping the distribution of seismic sources in time and space, *Geophys. J. Int.*, **157**(2), 589–594. 3.1, 3.2.2

Kao, H. & Shan, S.-J., 2007. Rapid identification of earthquake rupture plane using Source-Scanning Algorithm, *Geophys. J. Int.*, **168**(3), 1011–1020. 3.1, 3.2.2

Langet, N., Maggi, A., Michelini, A., & Brenguier, F., 2014. Continuous Kurtosis-based migration for seismic event detection and location, with application to Piton de la Fournaise Volcano, La Réunion, *Bull. Seismol. Soc. Am.*, **104**(1), 229–246. 3.2.2, 3.7

Larmat, C., Montagner, J.-P., Fink, M., Capdeville, Y., Tourin, A., & Clévédé, E., 2006. Time-reversal imaging of seismic sources and application to the great Sumatra earthquake, *Geophys. Res. Lett.*, **33**(19). 3.1

Larmat, C., Guyer, R., & Johnson, P., 2009. Tremor source location using time reversal: Selecting the appropriate imaging field, *Geophys. Res. Lett.*, **36**(22). 3.1

Liao, Y.-C., Kao, H., Rosenberger, A., Hsu, S.-K., & Huang, B.-S., 2012. Delineating complex spatiotemporal distribution of earthquake aftershocks: An improved source-scanning algorithm, *Geophys. J. Int.*, **189**(3), 1753–1770. 3.1

McMechan, G. A., 1982. Determination of source parameters by wavefield extrapolation, *Geophys. J. Int.*, **71**(3), 613–628. 3.1

Podvin, P. & Lecomte, I., 1991. Finite difference computation of traveltimes in very contrasted velocity models: a massively parallel approach and its associated tools, *Geophys. J. Int.*, **105**(1), 271–284. 3.2.1

Ramos-Martínez, J. & McMechan, G. A., 2001. Source-parameter estimation by full waveform inversion in 3D heterogeneous, viscoelastic, anisotropic media, *Bull. Seismol. Soc. Am.*, **91**(2), 276–291. 3.1

Ruigrok, E., Gibbons, S., & Wapenaar, K., 2016. Cross-correlation beamforming, *J. Seismol.*, pp. 1–14. 3.1, 3.2.3

Saragiotis, C. D., Hadjileontiadis, L. J., & Panas, S. M., 2002. PAI-S/K: A robust automatic seismic P phase arrival identification scheme, *IEEE Trans. Geosci. Remote Sens.*, **40**(6), 1395–1404. 3.1, 3.2.2

Shi, P., Angus, D., Nowacki, A., Yuan, S., & Wang, Y., 2018. Microseismic Full Waveform Modeling in Anisotropic Media with Moment Tensor Implementation, *Surv. Geophys.*, **39**(4), 567–611. 3.6

Shi, P., Nowacki, A., Rost, S., & Angus, D., 2019. Automated seismic waveform location using Multichannel Coherency Migration (MCM)–II. Application to induced and volcano-tectonic seismicity, *Geophys. J. Int.*, **216**(3), 1608–1632. 3.1, 3.7

Steiner, B., Saenger, E. H., & Schmalholz, S. M., 2008. Time reverse modeling of low-frequency microtremors: Application to hydrocarbon reservoir localization, *Geophys. Res. Lett.*, **35**(3). 3.1

Tarantola, A., 1984. Inversion of seismic reflection data in the acoustic approximation, *Geophysics*, **49**(8), 1259–1266. 3.1

Usher, P., Angus, D., & Verdon, J., 2013. Influence of a velocity model and source frequency on microseismic waveforms: some implications for microseismic locations, *Geophys. Prospect.*, **61**(s1), 334–345. 3.5

VanDecar, J. & Crosson, R., 1990. Determination of teleseismic relative phase arrival times using multi-channel cross-correlation and least squares, *Bull. Seismol. Soc. Am.*, **80**(1), 150–169. 3.1

Virieux, J. & Operto, S., 2009. An overview of full-waveform inversion in exploration geophysics, *Geophysics*, **74**(6), WCC1–WCC26. 3.6

Wang, S., Yuan, S., Yan, B., He, Y., & Sun, W., 2016. Directional complex-valued coherence attributes for discontinuous edge detection, *J. Appl. Geophys.*, **129**, 1–7. 3.1

Wapenaar, K., Van Der Neut, J., Ruigrok, E., Draganov, D., Hunziker, J., Slob, E., Thorbecke, J., & Snieder, R., 2011. Seismic interferometry by crosscorrelation and by multidimensional deconvolution: A systematic comparison, *Geophys. J. Int.*, **185**(3), 1335–1364. 3.1

Wassermann, J. & Ohrnberger, M., 2001. Automatic hypocenter determination of volcano induced seismic transients based on wavefield coherencean application to the 1998 eruption of Mt. Merapi, Indonesia, *J. Volcanol. Geoth. Res.*, **110**(1), 57–77. 3.1

Wu, Y. & McMechan, G. A., 1996. Elastic full-waveform inversion for earthquake source parameters, *Geophys. J. Int.*, **127**(1), 61–74. 3.1

Yuan, S., Wang, S., Luo, C., & He, Y., 2015. Simultaneous multitrace impedance inversion with transform-domain sparsity promotion, *Geophysics*, **80**(2), R71–R80. 3.6

Yuan, S., Liu, J., Wang, S., Wang, T., & Shi, P., 2018. Seismic waveform classification and first-break picking using convolution neural networks, *IEEE Geosci. Remote Sens. Lett.*, **15**(2), 272–276. 3.1

Zhebel, O. & Eisner, L., 2014. Simultaneous microseismic event localization and source mechanism determination, *Geophysics*, **80**(1), KS1–KS9. 3.1, 3.2.2

Chapter 4

Automated seismic waveform location using Multichannel Coherency Migration (MCM)–II. Application to induced and volcano-tectonic seismicity

P. Shi[1], A. Nowacki[1], S. Rost[1], and D. Angus[2]

[1] *School of Earth and Environment, University of Leeds, Leeds, United Kingdom*
[2] *ESG Solutions, Kingston, ON K7K 7K2, Canada*

Abstract

Locating microseismic events is essential for many areas of seismology including volcano and earthquake monitoring and reservoir engineering. Due to the large number of microseismic events in these settings, an automated seismic location method is required to perform real time seismic monitoring. The measurement environment requires a precise and noise-resistant event location method for seismic monitoring. In this paper, we apply Multichannel Coherency Migration (MCM) to automatically locate microseismic events of induced and volcano-tectonic seismicity using sparse and irregular monitoring arrays. Compared to other migration-based methods, in spite of the often sparse and irregular distribution of the monitoring arrays, the MCM can show better location performance and obtain more consistent location results with the catalogue obtained by manual picking. Our MCM method successfully locates many triggered volcano-tectonic events with local magnitude smaller that 0, which demonstrates its applicability on locating very small earthquakes. Our synthetic event location exam-

ple at a carbon capture and storage site shows that continuous and coherent drilling noise in industrial settings will pose great challenges for source imaging. However, automatic quality control techniques including filtering in the frequency domain and weighting are used to automatically select high quality data, and can thus effectively reduce the effects of continuous drilling noise and improve source imaging quality. The location performance of the MCM method for synthetic and real microseismic datasets demonstrates that the MCM method can perform as a reliable and automatic seismic waveform analysis tool to locate microseismic events.

4.1 Introduction

Microseismic or passive seismic monitoring has been used extensively in monitoring geo-industrial applications (e.g., hydraulic fracturing, carbon dioxide storage and mining setting (Power et al., 1976, Verdon et al., 2011, Gibowicz & Kijko, 2013, Shi et al., 2018a)) as well as hazard monitoring (e.g., volcano-seismology and slope stability (Wilks et al., 2017, Xu et al., 2011)). As a cost-effective monitoring technique, microseismic monitoring is used to demonstrate storage security of carbon capture and storage (CCS) (Verdon et al., 2010, Shi et al., 2018b). It is also an effective method for monitoring volcanoes and forecasting potential eruptions (McNutt, 1996, Lavallée et al., 2008). Microseismic monitoring can provide geomechanical deformation information induced by fluid injection or flow, which can be used to evaluate rock failure processes in the reservoir of a carbon storage site or volcanic edifice.

Noise is an inevitable feature of recorded seismic data. Typically, random noise is assumed to be stationary with a Gaussian distribution, whereas real noise is often non-stationary and so does not conform to a single Gaussian distribution (Birnie et al., 2016, Yuan et al., 2018b). With these features, seismic data with real noise are often more challenging for seismic processing and more difficult to deal with than Gaussian or white noise. For CCS, microseismic monitoring is often conducted during carbon dioxide injection. Therefore, the ambient noise due to the fluid flow and injection exists all the time during the injection process, especially for monitoring arrays which are deployed close to the injection well. Local drilling with associated continuous drilling noise can also affect the recorded seismic data significantly. The injection and drilling noise are continuous and are often coherent across many of the receivers. They can form a great challenge for microseismic event location in CCS (Barkved et al., 2002, Knudsen et al., 2006, Birnie et al., 2016, 2017). Therefore, suitable ways to reduce or remove real noise and obtaining accurate event location results are required.

For CCS and volcano seismicity, a large number of seismic events can happen within a short period, which can be very difficult and time-consuming to locate by manual arrival time picking (Yuan et al., 2018a). In addition, the ever increasing monitoring data volume and larger monitoring arrays also put great demands on automatic seismic

location algorithms for efficient microseismic monitoring. The traditional arrival time based location methods require phase identification and picking, thus are not suitable for automatic event location. Although there are ways to perform an automatic arrival time picking (Bai & Kennett, 2000, Maggi et al., 2009), manual picking is still required to increase the picking reliability when the signal-to-noise ratio of seismic data is low or the arrivals of seismic events are overlapped. There have been various migration-based location methods developed to automatically locate seismic events using recorded waveforms (Kao & Shan, 2007, Gharti et al., 2010, Drew et al., 2013, Grigoli et al., 2013a,b, Zhebel & Eisner, 2014, Langet et al., 2014, Cesca & Grigoli, 2015, Grigoli et al., 2016). Compared with arrival time based methods where the arrival times are determined by manual picking, automated waveform based location methods do not need phase picking and association, thus are more efficient and have the ability to identify more seismic events. Small, more numerous seismic events which cannot be picked manually or automatically can be effectively identified by fully utilizing the recorded full waveforms. Thus the automated waveform based location methods can help add more insights into the fracturing process and natural earthquakes. By using the waveforms and the matched filter technique, Peng & Zhao (2009) detected a large number of missing aftershocks along the Parkfield section of the San Andreas fault and used the newly detected seismic events to understand the postseismic deformation around the rupture zone associated with the mainshock of the 2004 Parkfield earthquake. However, the matched filter technique requires reliable waveform templates. Therefore, this technique is not suitable for research areas where there is no available event catalogue.

Migration-based methods have the potential to be applied as real time location schemes, yet the location reliability and accuracy of these methods is often unsatisfactory in presence of strong noise. Location accuracy is very important in terms of correctly imaging the fracture process and geometry, which can be used to reveal the source mechanism and deformation orientation. Large location errors during microseismic monitoring of CCS and volcano seismicity may contribute to huge economic loss or larger risk as the injection may be terminated prematurely if the induced fracture length has been exaggerated or volcano activity is underestimated because of mislocation of volcano seismicity. The other problem which often challenges migration-based location methods is the station coverage and distribution. Sparse monitoring stations hinder the utilization of waveform coherency for migration-based location methods, which causes poor noise-resistance and location performance. Irregular station distribution will reduce imaging resolution and lead to blurred location results. However, due to the restrictions of the actual deployment environment and cost, practical monitoring arrays are often sparse and irregularly distributed especially for natural earthquake monitoring arrays. Therefore, an automatic and precise seismic location method which can work on sparse and irregular monitoring arrays as well as efficiently with dense and/or regular networks is in great demand.

Shi et al. (2019) proposed a fully automated seismic location method based on waveform coherency. This automated location method utilizes Multichannel Coherency Migration (MCM) and is suitable for locating induced seismicity and natural earthquakes. Different to traditional migration-based location methods which locate the source by stacking waveforms of characteristic functions, MCM calculates the multichannel coherency among stations and stacks the coherency to reveal the source location and origin time. By utilizing multichannel waveform coherency, MCM exhibited excellent location performance with high resolution and outstanding noise resistance. The multichannel coherency has also been utilized to improve the horizontal imaging resolution in seismic interpretation (Yuan et al., 2017). Compared to traditional migration-based location methods, MCM can extract more effective information from seismic waveforms, which give it the ability to locate microseismic and resist interference with noise and other non-related events. The theory and synthetic tests of the multidimensional MCM event-location method can be found in Shi et al. (2019). Here, we demonstrate that the MCM location method can be used to automatically locate both injection induced and volcano-tectonic microseismic events especially when the monitoring array is sparse and/or irregularly distributed. We also compare and discuss the location results with other commonly used migration methods under different real noise levels using sparse and irregular monitoring arrays. First, as a feasibility study, we use the MCM to locate two volcano-tectonic earthquakes at the Uturuncu Volcano in Bolivia using a sparse monitoring array and also compare the location results with published event locations in the catalogue. We then apply the MCM to automatically locate triggered earthquakes following the M_w 8.8 Maule earthquake at Uturuncu (Jay et al., 2012) using four hours of continuous waveform data. Then, synthetic seismic data of an irregularly distributed monitoring array with real drilling noise were used to evaluate the location performance of different methods for induced seismicity. In order to obtain a satisfactory location result, quality control methods to remove the coherent drilling noise are explored and discussed. Finally, location performance and imaging resolution in different directions of different migration-based methods are analysed and discussed in detail.

4.2 Theory and computational efficiency analysis

In this section, we will briefly introduce the 2-dimensional MCM (for a more detailed description and the multidimensional MCM see Shi et al. (2019)). For MCM, at a particular imaging point k and origin time t_0, the correlation coefficient between the waveforms of two different stations is calculated by:

$$r_{ij} = \frac{\sum_{t=t_0}^{t_0+t_w} \left[d_i(t+t_{ki}) - \overline{d_i(t+t_{ki})}\right] \left[d_j(t+t_{kj}) - \overline{d_j(t+t_{kj})}\right]}{(N_t-1)\,\sigma_i\sigma_j}, \tag{4.1}$$

where r_{ij} is the correlation coefficient (i.e. coherency) between the waveforms at station i and j, d_i and d_j are the two input waveforms within the selected time window for station i and j, t_w is the coherency analysis time window for a particular seismic phase, N_t is the number of time samples in the time window, t_{ki} and t_{kj} are traveltimes of a particular seismic phase from imaging point k to the station i and j, σ is the standard deviation of the corresponding signal and the overlines denote averages.

After calculating correlation coefficients for all possible station pairs, the stacking function can be expressed as

$$p(x, y, z, t_0) = \frac{1}{N(N-1)} \left(\sum_{i<j}^{N} |r_{ij}^P| + \sum_{i<j}^{N} |r_{ij}^S| \right). \tag{4.2}$$

where r_{ij}^P and r_{ij}^S represent the waveform coherency of P- and S-phases for station pair ij, N is the number of stations and the number of unique receiver pairs equals $N(N-1)/2$, $p(x, y, z, t_0)$ is the final 4D imaging function and stores the stacked waveform coherency at position (x, y, z) and origin time t_0 (Shi et al., 2019).

The 4D migration volume contains all the information about source location and origin time. Locations (x_s, y_s, z_s) and origin times t_{0s} of seismic events can be identified by finding the maximum value above a preset coherency threshold within certain time periods

$$p(x_s, y_s, z_s, t_{0s}) = max_{t_0 \in [t_1, t_2]} \{p(x, y, z, t_0) \geq p_c\}. \tag{4.3}$$

As an automated seismic location method, only a few input parameters, i.e. length of coherency analysis time window t_w and coherency threshold p_c, are required for MCM in an event location process. The length of coherency analysis time window t_w should be equal to or larger than the approximate period of seismic phases (Shi et al., 2019). A longer time window is suggested in order to suppress the interference of noise and other incoherent phases when seismic data contain strong noise or coda waves. The coherency threshold p_c is determined according to the background noise level. A higher coherency threshold can help identify seismic events which have more probability to be real seismic events, but will also decrease the number of identified seismic events. It is worth noting that the migration process and the event identification process are two totally independent processes. So it is easy to adaptively adjust the coherency threshold according to a migration volume and choose a suitable threshold which can fulfil the requirements of the application.

For event locations based on manual picking, the computational efforts depend on the number of earthquake events in the time period. The more events there are, the more expensive it is to pick and locate them. However, for MCM, the computational cost is independent of the number of events. The computational cost is only related to the number of imaging points, the number of searched origin times and the number of stations. The whole MCM procedure is highly parallelizable, and the migration process

is quite independent on different scales (from imaging point level to origin time level). Therefore, parallel computing in MCM can be performed on different imaging points or different origin times according to actual requirements. Very little communication is required for MCM when performing parallel computations, e.g. maximum migration values of different origin times when performing parallel computing on different origin times or migration values of different imaging points when performing parallel computing on different imaging points. We implement MCM using the Message Passing Interface (MPI) and analyse its computational efficiency on a high performance cluster (Figure 4.1). Both P- and S-waves are used in the MCM calculation and the number of time samples within the P/S time window is 100. Figure 4.1 (a) shows the computational times for different numbers of imaging points (Ns) and origin times (Nt) used in the MCM. As can be seen in the figure, the computational cost increases linearly with the number of imaging points and origin times, which demonstrates that the MCM workload scales essentially perfectly. Figure 4.1 (b) shows the computational times for different numbers of stations (N) used in the MCM. As we can see in the figure, the computational cost increases rapidly with the number of stations. Actually, the computational cost is proportional to the number of unique station groups: $N \times (N-1)/2$ (as Figure 4.1 (b) blue line shows), which is in accordance with the theory of MCM (Shi et al., 2019). Figure 4.1 (c) shows the computational times and speedup ratios when different numbers of computing cores (Nc) are used. As expected the computational times (black line) decrease dramatically when more cores are used in the computation. The speedup ratios (blue line) are calculated by dividing the computational times of different cores by the computational time of a single core. Due to the high scalability of the MCM process, the speedup ratio of MCM is very close to the theoretical speedup ratio (red dashed line). Accordingly, we assume that the computational time is proportional to the number of imaging points, the number of origin times and the number of unique station pairs, and the speedup ratio equals the theoretical speedup ratio. Therefore, the computational time $t = k \times Ns \times Nt \times N \times (N-1)/Nc$, where k is a coefficient related to computer architecture. Using the data of Figure 4.1 (a-c), we obtain a coefficient of $k = 1.5 \times 10^{-7}$ second with the current settings. If real time processing is required, the MCM calculation time should be less than the length of the data. Here, we assume that the sampling interval for searched origin times is 0.1 second, and thus we have 10 origin times to process for each second of recorded seismic data. Therefore, for a real time processing, the required cores should fulfil $Nc \geq 10 \times k \times Ns \times N \times (N-1)$. Figure 4.1 (d) shows the required cores for real time processing when different numbers of stations and imaging points are used in MCM. The real time processing is expensive, but is still feasible with the current computer resources when the number of stations is not very large (e.g. $Ns \leq 40$). For sparse surface monitoring arrays, the number of deployed stations is usually smaller than 20. The number of imaging points can be reduced to less than 300K when locating seismic

events in a small region. Therefore, real time processing is completely feasible in this situation. For example, for the Uturuncu dataset which we will discuss in detail in the next section, 68 cores are needed to conduct real time processing (shown as the red dot in Figure 4.1 (d)). Here, we only implement MCM using CPUs and MPI. Because the whole MCM process is highly parallelizable and the computation of MCM can be simultaneously processed in large blocks of data, we anticipate much larger speedup ratios when using Graphics Processing Units (GPU), which we are currently exploring.

4.3 Location of shallow seismicity at Uturuncu volcano

Uturuncu is a long-dormant stratovolcano in Bolivia, which has an elevation of about 6000 m (Jay et al., 2012). Recent studies of surface deformation, fumarolic activity and the earthquake rate of Uturuncu show signs of unrest and potential of eruption again, which calls for close monitoring (Pritchard & Simons, 2004, Sparks et al., 2008, Jay et al., 2012). As shown in Figure 4.2, 15 three-component seismometers have been temporarily deployed surrounding the inflating Uturuncu from April 2009 to April 2010 (Pritchard, 2009). The farthest station is located about 25 km from the volcano summit. The seismometers have a sampling rate of 50 samples/s, which means the highest effective frequency of the recorded data is 25 Hz. Nine seismometers are short-period instruments and six seismometers are intermediate-period instruments. The tectonic setting of Uturuncu and the catalogue for these events located by manual picking can be found in Jay et al. (2012). We apply the MCM on the recorded continuous waveform data to show the potential of this method in a volcano-tectonic settings, using a sparse seismic network common in such environments.

4.3.1 Locating two local volcano-tectonic microearthquakes

First, we apply four different waveform migration methods to locate two local volcano-tectonic earthquakes at the Uturuncu and compare the location results. The magnitudes of these two local volcano-tectonic earthquakes are below M_L 1.0. The depths of the two shallow volcano-tectonic earthquakes are above the sea level. We use four different waveform migration techniques, i.e. envelope (Kao & Shan, 2007, Gharti et al., 2010), STA/LTA (Drew et al., 2013, Grigoli et al., 2013b), kurtosis (Langet et al., 2014) and MCM (Shi et al., 2019), to compare the performance in this setting. For STA/LTA migration, the short-term time window has been chosen to be 4 seconds and the long-term time window is 40 seconds. The time window for calculating kurtosis is 4 s. For MCM, a coherent analysis time window of 6 s and a two-channel based coherency scheme are used to locate the seismic events. The coherency threshold of MCM is set to 0.13. Because the monitoring array is very sparse, we set the weighting factors of all stations to 1, which means each trace is equally treated and used for migration.

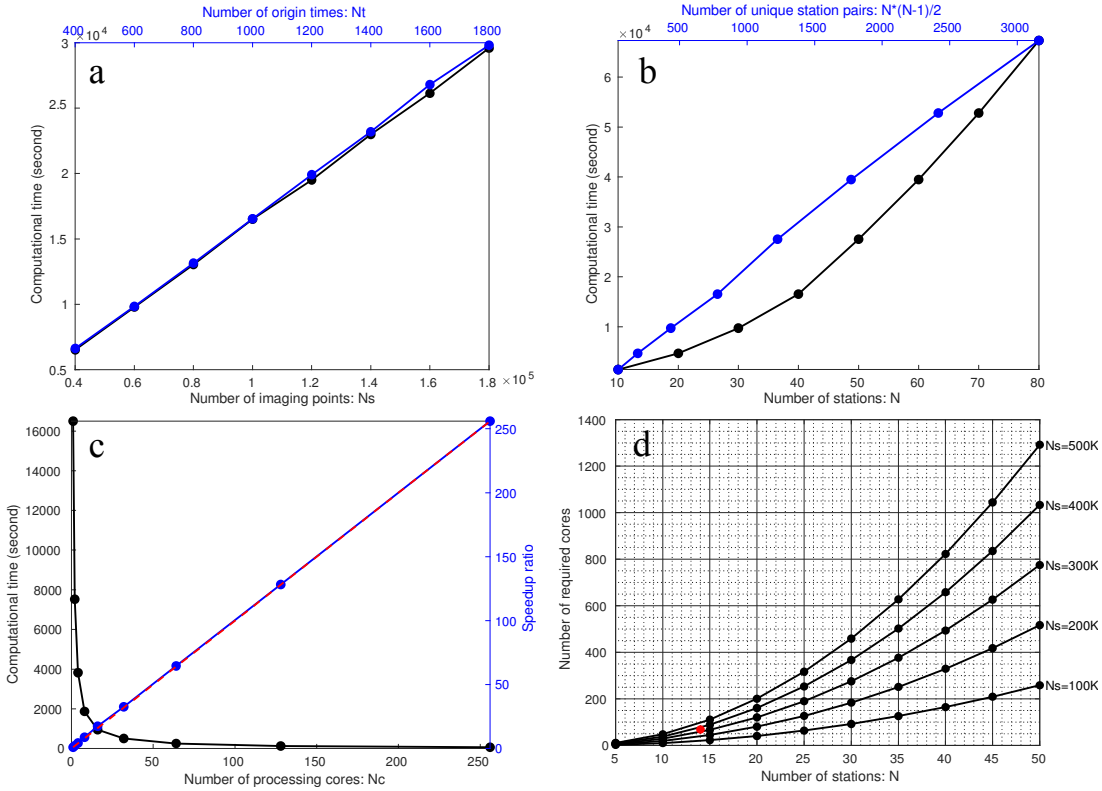

Figure 4.1: Computational efficiency analysis of the MCM location. The efficiency test is performed on the Intel E5-2670(2.6GHz) processor. (a) The computational times for different numbers of imaging points and searched origin times. Black line and the bottom X-axis show the variation of computational times with the number of imaging points, when the number of origin times and stations are fixed as 1000 and 40. Blue line and the top X-axis show the variation of computational times with the number of origin times, when the number of imaging points and stations are fixed as 100000 and 40. (b) The computational times for different numbers of stations, when the number of origin times and imaging points are fixed as 1000 and 100000. Black line and the bottom X-axis show the variation of computational time with the number of stations. Blue line and the top X-axis show the variation of computational time with the number of unique station pairs. Program runs on one core for (a) and (b). (c) The computational times (black line and left Y-axis) and speedup ratios (blue line and right Y-axis) when different numbers of cores are used. Red dashed line show the theoretical speedup ratios. The number of origin times, imaging points and stations are fixed as 1000, 100000 and 40. (d) The required cores used for real time processing under different numbers of stations and imaging points. Different black lines show the scenarios for different numbers of imaging points. The red dot shows the scenario for the following Uturuncu dataset, where 14 stations are deployed, 283556 imaging points are scanned and 68 cores are required for real time processing.

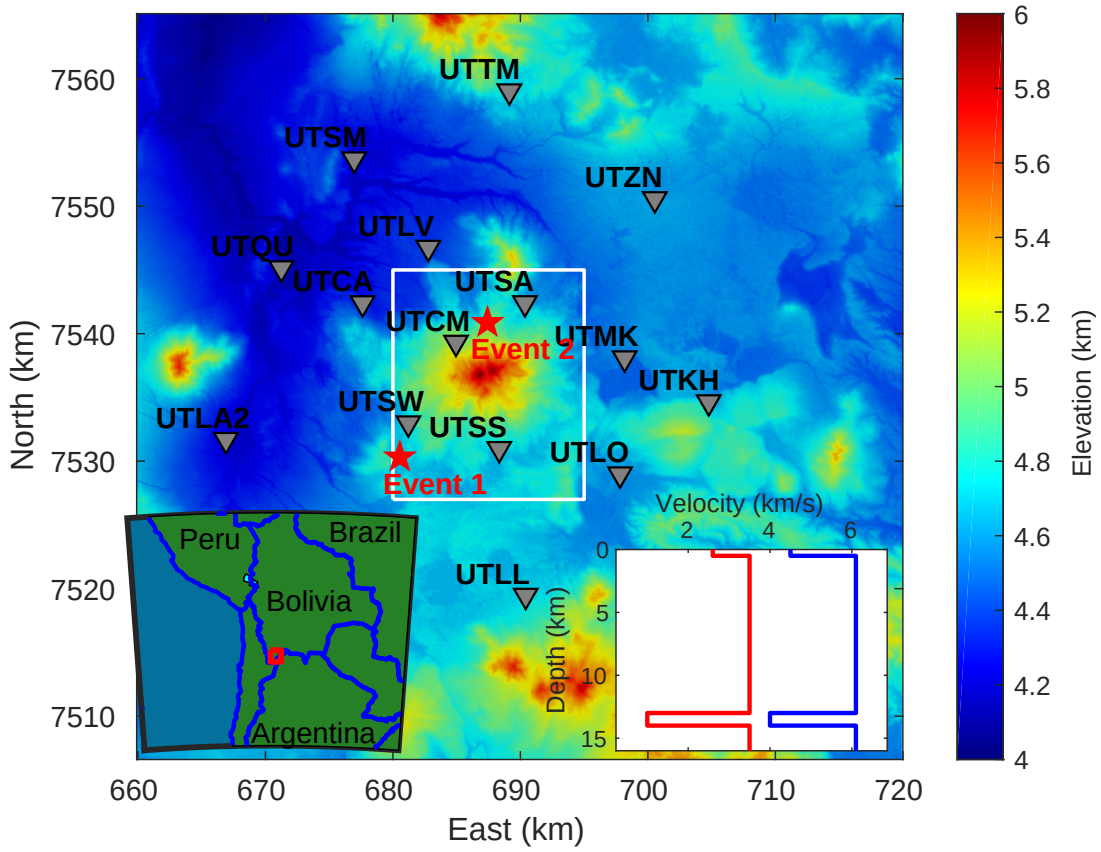

Figure 4.2: Location of the seismic stations and Uturuncu volcano (UTM zone: 19K). The stations are represented by gray triangles. Two local volcano-tectonic earthquakes in the catalogue are represented by red stars. The Uturuncu is located in the middle of the figure. The color in the figure represents elevation relative to the sea level. The lower left part exhibits a regional map, in which the red rectangle shows the research area. The lower right part exhibits the velocity model used in the event location, in which the red and blue lines show the P- and S-wave velocities. The white rectangle shows the imaging area (shown as Figure 4.11) for the four hours of continuous data.

The spatial and temporal intervals used in the source imaging are 100 m and 0.08 s respectively. Because the vertical component data show distinct arrivals of P-waves, we only utilize the direct P-wave to conduct MCM for the vertical component data. Similarly for the north-south and east-west components, we only utilize the direct S-wave to image the events. The coherency of the three component data are then added together to obtain the final imaging values of a particular origin time and space point. The location results of the migration methods are compared to the locations in the catalogue. The velocity model used in the event location is the same layered model as described in Jay et al. (2012).

Figure 4.3(a) shows the recorded three-component waveforms at station UTCA for the first event, whose local magnitude M_L is 0.63 (Jay et al., 2012). The direct P-wave and S-wave of this event are distinguishable in the recorded waveforms, but the waveforms contain extended coda. The whole waveform train containing direct waves and coda waves for this event is about 6 seconds. Figure 4.4 shows the vertical and horizontal profiles of the migration results for the four different waveform migration methods using all available data. The depth (Z-axis) is measured relative to the sea level. The layer at depth 0.5 km which shows a velocity increase can be seen clearly in the migration profiles. The catalogue location (Jay et al., 2012) of this event is displayed as a star in the figure for comparison. For the envelope and STA/LTA migration, the source energy is not well focused. Thus the event location results of these two methods are not reliable, probably because the envelope and STA/LTA cannot identify the event onset from the recorded waveforms. For kurtosis and MCM, the source energy is well focused, thus the location results are more useful. The event location result of the MCM shows better agreement to the location in the catalogue. The location deviations of the MCM result relative to the event in the catalogue are 0.584, 0.557 and 0.469 km in the X, Y and Z directions, respectively (Table 4.1). Figure 4.5(a) shows the stacking function of the MCM method at the position of the most coherent point. The stacking function jumps to the maximum value at about one coherent analysis time window earlier than the published origin time of the event and drops down to the noise level quickly. The estimated origin time of the MCM method can be determined from the maximum coherency time, the analysis time window and the period of the direct waves. This is in agreement with Shi et al. (2019). We will discuss this later in detail in the discussion section. The maximum coherency value is only about 0.16. A longer coherent analysis time window tends to decrease the overall waveform coherency as more data including noise are put into the coherent analysis. However, a longer time window is beneficial for obtaining a stable migration result. The coherency of the coda wave is also included to benefit the source imaging. For this volcano earthquake dataset, tests show that the analysis time window needs to be at least 1 s to eliminate the influence of the noise and pure coda waves. We used a time window of 6 s for both events to make the migration results more stable.

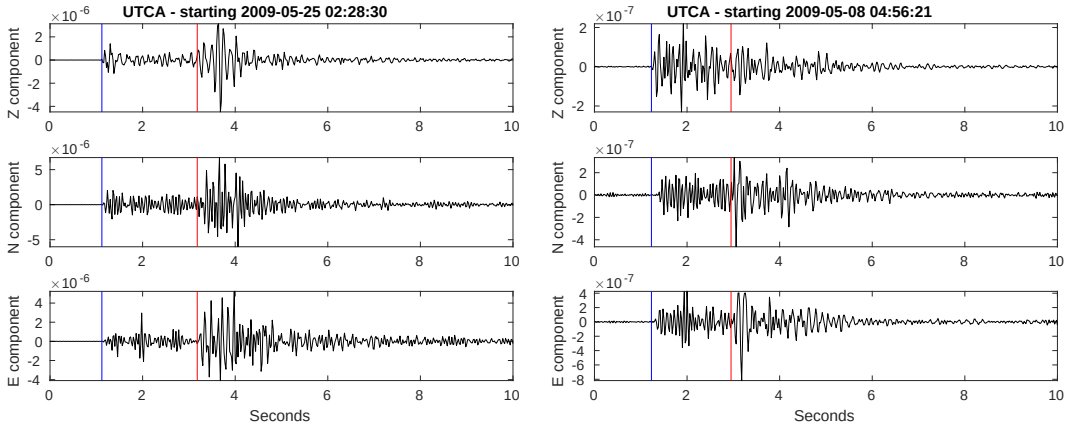

Figure 4.3: The recorded three component waveforms at station UTCA for the two shallow, local volcano-tectonic earthquake. The blue and red lines show the arrivals of P- and S-waves respectively. (a) Waveforms for the first event. The instrument response has been removed and the waveforms are filtered using a bandpass filter of 5-23 Hz. (b) Waveforms for the second event. The instrument response has been removed and the waveforms are filtered using a bandpass filter of 5-21 Hz.

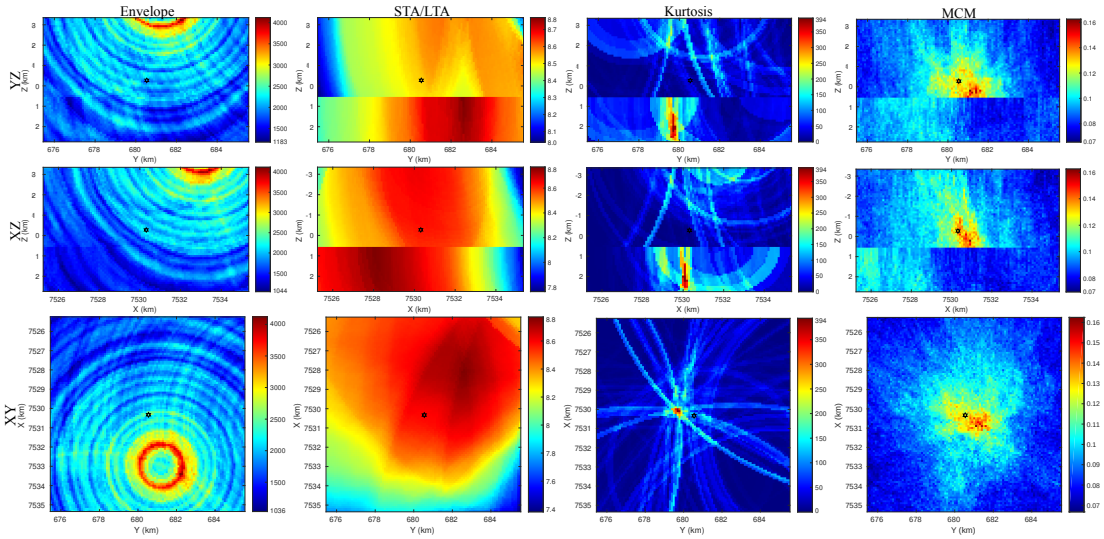

Figure 4.4: Migration profiles through the maximum migrated value for the first volcano-tectonic earthquake. The dark stars show the corresponding seismic event in the catalogue obtained by manual picking. The first column shows results of envelope, second column for STA/LTA, third column for kurtosis, fourth column for MCM. The first row shows YZ profiles, second row shows XZ profiles, third row shows XY profiles.

Table 4.1: Location results of different waveform migration methods for the Uturuncu shallow volcano-tectonic earthquake and comparison with the event in the catalogue. The origin time is relative to 2009-05-25 02:00:00 (UTC).

	Event location				Deviation from Catalogue			
	X (km)	Y (km)	Z (km)	T_0 (s)	ΔX (m)	ΔY (m)	ΔZ (m)	ΔT_0 (s)
Catalogue	7530.316	680.543	-0.269	1708.2	-	-	-	-
Envelope	7533.4	682.2	-3.2	1709.8	3084	1657	2931	1.6
STA/LTA	7528.0	682.6	1.0	1709.4	2316	2057	1269	1.2
Kurtosis	7530.1	679.7	2.0	1708.4	216	843	2269	0.2
Coherency	7530.9	681.1	0.2	1708.3	584	557	469	0.1

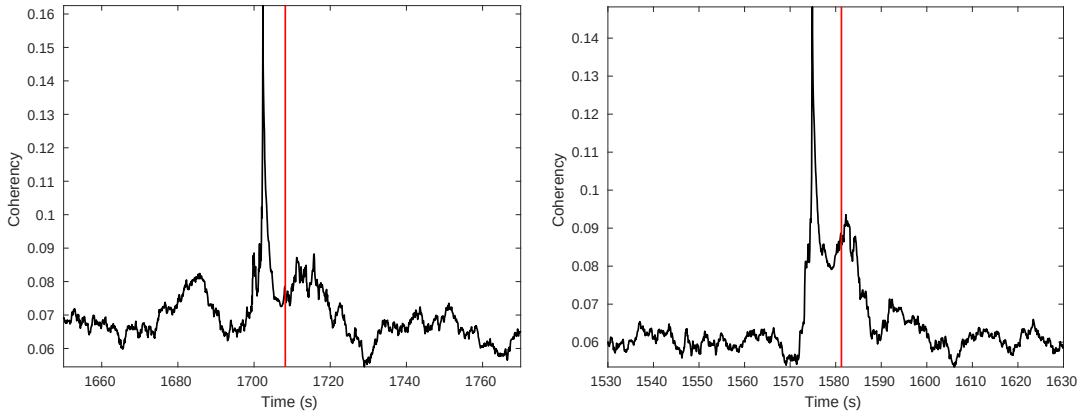

(a) (b)

Figure 4.5: The stacking functions of the MCM method at the position of the maximum migrated value. The red line shows the origin time of the event in the catalogue obtained by manual picking. (a) The stacking function for event 1. The time is relative to 2009-05-25 02:00:00. (b) The stacking function for event 2. The time is relative to 2009-05-08 04:30:00.

Table 4.1 shows the quantitative location results of the different migration methods and the comparison with the catalogue location. The origin time of this event for the MCM method in the table is estimated using the maximum coherent time plus the coherent analysis time window following Shi et al. (2019). The event location of the MCM method shows the best correlation to the event location in the catalogue with less deviation in the location and origin time. Predicted P- and S-wave arrival times for this event in the catalogue and the event located by MCM are compared on record sections in Figure 4.6. The direct P- and S-wave arrivals correspond well with the predicted P- and S-wave arrival times for MCM location in most stations. Therefore the location determined by MCM of this event is acceptable.

Figure 4.3(b) shows the recorded three-component waveforms at station UTCA for the second event, whose local magnitude M_L is -0.29. The direct P-wave can be well identified in the vertical component and the direct S-wave can be well identified in the north-south and east-west components. The coda waves following the direct P- and S-waves are obvious. Figure 4.7 shows the vertical and horizontal profiles of the migration results for the four different waveform migration methods. As with the migration results of the previous event, the envelope and STA/LTA migration methods do not focus the source energy appropriately. The migration results of the kurtosis and MCM method are quite similar. The horizontal locations of this event using the kurtosis and MCM method are consistent with the catalogue location with only little deviation. However, the located event depths of both kurtosis and MCM method are deeper than the event depth in the catalogue (1.72 km and 1.92 km deeper respectively). Nevertheless, compared to the horizontal location of the seismic event, the event depth is often not well constrained by the recorded data especially for surface arrays. The trade-off between event depth and origin time often makes event depth determination problematic and more difficult (Eisner et al., 2010). Figure 4.5(b) shows the stacking function of the MCM method at the position of the most coherent point. Table 4.2 shows the quantitative location results of the different migration methods and the comparisons with the catalogue. The location results of the MCM correspond very well with the catalogue in the horizontal directions (with very small deviations of 0.166 km and 0.181 km in the X and Y directions, respectively). Predicted P- and S-wave arrival times for this event in the catalogue and the event located by MCM are further compared on record sections in Figure 4.8. Probably because of the strong heterogeneity in the subsurface, the recorded waveforms at some stations are not very coherent with the waveforms at other stations. However, the migration results of the MCM method are not seriously affected and seem still reliable. From the record sections of the vertical component (Figure 4.8 first row), we can clearly see the recorded direct P-wave arrivals show better consistency with the theoretical P-wave arrival times in the record section of the MCM method. This further demonstrates the reliability of the MCM location results.

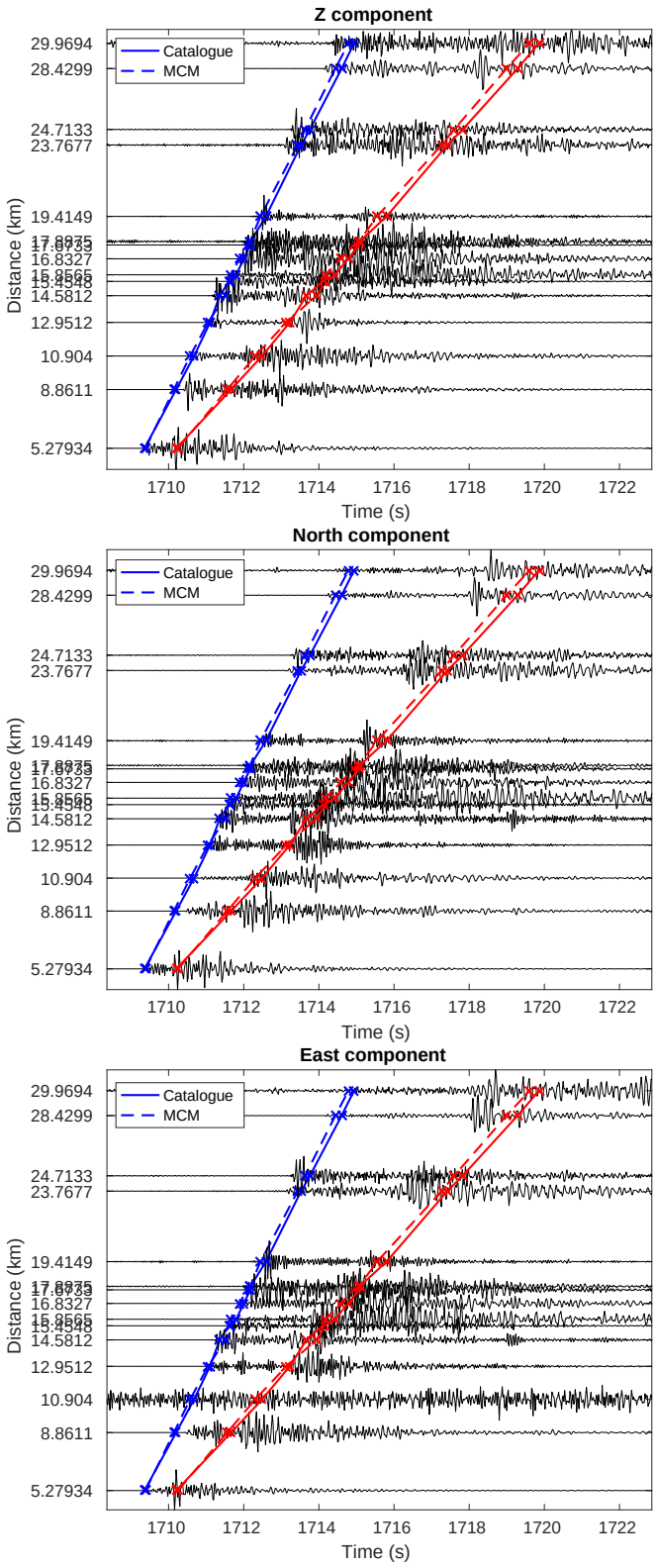

Figure 4.6: The three component record sections of the first event. The predicted P- and S-wave arrival times for this event in the catalogue and the event located by MCM are marked by solid and dashed lines respectively. The blue and red colors show the arrival times of the direct P- and S-wave respectively. The time in the figure is relative to 2009-05-25 02:00:00 (UTC).

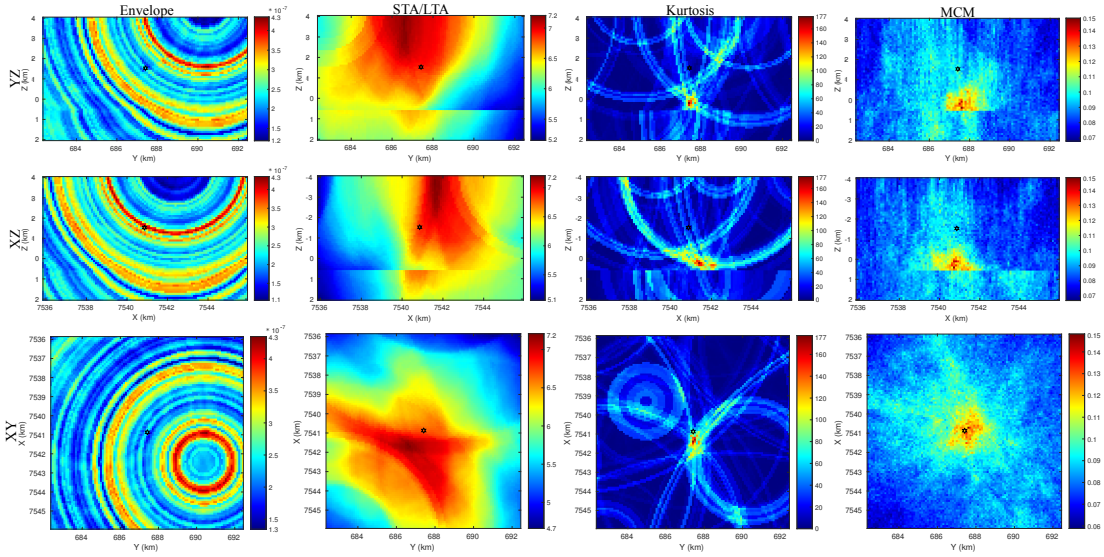

Figure 4.7: Migration profiles through the maximum migrated value for the second volcano-tectonic earthquake. The dark stars show the corresponding seismic event in the catalogue obtained by manual picking. The first column shows results of envelope, second column for STA/LTA, third column for kurtosis, fourth column for MCM. The first row shows YZ profiles, second row shows XZ profiles, third row shows XY profiles.

Table 4.2: Location results of different waveform migration methods for the Uturuncu shallow volcano-tectonic earthquake and comparison with the event in the catalogue. The origin time is relative to 2009-05-08 04:30:00 (UTC).

	Event location				Deviation from Catalogue			
	X (km)	Y (km)	Z (km)	T_0 (s)	ΔX (m)	ΔY (m)	ΔZ (m)	ΔT_0 (s)
Catalogue	7540.866	687.419	-1.523	1581.3	-	-	-	-
Envelope	7540.9	690.5	-1.6	1582.2	34	3081	77	0.9
STA/LTA	7541.6	686.6	-3.6	1582.9	734	819	2077	1.6
Kurtosis	7541.4	687.4	0.2	1580.9	534	19	1723	0.4
Coherency	7540.7	687.6	0.4	1580.7	166	181	1923	0.6

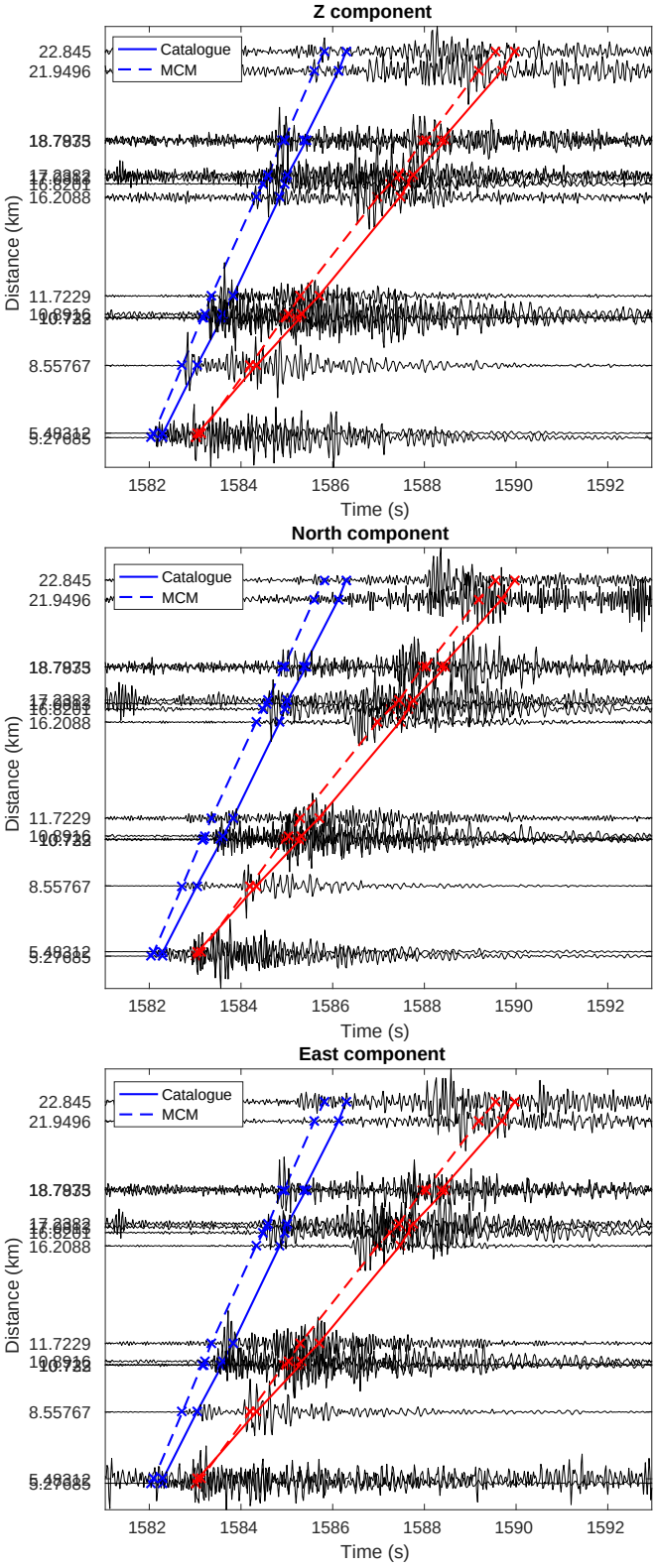

Figure 4.8: The three component record sections of the second event. The predicted P- and S-wave arrival times for this event in the catalogue and the event located by MCM are marked by solid and dashed lines respectively. The blue and red colors show the arrival times of the direct P- and S-wave respectively. The time in the figure is relative to 2009-05-08 04:30:00 (UTC).

The Uturuncu example shows that MCM can be used as a practical and precise seismic location method for automated volcano-tectonic and natural earthquake monitoring. As MCM utilizes the waveform coherency across different stations, it performs better under high noise conditions and can obtain a more accurate location result compared to other migration-based location methods. Sparse monitoring arrays will decrease imaging resolution and cause location uncertainties. The utilization of multi-channel coherency information in MCM can greatly expand available information used for location and improve imaging resolution (Shi et al., 2019), which is critical for seismic event location using sparse monitoring arrays.

4.3.2 Locating triggered events on four hours of continuous waveform data

The M_w 8.8 Maule earthquake on 27 February 2010 (at 06:34 UTC) triggered hundreds of earthquakes at Uturuncu with the passage of surface waves and the overtone phases of surface waves (Jay et al., 2012). Those triggered seismic swarms are recorded by the deployed Uturuncu monitoring arrays. According to Jay et al. (2012), the triggered events occurred with the onset of the Love and Rayleigh waves, and the earthquake rate reaches a maximum value of two events per minute with the passage of the Rayleigh wave overtones. We apply the MCM to automatically locate these triggered earthquakes using four hours of continuous data (06:00:00 to 10:00:00 UTC), which recorded most of the triggered events. The recorded waveform data at station UTCA are shown in Figure 4.9. As shown in the enlarged part of Figure 4.9, there are many small magnitude events which can be very difficult and time consuming to pick manually. As the triggered earthquakes start immediately after the surface wave train, many events occurred in a short time period with very close or overlapping waveform trains. Therefore, it will be very difficult to pick and associate different phases to a particular event. In addition, because of interference of noise and coda waves, it is also very difficult to accurately pick the P- and S-wave arrival times of small seismic events. The manual picking accuracy is highly dependent on human experience. The manual picking errors will inevitably cause location errors. As the MCM does not require picking and phase identification and the location accuracy of the MCM does not depend on event magnitude (waveform amplitude), it is very suitable to be used to automatically locate those dense triggered microseismic events.

The surface waves and surface wave overtones of the M_w 8.8 Maule earthquake not only trigger many seismic events in this area but also forms a big challenge for migration imaging using waveforms. Here, we filter waveforms using a frequency band of 4.2 - 21.6 Hz to exclude the influence of surface waves and low frequency noise. Because the sample rate (50 samples/s) is low, we suggest to use a long time window for coherency analysis in the MCM. Using a longer time window can improve the

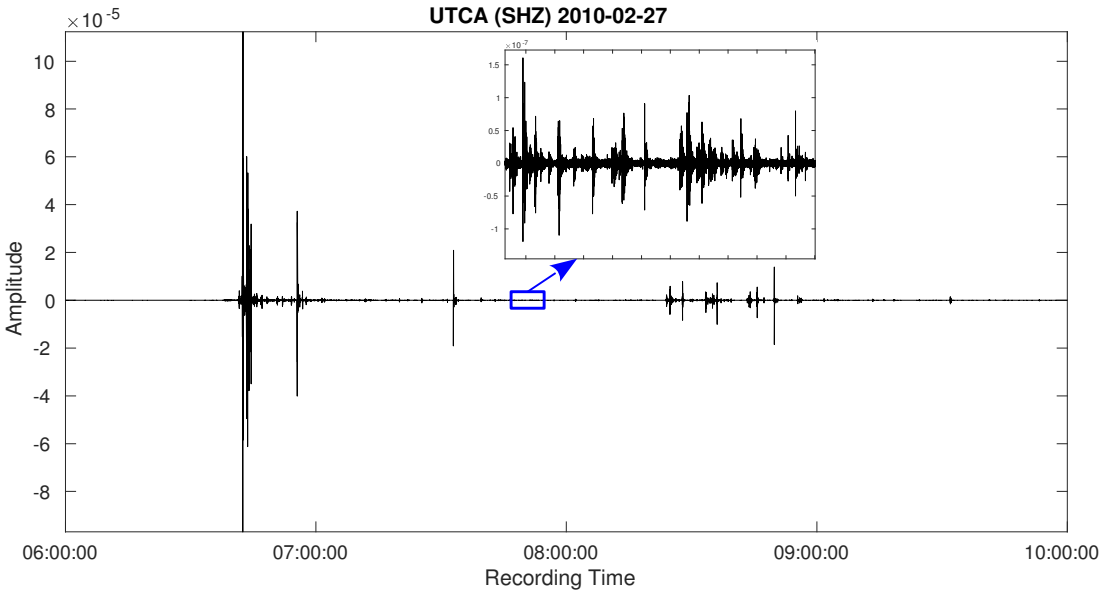

Figure 4.9: The recorded Z component waveforms at station UTCA. The recording time ranges from 06:00:00 to 10:00:00 (UTC). The waveforms within the blue rectangle are enlarged. The instrument response has been removed and the waveforms are filtered using a bandpass filter of 4.2-21.6 Hz.

imaging stability and quality in noisy situations. We adopt a four second time window for both P- and S-waves in the MCM to resist the interference of noise and coda waves. Similarly, we only utilize the direct P-wave to conduct MCM for the vertical component data, and only utilize direct S-wave for the horizontal component data. The coherency value of the P-wave for the vertical component data and coherency values of the S-wave for the two horizontal component data are then stacked together to form the final migration value. For conventional waveform migration methods which stack amplitudes or characteristic functions of amplitudes, S-phases are often assigned higher weighting factors because S-phases tend to have higher amplitude. However, the S-phase often interferes with coda and converted waves, thus tends to have lower waveform coherency across different stations. In contrast, the P-phase which arrives first often has higher coherency despite its lower amplitude. Therefore, we assign a weighting factor of 0.6 to the P-phase of the vertical component and factors of 0.2 to the S-phases of each of the two horizontal components (east-west and north-south), noting that the MCM is insensitive to amplitudes.

The imaging area is 18 km, 15 km and 8 km in north-south, east-west and vertical directions, respectively (as shown in Figure 4.2 white rectangle area). The imaging point interval is 200 m in all different directions. Therefore, there are 283,556 imaging points in total. The time interval for searching for origin times is 0.08 s. The total number of searched origin times in the four hours is about 180,000. We assume that two earthquakes will not occur at the same time or within a few origin time samples (0.08 s). Therefore, at each searched origin time, we only save the imaging point which has the

maximum coherency value. Figure 4.10 shows the variation of the maximum coherency value with different origin times in the four hours. When an earthquake occurs, at the correct origin time, the coherency values of each imaging point will all rise due to the arrival of the long waveform trains including direct, converted and coda waves. Therefore, we can observe many local peaks rising from the background noise in Figure 4.10, which potentially correspond to seismic events. We use a coherency threshold of 0.1. By identifying the maximum value of each local peak, we can find the location and origin time of each seismic event. We identify 560 local peaks in Figure 4.10, which are viewed as potential seismic events. We then check each potential seismic event using the corresponding record sections of these potential seismic events and verify 322 seismic events which have clear phase arrivals. The verified seismic events are shown as red dots in Figure 4.10. Although there are many events which do not show clear P- and S-phase arrivals, they may still be real seismic events, because the signal-to-noise ratio (SNR) for these events may be small (smaller than 1). Since the MCM has the ability to resist strong noise, it is not surprising that it can successfully identify seismic events below the noise level. The problem is that although identified by MCM, the weak seismic events with SNR below 1 cannot be effectively verified through their record sections at the present. By adopting stricter parameters (such as a higher coherency threshold, higher source prominence and longer origin time gap), we can also reduce the number of unverifiable seismic events and improve the proportion of confirmed seismic events. However, this would inevitably result in losing some small real seismic events which cannot be effectively verified by inspection of the record sections at the present. Therefore, further studies about detecting and verifying seismic events (especially events with low SNR) from migration traces/volumes are still needed. Here, since the verifying process is very quick and easy, in order to identify as many seismic events as possible, we adopt relatively relaxed parameters to identify the local maxima in the coherency time slice (Figure 4.10).

The existing catalogue has 114 seismic events in total in this four hour time period in this area, which are located by manual picking. For those 114 seismic events, 112 events (98.25%) have been successfully located by the MCM. In addition, the MCM has also automatically located 210 more seismic events than the existing catalogue, which have been verified on the record sections. By checking the corresponding record sections, we find that the MCM not only automatically locates many more triggered seismic events than the catalogue, but also the origin time estimates of most events are more accurate than the existing catalogue under the current velocity models. This demonstrates that MCM is an efficient and reliable automatic location method. Figure 4.11 shows the locations of the 322 verified seismic events and the 114 current catalogue events. In the figure, we can see that the distribution of automatically located seismic events is consistent with that of the events in the catalogue. There are two main earthquake clusters. One is located in the northern part of the study area and close to

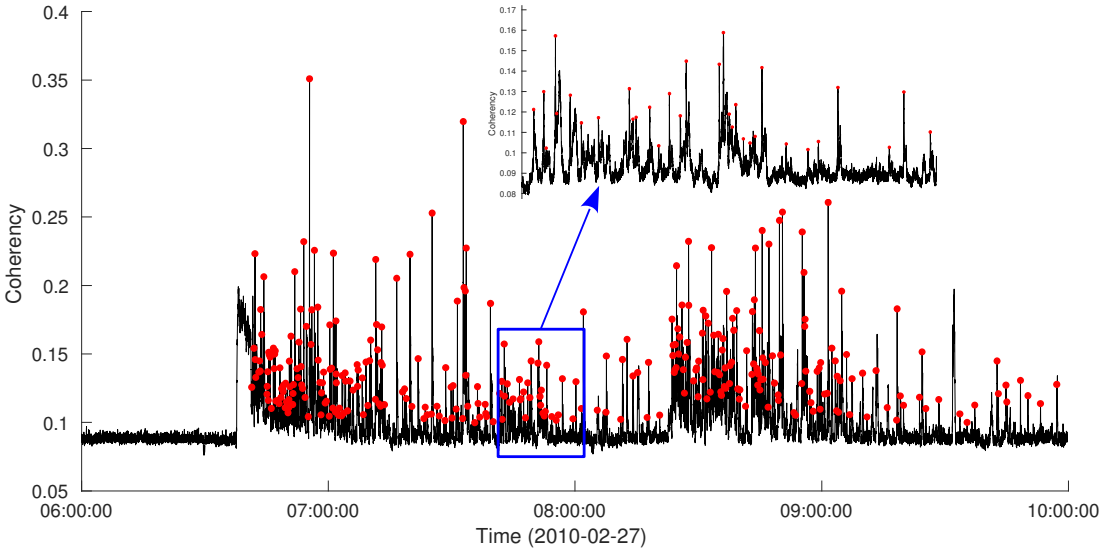

Figure 4.10: The maximum coherency value at each searched origin time for the four hours of continuous data. The time interval is 0.08 s. The part in the blue rectangle is enlarged. The red points show the 322 verified seismic events.

the volcano. This earthquake cluster occurred earlier (6 am to 8 am), and the events are mainly triggered by the surface waves (Love and Rayleigh waves) of the Maule earthquake. The other earthquake cluster occurred from 8 am to 10 am and is located in the southern part of the study area. The seismic events are mainly triggered by the surface wave overtones of the Maule earthquake.

Figure 4.12 shows a seismic event (referred to as event 1) which is both located by the MCM and the manual picking (catalogue). The MCM location result has a similar horizontal location as the catalogue result, but is deeper than the catalogue event. From the corresponding record sections (Figure 4.13), we can clearly see that the predicted arrival times of the MCM results have a much better correspondence with the P- and S-phase arrivals, especially for the S-phases of the horizontal components. This demonstrates that the MCM location results are reliable and have a better estimation of the origin times of seismic events. Figure 4.14 shows the migration profiles and record sections of a newly identified seismic event (referred to as event 2) by MCM, which is not in the existing catalogue. The source energy focuses nicely in the migration volume. The record sections which show clear P- and S-wave arrivals also indicate a real microseismic event occurred. It is worth noting that although event 2 is lower in event magnitude and has smaller amplitudes than event 1, the waveform coherency (0.22) of event 2 is higher than that of event 1 (0.17). For MCM, the waveform coherency not only depends on the amplitude (relating to event magnitude and SNR), but is also influenced by the interference of coda waves, converted waves and arrivals from other events. Thus, it is not surprising that a small seismic event can have higher waveform coherency and focussing of migration energy than a larger seismic event when the small

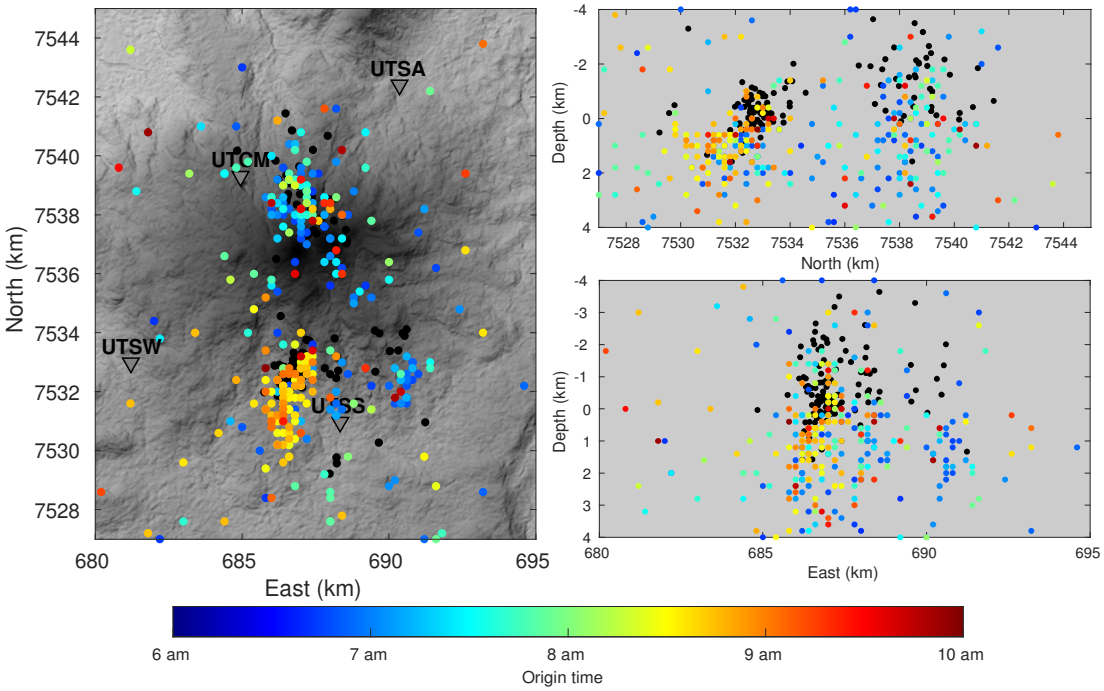

Figure 4.11: The earthquake locations on the horizontal and vertical profiles. Black dots show the 114 event locations in the existing catalogue. The color-coded dots show the verified 322 event locations for the MCM. The color represents the origin times of earthquake events.

event is less affected by interference of other non-coherent waves. This characteristic makes MCM very suitable for locating microseismic events.

Many more seismic events have been identified by MCM in this four hour time period than the published catalogue, which greatly complements the catalogue. We provide our extended catalogue in the supplementary material. Figure 4.15 shows the number of triggered seismic events within the four hours. With this more complete catalogue, we find that rates of triggered events rise shortly after the passage of surface waves or surface wave overtones. Different to Jay et al. (2012), who conclude that rates of triggered events increased to a peak value of two events per minute with the passage of the X2/X3 Rayleigh wave overtones, we find that earthquake rates reach a peak value of about five events per minute after the passage the G1/R1 surface waves (Figure 4.15). An increase of seismicity after the passage of X2/X3 is noticeable, but only reaches about three events per minute.

4.4 Aquistore synthetic data with real noise

Synthetic waveform data with added Gaussian noise is often used in testing the performance of location algorithms. However in reality, the real noise field is not white, stationary or Gaussian (Birnie et al., 2016). Several noise studies have shown that seismic noise is often variable in space and time, leading to increased difficulty in source

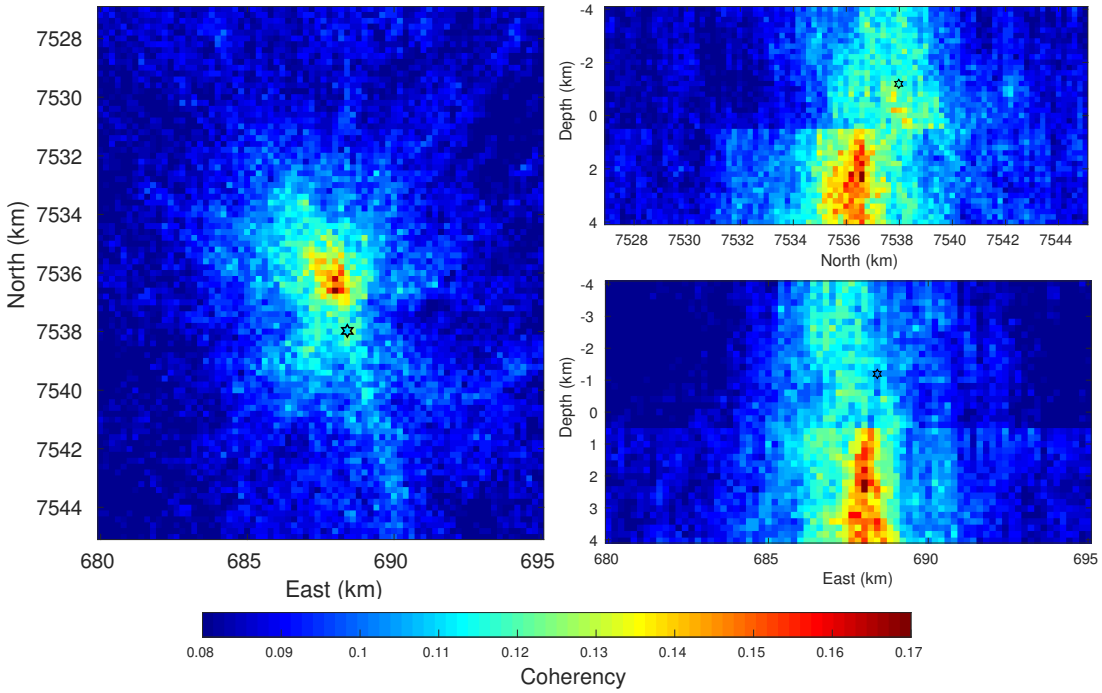

Figure 4.12: Horizontal and vertical profiles at the maximum value of the migration volume for seismic event 1. Color represents the migration value (coherency). Black star represents the event location in the catalogue.

imaging (Birnie et al., 2017). In this section, we apply the MCM location algorithm to the Aquistore noise dataset to examine the location performance in the presence of real seismic noise. The Aquistore noise data have been extracted from a permanent surface array installed at the Aquistore carbon dioxide storage site (Roach et al., 2015, Birnie et al., 2016, 2017). The monitoring data used here were recorded by the surface array during the drilling and construction phase of the injection and observation wells prior to CO_2 injection. Therefore, significant drilling noise and non-stationary noise were recorded in the dataset. No injection-related or induced seismic events are recorded in this period, which makes the recorded time-series an excellent dataset for investigating the effect of real seismic noise on seismic location. Figures 4.16 (a) and (b) show the surface array geometry and velocity model of the Aquistore area. The surface array consists of 50 buried geophones (34 in North-south direction and 16 in East-west direction) with a sampling frequency of 500 Hz.

We generate waveform seismic data using the propagator matrix technique of Zhu & Rivera (2002) for both a shallow and a deep event (Figures 4.16 (c-e)). The shallow and deep events are located at a depth of 2.55 km and 3.15 km, respectively. The deep event has been placed in a thin and relatively low velocity layer. There are also many thin layers above and below the deep event (Figures 4.16 (b-e)), which may cause difficulty in imaging the deep event. We use the shallow and deep events to examine the influence of complex velocity model on the migration result. For both the shallow

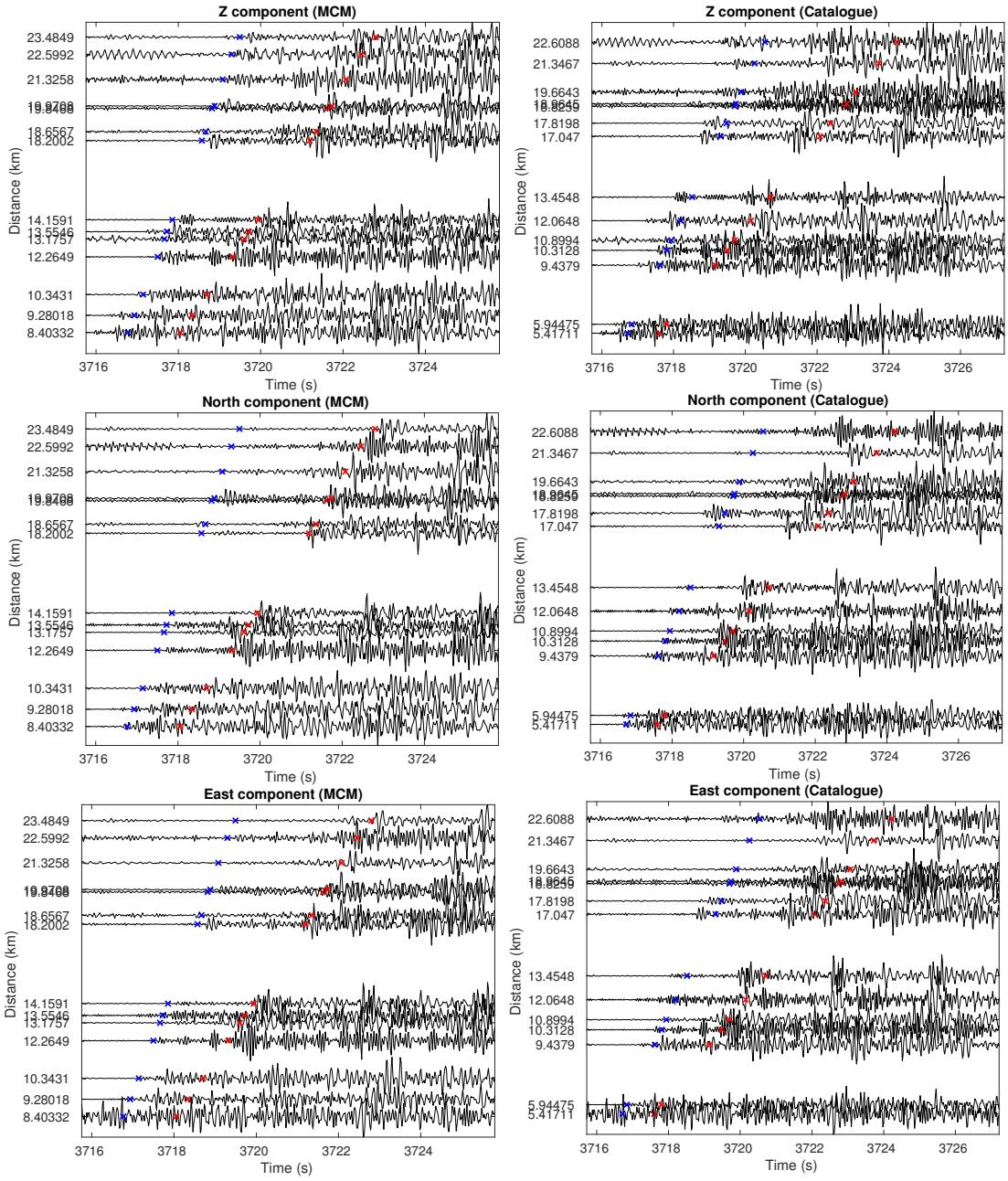

Figure 4.13: Three component record sections for seismic event 1. The predicted P- and S-wave arrival times are marked by blue and red crosses, respectively. Left panel: record sections for the MCM location result. Right panel: record sections for the catalogue location result. The time in the figure is relative to 2010-02-27 06:00:00 (UTC).

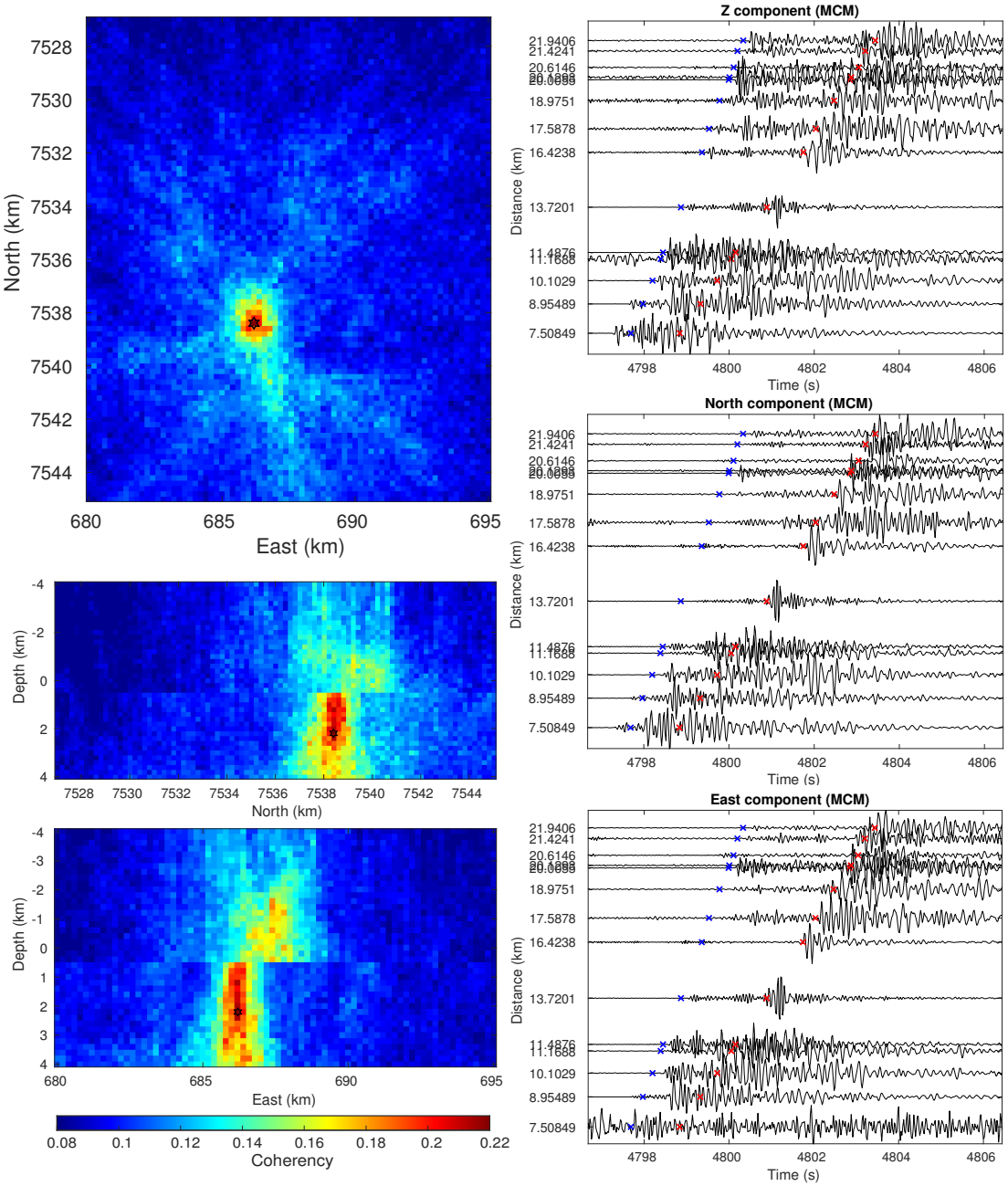

Figure 4.14: Horizontal and vertical migration profiles and three component record sections for seismic event 2, which is newly detected by MCM and not in the existing catalogue. The predicted P- and S-wave arrival times are marked by blue and red crosses on the record sections, respectively. Left panel: horizontal and vertical profiles at the maximum value of the migration volume. Color represents the migration value and black star shows the final event location. Right panel: record sections for this event.

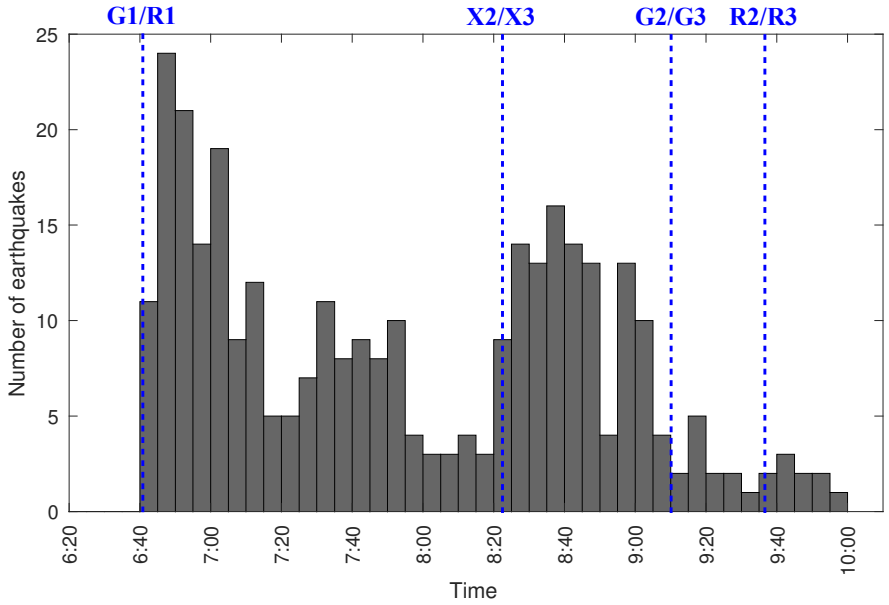

Figure 4.15: Histogram of Uturuncu triggered events from the M_w 8.8 Maule earthquake for the four hours (6 am to 10 am) in 5-min bins. There are no seismic events from 6:00 am to 06:40 am. Blue dashed lines show the approximate arrival time of surface wave trains. G1/R1 represents the minor-arc Love (G1) and Rayleigh (R1) waves. X2/X3, G2/G3 and R2/R3 represent different surface wave overtones (Jay et al., 2012).

and deep event, a 45° dip-slip double-couple source with 40 Hz peak frequency is used to give a specified radiation pattern. The recorded real noise (Birnie et al., 2016) is added to the synthetic data to mimic as closely as possible a 'real' dataset with varying signal-to-noise ratios. The SNR is defined by the ratio of the maximum amplitude between signal and noise. This kind of semi-synthetic dataset enables a quantitative evaluation of the location errors in the presence of different realistic noise scenarios and has been employed to evaluate the monitoring performance of a dedicated seismic monitoring array (López-Comino et al., 2017). The synthetic data and noise data are shown in Figure 4.17. After adding noise, the arrival of the direct P-wave cannot be easily recognized. Stations 18-24 and 41-43 are deployed near the injection and observation well (as shown in Figure 4.16(a)), and thus are seriously contaminated by drilling noise (Figure 4.17c). The non-stationarity and spatial variability of the noise will make event location more difficult.

4.4.1 Location results for shallow event

We compare the location results of different migration methods using waveform envelope, STA/LTA and kurtosis as characteristic functions and also the MCM method for different SNRs. The same monitored real noise of different levels have been added into the synthetic dataset to make the semi-synthetic datasets of different SNRs. The SNRs are chosen to be infinite (noise free), 1, 0.5, 0.25 and 0.025 respectively. We then analyse the influence of SNRs to location results and compare the performance of different

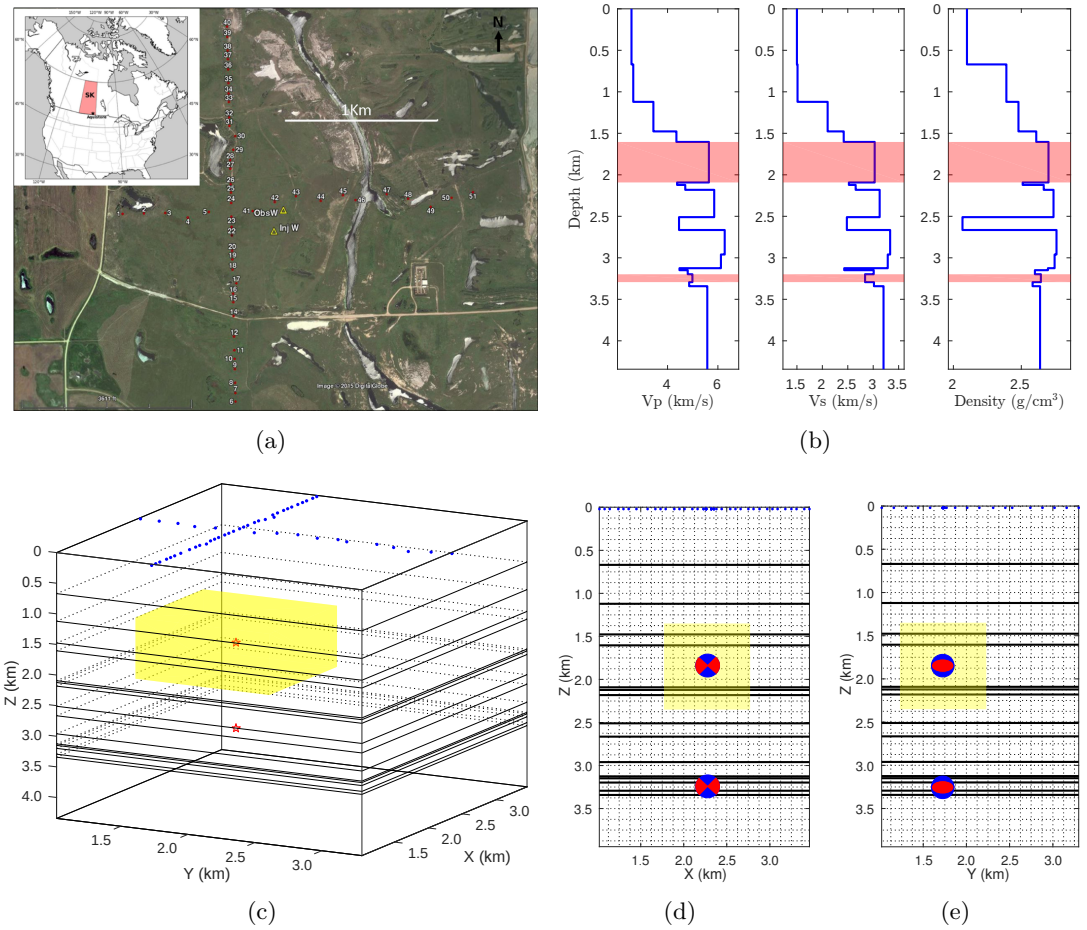

Figure 4.16: (a) Aquistore permanent seismic array geometry. Geophones are denoted by red dots alongside the station number, while the observation and injection wells are illustrated by yellow triangles. (From Birnie et al. (2016)). (b) P- and S-wave velocity model and density model in Aquistore area. The red color highlights two target layers where the seismic events are located. (c) The numerical model space of the Aquistore area. Vertical (d) XZ and (e) YZ profiles of the numerical model. The red stars shows the locations of two seismic events, whose depth are 1.85 km and 3.25 km respectively. Blue points represent the surface geophones. The yellow color exhibits the imaging area of the shallow event. Source radiation patterns are shown in the vertical profiles using a beach ball with red and blue colors.

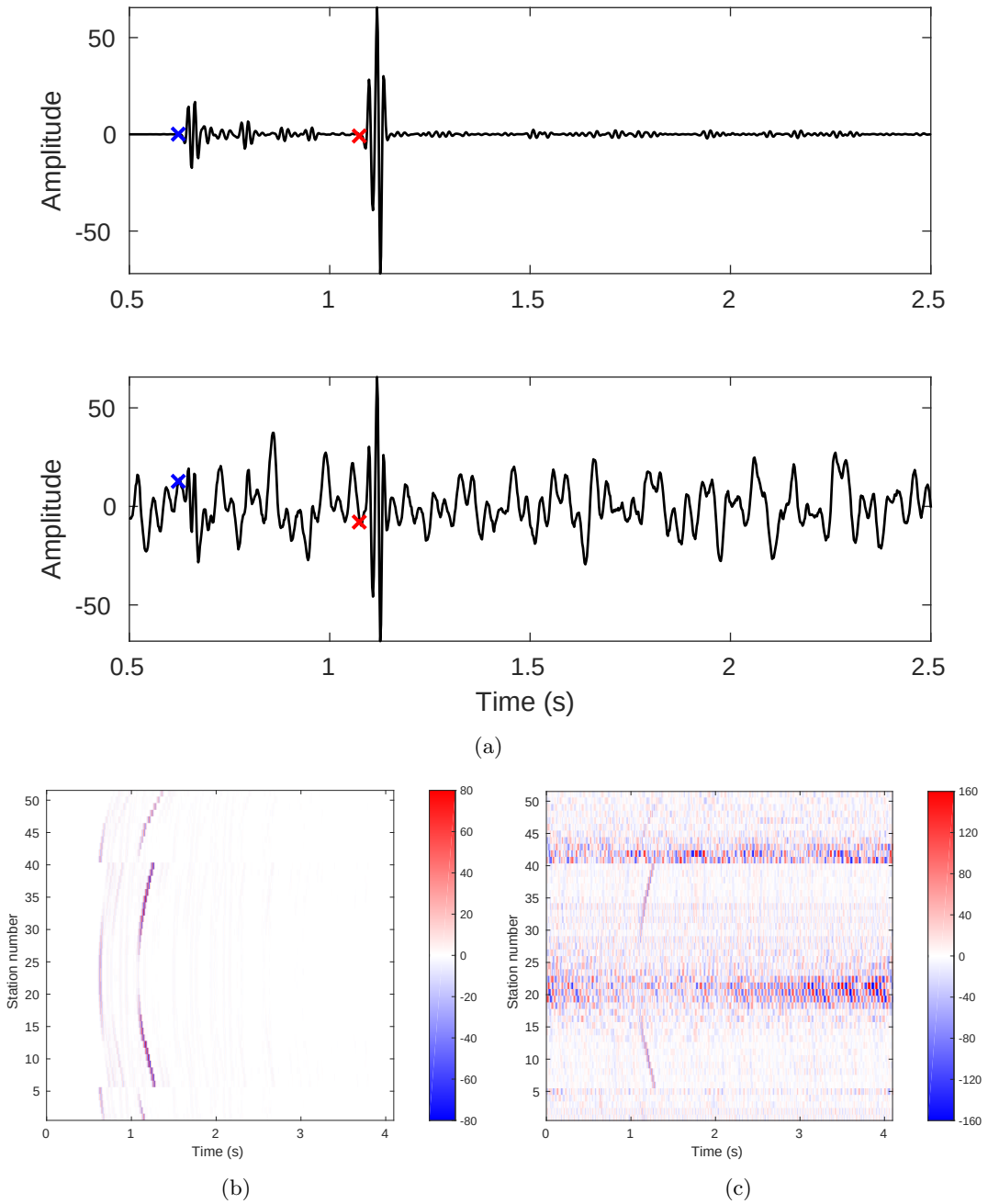

Figure 4.17: (a) The recorded waveform data at station 30 before (top) and after (bottom) adding real noise. The blue and red crosses show the arrivals of P- and S-phases. (b) The synthetic noise-free seismic profile. (c) The seismic profile after adding real noise. The SNR is 0.5.

migration methods under different SNR situations. Figure 4.18 compares the migration results for the four different methods when the SNR is 1 (for a complete comparison of different SNRs, see supplementary material Figures B.1-B.3). When the SNR is larger than 0.25, the MCM exhibits the best resolution and location performance in both the horizontal and vertical directions. Due to the use of the derivative (Langet et al., 2014), the kurtosis seems to have better resolution in the XZ profile (as shown in Figure 4.18). However the location results of kurtosis migration are often biased due to the trade-off between depth and origin time. The results also show that receiver distribution influences the results of the locations. Compared to the X direction, the image in the Y direction relies on fewer geophones leading to increased location uncertainty in that direction, and therefore the envelope, STA/LTA and kurtosis methods show poorer resolution in the Y direction (as shown in Figure 4.18). However the MCM still maintains very good resolution in the Y direction. The location results of the envelope, STA/LTA and kurtosis methods are often biased in the Z direction. When the SNR is below 0.25, the MCM fails to locate the source, because the noise recorded during drilling and construction of the injection well is pervasive over all the traces, especially notable in the traces which are close to the injection well. The drilling and construction noise coming from the injection well is continuous in time, and so leads to continuous coherent noise on all the traces. When the SNR is below 0.25, the drilling noise dominates the wavefield in all the traces. The continuous (both in space and time) and coherent drilling noise contributes to the failure of the MCM method when the SNR is below 0.25. The other methods also fail to locate the source accurately because of strong noise contamination. When the SNR is 0.025, all the methods fail to locate the source. However, approaches have been developed to 'whiten' the noise and hence to reduce the influence of coherent noise (Birnie et al., 2017).

The automatic weighting scheme can be integrated into the multidimensional MCM flexibly (Shi et al., 2019), which gives MCM the ability to conduct automatic quality control of the input data. We devise an automatic quality control scheme to deal with the drilling noise and surmount the SNR limit in the presence of continuous drilling noise. The automatic quality control scheme comprises weighting and filtering. The weighting factors (Shi et al., 2019; equation 3) are determined by evaluating the amplitude of each trace. Because the continuous drilling noise will normally contaminate a whole trace, here we use an average absolute amplitude ratio to discriminate very noisy traces and apply a weighting coherency calculation scheme to all traces. The absolute amplitude ratio of a trace is defined as the ratio of the average absolute amplitude of the trace to the average absolute amplitude of all traces ($a_i = \overline{|\mathbf{d}_i|}/\overline{|\mathbf{D}|}$, a_i is the absolute amplitude ratio of the i-th trace, $\mathbf{d}_i$ is the waveform amplitudes of the i-th trace and $\mathbf{D}$ is the amplitudes of all traces). Figure 4.19 shows the absolute amplitude ratios of different stations for the noisy datasets with different SNRs. For traces which are highly contaminated by continuous drilling noise, the energy of this trace will be much

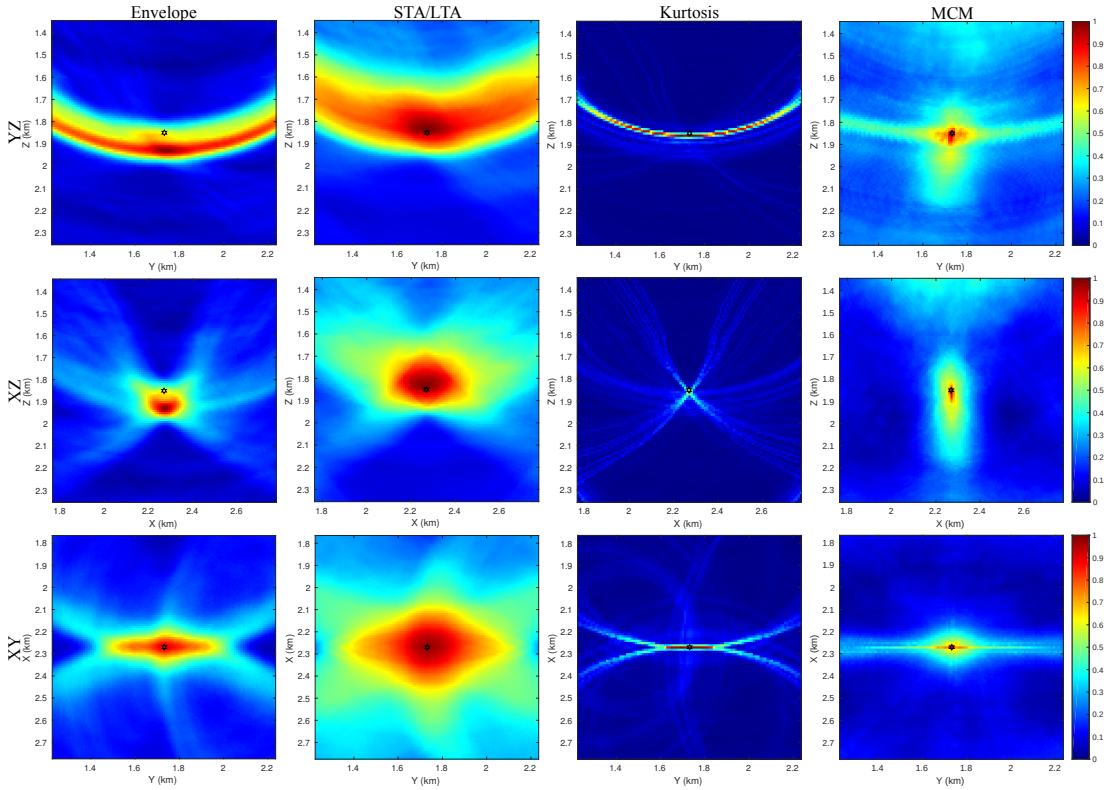

Figure 4.18: Profiles of the migration results through the true source location for the four methods. The SNR is 1. The dark star in the center shows the true source location. The first column shows results of envelope, second column for STA/LTA, third column for kurtosis, fourth column for MCM. The first row shows YZ profiles, second row shows XZ profiles, third row shows XY profiles.

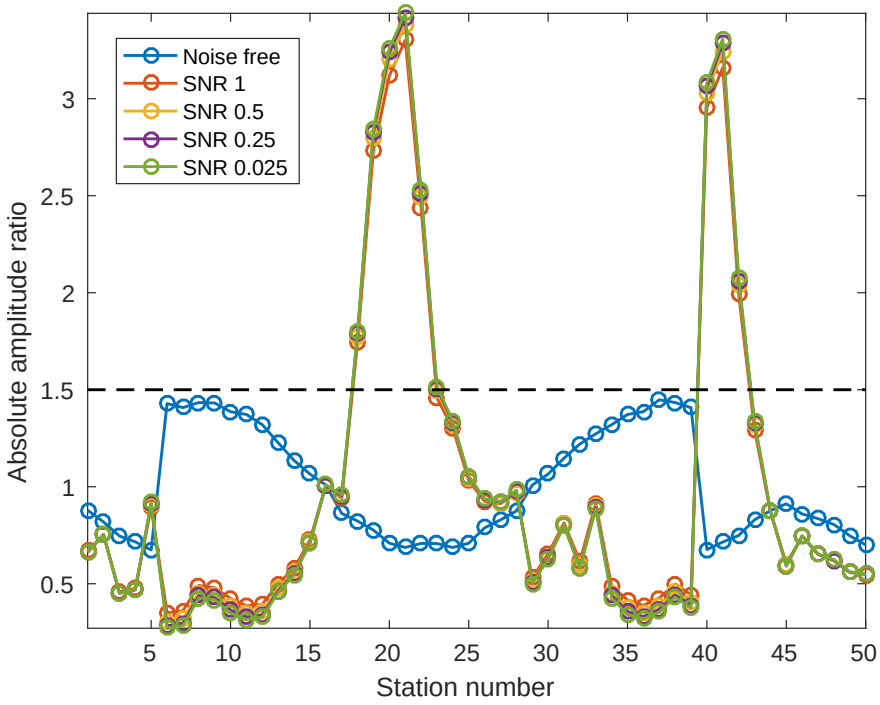

Figure 4.19: The absolute amplitude ratios for different stations under different SNR scenarios. The absolute amplitude ratio of different traces is defined as the ratio of the average absolute amplitudes of a trace to the average absolute amplitude of all traces. The black dashed line shows an absolute amplitude ratio of 1.5.

larger than the average energy over the whole traces, which will contribute to a high absolute amplitude ratio (as shown in Figure 4.19). Through inspecting the absolute amplitude ratios of all traces, we can identify high quality traces and thus stabilize the migration result. We set an absolute amplitude ratio limit of 1.5. Above this limit, the weighting factor of this trace will be set to 0, otherwise the weighting factors are 1. Because our waveform coherency is evaluated through correlation coefficient, the absolute value of the amplitude will not affect the coherency calculation. Therefore, weighting values of 0 or 1 rather than sliding values are assigned to exclude or include traces in the coherency calculation. Through weighting, we select high quality data to conduct migration and exclude traces with very high absolute amplitude ratio (which means extremely low SNR for that trace). As shown in Figure 4.19, traces 19-24 and 41-43 which are close to the observation and injection wells are highly contaminated by the drilling noise (consistent with Figures 4.16 and 4.17). Therefore, after weighting these traces will be excluded from the dataset used for imaging. Before calculating multichannel waveform coherency or characteristic functions, the selected data are filtered in the frequency domain. Because the drilling and construction of the injection well are low-frequency processes, we applied a 6th-order highpass Butterworth filter with a cutoff frequency of 50 Hz to the semi-synthetic data to remove the low frequency drilling noise.

The migration results with automatic quality control scheme (weighting and filtering) are shown in Figure 4.20 and the SNR before filtering is 0.025 (for a complete comparison of different SNRs, see supplementary materials Figures B.4-B.6). Through the automatic quality control scheme, the imaging quality of the four migration methods becomes better and the imaging resolution also improves especially for low SNR scenarios. The MCM exhibits better location results with higher resolution compared to the other methods for all SNR situations. When the SNR is above 0.025, MCM can locate the source accurately without deviation, while the other three methods all have location deviations. When the SNR is 0.025, only the MCM can locate the source correctly with a minimal deviation of 20 m. With such a low SNR, the STA/LTA method focused at the shallow part of the true source position with very low imaging resolution, while the kurtosis method cannot focus correctly. Because of the non-Gaussian property of the real noise and the sensitivity of the characteristic function of the kurtosis method, the kurtosis method is more susceptible to the array geometry. An irregular and/or sparse monitoring array will tend to bias the location results of the kurtosis method. Thus the location results of the kurtosis method are less stable compared to the other three methods. Figure 4.21 shows the location errors of the four methods under different SNRs with/without automatic quality control scheme. The MCM method outperforms the other methods at all noise levels when the automatic quality control scheme is applied (Figure 4.21(b)). The implemented automatic quality control scheme using filtering and weighting can effectively improve the location accuracy for most tested methods.

4.4.2 Location results for deep event

The location results for the deep event with a SNR of 1 are shown in Figure 4.22. Since the SNR is relatively high, for consistency and better comparison with the migration results of the shallow event (Figure 4.18), original data without automatic quality control are used for migration. The velocity model above the deep event is more complicated as it contains thin layers and large velocity contrasts. However, compared to the shallow event, the location results of the deep event are not seriously affected by the complexity of the velocity model. Due to the increase of the velocity in the imaging area, the arrival time differences between the adjacent imaging points become smaller, which is detrimental for distinguishing the phase arrivals. Correspondingly the imaging resolution for all the 4 methods decreases compared to imaging results of the shallow event (as can be seen in the comparison of Figure 4.18 and 4.22). The imaging results of the envelope and STA/LTA methods still have large deviations in the vertical direction, while the MCM and kurtosis methods locate the deep event accurately. The imaging results of the MCM exhibit high resolution in the horizontal direction. However, the resolution in the vertical direction deteriorates compared to the results of the shallow event. The degradation of the vertical resolution is related to the chosen length of

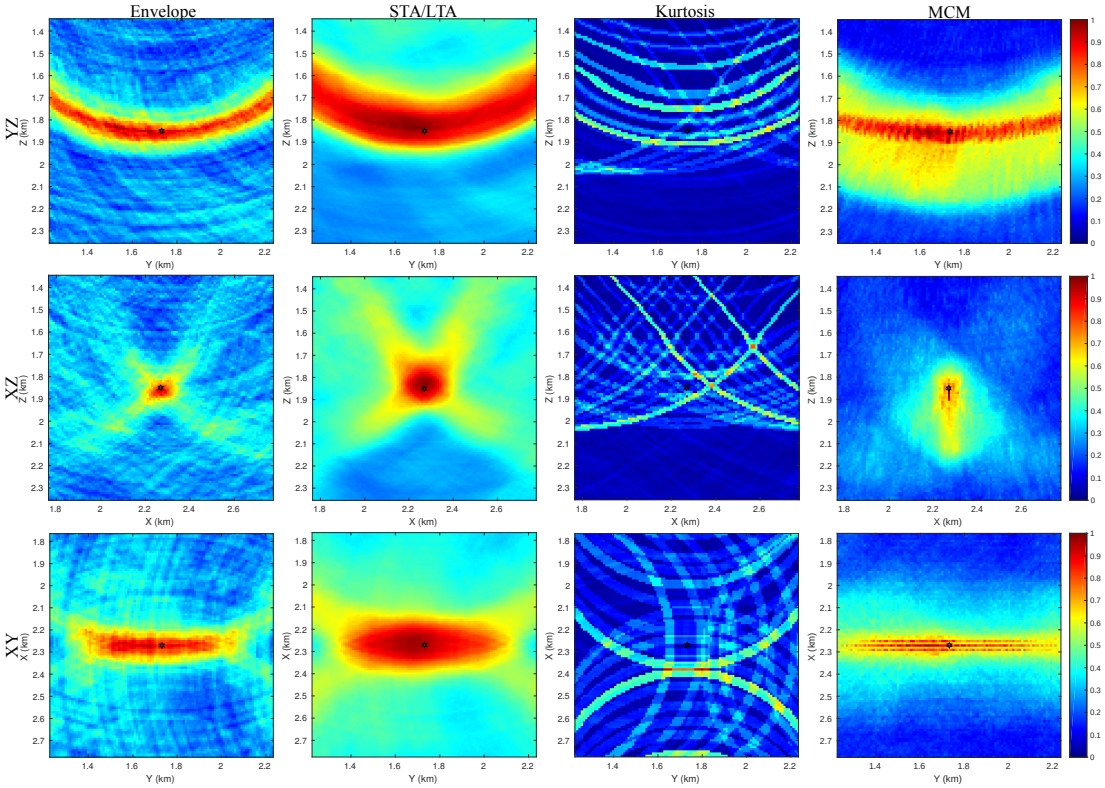

Figure 4.20: Profiles of the migration results through the true source location with automatic quality control scheme (weighting and filtering). The SNR is 0.025. The dark star in the center shows the true source location. The first column shows results of envelope, second column for STA/LTA, third column for kurtosis, fourth column for MCM. The first row shows YZ profiles, second row shows XZ profiles, third row shows XY profiles.

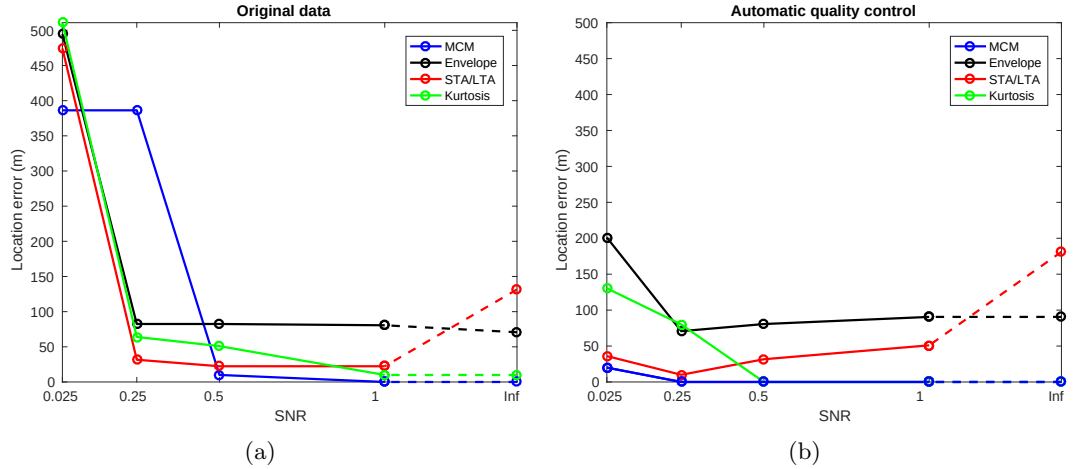

Figure 4.21: The location errors of the four methods under different SNRs with (a) original data and (b) automatic quality control scheme (weighting and filtering).

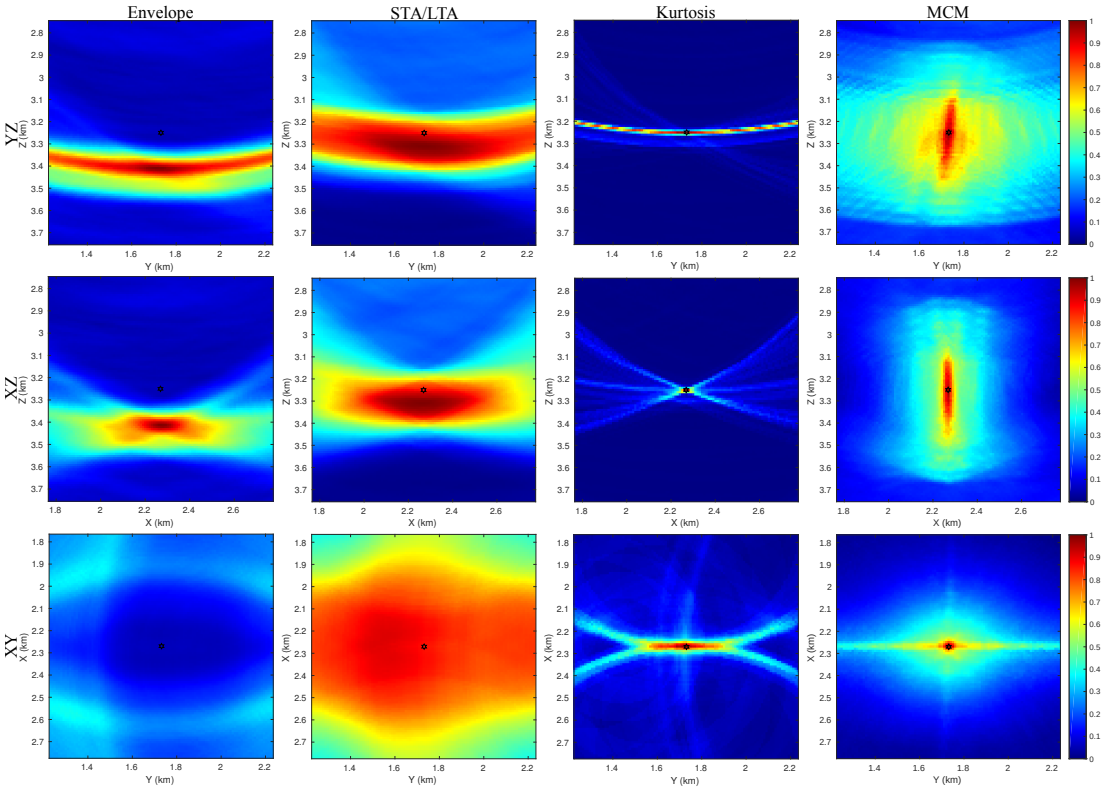

Figure 4.22: Migration profiles through the true source location of the deep event. The SNR is 1. The dark star in the center shows the true source location. The first column shows results of envelope, second column for STA/LTA, third column for kurtosis, fourth column for MCM. The first row shows YZ profiles, second row shows XZ profiles, third row shows XY profiles.

the time window of the coherence analysis as well as the velocity of the imaging area. Although the same time window is applied in the imaging of the shallow and deep events, the higher velocity of the deep event layer contributes to the reduction of the vertical resolution. Using a smaller time window can improve the imaging resolution, but at the expense of reducing noise suppression ability.

Figure 4.23 shows the stacking functions of the four methods at the true source location of the deep event. The four methods all exhibit excellent source prominence at the correct origin time. Time windows for both P- and S-phases are simultaneously used in the migration. The pink area around -0.6 second in Figure 4.23 highlights the time range where P-phases move into the stacking window of the S-phases when searching for origin time. Meanwhile, the pink area around 0.7 second highlights the time range where S-phases move into the stacking window of the P-phases. For the stacking functions of the envelope and STA/LTA methods, a notable peak can be observed at these times. However, the MCM can effectively suppress this kind of disturbance and avoid identifying unrealistic events.

From the results of the Aquistore dataset, we can see that MCM can be used as an effective migration method to automatically locate microseismic events induced by

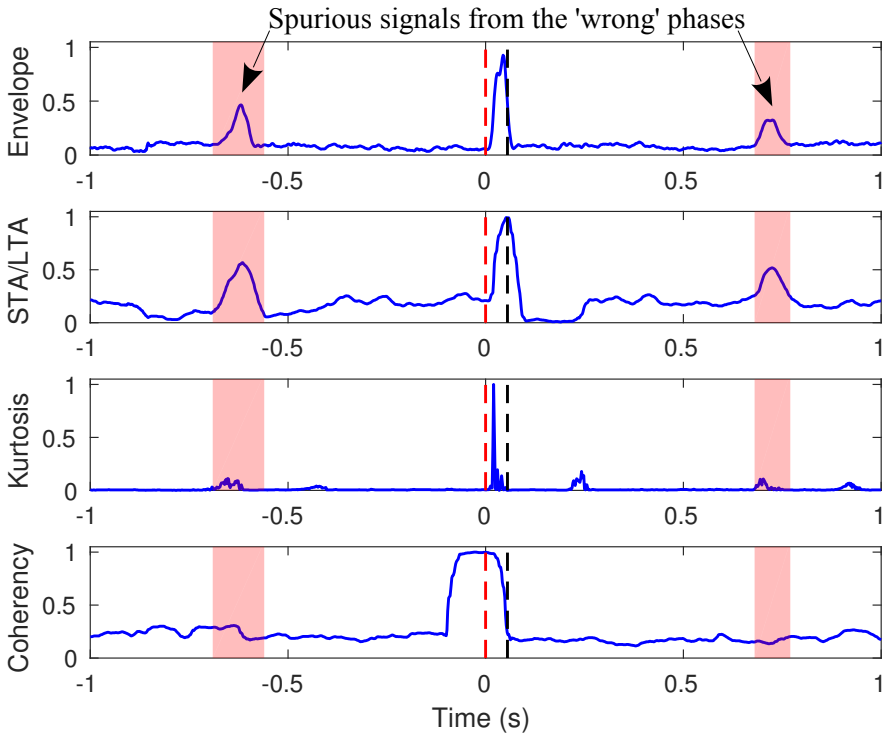

Figure 4.23: The stacking functions of the four methods at the true source location of the deep event for the Aquistore noise data. The red dashed lines show the origin time of the source time function and the black dashed lines show the end time of the source time function. The pink areas around -0.6 s and 0.7 s highlight the time range where P-/S-phases move into the stacking window of the S-/P-phases when searching for origin time. The SNR is 1.

fluid injection or hydraulic fracturing. Although drilling or injection noise can pose big challenges for source imaging, different ways can be adopted to acquire reliable seismic location results. Irregularly distributed monitoring arrays will lead to unbalanced imaging resolution in different directions. However, due to the utilization of multichannel waveform coherency, MCM can acquire higher and much more balanced imaging resolution in different directions compared to other migration-based methods. As traveltime differences between adjacent imaging points in low velocity zone are larger, the imaging results in the low velocity zone (i.e. a shallow event) are better than those in a high velocity zone (i.e. at greater depths), and the source imaging resolution in the low velocity zone is also higher than that in the high velocity zone.

4.5 Discussion

For the synthetic data case, the stacked coherency trace will normally exhibit a flat top as we have discussed in detail in Shi et al. (2019). However, for real data, such flat tops may not exist because of strong interference from noise and coda waves (as shown in Figure 4.5). Typically, one records and takes the time and position which has the maximum coherency value as the origin time and location of a seismic event. However due to a systematic bias between the origin time and the maximum coherent time, calibration is needed in order to obtain an accurate estimation of the origin time of the seismic event. As shown in Figure 4.24, similar to synthetic data, the coherency will start to rise at one coherent analysis time window (referred to as Tw) before the correct source origin time (referred to as T_0). For real seismic data, because of subsurface heterogeneity, there are many coda waves following the direct P- and S-phases. Those coda waves often show lower coherency compared to direct phases and have high amplitudes compared to background noise. Here, we assume the coda waves are incoherent. Therefore, the maximum coherency value will appear one period (referred to as T) of the direct phase after the rise of the coherency. That is to say the maximally coherent time (referred to as $Tmax$) is $Tw - T$ ahead of the correct source origin time. So the calibration equation for source origin time is $T_0 = Tmax + Tw - T$. Since it is easy to obtain a good estimate of the period of the direct phase, we can perform the origin time calibration easily and efficiently. If the direct phases have high SNR and coda waves are partly coherent, we may see a small flat top around Tmax or the maximum coherency value appears around the theoretical maximally coherent time (as shown in Figure 4.24 the dashed line). Thus in this situation, the estimate of the origin time will be affected and shows a small deviation. However, according to our experience of processing the Uturuncu dataset, after calibration we can have a good estimation of source origin times. Finally, in the stacked coherency trace, waveform coherency will decrease to background noise level at one coherent analysis time window after the maximally coherent time.

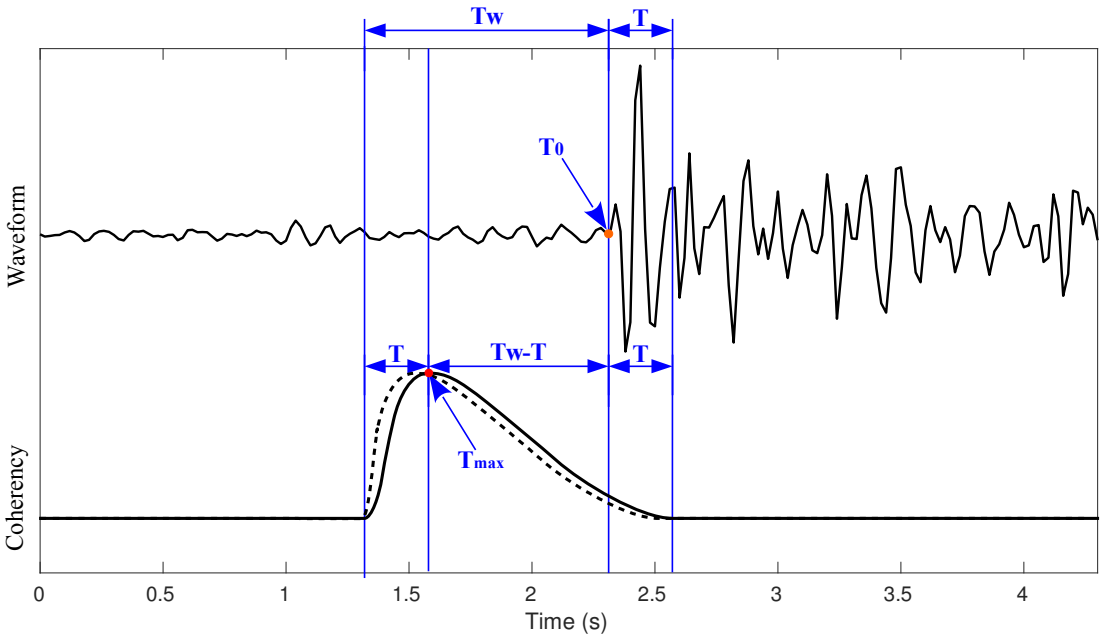

Figure 4.24: Schematic diagram showing recorded waveforms and the corresponding stacked coherency trace. Tw is the length of coherent analysis time window, and T is the period of direct wave. The orange dot shows the arrival time of direct wave, and the red dot shows the maximum coherency value at the stacked coherency trace. For the stacked coherency trace, the solid line shows the maximum coherency value appearing at T time after the rise of waveform coherency, and the dashed line shows the maximum coherency value appearing within T time after the rise of waveform coherency.

For the Uturuncu dataset, only a few stations are available for source location, which negatively affects the MCM imaging. However compared to other migration-based methods, in spite of the very sparse monitoring array, MCM still obtains more reliable and precise location results by the use of multichannel waveform coherency. A dense array with wide aperture and azimuth coverage will greatly improve the imaging quality, especially when a long analysis time window is used. When the stations are widely spread, the traveltime differences to different stations will be large. Thus the migration result of the MCM will be better and the influence of the continuous coda waves can also be reduced. High frequency information in the recorded data is important for improving the imaging resolution. For the Uturuncu dataset, because of a low sampling rate, the highest effective frequency is limited to 25 Hz. The volcano-tectonic earthquakes often contain high-frequency content above this cut-off frequency. The insufficient sampling of the waveform data (as can be seen in the Figure 4.3(b)) has limited the imaging resolution and quality. Despite the sparse recording array and the lack of high frequency content, the MCM still obtains reliable event locations. When possible, we recommend volcano monitoring arrays record at at least 100 Hz to facilitate future automatic volcano-tectonic event determination.

For natural earthquakes, strong coda waves are often observed in the seismograms. The strong coda waves can have a significant influence on the envelope of the waveforms and can also seriously affect the event detection using approaches such as STA/LTA and kurtosis. Thus the location performance of the envelope, STA/LTA and kurtosis migration methods will be negatively affected by the coda waves. Only when the coda waves of different stations are long-lasting and coherent, they will have a negative impact on the MCM migration. The continuous coherent coda waves will make the MCM source imaging ambiguous. One way to deal with coherent coda waves is to increase the analysis time window for the coherency calculation. By using a longer time window, the whole waveform train can be included in the coherent analysis and the direct P- or S-waves as well as the coda waves are utilized to image the source event. Thus in this way the coherency of the coda waves can be fully utilized to improve the event location, however at the expense of reducing the imaging resolution. If coda waves are incoherent, a short analysis time window is suggested to improve waveform coherency value and imaging resolution.

For event location at the Uturuncu, although the same velocity model used in obtaining the event catalogue is utilized for location here, the event locations of the waveform migration method are different to the event location in the catalogue, especially in event depth. The discrepancy may come from different types of information being used in the event location. For events in the catalogue, only the arrival times of the direct P- and S-waves obtained by manual picking are used in the event location. However for waveform migration methods, the recorded waveforms from different stations are directly used to locate the seismic event. MCM automatically identify the

maximum coherent time according to recorded traces and the predicted phase arrival times are thus slightly different from the manually picked arrival times. Regardless of velocity model, the location result of the arrival time based methods will be affected by the accuracy of manual picking, especially for low magnitude events. The location result of migration based methods is mainly affected by the signal-to-noise ratio and medium heterogeneity, which influence the recorded waveforms.

In the record sections (Figures 4.6 and 4.8), the recorded direct P- and S-wave arrivals at some stations do not show a good consistency with the theoretical arrival times. And despite most direct P-wave arrivals corresponding very well to the theoretical arrival times, the recorded S-waves often arrive earlier than the theoretical S-wave arrival times. This discrepancy likely comes from the velocity model used in the event location. Here we just applied a layered velocity model with a constant v_p/v_s ratio of 1.75. In reality, the subsurface can have strong lateral velocity heterogeneity as well as varying v_p/v_s ratio. The S-wave velocity model obtained by ambient noise tomography (Jay et al., 2012) reveals the velocity heterogeneity in the Uturuncu area. If the velocity model is very rough, it is worthwhile to adopt a method which can simultaneously locate the source and update the velocity model. In this way, we can improve the event location accuracy and obtain a more precise velocity model at the same time. By adjusting both the event location and velocity model iteratively, the location results can match the arrivals of seismic phases more precisely. Nevertheless, this is beyond the scope of this study.

For general waveform location methods based on the stacking of characteristic functions, the imaging resolution in different directions is highly dependent on the array distribution. More geophones in a certain spatial direction increases resolution in that direction. However, if one direction is better sampled than the other directions, the imaging results will be dominated by the waveform stacking in that direction. Thus the imaging resolution in other directions (especially in the perpendicular direction) will be degraded (as can be seen in the comparison between the first and second rows in Figure 4.18). If we want to achieve equal resolution in different directions when locating the source, evenly distributed geophones are required. However, MCM utilizes the coherency between all possible receiver pairs, therefore the information from different directions can achieve a better balance improving the MCM locations compared to the other methods. For an irregularly distributed monitoring array, assuming n_p stations have been deployed in the predominant direction, whereas n_c stations ($n_p > n_c$) are deployed in the non-predominant direction. The contribution from non-predominant direction to the whole migrated volume for MCM ($2n_pn_c/\left[(n_p+n_c)(n_p+n_c-1)\right]$) is always higher than that for conventional migration-based methods ($n_c/(n_p+n_c)$). For MCM, due to the use of multichannel waveform coherency across all the stations, the effective information from non-predominant direction can occupy a higher proportion in migration compared to other conventional single-channel-based location methods.

Therefore, the imaging results of MCM are less affected by the irregular distribution of the receivers, and the imaging resolution in different directions are well balanced.

As shown in the imaging results of the Aquistore real noise data, the location results of the envelope and STA/LTA methods often show large deviations in depth. This is because the characteristic functions such as envelope and STA/LTA cannot represent the arrival times of the P- and S-phases accurately. For envelope and STA/LTA, the maximum value of the characteristic function often appears later than the correct arrival times of the P- and/or S-waves. For example, if the source time function is a Ricker wavelet, the maximum value of the envelope is located at the peak amplitude of the P- and S-phases, not at the accurate arrival times of the P- and S-phases, i.e. a half-period later. The characteristic function represents a transformation on the original waveform, and the transformation on recorded waveforms of different stations can have different effects because of noise, source radiation pattern, instrument response, etc. Thus the delayed times corresponding to the correct arrival times can be different for different traces. This will lead to a trade-off between the location depth and the origin time of the event. Finally, both the depth and origin time of the location results can be biased. For the kurtosis method, due to the application of the derivative of kurtosis (Langet et al., 2014), it can represent the arrival times of the P- and S-waves more accurately. Thus less deviations in depth are observed in the location results. However, the kurtosis method is more affected by noise and irregular array geometry. The location results are not stable compared to the other methods, and deviations in depth can easily appear when it cannot represent the arrival time correctly. For MCM, due to the use of multichannel waveform coherency among different traces, the maximum coherency value will appear at the correct arrival times of the P- and S-waves and waveform coherency will decrease rapidly when they deviate from the correct source location (Shi et al., 2019). There is less trade-off between location depth and origin time. Therefore, the MCM can accurately identify the source location and also the origin times with higher resolution.

Continuous coherent noise such as drilling noise remains a challenge for MCM. The coherent noise which is continuous both in space and time will lead to high coherency values between all receiver pairs, thus contributing to the failure of MCM when the coherent noise level is too high. Removing the continuous coherent noise is key to overcoming this problem. If the coherent noise in the recorded data falls into a specific frequency band, we can use frequency filtering or frequency-wavenumber filtering to remove the coherent noise and improve the imaging quality. For microseismic monitoring, the main coherent noise such as the drilling noise and injection noise are often low frequency noise (less than tens of Hz), while the dominant frequency of the microseismic signals are often relatively very high (from tens to thousands of Hz). Therefore, this kind of low frequency noise can be separated and removed from the microseismic dataset by filtering. Automatic quality control techniques such as weighting and

filtering are effective ways to mitigate the effects of noise and improve imaging quality.

4.6 Conclusions

In this paper, we applied the MCM method (Shi et al., 2019) to locate microseismic events in a reservoir and a volcanic setting in the presence of realistic noise. The location results of triggered volcano-tectonic earthquakes demonstrate the feasibility of using MCM method to locate natural earthquakes recorded by sparse arrays. The MCM can automatically locate many triggered events which are difficult and time consuming to manually pick. The MCM has the ability to locate microseismic events which are otherwise often neglected by researchers. Using MCM, we can efficiently obtain a more complete catalogue, which can help us better understand the subsurface earthquake process. The newly obtained seismic catalogue at Uturuncu using MCM can be found in the supplementary material. The predicted arrival times of P- and S-phases at different stations are also attached, which can be used for further studies such as relocation. Compared to other migration based methods, MCM shows more reliable location results and performs better in high noise, sparse monitoring array and strong coda situations. The Aquistore real noise case demonstrates the excellent imaging performance of the MCM in the presence of strong realistic noise. Even though strong coherent noise exists in all traces, the MCM can still locate the source accurately. Usual quality control techniques such as the frequency filtering and weighting are feasible ways to remove coherent drilling or injection noise, the latter of which we employ in an automatic way. Compared to the other methods, the location results of the MCM have higher resolution and are more stable.

Computational efficiency tests of the MCM show that the MCM is highly scalable and parallelizable. The parallel MCM code can achieve a high speedup ratio easily, which gives MCM the ability to perform real time processing. Seismic location with sparse and/or irregularly distributed monitoring array is problematic and difficult. MCM can expand the effective information used for locating by calculating multichannel waveform coherency across different stations, thus in this way improving the location performance with sparse array. When the monitoring array is irregularly distributed, MCM imaging resolution in different directions can also be well balanced due to the use of pairwise handling among all available stations. Compared to other single-channel-based location methods, the location result of MCM is less affected by the irregular and/or sparse distribution of the receivers, and the imaging resolutions in different directions are higher and well balanced. The MCM code is open source and can be downloaded from `https://github.com/speedshi/seisloc`. The MCM code is written in FORTRAN and further developments of the MCM software will be released in the future.

Acknowledgements

We would like to thank Claire Birnie and the Petroleum Technology Research Centre (PTRC) for access to Aquistore Data. Aquistore is an independent research and monitoring project managed by the PTRC which intends to demonstrate that storing liquid carbon dioxide (CO_2) deep underground (in a brine and sandstone water formation), is a safe, workable solution to reduce greenhouse gases (GHGs). Seismic data for the Uturuncu volcano-tectonic earthquakes were obtained via the IRIS DMC from stations in 'The life cycle of Andean volcanoes:Combining space-based and field studies (ANDIVOLC/Cornell)' Network run by the Cornell University (doi: 10.7914/SN/YS_2009). A. Nowacki is supported by a Leverhulme Early Career Fellowship and the Natural Environment Research Council (grant NE/R001154/1).

References

Bai, C.-y. & Kennett, B., 2000. Automatic phase-detection and identification by full use of a single three-component broadband seismogram, *Bull. Seismol. Soc. Am.*, **90**(1), 187–198. 4.1

Barkved, O., Gaucher, E., Hornby, B., Kristiansen, T., & Maisons, C., 2002. Analysis of seismic recordings during injection using in-well permanent sensors, in *64th EAGE Conference & Exhibition*. 4.1

Birnie, C., Chambers, K., Angus, D., & Stork, A. L., 2016. Analysis and models of pre-injection surface seismic array noise recorded at the Aquistore carbon storage site, *Geophys. J. Int.*, **206**(2), 1246–1260. 4.1, 4.4, 4.4, 4.16

Birnie, C., Chambers, K., & Angus, D., 2017. Seismic arrival enhancement through the use of noise whitening, *Phys. Earth Planet. In.*, **262**, 80–89. 4.1, 4.4, 4.4.1

Cesca, S. & Grigoli, F., 2015. Chapter two-full waveform seismological advances for microseismic monitoring, *Adv. Geophys.*, **56**, 169–228. 4.1

Drew, J., White, R. S., Tilmann, F., & Tarasewicz, J., 2013. Coalescence microseismic mapping, *Geophys. J. Int.*, **195**(3), 1773–1785. 4.1, 4.3.1

Eisner, L., Hulsey, B., Duncan, P., Jurick, D., Werner, H., & Keller, W., 2010. Comparison of surface and borehole locations of induced seismicity, *Geophys. Prospect.*, **58**(5), 809–820. 4.3.1

Gharti, H. N., Oye, V., Roth, M., & Kühn, D., 2010. Automated microearthquake location using envelope stacking and robust global optimization, *Geophysics*, **75**(4), MA27–MA46. 4.1, 4.3.1

Gibowicz, S. J. & Kijko, A., 2013. *An introduction to mining seismology*, vol. 55, Elsevier. 4.1

Grigoli, F., Cesca, S., Amoroso, O., Emolo, A., Zollo, A., & Dahm, T., 2013a. Automated seismic event location by waveform coherence analysis, *Geophys. J. Int.*, **196**(3), 1742–1753. 4.1

Grigoli, F., Cesca, S., Vassallo, M., & Dahm, T., 2013b. Automated seismic event location by travel-time stacking: An application to mining induced seismicity, *Seismol. Res. Lett.*, **84**(4), 666–677. 4.1, 4.3.1

Grigoli, F., Cesca, S., Krieger, L., Kriegerowski, M., Gammaldi, S., Horalek, J., Priolo, E., & Dahm, T., 2016. Automated microseismic event location using master-event waveform stacking, *Sci. Rep.*, **6**, 25744. 4.1

Jay, J. A., Pritchard, M. E., West, M. E., Christensen, D., Haney, M., Minaya, E., Sunagua, M., McNutt, S. R., & Zabala, M., 2012. Shallow seismicity, triggered seismicity, and ambient noise tomography at the long-dormant Uturuncu Volcano, Bolivia, *Bull. Volcanol.*, **74**(4), 817–837. 4.1, 4.3, 4.3.1, 4.3.2, 4.3.2, 4.15, 4.5

Kao, H. & Shan, S.-J., 2007. Rapid identification of earthquake rupture plane using Source-Scanning Algorithm, *Geophys. J. Int.*, **168**(3), 1011–1020. 4.1, 4.3.1

Knudsen, S., Havsgård, G., Berg, A., & Bostick, T., 2006. Flow-induced noise in fiber-optic 3C seismic sensors for permanent tubing-conveyed installations, in *68th EAGE Conference and Exhibition incorporating SPE EUROPEC 2006*. 4.1

Langet, N., Maggi, A., Michelini, A., & Brenguier, F., 2014. Continuous Kurtosis-based migration for seismic event detection and location, with application to Piton de la Fournaise Volcano, La Réunion, *Bull. Seismol. Soc. Am.*, **104**(1), 229–246. 4.1, 4.3.1, 4.4.1, 4.5

Lavallée, Y., Meredith, P., Dingwell, D., Hess, K., Wassermann, J., Cordonnier, B., Gerik, A., & Kruhl, J., 2008. Seismogenic lavas and explosive eruption forecasting, *Nature*, **453**(7194), 507. 4.1

López-Comino, J., Cesca, S., Kriegerowski, M., Heimann, S., Dahm, T., Mirek, J., & Lasocki, S., 2017. Monitoring performance using synthetic data for induced microseismicity by hydrofracking at the Wysin site (Poland), *Geophys. J. Int.*, **210**(1), 42–55. 4.4

Maggi, A., Tape, C., Chen, M., Chao, D., & Tromp, J., 2009. An automated time-window selection algorithm for seismic tomography, *Geophys. J. Int.*, **178**(1), 257–281. 4.1

McNutt, S. R., 1996. Seismic monitoring and eruption forecasting of volcanoes: a review of the state-of-the-art and case histories, in *Monitoring and mitigation of volcano hazards*, pp. 99–146, Springer. 4.1

Peng, Z. & Zhao, P., 2009. Migration of early aftershocks following the 2004 Parkfield earthquake, *Nat. Geosci.*, **2**(12), 877. 4.1

Power, D. V., Schuster, C. L., Hay, R., & Twombly, J., 1976. Detection of hydraulic fracture orientation and dimensions in cased wells, *J. Pet. Technol.*, **28**(09), 1–116. 4.1

Pritchard, M., 2009. The life cycle of Andean volcanoes:Combining space-based and field studies, *International Federation of Digital Seismograph Networks. Other/Seismic Network. 10.7914/SN/YS_2009*. 4.3

Pritchard, M. & Simons, M., 2004. An InSAR-based survey of volcanic deformation in the central Andes, *Geochem. Geophys. Geosyst.*, **5**(2). 4.3

Roach, L. A., White, D. J., & Roberts, B., 2015. Assessment of 4D seismic repeatability and CO2 detection limits using a sparse permanent land array at the Aquistore CO2 storage site, *Geophysics*, **80**(2), WA1–WA13. 4.4

Shi, P., Angus, D., Nowacki, A., Yuan, S., & Wang, Y., 2018a. Microseismic Full Waveform Modeling in Anisotropic Media with Moment Tensor Implementation, *Surv. Geophys.*, **39**(4), 567–611. 4.1

Shi, P., Yuan, S., Wang, T., Wang, Y., & Liu, T., 2018b. Fracture Identification in a Tight Sandstone Reservoir: A Seismic Anisotropy and Automatic Multisensitive Attribute Fusion Framework, *IEEE Geosci. Remote Sens. Lett.*, **15**(10), 1525–1529. 4.1

Shi, P., Angus, D., Rost, S., Nowacki, A., & Yuan, S., 2019. Automated seismic waveform location using Multichannel Coherency Migration (MCM)–I. Theory, *Geophys. J. Int.*, **216**(3), 1842–1866. 4.1, 4.2, 4.2, 4.2, 4.3.1, 4.3.1, 4.3.1, 4.4.1, 4.5, 4.5, 4.6

Sparks, R. S. J., Folkes, C. B., Humphreys, M. C., Barfod, D. N., Clavero, J., Sunagua, M. C., McNutt, S. R., & Pritchard, M. E., 2008. Uturuncu volcano, Bolivia: Volcanic unrest due to mid-crustal magma intrusion, *Am. J. Sci.*, **308**(6), 727–769. 4.3

Verdon, J., Kendall, J.-M., White, D., & Angus, D., 2011. Linking microseismic event observations with geomechanical models to minimise the risks of storing CO2 in geological formations, *Earth Planet. Sci. Lett.*, **305**(1), 143–152. 4.1

Verdon, J. P., Kendall, J.-M., White, D. J., Angus, D. A., Fisher, Q. J., & Urbancic, T., 2010. Passive seismic monitoring of carbon dioxide storage at Weyburn, *The Leading Edge*. 4.1

Wilks, M., Kendall, J.-M., Nowacki, A., Biggs, J., Wookey, J., Birhanu, Y., Ayele, A., & Bedada, T., 2017. Seismicity associated with magmatism, faulting and hydrothermal circulation at Aluto Volcano, Main Ethiopian Rift, *J. Volcanol. Geoth. Res.*. 4.1

Xu, N., Tang, C., Li, L., Zhou, Z., Sha, C., Liang, Z., & Yang, J., 2011. Microseismic monitoring and stability analysis of the left bank slope in Jinping first stage hydropower station in southwestern China, *Int. J. Rock Mech. Min. Sci.*, **48**(6), 950–963. 4.1

Yuan, S., Wang, S., Ma, M., Ji, Y., & Deng, L., 2017. Sparse Bayesian learning-based time-variant deconvolution, *IEEE Trans. Geosci. Remote Sens.*, **55**(11), 6182–6194. 4.1

Yuan, S., Liu, J., Wang, S., Wang, T., & Shi, P., 2018a. Seismic waveform classification and first-break picking using convolution neural networks, *IEEE Geosci. Remote Sens. Lett.*, **15**(2), 272–276. 4.1

Yuan, S., Wang, S., Luo, C., & Wang, T., 2018b. Inversion-Based 3-D Seismic Denoising for Exploring Spatial Edges and Spatio-Temporal Signal Redundancy, *IEEE Geosci. Remote Sens. Lett.*, (99), 1–5. 4.1

Zhebel, O. & Eisner, L., 2014. Simultaneous microseismic event localization and source mechanism determination, *Geophysics*, **80**(1), KS1–KS9. 4.1

Zhu, L. & Rivera, L. A., 2002. A note on the dynamic and static displacements from a point source in multilayered media, *Geophys. J. Int.*, **148**(3), 619–627. 4.4

Chapter 5

Discussion and conclusions

5.1 Conclusions

With the development of seismic acquisition and processing techniques, analysis of seismic waveforms has become an essential part of probing the structure and dynamics of the Earth. Seismic waveforms contain much more information about the properties of the Earth's interior than just the traveltimes of seismic phases. Seismic waveforms have been increasingly utilized in various geophysical methods, such as seismic interferometry (Schuster, 2009) and full waveform inversion (Virieux & Operto, 2009), to better understand the Earth. In this thesis, I have developed a seismic full waveform modeling tool and a waveform based seismic location method to try to utilize seismic waveforms. The developed modeling tool (Chapter 2) and location method (Chapter 3) apply to general heterogeneous and anisotropic media, and are particularly suitable for applications in the field of microseismic monitoring. Numerical analysis about computational efficiency and accuracy of these two methods are discussed in this thesis. Practical applications including synthetic and real data examples are also displayed and discussed in the corresponding chapters. The developed methods can help extract more information from seismic full waveforms and gain a better understanding of the Earth.

Seismic anisotropy is an important property of the subsurface medium especially for shales where hydraulic fracturing is often implemented. Seismic anisotropy can be caused by shape preferred orientation (SPO) of cracks and lattice preferred orientation (LPO) of minerals. Seismic anisotropy has been used to determine the orientation of subsurface cracks and to infer mantle flow directions (Verdon et al., 2009, Verdon & Kendall, 2011, Savage, 1999). It is often very difficult to obtain an accurate estimation of seismic anisotropy in the subsurface. Therefore, in many seismic data processing, interpretation and inversion processes, seismic anisotropy is generally ignored and an isotropic model is assumed. The effects of seismic anisotropy on the interpretation and inversion of seismic data mainly come from the exclusion of seismic anisotropy

when it actually cannot be ignored. For seismic location, seismic source mechanism characterization, seismic tomography and other seismic data processing procedures in anisotropic media, if seismic anisotropy is not correctly taken into account, the obtained results will have errors and can thus affect further studies. Obtaining the traveltimes and Green's function in anisotropic media is key to performing anisotropic seismic processing, interpretation and inversion.

My seismic waveform modeling tool can help analyse the effects of variations of elastic properties (including anisotropy) of rocks on seismic waveforms. I investigate the effects of seismic anisotropy on seismic traveltime, amplitude and radiation pattern, and also further discuss the effects of seismic anisotropy on the determined seismic location. After analysing the modeling datasets, I discuss potential ways of retrieving seismic anisotropy from recorded seismic data. Furthermore, I utilize the developed seismic modeling tool to generate synthetic datasets for the new seismic waveform based location method that I have developed in Chapters 3, 4 and Shi et al. (2019a,b). The seismic modeling tool provides the basis for numerical analysis of the performance of the new seismic location method. In particular, the modeling tool is used to generate synthetic waveforms with different signal-to-noise ratios (SNRs) and different monitoring geometries. Therefore, the performance of the new location method in noisy situations and under various monitoring geometries can be quantitatively evaluated. My methods developed in this thesis hopefully can make a step forward towards the full waveform seismic processing, interpretation and inversion, and provide better images and insights into the Earth's interior. In this section, I will provide an overview of the key achievements of my thesis.

Key achievement 1: Development of a seismic full wavefield forward modeling tool (Chapter 2).

The developed seismic full wavefield modeling tool can simulate seismic full wavefield propagation in heterogeneous and anisotropic media using arbitrary moment tensor sources. The velocity model can have arbitrary complexity in heterogeneity, thus the seismic wavefield in very complex models such as random media can be calculated and studied. The seismic modeling tool applies to the isotropic, vertical transverse isotropic (VTI), horizontal transverse isotropic (HTI) and orthorhombic media which are common effective media for shale and fractured rocks. The Thomsen parameters (Thomsen, 1986) or the elastic tensor of the medium can be used to specify the anisotropy of the medium. The modeling tool can use arbitrary moment tensors including double-couple sources which are common for natural earthquake and non-double-couple sources which are common for hydraulic fracturing. The modeling tool adopts a standard staggered-grid finite-difference (FD) scheme with tenth-order in the space domain and second-order in the time domain. The numerical analysis shows the modeling tool can provide sufficient accuracy for anisotropic modeling with arbitrary moment

tensor sources. Due to the use of a standard staggered-grid FD scheme, interpolation of wavefield components is not required in the wavefield simulation in isotropic, VTI, HTI and orthorhombic media.

The modeling tool can be used to generate the Green's function in heterogeneous and anisotropic media, and thus can be further used in moment tensor inversions to characterize source mechanisms. Seismic full waveforms of various monitoring geometries including surface, buried and downhole arrays can be simulated and analysed. The synthetic waveforms can be used to test and verify the accuracy of various seismic imaging methods under different settings, e.g. monitoring geometry and model complexity. As a forward modeling tool, it can also be used for reverse time migration and full waveform inversion to image the seismic sources or subsurface velocities in anisotropic media. My developed wave propagation algorithm provides the community with a fast and accurate way to calculate wave propagation in realistic media using various seismic sources.

Key achievement 2: Investigation of the effects of seismic anisotropy on seismic amplitudes, radiation patterns and seismic location and provision of ways to obtain seismic anisotropy of the subsurface (Chapter 2).

Seismic anisotropy will affect the propagation of seismic waves, and thus can affect the amplitudes, phases and frequency contents of the recorded seismic data. Recorded seismic data in anisotropic and isotropic medium can show big differences. Therefore, ignoring seismic anisotropy can lead to a wrong seismic interpretation and incorrect inversion results. I demonstrate that if seismic anisotropy is ignored, seismic event locations based on dense local stations and accurate picks can still have a location error of hundreds of meters in anisotropic media, which is unacceptable for microseismic monitoring. For microseismic monitoring of hydraulic fracturing and mining, a few hundred meters of location error can be fatal for assessing the stimulation effect or estimating risk. My anisotropic modeling tool can be used to acquire seismic waveforms and traveltimes in anisotropic models and can thus contribute to the accurate inversion of seismic sources and velocity models. I demonstrate that it is feasible to extract the anisotropic information of the subsurface through analysing the traveltimes and amplitudes of recorded seismic data. If the seismic anisotropy is related to subsurface fractures such as induced fractures during fracking, it is possible to identify the distribution mode of fracture networks (e.g. horizontal or vertical aligned) and to estimate the orientation and density of the subsurface fractures. Those parameters are key factors to evaluate the stimulation effects during a hydraulic fracturing. Therefore my waveform modeling algorithm and proposed anisotropy estimation method will contribute to the better characterization of underground reservoirs and storage.

Key achievement 3: Development of an automated multichannel cross-

correlation based seismic location method for continuous seismic data (Chapters 3 and 4).

Conventional arrival time based seismic location methods require the picked arrival times of different seismic phases. The identification and picking of seismic phases requires extensive human involvement and can take months when dealing with large datasets and many seismic events. So it is inefficient for modern datasets. In contrast to conventional arrival time based seismic location methods, the developed location method: Multichannel Coherency Migration (MCM) does not require phase identification, picking and association. The location process of MCM is automatically performed on continuous seismic waveforms. The computational cost of MCM only depends on the length of seismic recordings and the number of stations and imaging points, and is not related to the number of seismic events, which makes it efficient for large datasets containing many seismic events. MCM can be easily parallelized on different scales (imaging points and/or recording times), and there is little information exchange between different computing nodes. My numerical analysis on parallel computing shows that MCM is highly scalable approaching the theoretical speedup ratio. Since MCM does not rely on phase identification and picking and can be efficiently parallelized, it is very suitable and efficient for long term and real time seismic event location and monitoring. I apply MCM to locate induced earthquakes beneath Uturuncu volcano, where seismicity is induced by the passage of surface waves caused by the M 8.8 2010 Maule earthquake. MCM automatically detects and locates 98% of 114 hand-picked catalogue events (Shi et al., 2019b). In addition, 322 verified additional events which have not been previously detected are automatically detected and located by MCM.

In situations where many seismic events occur over a short time period (e.g. common for hydraulic fracturing), the phase arrivals of different seismic events may overlap. It can be very difficult to identify, pick and associate the picked arrivals to a specific seismic event. In addition, when the SNR of the seismic data is less than 1, phase picking can be impossible. Thus, many weak seismic events which are masked by noise cannot be identified and located using conventional methods. However, for MCM, the waveforms are automatically migrated to the correct source locations, thus MCM does not require phase identification and association. Therefore, MCM is suitable to tackle those situations. For conventional location methods, the location accuracy is largely dependent on the picking accuracy, thus depends on SNR and human experience. MCM can automatically find the seismic location which has a maximum waveform coherency. Therefore, the event location is purely determined by recorded seismic data and the location accuracy is not related to the human accuracy while phase picking. The event location results of MCM can be used as input for double-difference location methods (Waldhauser & Ellsworth, 2000) to further improve the location accuracy. The event locations and the associated arrival times which are automatically obtained by MCM can also be used as initial constraints to manual picking for further improving location

reliability and accuracy. My developed seismic location method improves our ability to automatically and accurately locate weak seismic events in noisy surface seismic data.

Key achievement 4: By utilizing waveform coherency, MCM has the ability to locate weak seismic events (Chapters 3 and 4).

Conventional migration based location methods directly stack seismic amplitudes or characteristic functions of seismic traces to image seismic sources. Therefore, seismic events with large amplitude/magnitude will have large stacking/migration values and the source imaging space will be dominated by those strong seismic events. The weak seismic events (microseismic) and seismic events below the noise level cannot be well imaged. In contrast to conventional migration methods, MCM calculates and stacks waveform coherency to image seismic sources. In theory, the waveform coherency is not related to waveform amplitude or event magnitude. Using both synthetic and real seismic data, I have demonstrated that waveform coherency of a weak seismic event can be larger than that of a strong seismic event. Therefore, MCM has the ability to image and locate microseismic events. MCM can automatically locate more microseismic events which will otherwise be neglected by the conventional picking-based or migration-based methods, and thus can obtain an improved seismic catalogue with a much lower magnitude threshold. The improved catalogue can be further used in any other seismic analysis such as investigating b-values and seismic tomography. MCM presented in this work allows us to precisely detect and locate more events than has been possible using automatic methods before.

Key achievement 5: By stacking the waveform coherency of different station pairs, MCM is very noise resistant and shows high imaging resolution (Chapters 3 and 4).

Conventional migration based location methods stack the characteristic functions of different traces to calculate the migration value of each imaging point. Thus for a particular imaging point, there are N values to be stacked (N is the number of stations). However, for MCM, the migration process is based on the cross-correlation of waveforms from different station pairs or groups. The migration value of each imaging point is calculated by stacking the correlation coefficients of different station pairs or groups. Therefore for a particular imaging point, there are M values to be stacked. M is the number of unique station pairs or groups. For 2D MCM, M is equal to $N \times (N-1)/2$. Due to the utilization of waveform cross-correlation, more information is extracted from the recorded seismic waveforms to image a seismic source. The synthetic and real data examples show MCM is more noise resistant and has higher imaging resolution than conventional migration location methods. The location example with real noise from a carbon capture and storage site shows MCM works well even when the SNR of seismic data is as low as 0.025. With strong noise resistance, MCM is able to locate

microseismic events and can help us acquire a more complete seismic catalogue for further studies.

Key achievement 6: Due to the use of station pairs or groups in migration, MCM shows a balanced imaging resolution in different directions (Chapter 4).

The deployment of a seismic monitoring array is constrained by practical considerations during the deployment, such as topography and geomorphology. In many situations, irregular monitoring arrays have to be deployed. The imaging results are dominated by the direction with more stations and the imaging resolution in this direction is much higher than that of the other directions. However, the migration process of MCM is based on station pairs or station groups, and information from different directions is mixed to image a seismic source. The imaging resolution of MCM achieves a balance in different directions. Both synthetic and real data examples demonstrate that MCM performs better on irregular and/or sparse monitoring arrays than other conventional migration-based location methods. With a balanced imaging resolution, MCM is able to image seismic events more accurately.

5.2 Technique details and computational efficiency for MCM location method

5.2.1 Identifying seismic events in a migration data volume

One of the key procedures in the MCM (Chapter 3) is to identify seismic events in a 4D migration volume. If the imaging space is limited (e.g. less than millions of imaging points) and the time range of recorded seismic data is short (e.g. less than thousands of sampled origin time points), we can save the complete 4D migration data volume and further identify seismic events by finding local maxima in the data volume. However, when dealing with continuous seismic data or imaging of a large model, the complete 4D migration data volume will be too big to store and search (with volumes easily larger than tens of Gigabytes). Therefore, compressed sensing and storage of the complete migration volume is required.

There are two strategies to compressively store the migration volume. One is to only store the maximum migration value at every imaging point. For this strategy, only one migration value is stored per imaging point during the migration process at different origin times. Therefore, the final storage volume is only related to the number of imaging points. However, this strategy cannot be used to identify seismic events which occur at the same position since only the seismic event with the maximum migration value will be identified at a position. In addition, a seismic event with lower migration values can be easily masked by a strong seismic event nearby which has

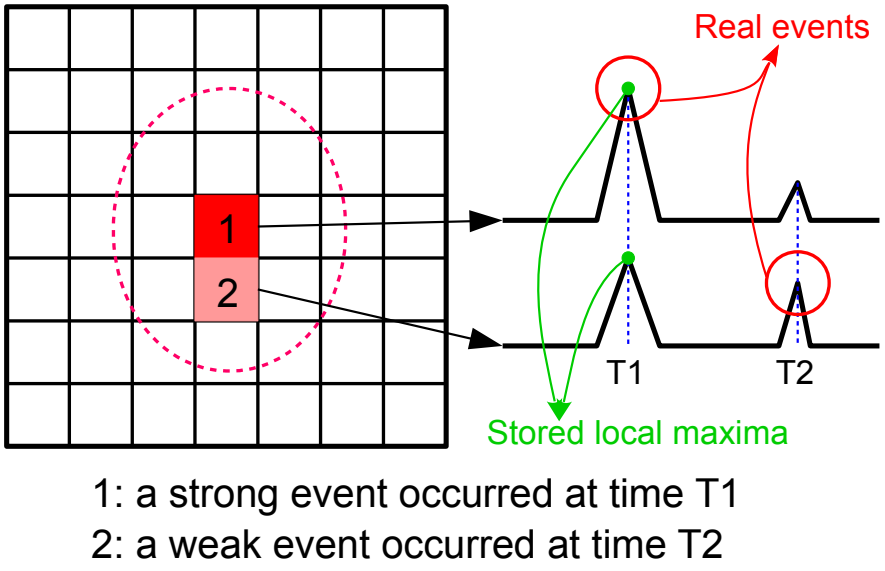

Figure 5.1: Schematic diagram of the migration and location process for only storing the maximum migration value at each imaging point. The left panel shows the imaging space and the color and number label show the locations of two seismic events occurred nearby but at different times. Red dashed line shows the influence area of the strong event. The imaging points within the influence area will have relatively high migration values at the origin time of the strong event compare to other imaging points. The solid lines on the right panel show the migration traces for the two corresponding imaging points 1 and 2. The strong event 1 occurred at time T1 and the weaker event 2 occurred at time T2 (indicated by the blue dashed lines and red circles in the migration traces). The weak event 2 is located within the influence area of the strong event 1. The green dots show the identified and stored maximum migration value at the imaging points 1 and 2. Due to the influence of the nearby strong event 1, at the imaging point 2 the migration value at time T1 is taken and saved. Therefore, the real seismic event 2 has been masked and omitted.

a higher coherency value (independent of the origin time difference between the two events), and thereby will be discarded due to the limited spatial resolution (Figure 5.1). Thus, this strategy may lead to a poor spatial resolution with many weak seismic events around strong events being omitted. The other strategy is to only store the maximum migration value at every sampled origin time. For this strategy, only one migration value is stored per origin time during the migration process of different imaging points. Therefore, the final storage volume is only related to the number of searched origin time points. However, this strategy cannot be used to identify seismic events which occur at the same time since only the seismic event with the maximum migration value can be identified at an origin time. In addition, the seismic event with lower migration values can be easily masked by a strong event occurring at a similar time (independent of the distance between the two events), and will be discarded due to the limited temporal resolution (Figure 5.2). Thus, this strategy may lead to a poor temporal resolution with many weak seismic events occurring within a time window of the origin time of strong events are omitted.

Since it is not rare that seismic events occur at similar positions especially for

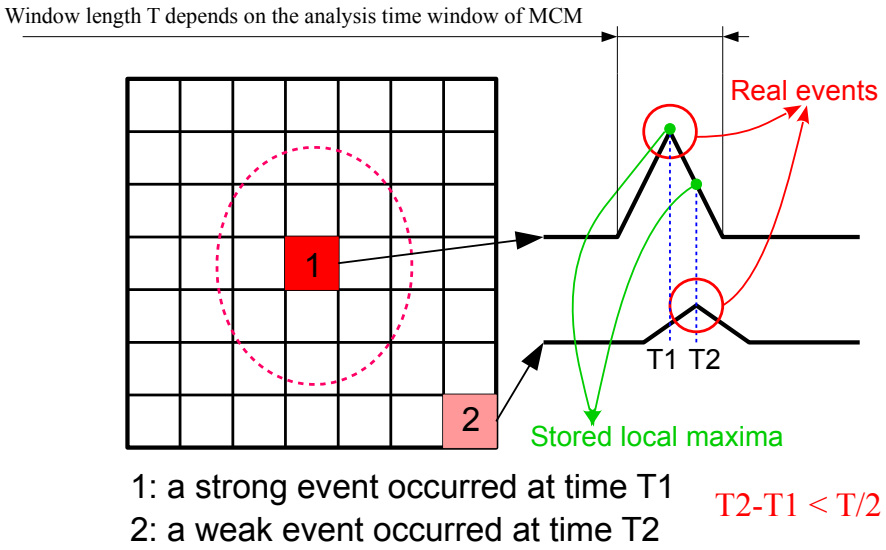

Figure 5.2: Schematic diagram of the migration and location process for only storing the maximum migration value at each sampled origin time. The left panel shows the imaging space and the grids with color and number label show the locations of two seismic events occurring closely in time but at distance. Red dashed line shows the influence area of the strong event. The solid lines on the right panel show the migration traces for the two corresponding imaging points 1 and 2. The strong event 1 occurred at time T1 and the weaker event 2 occurred at time T2 (indicated by the blue dashed lines and red circles in the migration traces). The weaker event 2 occurs within the time window where the strong event 1 can exert a big influence. The time window T essentially depends on the coherency analysis time window of MCM and the period of the signals. The green dots show the identified and stored maximum migration value at the searched origin time T1 and T2. Due to the influence of the strong event 1, at the origin time T2 the migration value of the imaging point 1 is taken and saved. Therefore, the real seismic event 2 has been masked and omitted.

long term seismic monitoring (e.g. months or years) or for real time seismic monitoring during stimulation, I currently adopt the second strategy in MCM. The fact that seismic events often cluster at locations also favours the second strategy. This means we often need to identify closely-located events at different origin times. Therefore, a seismic location method with high spatial resolution rather than high temporal resolution is needed in this situation. In addition, seismic events occurring at exactly the same time or within a single analysis time window of MCM are not a common situation, and a temporal resolution of several seconds (tens or hundreds of millisecond for microseismic) is generally enough for most scenarios. There are ways to implement an improved compressed sensing strategy. Storing multiple values instead of a single maximum value at an imaging point or origin time can solve the aforementioned problems of the two strategies. This will involve finding local maxima in the 1D migration trace of an imaging point for the first strategy or finding local maxima in the 3D migration volume of an searching origin time for the second strategy. However, finding local maxima in a 1D or 3D dataset which correspond to true seismic events still need further development.

Real seismic events still need to be detected on the compressed migration traces. I explored different ways to detect seismic events from the stored migration traces. The first one is achieved by examining the duration of the potential seismic event. When there is a seismic event in the migration data volume, migration values of the imaging points around the true source location will be high over a certain time period (roughly longer than a coherency analysis time window). In contrast when there is no seismic event in the migration data volume, the maximum migration value of random noise at different searched origin times will randomly appear at imaging points in the migration space. Since we have stored the maximum migration values at each sampled origin time, we can identify seismic events by examining whether the maximum migration values of a continuous time period appear within a certain distance (referred to as pseudo seismic cluster, Figure 5.3). Seismic location and origin time can thus be determined by selecting the imaging point with maximum migration value in the valid pseudo seismic cluster.

The other way to detect a seismic event on the compressed migration traces is to identify local peaks in the migration traces. When an earthquake occurs, due to the generated wavefield of seismic source in the imaging space, the coherency values of all imaging points will rise over a time period covering the correct source origin time. And the maximum migration value at the correct source origin time will be a peak in the compressed migration trace (Shi et al., 2019b). Through identifying peak values in migration traces, we can detect potential seismic event locations (Figure 5.4 a). Due to the interferences of noise and coda waves, not all local peaks are true seismic events. Some peaks come from the energy of long waveform trains generated by scattering. Thus a further refinement to discriminate the real and fake seismic events is required, or more stringent parameters (such as higher coherency threshold, higher

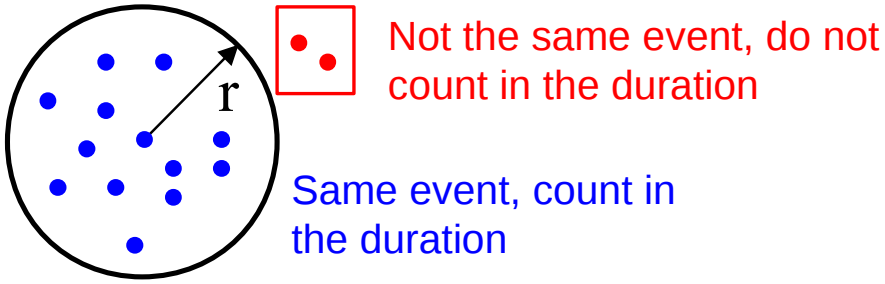

Figure 5.3: Identifying seismic events using the duration of the potential seismic event. Maximum migration value over a continuous time period (around the correct source origin time) will appear within a certain distance (around the correct source location) when there is a seismic event in the migration data volume. This is referred to as a pseudo seismic cluster shown as blue points in the figure. Red points show maximum migration values which are outside the predefined distance and will not count in the pseudo seismic cluster.

source prominence and longer origin time gap) should be adopted in identifying the local peaks from migration traces (Shi et al., 2019b). At the present, the identified local maxima are verified through analysis of a record section to help determine whether they are true seismic events (Figure 5.4 b). Since it is easy to verify a seismic event from the corresponding record section and the verification process is essentially an image recognition process, machine learning algorithms have the potential to contribute an automatic verification process. From my experience on synthetic and real datasets, this way to identify seismic event from migration trace works better and is currently adopted in the MCM algorithm.

5.2.2 Key parameters in MCM

The frequency band of the input seismic data and the coherency analysis time window are the key parameters for MCM. They can have a big influence on the migration results of MCM. These parameters need to be adjusted according to the nature of the recorded seismic data. For the choice of frequency band of the input data, the main objective is to increase the waveform coherency of the signals and reduce the effects of noise (both coherent and incoherent). At low frequencies (below 1 Hz), the surface waves of large earthquakes and other low frequency sources are potentially interfering with the imaging of local earthquakes and microseismics. At high frequencies (tens or hundreds of Hz), high frequency noise is usually detrimental to imaging seismic sources. Therefore, a bandpass frequency filter is generally used to filter out low frequency interference and high frequency noise, and thus increasing the waveform coherency of effective signals and the imaging resolution. The choice of frequency band is largely dependent on the type and magnitude of seismic sources. For natural earthquakes, the effective frequency band of seismic sources depends on the earthquake magnitude. For large earthquakes, the dominant frequency can be a few Hz. For microseismics, the dominant frequency can be as large as hundreds or even thousands of Hz. When determining the frequency

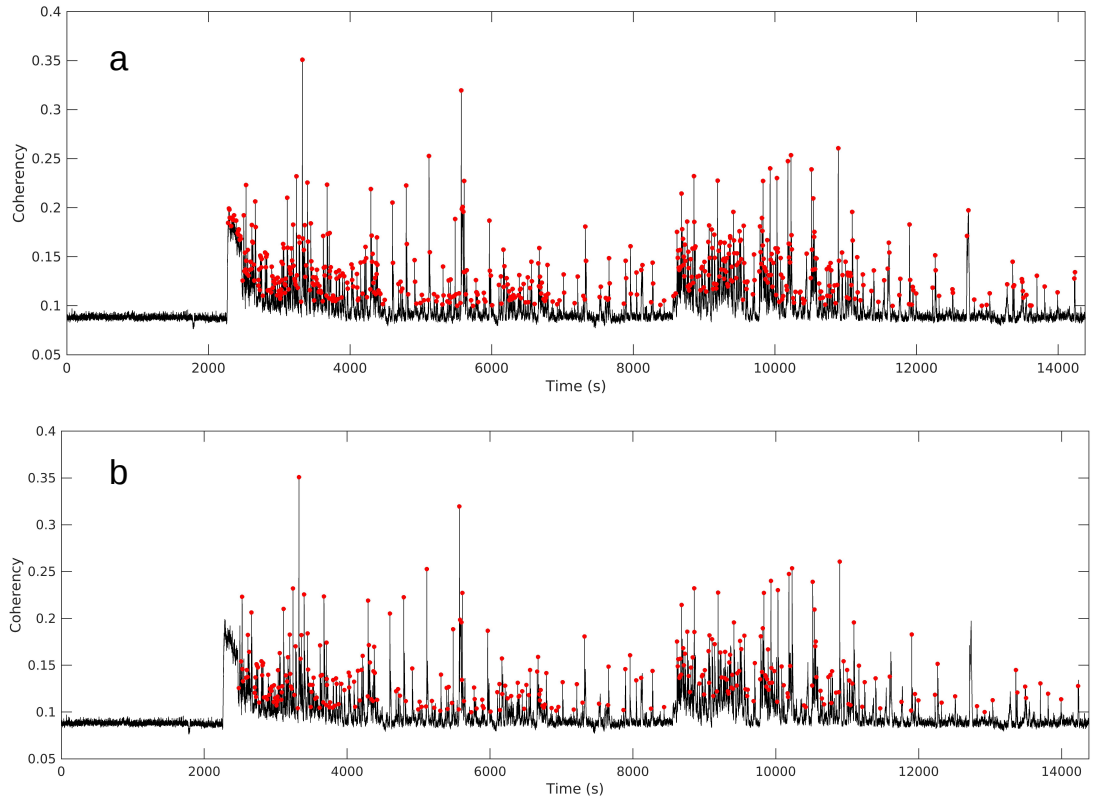

Figure 5.4: Identifying seismic events through finding local peaks in the compressed migration traces. The black lines show the compressed migration traces, i.e. the maximum migration values at each searched origin times. Red points show the identified local peaks in the migration traces, i.e. potential seismic events. (a) Migration trace with all the identified local peaks. (b) Migration trace with the verified local peaks (through the corresponding seismic record sections).

band of the input data for MCM, one should consider and include the effective frequency range of seismic sources of interest.

The length of the coherency analysis time window of MCM will affect the reliability and resolution of imaging results of MCM. Origin times of seismic events are also calibrated according to the time window length and the approximate period of signals in MCM. A longer time window can lead to more reliable migration results in the presence of noise, while a short time window can improve the temporal resolution of migration results of MCM. In general, the time window should be no less than the period of the effective signals, i.e. direct P- and S-phases, in order to fully evaluate the waveform coherency of seismic signals. As more data points are used in the coherency calculation, a longer time window can improve the reliability of migration results of MCM and suppress random noise. Therefore, the choice of time window length depends on the period of signals and the SNR of the input dataset. If the SNR of seismic data is high (e.g. larger than 2), the time window length should be equal to or slightly larger than the period of signals. If the SNR of seismic data is low (e.g. less than 1), a longer time window (e.g. 5-10 times of the period of signals) should be used to stabilize the migration results and suppress noise. For seismic data containing strong coda and surface waves, the coda and surface waves may result from complex heterogeneities of subsurface, thus will undermine the waveform coherency of the primary phases (i.e. direct P- and S-phases). In this situation, a long time window should be used. My experience from a volcanic earthquake dataset (Chapter 4) which contains strong coda and surface waves suggests that a time window of ten times the period of signals can produce reliable migration results for MCM. For seismic data which has a low time sampling rate, a long time window should also be used to assure that adequate time samples have been included into the coherency analysis. The time window length of MCM can range from tens of milliseconds for high-sampling rate microseismic data to seconds for local earthquake monitoring data containing strong coda waves.

5.2.3 Computational efficiency of MCM

For picking-based location methods, manual picking can be costly in terms of processing time especially for picking large numbers of seismic events. In contrast, migration-based location methods work directly on recorded seismic waveforms and the location effort is independent of the number of seismic events. Therefore, the migration-based location methods are very suitable for locating earthquakes which occur densely in a short time period, such as induced microseismic events by hydraulic fracturing. For conventional migration-based location methods, the computational cost is linearly proportional to $N_s \times N_t \times N$ (N_s is the number of imaging points, N_t is the number of sampled origin times, N is the number of seismic stations). For the MCM, the computational cost is proportional to $N_s \times N_t \times M \times 10M_t$ (M is the number of station groups used in MCM and M_t is the number of time samples within the coherency analysis time window) (Shi

et al., 2019a). M equals $N \times (N-1)/2$ for the commonly used two-dimensional MCM and equals $\frac{N!}{m!(N-m)!}$ for the m-dimensional MCM. The computational cost of MCM increases rapidly with station numbers, which makes it unsuitable for processing large monitoring arrays giving the current computing power.

However, the MCM algorithm can be parallelized very efficiently. The computational efficiency analysis of MCM (Shi et al., 2019b) shows that MCM can achieve a very high speedup ratio (close to the theoretical speedup ratio) on many computing nodes using Message Passing Interface (MPI). The largest computational burden of MCM algorithm concentrates on the cross-correlation between waveforms of station groups. The correlation calculation is a linear process, and the calculation at each imaging point and sampled origin time is independent of the calculation of the other imaging points and origin times. Thus this process can be perfectly parallelized, and communication between different computing nodes is only needed when outputting migration results. Since graphics processing units (GPUs) have many computing cores and can perform well on specialised tasks such as the cross-correlation (Clark et al., 2013), the MCM algorithm can be very efficient if parallelized on both central processing units (CPUs) and GPUs, and can thus be suitable for real time seismic monitoring.

5.3 Limitations of MCM location method

MCM still faces several challenges which need to be carefully considered in practical applications. The first challenge is computational effort. As an automated seismic location method, MCM is much more expensive than other conventional migration-based location methods. The computational cost of conventional migration-based location methods grows linearly with the number of stations, while the computational cost of MCM increase exponentially with the number of stations. This feature contributes to the high imaging resolution and strong noise resistance of MCM, however also limits the application of MCM to very large monitoring arrays (e.g. contain hundreds or thousands of stations). Although parallel computing can be used in MCM, the exorbitant computational cost on very large arrays still makes MCM inapplicable. The utilization of full-dimensional MCM can significantly reduce the computational cost. But the location results of full-dimensional MCM compared to two-dimensional MCM still need further studies.

MCM mainly utilizes waveform coherency to locate seismic events. Thus the degeneration of waveform coherency will largely affect the location results of MCM. The waveform coherency will be affected by subsurface heterogeneity, coda wave interference and ambient noise. When waveform coherency between different stations is totally devastated by these factors, MCM will not be applicable. The location process of MCM is a highly non-linear process. The location results of MCM are not directly related to the arrival times of seismic phases or the velocity model. Therefore, in contrast to

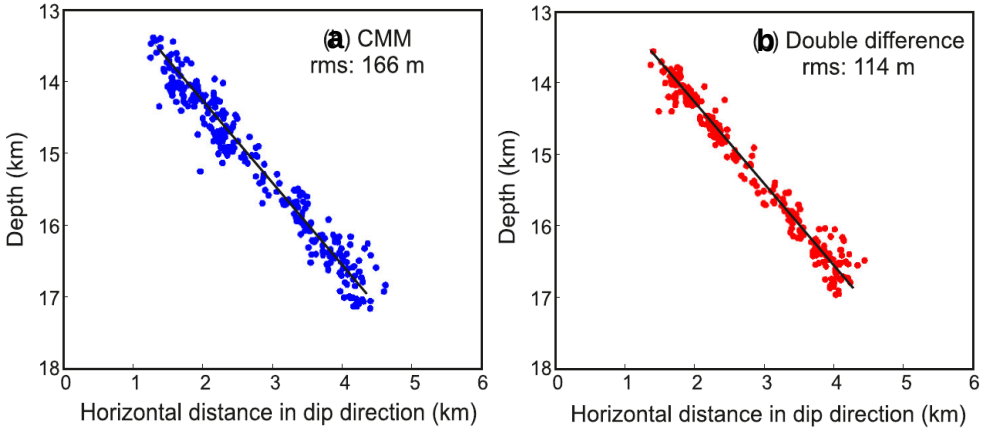

Figure 5.5: Seismic location results using migration-based method and double-difference method. (a) Automatic seismic location results using migration-based method. Blue points show the located seismic events. (b) Seismic relocation results of double-difference method using the results in (a) and manual refinement of the corresponding arrival times. Red points show the relocated seismic events. The relocation results have a smaller arrival time residual than the automated location results, which indicates more accurate location results. Figure modified from Drew et al. (2013).

picking and arrival time-based location methods, the location uncertainty of MCM is difficult to estimate at the present.

5.4 Further applications of MCM location results

The location results of MCM can be further used in many other seismic processing procedures such as earthquake relocation, seismic tomography and source mechanism characterization. Thus the combination of MCM and other seismic techniques have the potential to lead to automated seismic location and relocation, velocity model determination and source mechanism characterization based on continuous seismic waveforms.

5.4.1 Earthquake relocation using relative location methods

MCM can automatically locate seismic events and output the theoretical arrival times of the direct P- and S-phases of seismic events. The obtained seismic catalogue and the corresponding arrival times can be used as inputs for relative location methods to relocate the seismic events. By utilizing relative location methods such as double-difference location method (Waldhauser & Ellsworth, 2000), a more compact and accurate seismic locations can be obtained (Figure 5.5). The MCM location results and the corresponding theoretical arrival times can also be used as constraints for a further manual refinement of arrival times. The refinement results can be further used for earthquake relocation or seismic tomography. It is more convenient and efficient than direct phase picking from seismic records.

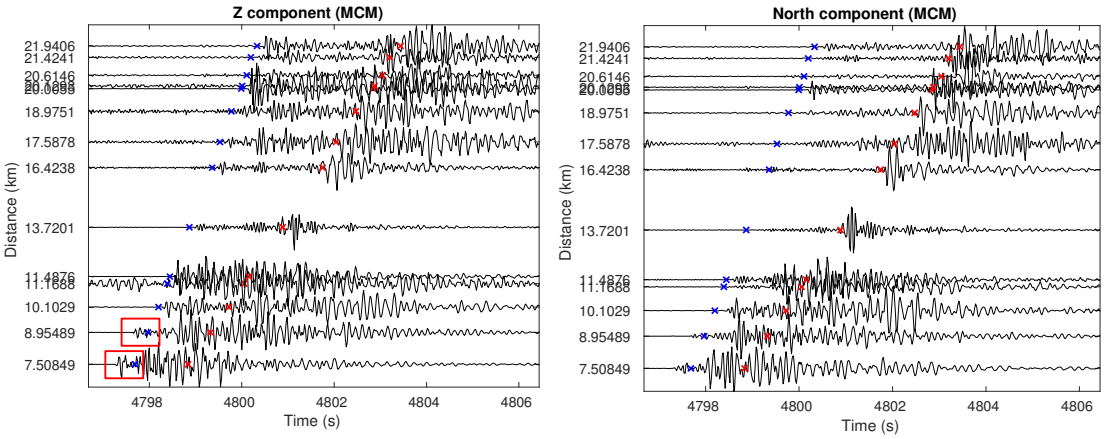

Figure 5.6: Record sections of a seismic event which is automatically located by MCM. Blue crosses show the predicted theoretical arrival times of direct P-phases. Red crosses show the predicted theoretical arrival times of direct S-phases. Left panel: record section of the Z component. Right panel: record section of the north component. Red rectangles highlight the mismatch of the theoretical and the actual arrival times.

5.4.2 Velocity model update using seismic tomography methods

In practice, accurate velocity model is always difficult to obtain. Uncertainties in velocity model will inevitably bias seismic location results, thus will lead to the mismatch between the observed records and the theoretical predictions. In MCM location results, the mismatch between the predicted arrival times and the actual arrival times can be observed (Figure 5.6). MCM can automatically locate seismic events according to the overall waveform coherency across all the stations and selected phases. Thus the predicted phase arrival times is an overall reflection of all stations and selected phases, not a direct reflection of the phase arrival of an individual station. The predicted arrival times produced by MCM show the most coherent time of waveforms under the current velocity model and SNR, and will be different from the actual arrival times if the adopted velocity model is inaccurate. Relocation results of MCM or manual refinement of MCM results can be used in seismic tomography to obtain a more accurate velocity model. The updated velocity model can lead to more coherent MCM location results with a better matching with recorded data. An iterative process of MCM location and seismic tomography might contribute to automated seismic location and velocity determination using continuous seismic waveforms.

5.4.3 Source mechanism characterization using moment tensor inversion

The source mechanism is important in revealing the nature of the seismic event. It can be used to evaluate the induced fracture pattern in hydraulic fracturing, and can determine the fault orientation during an earthquake. Moment tensor inversion is an efficient way to determine source mechanisms. Moment tensor inversion requires

reliable seismic location results. The conventional seismic location method based on arrival time picking require human involvement and thus is not suitable for automated and real time processing. If a Green's function library is available, moment tensor inversion can be conducted based on the location results of MCM. Integrating MCM and moment tensor inversion can contribute to an automated seismic location and source mechanism determination process. The Green's function library in a particular region can be precalculated using various forward modeling methods such as my forward modeling tool (Shi et al., 2018). Therefore, real time seismic location and source mechanism determination based on MCM and moment tensor inversion is feasible, which is important for real time fracturing assessment during hydraulic fracturing.

5.5 Applications and importance of identifying microseismic events

For conventional seismic location methods, microseismic events are always difficult to detect and locate. One reason is that microseismic events normally have small amplitudes and thus have low SNRs; the other reason is that they exist in large numbers and thus it is expensive to manually identify and pick them. Due to the strong noise resistance of MCM, MCM can automatically locate microseismic events below the noise level. Therefore, MCM can generate a more complete seismic catalogue with much lower detection threshold of magnitude than conventional seismic location methods. The MCM location results can be further used to investigate b-values, tomography and any other seismic analysis based on microearthquakes. Rock failure and crack opening in the subsurface generate microseismic events. Thus a complete seismic catalogue can be used to fully evaluate the stimulation effect in reservoir enhancement (such as hydraulic fracturing) and mitigate potential seismic hazard such as in mining. Microseismic events are also related to many natural processes such as magma incursion and fault creeping (Green et al., 2015, Rubin et al., 1999). Microseismic events can help study the physical mechanisms behind these phenomena.

5.6 Future work

The developed seismic modeling tool applies to isotropic, VTI, HTI and orthorhombic media. However, tilted fractures can be stimulated in hydraulic fracturing. Rock with massive aligned tilted fractures or dipping layers can be approximated as a tilted transverse isotropic (TTI) medium. In order to simulate wave propagation in TTI media, I plan to extend the modeling tool and make it applicable to TTI or general anisotropic media.

Currently, conventional absorbing boundary conditions are used in the developed seismic modeling tool. Weak boundary reflections can still be observed in the modeling.

The non-physical boundary reflections can interfere with other effective signals and further interfere the interpretation and inversion of seismic data. Perfectly matched layer can attenuate the boundary reflections better. Therefore, in the future I plan to implement perfectly matched layer boundary condition into the modeling tool.

For hydraulic fracturing, many microseismic events can occur over a short time period. The waveforms of different seismic events can overlap and the recorded wavefield often contains waveforms from different seismic events. I plan to extend the modeling tool and make the modeling tool suitable for the simulation of multiple sources with independent source time functions and source mechanisms.

In contrast to traveltime inversion based location methods, it is difficult to estimate the location uncertainties of the migration based location methods. Inaccurate velocity models will affect the theoretical traveltimes and thus can further affect location performance. For traveltime inversion based location methods, it is relatively easy to estimate location uncertainties, because the relationship between location results and arrival time deviations due to picking or velocity uncertainty is straight forward. However, migration-based location methods image seismic sources through focusing source energy and the relationship between seismic location and seismic waveforms is not straight forward. In addition, many migration-based location methods are based on characteristic functions rather than recorded waveforms, which makes it more difficult to estimated location uncertainties. For traveltime-based location methods, the arrival time residuals at trial source locations are the direct representatives of location accuracy and can be used to estimate the location uncertainty (Lomax et al., 2000). Similarly, the migration values at different trial source locations could also related to the location accuracy and thus related to location uncertainties. However, for MCM and other migration-based location methods, the uncertainty estimation based on migration values of each imaging point still needs further study.

The computational efficiency of MCM still need further improvement. Since the MCM performs migration based on station groups, it can extract much more information for migration compared to conventional migration methods. However, this also brings much more computational cost especially when monitoring arrays contain many seismic stations. The MCM software still need further development. I plan to further improve the computational efficiency of the MCM software using parallel computing such as GPUs and MPI. The computational efficiency of MCM can also be improved by utilizing full-dimensional MCM. For full-dimensional MCM, all the stations are classified into one group. Therefore, the correlation coefficient is only calculated once and no stacking process is needed in the migration. This unique correlation coefficient is the final imaging value at a particular imaging point. In this way, the computational burden can be reduced greatly. However, the way of calculating multidimensional correlation coefficient still need further study and analysis. The performance of multidimensional MCM also need further analysis and verification.

Multicomponent seismic data are often recorded in seismic monitoring. At the present, the MCM imaging data volumes of individual component data are stacked to obtain a unique imaging data volume of a particular imaging area. The stacking process of different imaging data volumes can be weighted according to the data qualities of different component data. However, a more effective way to utilize multicomponent data to perform MCM and image the source still need to be explored. A potential way can be rotating the coordinate axis to maximise the SNR of recorded data and then performing MCM based on the rotated seismic data.

In addition, effectively identifying seismic events in the migration data volume also requires further research. Global optimization algorithms such as simulated annealing, genetic algorithm, neighbourhood algorithm and differential evolution, can be used to efficiently find the maximum imaging value in the whole migration data volumes at a particular origin time. Therefore, it is also an effective way to improve the computational efficiency of the MCM method. In addition, Monte Carlo method can also be used to search for the maximum value in the migration data volume and increase the computational efficiency of MCM.

Magnitude of seismic event can provide valuable information. Since MCM is an automatic seismic location method, further expansion of the MCM software is to automatically perform moment tensor inversion and obtain the earthquake magnitude based on the location results of MCM.

5.7 Concluding remarks

In this thesis, I have developed a seismic forward modeling algorithm and a waveform-based seismic location method. My developed methods can help us better understand the subsurface structures and earthquakes through seismic waveforms. Both algorithms have been parallelized and are highly efficient, which makes them suitable for processing real datasets. My developed seismic forward modeling algorithm is able to simulate wave propagation in heterogeneous and anisotropic media using arbitrary moment tensor sources. Wavefields in various anisotropic media have been generated and analysed. Based on the modeling results, the effects of seismic anisotropy on seismic location are displayed and feasible ways of obtaining subsurface anisotropy are also discussed. My developed seismic location method utilizes waveform coherency among different receiver groups to automatically detect and locate weak seismic events. This event location method has ability to accurately locate microseismic events in noisy data with high imaging resolution. A more complete seismic catalogue with a much lower detection threshold of seismic magnitude can be obtained, which can benefit further studies such as tomography and b-values. This thesis has contributed to the full waveform processing, interpretation and inversion of seismic data, as well as the development of novel seismic modeling and location algorithms that can be applied to various situations.

References

Clark, M. A., Plante, P. L., & Greenhill, L. J., 2013. Accelerating radio astronomy cross-correlation with graphics processing units, *Int. J. High Perform. Comput. Appl.*, **27**(2), 178–192. 5.2.3

Drew, J., White, R. S., Tilmann, F., & Tarasewicz, J., 2013. Coalescence microseismic mapping, *Geophys. J. Int.*, **195**(3), 1773–1785. 5.5

Green, R. G., Greenfield, T., & White, R. S., 2015. Triggered earthquakes suppressed by an evolving stress shadow from a propagating dyke, *Nat. Geosci.*, **8**(8), 629–632. 5.5

Lomax, A., Virieux, J., Volant, P., & Berge-Thierry, C., 2000. Probabilistic earthquake location in 3D and layered models, in *Advances in seismic event location*, pp. 101–134, Springer. 5.6

Rubin, A. M., Gillard, D., & Got, J.-L., 1999. Streaks of microearthquakes along creeping faults, *Nature*, **400**(6745), 635. 5.5

Savage, M., 1999. Seismic anisotropy and mantle deformation: what have we learned from shear wave splitting?, *Rev. Geophys.*, **37**(1), 65–106. 5.1

Schuster, G., 2009. *Seismic interferometry*, Cambridge University Press. 5.1

Shi, P., Angus, D., Nowacki, A., Yuan, S., & Wang, Y., 2018. Microseismic Full Waveform Modeling in Anisotropic Media with Moment Tensor Implementation, *Surv. Geophys.*, **39**(4), 567–611. 5.4.3

Shi, P., Angus, D., Rost, S., Nowacki, A., & Yuan, S., 2019a. Automated seismic waveform location using Multichannel Coherency Migration (MCM)–I. Theory, *Geophys. J. Int.*, **216**(3), 1842–1866. 5.1, 5.2.3

Shi, P., Nowacki, A., Rost, S., & Angus, D., 2019b. Automated seismic waveform location using Multichannel Coherency Migration (MCM)–II. Application to induced and volcano-tectonic seismicity, *Geophys. J. Int.*, **216**(3), 1608–1632. 5.1, 5.2.1, 5.2.3

Thomsen, L., 1986. Weak elastic anisotropy, *Geophysics*, **51**(10), 1954–1966. 5.1

Verdon, J., Kendall, J.-M., & Wüstefeld, A., 2009. Imaging fractures and sedimentary fabrics using shear wave splitting measurements made on passive seismic data, *Geophys. J. Int.*, **179**(2), 1245–1254. 5.1

Verdon, J. P. & Kendall, J.-M., 2011. Detection of multiple fracture sets using observations of shear-wave splitting in microseismic data, *Geophys. Prospect.*, **59**(4), 593–608. 5.1

Virieux, J. & Operto, S., 2009. An overview of full-waveform inversion in exploration geophysics, *Geophysics*, **74**(6), WCC1–WCC26. 5.1

Waldhauser, F. & Ellsworth, W. L., 2000. A double-difference earthquake location algorithm: Method and application to the northern Hayward fault, California, *Bull. Seismol. Soc. Am.*, **90**(6), 1353–1368. 5.1, 5.4.1

Appendix A

Supplemental material Chapter 1

A.1 Summary of some open source location software packages

Various seismic location methods all rely on efficient realization to become useful in practical applications. Here, I summarize some free available open source location software packages and list the access websites and the corresponding references in Table A.1.

Table A.1: Summary of some free access source location software packages

Name	Methodology	Inputs	Website	References
1. HYPO71	linearized inversion	arrival times	Link	Lee & Lahr (1975), Lee & Valdes (1985)
2. HYPOINVERSE	linearized inversion	arrival times	Link	Klein (1978, 2002)
3. HYPOELLIPSE	linearized inversion	arrival times	Link	Lahr (1999)
4. HYPOCENTER	linearized inversion	arrival times	Link	Lienert et al. (1986), Lienert & Havskov (1995)
5. HYPOSAT	linearized inversion	arrival times	Link	Schweitzer (2001, 2018)
6. NonLinLoc	grid search	arrival times	Link	Lomax et al. (2000, 2001)
7. Bayesloc	grid search	arrival times	Link	Myers et al. (2007, 2009)
8. HypoDD	relative location	arrival times	Link	Waldhauser & Ellsworth (2000), Waldhauser (2001)
9. WaveLoc	waveform migration	waveforms	Link	Langet et al. (2014)
10. BackTrackBB	waveform migration	waveforms	Link	Poiata et al. (2016)
11. Seisloc	waveform migration	waveforms	Link	Shi et al. (2019a,b)

References

Klein, F. W., 1978. Hypocenter location program HYPOINVERSE: Part I. Users guide to versions 1, 2, 3, and 4. Part II. Source listings and notes, Tech. rep., US Geological Survey,. A.1

Klein, F. W., 2002. User's guide to HYPOINVERSE-2000, a Fortran program to solve for earthquake locations and magnitudes, Tech. rep., US Geological Survey. A.1

Lahr, J. C., 1999. *HYPOELLIPSE: A computer program for determining local earthquake hypocentral parameters, magnitude, and first motion pattern*, Citeseer. A.1

Langet, N., Maggi, A., Michelini, A., & Brenguier, F., 2014. Continuous Kurtosis-Based Migration for Seismic Event Detection and Location, with Application to Piton de la Fournaise Volcano, La Réunion, *Bull. Seismol. Soc. Am.*, **104**(1), 229–246. A.1

Lee, W. & Valdes, C., 1985. HYPO71PC; a personal computer version of the HYPO71 earthquake location program, Tech. rep., US Geological Survey,. A.1

Lee, W. H. K. & Lahr, J. C., 1975. HYPO71 (revised): A computer program for determining hypocenter, magnitude, and first motion pattern of local earthquakes, Tech. rep., US Geological Survey,. A.1

Lienert, B. R. & Havskov, J., 1995. A computer program for locating earthquakes both locally and globally, *Seismol. Res. Lett.*, **66**(5), 26–36. A.1

Lienert, B. R., Berg, E., & Frazer, L. N., 1986. HYPOCENTER: An earthquake location method using centered, scaled, and adaptively damped least squares, *Bull. Seismol. Soc. Am.*, **76**(3), 771–783. A.1

Lomax, A., Virieux, J., Volant, P., & Berge-Thierry, C., 2000. Probabilistic earthquake location in 3D and layered models, in *Advances in seismic event location*, pp. 101–134, Springer. A.1

Lomax, A., Zollo, A., Capuano, P., & Virieux, J., 2001. Precise, absolute earthquake location under Somma–Vesuvius volcano using a new three-dimensional velocity model, *Geophys. J. Int.*, **146**(2), 313–331. A.1

Myers, S. C., Johannesson, G., & Hanley, W., 2007. A Bayesian hierarchical method for multiple-event seismic location, *Geophys. J. Int.*, **171**(3), 1049–1063. A.1

Myers, S. C., Johannesson, G., & Hanley, W., 2009. Incorporation of probabilistic seismic phase labels into a Bayesian multiple-event seismic locator, *Geophys. J. Int.*, **177**(1), 193–204. A.1

Poiata, N., Satriano, C., Vilotte, J.-P., Bernard, P., & Obara, K., 2016. Multiband array detection and location of seismic sources recorded by dense seismic networks, *Geophys. J. Int.*, **205**(3), 1548–1573. A.1

Schweitzer, J., 2001. HYPOSAT–An enhanced routine to locate seismic events, *Pure Appl. Geophys.*, **158**(1-2), 277–289. A.1

Schweitzer, J., 2018. HYPOSAT 6 and HYPOMOD 2. A.1

Shi, P., Angus, D., Rost, S., Nowacki, A., & Yuan, S., 2019a. Automated seismic waveform location using Multichannel Coherency Migration (MCM)–I. Theory, *Geophys. J. Int.*, **216**(3), 1842–1866. A.1

Shi, P., Nowacki, A., Rost, S., & Angus, D., 2019b. Automated seismic waveform location using Multichannel Coherency Migration (MCM)–II. Application to induced and volcano-tectonic seismicity, *Geophys. J. Int.*, **216**(3), 1608–1632. A.1

Waldhauser, F., 2001. HypoDD–A Program to Compute Double-Difference Hypocenter Locations (HypoDD version 1.0-03/2001), *US Geol. Surv. Open File Rep., 01*, **113**. A.1

Waldhauser, F. & Ellsworth, W. L., 2000. A double-difference earthquake location algorithm: Method and application to the northern Hayward fault, California, *Bull. Seismol. Soc. Am.*, **90**(6), 1353–1368. A.1

Appendix B

Supplemental material Chapter 4

This supporting information provides figures related to the migration profiles of the Aquistore noisy dataset under different signal-to-noise ratios (SNRs). Figures B.1-B.3 show the corresponding vertical and horizontal migration profiles under different SNRs without using the automatic quality control scheme. Figures B.4-B.6 show the show the corresponding vertical and horizontal migration profiles under different SNRs using the automatic quality control scheme.

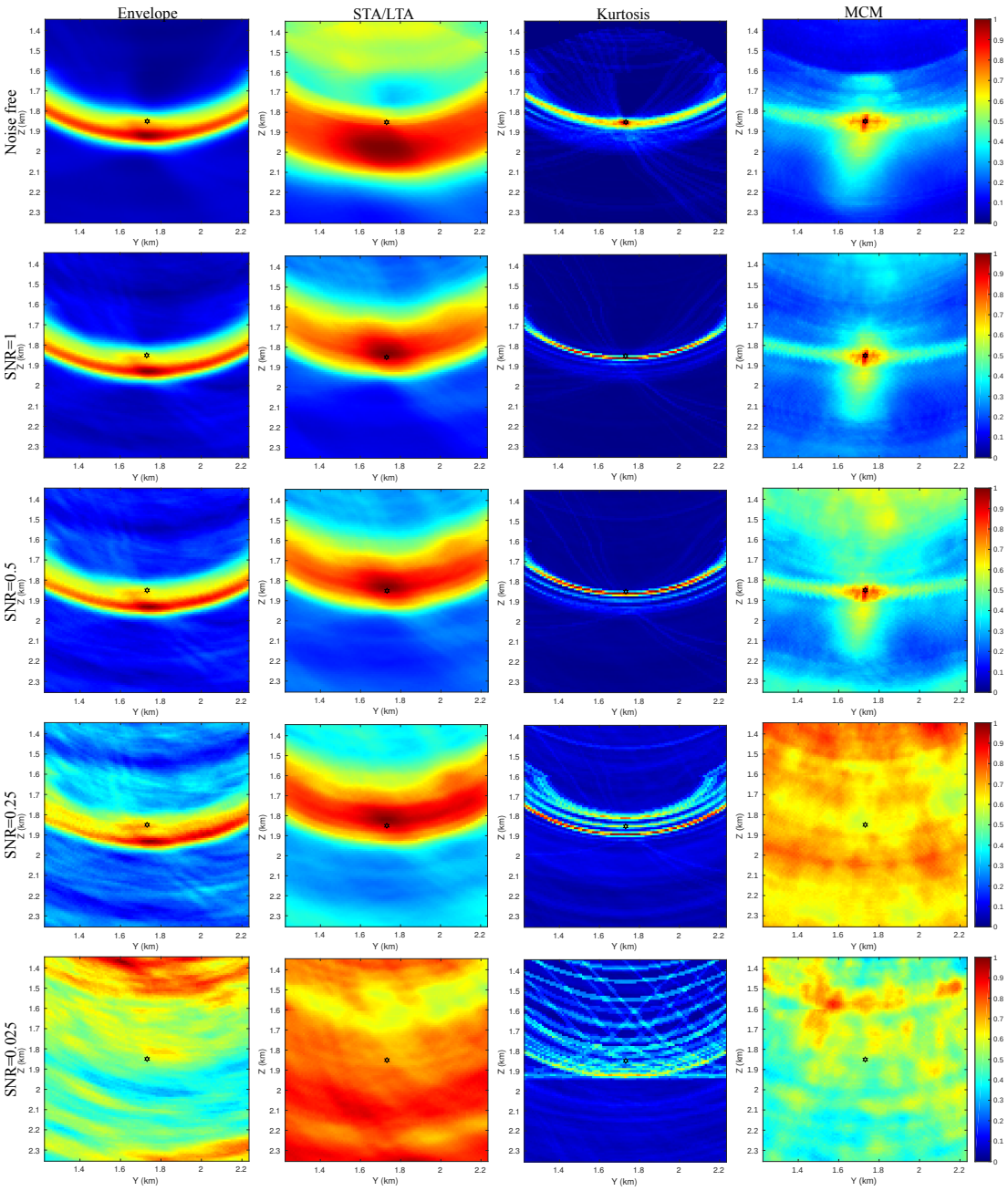

Figure B.1: Vertical profiles (YZ profiles) through the true source location of the migration results under different SNRs for the four methods. The dark star in the center shows the true source location. The first column shows results of envelope, second column for STA/LTA, third column for kurtosis, fourth column for MCM. The first row shows the results when data is free of noise, second row for SNR is 1, third row for SNR is 0.5, fourth row for SNR is 0.25, fifth row for SNR is 0.025.

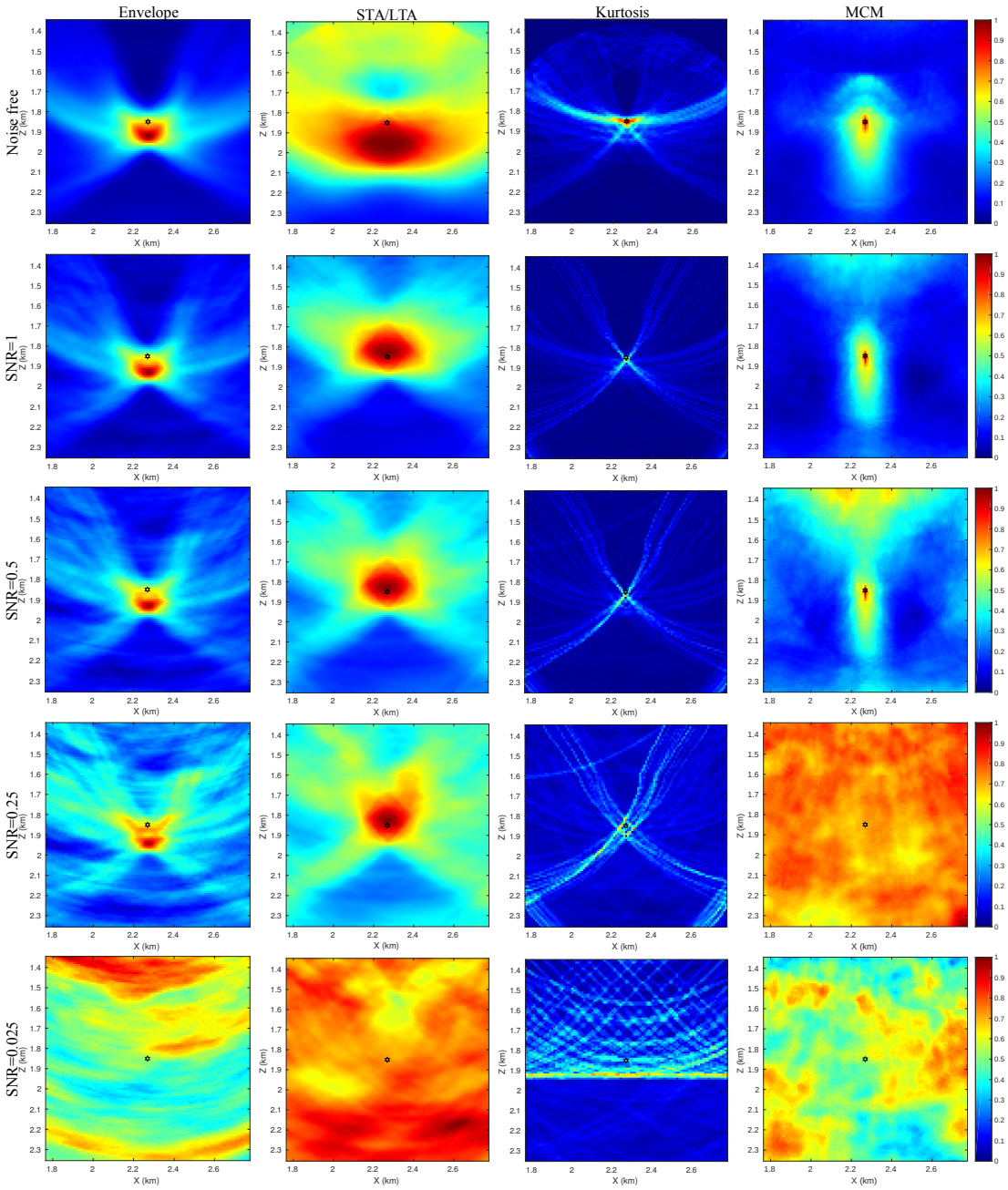

Figure B.2: Vertical profiles (XZ profiles) through the true source location of the migration results under different SNRs for the four methods. The dark star in the center shows the true source location. The first column shows results of envelope, second column for STA/LTA, third column for kurtosis, fourth column for MCM. The first row shows the results when data is free of noise, second row for SNR is 1, third row for SNR is 0.5, fourth row for SNR is 0.25, fifth row for SNR is 0.025.

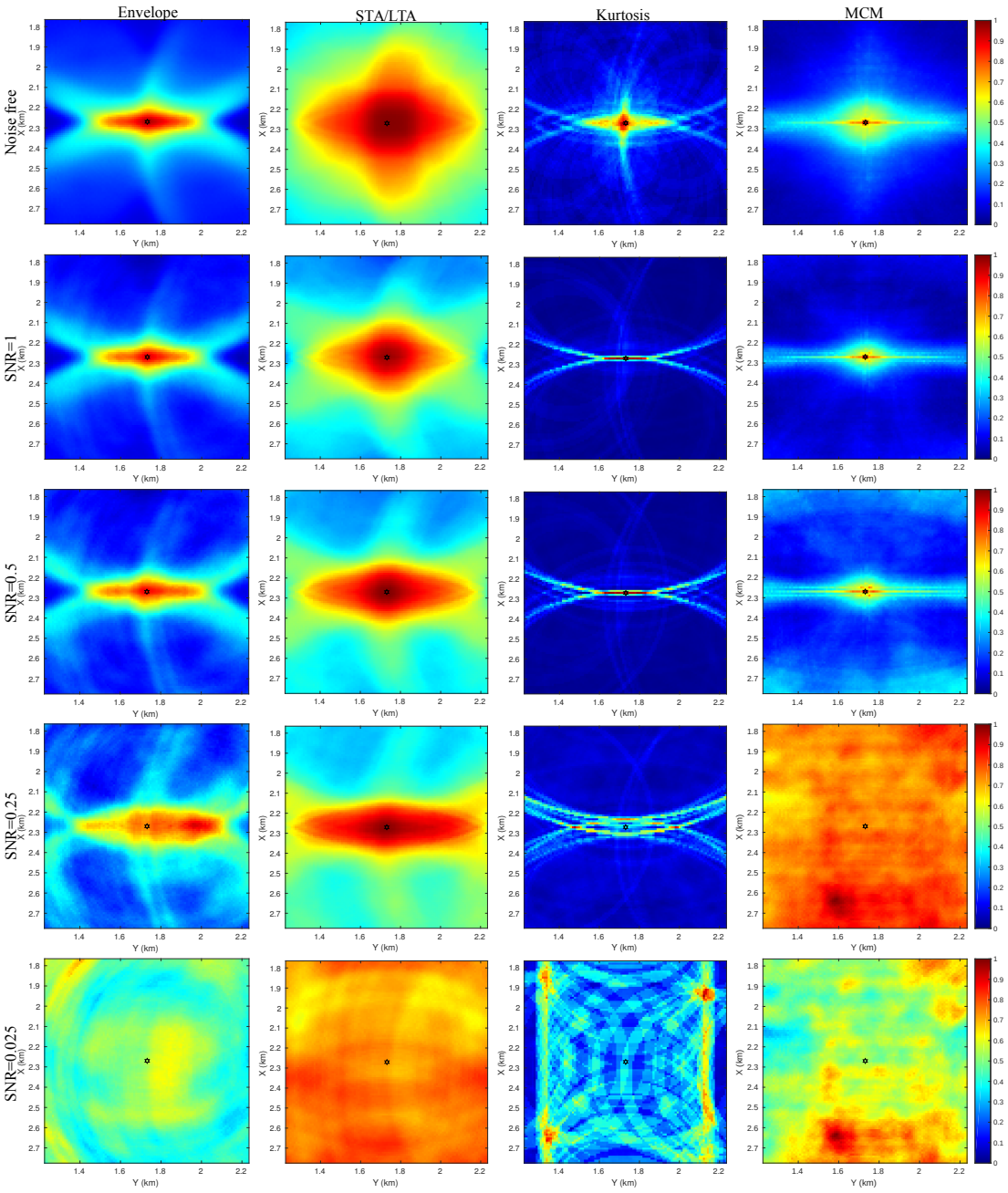

Figure B.3: Horizontal profiles (XY profiles) through the true source location of the migration results under different SNRs for the four methods. The dark star in the center shows the true source location. The first column shows results of envelope, second column for STA/LTA, third column for kurtosis, fourth column for MCM. The first row shows the results when data is free of noise, second row for SNR is 1, third row for SNR is 0.5, fourth row for SNR is 0.25, fifth row for SNR is 0.025.

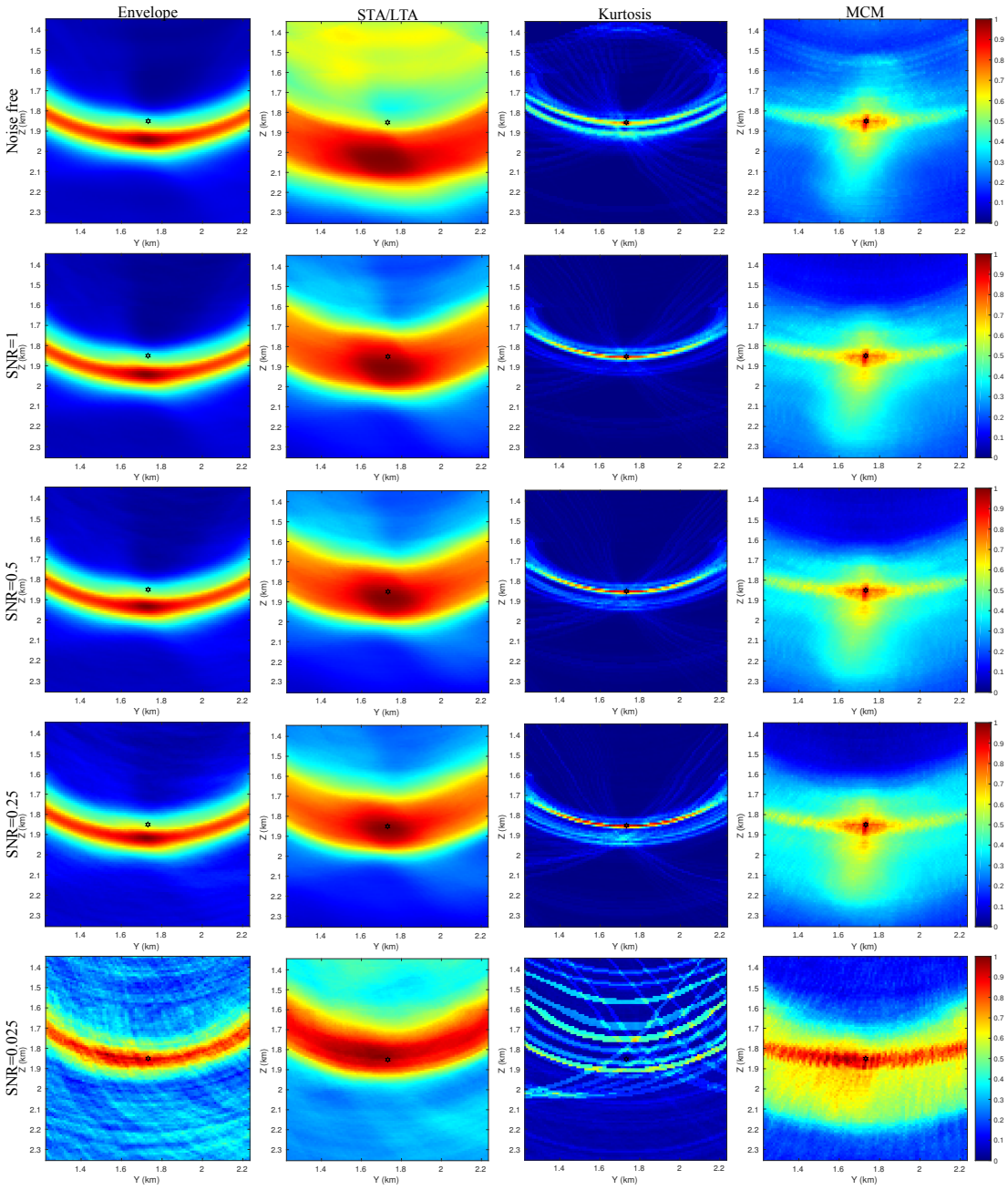

Figure B.4: Vertical profiles (YZ profiles) through the true source location of the migration results with automatic quality control scheme (weighting and filtering) under different SNRs. The dark star in the center shows the true source location. The first column shows results of envelope, second column for STA/LTA, third column for kurtosis, fourth column for MCM. The first row shows the results when data is free of noise, second row for SNR is 1, third row for SNR is 0.5, fourth row for SNR is 0.25, fifth row for SNR is 0.025.

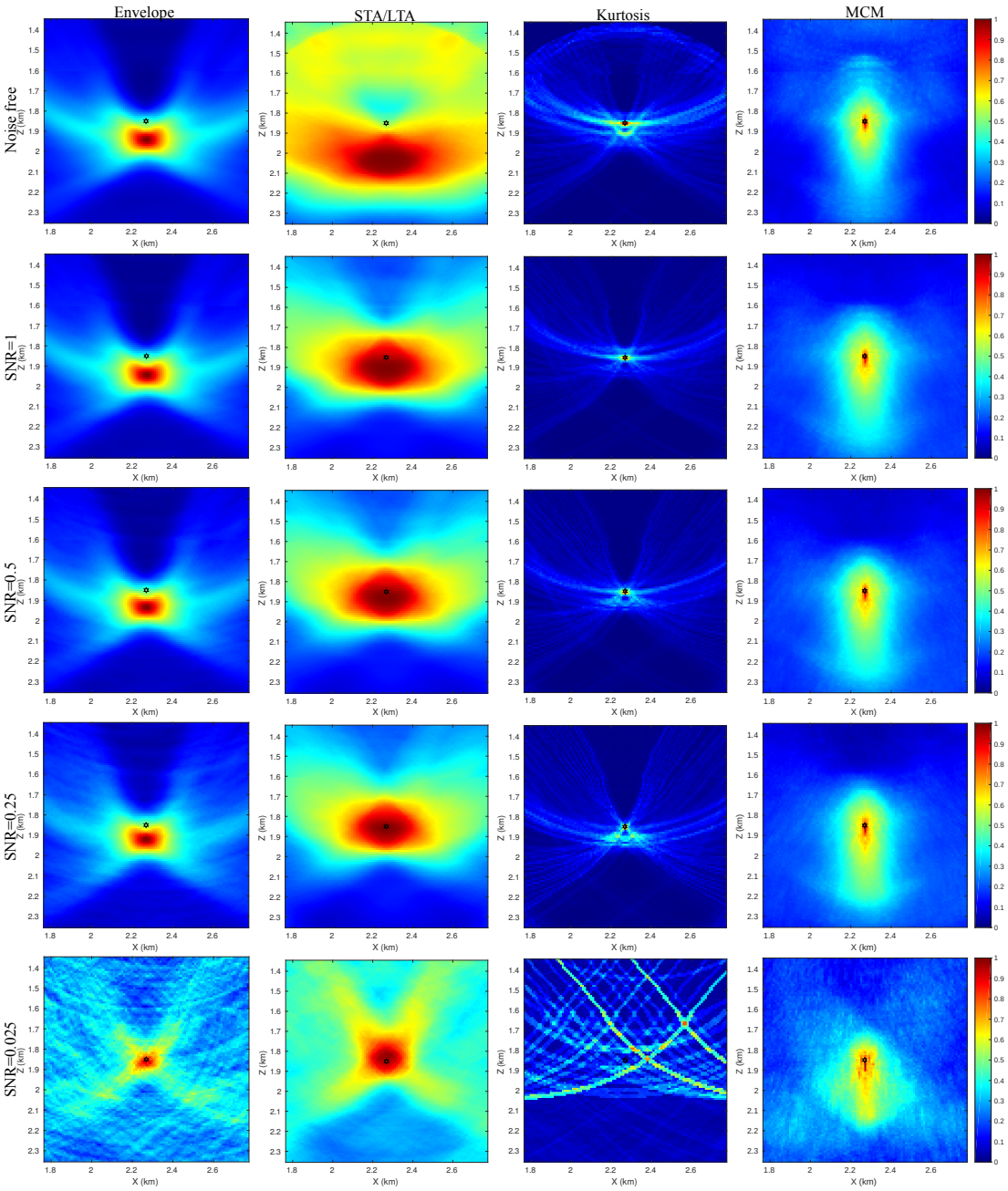

Figure B.5: Vertical profiles (XZ profiles) through the true source location of the migration results with automatic quality control scheme (weighting and filtering) under different SNRs. The dark star in the center shows the true source location. The first column shows results of envelope, second column for STA/LTA, third column for kurtosis, fourth column for MCM. The first row shows the results when data is free of noise, second row for SNR is 1, third row for SNR is 0.5, fourth row for SNR is 0.25, fifth row for SNR is 0.025.

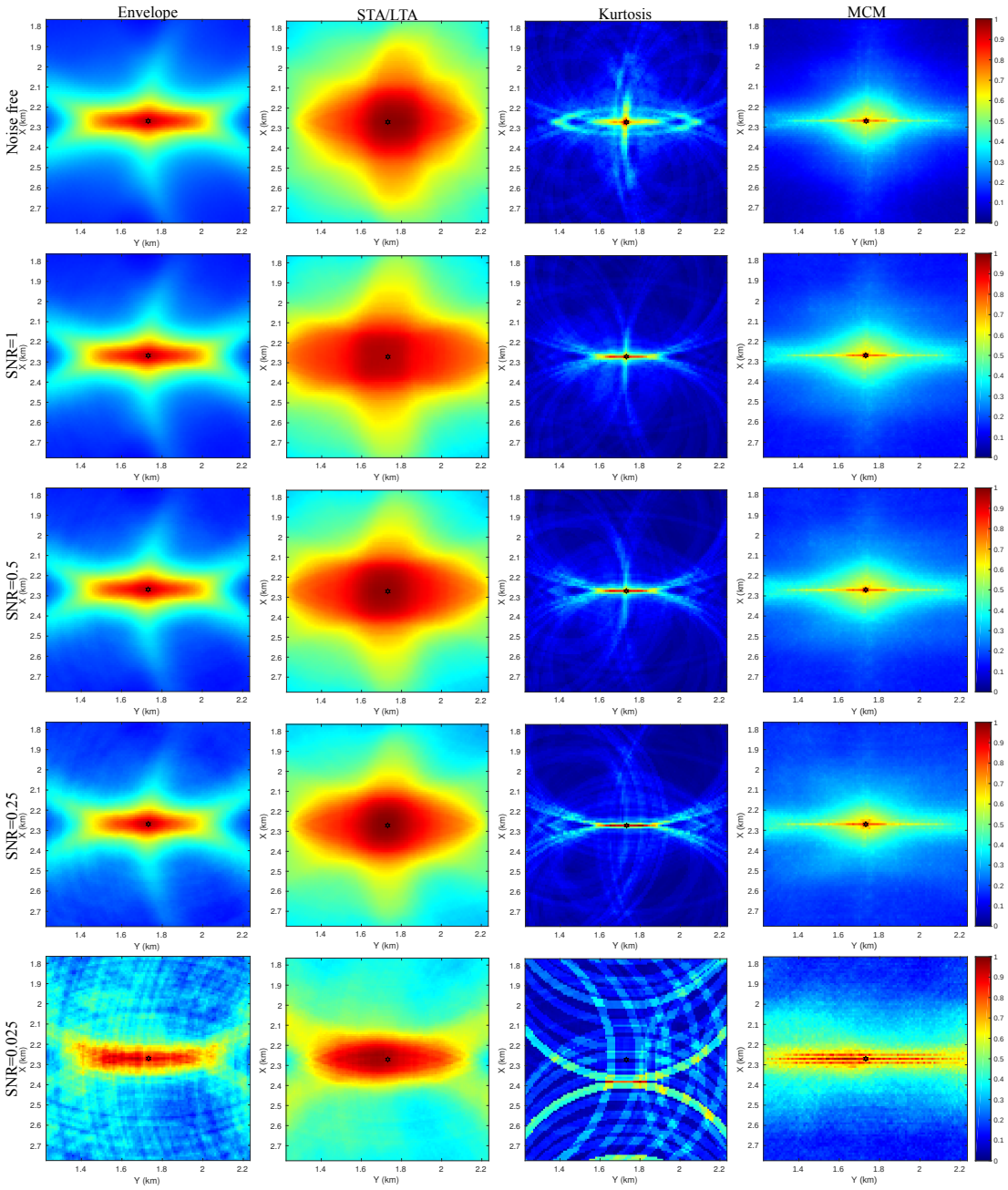

Figure B.6: Horizontal profiles (XY profiles) through the true source location of the migration results with automatic quality control scheme (weighting and filtering) under different SNRs. The dark star in the center shows the true source location. The first column shows results of envelope, second column for STA/LTA, third column for kurtosis, fourth column for MCM. The first row shows the results when data is free of noise, second row for SNR is 1, third row for SNR is 0.5, fourth row for SNR is 0.25, fifth row for SNR is 0.025.